Time-Encoded Thermal Neutron Imaging Using Large-Volume Pixelated CdZnTe Detectors

by

Steven T. Brown

A dissertation submitted in partial fulfillment
of the requirements for the degree of
Doctor of Philosophy
(Nuclear Engineering and Radiological Sciences)
in The University of Michigan
2017

Doctoral Committee:

Professor Zhong He, Chair
Professor Jeffrey A. Fessler
Professor Igor Jovanovic
Professor Sara A. Pozzi

To Emily

ACKNOWLEDGEMENTS

I owe a great deal to the wonderful people who have supported, influenced, and believed in me during my years as a graduate student in Ann Arbor. Without them, I would have never discovered or pursued my interests in engineering, and surely not to the level I've reached today.

Throughout my graduate career, Professor Zhong He has gone far beyond his duties as my academic advisor. I have learned an immense amount from him technically; his thoughtful, principled approach to problem solving is something I will always strive for. He obviously cares deeply about his students, and I consider myself very fortunate to have worked under him. I would also like to thank my other committee members, Professors Sara Pozzi, Igor Jovanovic, and Jeffrey Fessler, for their input and time spent on this work. Most notably, Professor Fessler has taught me a great deal about the statistics of image reconstruction during his years of involvement with my work and education.

My undergraduate advisor, Professor James Baciak, was the first person to encourage me to pursue my interests in radiation detection outside of class. I owe him a great deal, including introducing me to Dr. Carolyn Seifert, who was my advisor for two summers at Pacific Northwest National Lab. They were both students of Professor He's, and I am grateful for their guidance and endorsement as I transitioned to graduate school.

The Orion group at UM is a very special group of people, and I am absolutely privileged to have worked with them. I would like to thank a few of these members

who were especially helpful during my final months of measurements. First of all, Bennett Williams was always on call for repairing malfunctioning equipment during my measurement campaigns; all imaging results here are in part the result of his handiwork. Jiawei Xia developed a peak fitting algorithm which I used to measure photopeak efficiency for thermal neutron detection, one of my main results. My many fruitful discussions with David Goodman over the years have surely improved the quality of my thesis work, in more ways than I can enumerate. He also helped with setting up neutron experiments and processing the data to form images from the ^{3}He tube.

Thanks also goes out to Sean O'Neal, Jiyang Chu, Michael Streicher, and Daniel Shy who helped review this work along with the previous group members. Dr. Yuefeng Zhu, in addition to providing invaluable technical advice throughout my graduate career, wrote the XCORR2 code in Appendix C which I used for imaging. Dr. Shaun Clarke and Dr. Angela Di Fulvio kindly helped arrange my neutron experiments. Kevin Moran is the mechanical engineer who did a fantastic job building the time-encoding system in this work, and Dr. Jason Jaworski generously helped program its movement in his spare time.

I'd also like to thank some close friends I met during my time here: Drs. Jeffrey Fein, William Koehler, and Michael Streicher. My experience in Ann Arbor would simply not be the same without them. My family in Florida, Christopher, Gail, and Emily Brown, have always been incredibly supportive; their love and encouragement are the true basis of my success. Above all, I would like to thank my lovely fiancé, Emily Lake. Now that my thesis is finished, I should start another book to outline the ways she makes this all worthwhile.

This material is based upon work supported by the National Science Foundation Graduate Research Fellowship Program under Grant No. F031543 and DOE NA-22 Office (Award #: DE-NA002132).

TABLE OF CONTENTS

DEDICATION ii

ACKNOWLEDGEMENTS iii

LIST OF FIGURES viii

LIST OF TABLES xv

LIST OF APPENDICES xvi

LIST OF ABBREVIATIONS xvii

ABSTRACT xix

CHAPTER

I. Introduction 1

1.1 Transmission versus Emission Imaging 2
1.2 Overview of Thermal Neutron Imaging 4
1.3 Mechanism for Thermal Neutron Detection in CdZnTe 7
1.4 Introduction to Time-Encoded Imaging 10
1.5 History of Time-Encoded Imaging 15
1.6 Contributions and Summary of this Work 19

II. Overview of Pixelated CdZnTe Detectors 21

2.1 Detection of Ionization Events 21
2.1.1 Charge Generation 24
2.1.2 Small Pixel Effect 26
2.2 Gamma-Ray Imaging 32
2.2.1 Compton Imaging 33
2.2.2 Coded Aperture Imaging 35
2.3 Limitations Related to Coded Imaging 38
2.3.1 Spatial 38

2.3.2 Temporal 42

III. Thermal Neutron Emission and Cd Capture 46

3.1 Nature of Thermal Neutron Emissions 46
3.1.1 Energy and Velocity Distributions 46
3.1.2 Neutron Moderation Process 49
3.2 Cd Capture in CdZnTe 57
3.2.1 Energies and Multiplicity of Cascade Gamma Rays . 60
3.2.2 Spatial Distribution of 558 keV Interactions 64

IV. Measured Thermal Neutron Detection Performance 69

4.1 Measurement of Cascade Gamma Rays at NARS 70
4.1.1 Modulation of Neutron Beam with ^{6}Li Glass Plate . 71
4.1.2 Observation of Coincident Cascade Gamma Rays . . 74
4.1.3 Spatial Discrimination of Neutrons and Gamma Rays 75
4.2 Measured Detection Efficiency 86
4.3 Directionality from Surface Illumination 92
4.4 Discussion and Conclusion 99

V. Time-Encoded Imaging Theory 103

5.1 Measurement Setup for Planar Coded Imaging 103
5.2 Encoding-Decoding Process Using Imperfect Detectors 107
5.2.1 Time Domain (Time-Encoded Imaging) 108
5.2.2 Spatial Domain (Coded Aperture Imaging) 110
5.2.3 Combined Time and Spatial Domains 112
5.3 Coded Imaging Using Cyclic Difference Sets 114
5.3.1 One-Dimensional Codes 114
5.3.2 Two-Dimensional Codes 116
5.3.3 Signal-to-Noise Ratio of (M)URAs 118
5.4 Summary 120

VI. Time-Encoded Imaging System Design 121

6.1 Mask Positioning System 121
6.2 Gamma-Ray Mask 126
6.3 Thermal Neutron Mask 126
6.3.1 Signal-to-Noise Ratio 127
6.3.2 Effect of Neutron Speed Distribution 132

VII. Gamma-Ray Imaging Performance 135

7.1 ^{57}Co Measurements 136

7.1.1 Check Source, Close to Mask . . . 136
7.1.2 Check Source, Away from Mask . . . 139
7.1.3 Flexible Marker, Coiled . . . 141
7.2 Uranium Metal Measurements . . . 145
7.2.1 Highly Enriched Uranium Metal Disks . . . 145
7.2.2 Natural and Depleted Uranium Metal Disks . . . 147
7.2.3 Radiation Signature Training Device . . . 149
7.3 Discussion and Conclusion . . . 154

VIII. Thermal Neutron Imaging Performance . . . 155

8.1 Single Moderated ^{252}Cf Source . . . 156
8.2 Two Moderators and ^{252}Cf Source . . . 164
8.3 Images from ^{3}He Tube . . . 166
8.4 Signal-to-Noise Ratio . . . 170
8.5 Discussion and Conclusion . . . 175

IX. Summary and Future Work . . . 178

9.1 Summary . . . 178
9.2 Suggestions for Future Work . . . 180

APPENDICES . . . 182

BIBLIOGRAPHY . . . 197

LIST OF FIGURES

Figure

1.1 Illustration of time coding, as described in the text. (a) Three point-like sources emit particles isotropically in front of a single detector, with a counter-clockwise-rotating disk between them that blocks incident radiation except through a single hole. (b) Measured signal versus disk angular position. 12

1.2 Two detectors viewing two sources. The perspective from d_2 provides the distance and intensities of the two sources away from d_1, a demonstration of the utility of parallax in the near field. 13

1.3 Two detectors viewing four sources. Only measurements at two angular positions, θ_1 and θ_2, are needed to resolve all four source intensities. 14

2.1 Attenuation coefficients for gamma-ray interactions in $Cd_{0.9}Zn_{0.1}Te$ as a function of gamma-ray energy. Each curve is the product of the mass attenuation coefficients tabulated by NIST in cm^2/g [1] and CdZnTe mass density 5.78 g/cm^3 [2]. 23

2.2 Anode layouts for (a) gridded and (b) simple pixel detectors [3]. . . 28

2.3 Weighting potentials calculated for the simple pixel detector geometry. 29

2.4 highly enriched uranium (HEU) gamma-ray spectra measured by the Orion 4-detector and Polaris SP 18-detector systems at the Y-12 Nuclear Detection and Sensor Testing Center (NDSTC). 32

2.5 Back-projection Compton image of a point-like source of 662 keV gamma rays from ^{137}Cs using the Polaris II CdZnTe array and UMImaging software. 35

2.6 (a) Polaris 18-detector CdZnTe array. (b) 17×17 modified uniformly redundant array (MURA) pattern. 36

2.7 (a) Map of counts on Polaris 3×3 CdZnTe detector array. (b) Image from correlation with MURA pattern pictured in Figure 2.6(b). . . 37

2.8 Counts on each pixel of Polaris II due to a flood irradiation of gamma rays at different energies and incident angles. "Perpendicular" refers to a far field source centered with the array cathodes, and "angled" is a far field source offset towards the right from the plane's centerline into the page. 40

2.9 Time behavior of uranium K_α x-ray count rate (95 keV and 98 keV) during depleted uranium (DU) measurement using Polaris SP. (a) Counts versus time for plane B, the only working detector plane. (b) discrete Fourier transform (DFT) of count rate with its mean (DC) value subtracted. 44
2.10 Statistical behavior of 511-keV photopeak count rate over time during uniform ^{22}Na irradiation of Polaris SP. (a) Counts versus time for each plane, each with nine detectors. (b) Counts versus time for three representative detectors. (c) Distribution of count rates for detector 13. (d) Distribution of count rates for channel 98 of detector 13, the pixel which recorded the most counts. 45
3.1 Characteristic energy and velocity distributions for neutrons in thermal equilibrium at room temperature. (a) Neutron flux distribution in energy. (b) Reaction rate distributions in velocity normalized to their integrals for $1/v$ materials and Cd. 48
3.2 Plot of carbon cross section versus neutron energy, adapted from [4]. Solid lines are from ENDF/B-VII.1 [5] and lines with data points are from the XFOR library [6]. Boxed numbers are labeled cross section features described in the text. 51
3.3 Calculated neutron spectra leaving ^{252}Cf surrounded by spherical polyethylene of various thicknesses. Sphere inner diameter was 3 in. 57
3.4 (a) Cross sections for reactions with several low-Z nuclides used commonly in neutron detection. (b) Exceptionally high radiative capture cross sections exhibited by several common nuclides. All cross sections were taken from ENDF/B-VII.1 evaluated nuclear data [5] except for ^{135}Xe(n,γ), taken from the JEFF-3.1 Nuclear Data Library [7]. 59
3.5 ^{114}Cd nuclear level scheme for levels below 1365 keV only [8], with chart generated using the National Nuclear Data Center (NNDC) website [9]. The black text provides each level energy in keV as well as spin-parity, the green text indicates the half life for each level, and the blue text is the gamma-ray energy in keV corresponding each transition. The vertical separation of levels is proportional to their energy difference. Levels on the left correspond to the ground state rotational band. 62
3.6 Yield of gamma rays from ^{113}Cd capture, downloaded from CapGam of NNDC [10]. Uncertainties also reported there. Gamma-ray lines identified in gamma-ray spectra recorded using the Polaris SP pixelated CdZnTe array as part of this work are indicated with red boxes. 63

3.7 (a) Exponential attenuation of thermal neutrons in CdZnTe, the resulting 1-D interaction distribution of 558 keV cascade gamma rays according to Equation 3.18, and attenuation of 558 keV gamma rays from a far-field source for comparison. (b) Comparison between 558 keV interaction distributions in the x direction for a 1.5-cm-thick pixelated CdZnTe detector, predicted by Equation 3.18 and calculated using Geant4, as described in the text. 66
3.8 Calculated interaction distributions of 558 keV gamma rays in a single 2 cm × 2 cm × 1.5 cm CdZnTe crystal for (a) one- and (b) two-pixel events due to a pencil beam of thermal neutrons incident at the center x and y pixel (6,6) above. Two-pixel event locations were chosen according to the first interaction, where the sequence was chosen using the simple comparison method. Calculated using Geant4. 67
4.1 (a) Polaris Separable Plane (SP) system with both plane's cathodes facing a button source of gamma rays. (b) Output of the beam port at the Nuclear Analysis and Radiation Sensor (NARS) laboratory. The beam was incident from the bottom of the picture, through the round sample chamber, and onto the cathodes of Polaris SP's plane B, positioned near the center of the photograph. 71
4.2 Gamma-ray energy spectra for thermal neutrons incident on Polaris SP CdZnTe array. (a) Spectra for unshielded neutron beam and shielded by ^{6}Li glass plate. (b) Unshielded spectrum separated by the number of triggered pixels per event. 72
4.3 Spatial distribution of 1- and 2-pixel events for three different gamma-ray energy windows. The circular shape of the thermal neutron beam can be seen at the right side of the array. The ^{6}Li glass plate partially blocked the beam, leaving the bottom right detector most exposed to thermal neutrons. 73
4.4 Coincidence energy spectra for events which fall within energy windows corresponding to the sum of two coincident cascade gamma rays from Cd capture. Measured using Polaris SP at the NARS laboratory. 76
4.5 Selected coincidence spectra from Figure 4.4 with additional spatial filters as described in the text. Measured using Polaris SP at the NARS laboratory. 77
4.6 2-D representation of Polaris SP detector array during cathode irradiation of a mixed thermal neutron and gamma ray beam at NARS. The beam is incident from the top of the page (-z direction) onto the cathodes, located at z = 15 mm (pixelated anodes at z = 0). (a) 1-pixel, (b) 2-pixel, and (c) 3-pixel interactions from both cascade and background gamma-ray events are illustrated along with vectors indicating their position coordinates, as described in the text. 78
4.7 Depth-separated, gamma-ray energy spectra for all 1-pixel events measured by Polaris SP's plane B during thermal neutron irradiation of its cathodes. Depth, equivalent to f_d of Equation 4.1, is labeled as distance from anodes, i.e., the cathode's position was at 15 mm. . . 79

4.8 Depth-separated, gamma-ray energy spectra for all 2-pixel events measured by Polaris SP's plane B during thermal neutron irradiation of its cathodes. Cascade gamma ray lines are indicated by arrows. 80
4.9 Individual gamma-ray energy spectra for all 2-pixel events measured by Polaris SP's plane B during thermal neutron irradiation of its cathodes. Here, events are classified by distance between interactions, or f_s of Equation 4.2. 81
4.10 Depth-separated, gamma-ray energy spectra for all 3-pixel events measured by Polaris SP's plane B during thermal neutron irradiation of its cathodes. 82
4.11 Gamma-ray energy spectra for all 3-pixel events measured by Polaris SP's plane B during thermal neutron irradiation of its cathodes. Here, cascade gamma rays that interact only once via photoelectric effect are classified by their separation distance from the other two interactions, i.e., f_p of Equation 4.3. 83
4.12 Gamma-ray energy spectra for all 3-pixel events measured by Polaris SP's plane B during thermal neutron irradiation of its cathodes. Here, cascade gamma rays that scatter once before absorption are classified by larger separation distance from a third interaction, described by feature f_C of Equation 4.4. 84
4.13 Ratio of background-subtracted 558-keV peak area to total area with background for (a) depth-separated and (b) distance-separated spectra. 85
4.14 (a) BF_3 and (b) ^{3}He (right) pulse height spectra. Vertical dashed lines indicate acceptance range for neutron-induced pulses during the experiment. The broad "bump" in counts between channels 100 and 1000 of the BF_3 spectrum is a known feature of this particular detector and is assumed to be noise. 87
4.15 Experimental setup for efficiency measurement. (Left) Photograph. (Right) Diagram from top-down perspective. 88
4.16 Gamma ray energy spectra using the sum-energy of each event and the energy of all combinations of interactions for each event. 90
4.17 (a) Exponential fit to gamma-ray continuum. (b) Background-subtracted spectrum with fits for 511 keV and 558 keV photopeaks. 91
4.18 Background-subtracted CdZnTe gamma-ray spectra generated by thermal neutrons from 1 Ci PuBe in paraffin; measurement with 1 in borated polyethylene was subtracted from without. 95
4.19 Intensity attributed to each side of the array via Compton imaging for each orientation. The legend provides the (polar,azimuthal) angle to the source in degrees. 97
4.20 Representative comparison between simulation and measurement showing relative 558 keV counts amongst detectors. This plot is for the left-side-facing, or (90°,90°) orientation of the source relative to the detector array. 99

4.21 Maps of squared difference between simulation and measurement as a function of neutron emission direction from around the CdZnTe array for each measurement. Dark areas have lower squared difference, with a ceiling of 0.3 set to white to better compare each shape. The least squared difference for each measurement is indicated by the ∘ symbol. This is the estimated direction from thermal neutron capture. The + symbol indicates the direction estimated by the centroid of the Compton image of 2.2 MeV H capture in the paraffin. 102
5.1 Planar coded imaging geometry, adapted from [11]. 104
6.1 Screen captures of Mira system design from Solidworks CAD software. A single plane of Polaris SP was positioned on detector stage, pictured with purple backing in (a), and orange front face in (b). Stepper motors are pictured in black at the ends of the vertical and horizontal ball screws for x and y movement of the mask between object and detector. 122
6.2 Block diagram for a time-encoded measurement using Mira and Polaris SP. 123
6.3 Evidence for Poisson distribution of time between events during a laboratory background measurement, indicating the acquisition of proper event timing information from the FPGA on board Polaris SP. 124
6.4 1-D representation of geometry and mask movement scheme utilized for time-encoded imaging. The example mask pattern is based on a (7,3,1)-cyclic-difference set. 125
6.5 Basic pattern and mask used for time-encoded gamma-ray imaging. 127
6.6 Plot of correction factor, η, versus projected (magnified) mask element pitch, mp_m, at the detector plane. 130
6.7 Predicted signal-to-noise ratio (SNR) of object pixels in an image of the BeRP ball reflected by polyethylene after one hour measurement using a coded aperture mask with element pitch $p_m = 1.6$ cm. SNR is plotted for a range of distances between the detector, mask, and object. Dotted contour lines indicate the number of image pixels subtended by the source at each configuration. Solid contour lines show the number of hours required to achieve SNR of 10. 131
6.8 MURA pattern and actual mask used for time-encoded thermal neutron imaging. Note that dark elements in (a) correspond to light-colored BN tiles in (b). 132
6.9 Reaction rate time distributions in time for thermal neutrons at $T = 290$ K traveling 1 m between a perfectly-attenuating time-coded aperture and thin detector of various σ. 133
7.1 ^{57}Co gamma-ray energy spectrum measured using Polaris SP. 136
7.2 Measured patterns and images reconstructed via correlation with the mask pattern. Each image pixel is 1.5 mm on a side. The data used was either from the entire array, center detector, or center anode pixel. Image grid lines have 1 cm pitch. 138
7.3 Distribution of intensities outside the peak in Figure 7.2(f). 139

7.4 Effect of parallax at several image planes reconstructed using different distances from the mask, where the true distance was $a = 7.5$ cm. Each image uses 2.8×10^6 counts. 140
7.5 Reconstructed intensities at 122 keV as a function of distance from the mask, where true distance was $a = 7.5$ cm. Each image uses 2.8×10^6 counts. 142
7.6 Reconstructed image with photograph for reference. The tube containing ^{57}Co solution has inner diameter of 0.8 mm and outer diameter of 2.4 mm. Grid lines have 1 cm spacing, and color scale maximum is set at maximum pixel value outside aliased areas on right and bottom of edges image. 143
7.7 Separation between peaks from ^{57}Co solution within tubes, which have inner diameter 0.79 mm and outer diameter 2.38 mm. The higher peaks are aliased, i.e., they are the result of two overlapping parts of the tube. 145
7.8 Reconstructed images using 1.7×10^7 counts at 122 keV for different source-to mask distances, where the true distance was $a = 2$ cm. Color scale is cut off at zero to improve contrast. Grid lines have 1 cm spacing. 146
7.9 Reconstructed images of 3-cm-diameter, 54% (top) and 70% enriched (bottom) HEU metal disks at different source-to-mask distances, a. In total, 5.6×10^6 1-pixel counts between 80 keV to 215 keV were used. Color scales are cut off at zero to improve contrast, and grid lines have 1 cm spacing. 148
7.10 Reconstructed images and spectrum from 3-cm-diameter, DU (top disk) and natural uranium (NU) (bottom disk) metal disks at different distances from mask, a. In total, 1.6×10^6 1-pixel counts between 90 keV and 117 keV were used. Color scale is cut off at zero to improve contrast, and image grid lines have 1 cm spacing. 150
7.11 Photograph of two Radiation Signature Training Device (RSTD)s [12]. One has top hemisphere removed, revealing its DU core at center. The outer layer consists of an Al-HEU alloy enclosed in a thin Al shell. 151
7.12 Reconstructed images of HEU (top, from 80 keV to 215 keV) and DU (bottom, at 1001 keV) portions of RSTD sphere. Dotted line on Compton images are circles centered at the maximum pixel with radius equal to RSTD's (6.3 cm or about 15°), centered at $a = 8.0$ cm. For time coded images, 2.7×10^7 1-pixel events were used, color scale is cut off at zero to improve contrast, and grid lines have 1 cm spacing. 153
8.1 Photographs of first experimental setup. 156
8.2 Gamma-ray energy spectra from 1 h imaging data separated by number of anode pixel triggers. Inset plot is a zoom-in on the 558-keV peak and energy window, using a linear y scale. 157

8.3 Pattern and image at 558 keV from 8 h measurement, or 1.4×10^5 counts. Grid lines have 10 cm pitch. 158
8.4 Reconstructed, over-sampled images at 558 keV. Grid lines have 10 cm pitch. 159
8.5 Reconstructed images at different object distances away from the mask, a. Both 1- and 2-pixel, 558-keV interactions were used for each image, in total 1.4×10^5 counts. Color scaled is cut off at zero to improve contrast. Grid lines have 10 cm pitch. 160
8.6 Reconstructed intensities at 558 keV as a function of distance from the mask, a, using 1.4×10^5 counts. White dashed lines intersect maximum intensity pixel. 161
8.7 Images at 558 keV reconstructed via correlation using events from different depths away from the anode. (a) Between 2 mm to 6 mm from anode. (b) Between 10 mm to 14 mm from anode. (c) Vertical image slices. (d) Horizontal image slices. (e) Energy spectra for different depths. White dashed lines in (a) and (b) mark locations of image slices for (c) and (d). Grid lines in (a) and (b) have 10 cm pitch. 163
8.8 Photographs of second experimental setup. 165
8.9 Images reconstructed from separate data from near and far moderators, each using the 558 keV gamma-ray signal. Image grids have 10 cm pitch. 165
8.10 558-keV images reconstructed at different distances from the mask, a, using 3.2×10^5 counts. Color scale is truncated at zero to improve contrast, and grid lines have 10 cm pitch. 167
8.11 (a) Gamma-ray energy spectrum and (b) back-projected Compton image at 2.2 MeV from UM Imaging [13]. Sources are centered at about 100° azimuthal and 110° polar. Note that in this plot, 180° polar is straight up from the detector and 0° polar is down, so the image appears to be vertically flipped relative to the neutron images. 168
8.12 Polaris SP and ^{3}He tube positioned above. Photograph was taken prior to constructing the borated polyethylene box for the second experiment. 169
8.13 Measured patterns and reconstructed images using ^{3}He tube during measurements of Section 8.2. Each image pixel subtends a $2.6° \times 2.6°$ solid angle. 171
8.14 (a) SNR versus counts for first and second data sets, as described in the text. Theory is based on a background estimate made during the first set of measurements and Equation 5.17. (b) Variance of pixels outside of the source region versus number of counts. Dashed line is variance equals counts. 173
A.1 Side view, single moderator. All lengths in cm. 183
A.2 Top view, single moderator. All lengths in cm. 184
A.3 Top view, two moderators. Moderator nearer to detector was raised an additional 8.3 cm out of page using two Al boxes (not pictured). All lengths in cm. 185

LIST OF TABLES

Table

2.1 Comparison of selected semiconductor characteristics [14]. 25
3.1 Slowing down parameters of commonly-used moderators, adapted from Table 8-1 of [4]. 53
3.2 Transitions of intensity $\geq 1\%$ for the excited compound ^{114}Cd nucleus as a result of ^{113}Cd capture, organized by intensity. Parameters given are the transition energy, intensity expressed in percent of ^{113}Cd captures [10], gamma-ray multipolarity [8], and total internal conversion coefficient (ICC) [15]. Multipolarity information was not available for transitions above 5 MeV. 64
4.1 List of parameters for both neutron detectors used in the experiment. 87
4.2 Experimental count rates from both neutron detectors and conversion to neutron flux. 88
4.3 Coordinate system assigned to the array, corresponding to Figures 4.19 and 4.21. Left and Right are outward-facing directions normal to the cathodes of each plane. 98
4.4 Comparison of thermal neutron source directions estimated from the centroid of the 2.2 MeV H capture line and Cd capture. All values in degrees. 100
5.1 Difference table for the $(11, 5, 2)$-cyclic-difference set $\{1, 3, 4, 5, 9\}$. Due to the special properties of the cyclic difference set, each difference between the 5 numbers in the top row and left column modulo 11 appears precisely 2 times. 115

LIST OF APPENDICES

Appendix

A. Experimental Setup For Thermal Neutron Imaging 183

B. Arduino Program for Mask Movement 186

C. Matlab Functions for Image Reconstruction 194

LIST OF ABBREVIATIONS

SNR signal-to-noise ratio

SNM special nuclear material

FOV field of view

URA uniformly redundant array

MURA modified uniformly redundant array

RMC rotating modulated collimator

SPRINT Single Photon RINg Tomograph

HDPE high-density polyethylene

PRISM Portable Rotating Imager using Self Modulation

ML maximum likelihood

EM expectation maximization

EXIST Energetic X-ray Imaging Survey Telescope

SP Separable Plane

NARS Nuclear Analysis and Radiation Sensor

OSURR Ohio State University Research Reactor

PCB printed circuit board

MFP mean free path

NNDC National Nuclear Data Center

ICC internal conversion coefficient

MFP mean free path

GMI Gamma-Medica-Ideas

ASIC application specific integrated circuit

PSF point spread function

URA uniformly redundant array

MURA modified uniformly redundant array

FWHM full width at half maximum

NDSTC Nuclear Detection and Sensor Testing Center

HEU highly enriched uranium

DFT discrete Fourier transform

DU depleted uranium

RSTD Radiation Signature Training Device

NU natural uranium

SOE stochastic origin ensembles

FPGA field-programmable gate array

BeRP Be-Reflected Plutonium

ABSTRACT

Time-Encoded Thermal Neutron Imaging Using Large-Volume Pixelated CdZnTe Detectors

by

Steven T. Brown

Chair: Zhong He

CdZnTe detectors are commonly used for room-temperature gamma-ray spectroscopy and imaging in a variety of applications including nuclear security, nuclear medicine, and space science. The material's long-established sensitivity to thermal neutrons, however, is less utilized. Generally speaking, the performance of neutron detectors based on the Cd capture reaction is limited by the physical nature of the reaction itself. Multiple gamma rays are emitted promptly following each capture event, which consists of one realization of many possible combinations of gamma-ray lines. Although the gamma-ray cascade can reduce photopeak efficiency in conventional devices, this work demonstrates that pixelated CdZnTe can recover losses by reading out each gamma-ray interaction separately. Including coincident events, the measured 558-keV photopeak efficiency for a 3 $\times$ 3 array of 2 cm $\times$ 2 cm $\times$ 1.5 cm pixelated CdZnTe detectors was about 10%, i.e., ten 558 keV photopeak events per 100 incident thermal neutrons. This was in good agreement with its calculated value. Initial measurements also show that neutron-gamma discrimination beyond simple energy windowing is possible when incorporating the 3-D interaction locations of gamma

rays provided by the pixelated readout.

In this work, we developed and successfully demonstrated a proof-of-principle time-encoding system for thermal neutron imaging using pixelated CdZnTe. Time encoding was chosen because it is not limited by the detector's position resolution or spatial extent. These issues are exacerbated by Cd capture due to the dispersal of cascade gamma rays throughout the device. The system was first tested using a MURA-based, W-metal mask with both ^{57}Co and U-metal gamma-ray sources. About 0.3° angular resolution within a 22° field of view was achieved for gamma rays, and good image uniformity was observed for objects of moderate spatial extent. A MURA-based thermal neutron mask was then constructed using 1-mm-thick BN tiles, which attained roughly 4° angular resolution within a 50° field of view when measuring HDPE-moderated ^{252}Cf. Two different thermal neutron imaging measurements were taken, with one and two moderators within the field of view. Reconstructed images corresponded well with the 3-D locations and sizes of moderators, and have predictable signal-to-noise ratio. We believe the experimental imaging results provided here warrant further studies on the use of CdZnTe for other thermal neutron imaging scenarios.

CHAPTER I

Introduction

CdZnTe is a wide-bandgap semiconductor material that is known within the nuclear detection community for its use in room-temperature gamma-ray spectrometers. The sensitivity of these systems is often enhanced using large-volume crystals, on the order several cubic centimeters. A single-polarity charge-sensing electrode configuration is generally used to achieve good energy resolution with thick CdZnTe despite the material's poor hole transport properties. Among these electrode configurations is the pixelated anode array, which can provide 3-D voxelization of a single detector's response, allowing for voxel-wise calibration to correct for material nonuniformities. The additional knowledge of each ionization's 3-D position, including that of coincident interactions, also makes large-volume pixelated CdZnTe a versatile tool for radiation imaging. Hence, this technology is being used for gamma-ray imaging spectrometers in a growing number of industries including commercial nuclear power [16], proton cancer therapy [17], space science, and nuclear security.

This work was originally motivated by a question known as the "black box" problem for nuclear security. If a user, carrying a pixelated CdZnTe-based detector, happened upon a sealed container emitting radiation, how much could that person passively determine about the container's contents? Given the context, emissions from this container might include characteristic x rays, gamma rays, and neutrons of both

fast and thermal energies. While CdZnTe's x- and gamma-ray capabilities are widely known, the material also has a less-utilized but long-established sensitivity to thermal neutrons [18]. Fast neutron sensitivity via elastic and inelastic scattering has also been recently experimentally demonstrated [19]. Collectively, there is a large amount of diverse information to be gleaned about a black box using a CdZnTe detector.

Thermal neutrons can often provide complementary information to particles streaming directly from special nuclear material (SNM). Rather than inform a user about the radioactive object itself, thermal neutron imaging can provide the size and shape of moderating materials nearby. Hence, the configuration of low-Z objects within a black box, such as high explosives, could in principle be determined. Other thermal neutron imaging applications include warhead counting [20, 21], explosives detection [22, 23], monitoring of stored spent nuclear fuel [24], and stand-off detection of SNM [25, 26, 27]. The pursuit of this capability for CdZnTe has led to the application of time-encoded imaging and the body work herein.

1.1 Transmission versus Emission Imaging

An image is the visual depiction of a subject whether it's conveyed using visible light, as in conventional photography, or other particles not directly detectable by the human eye. Images of ionizing radiation fall into the latter category and are the objective of radiation imaging. Perhaps the most widely recognizable example of radiation imaging is x-ray radiography used for diagnosis in medicine. In this application, x rays travel through a patient's body and some are absorbed, depending on the density of electrons in the material along their path. The distribution of unattenuated x rays then conveys information about intervening biological tissues, such as the structure and density of bones to tell if there's been a fracture.

Unbound neutrons, i.e., those free from an atomic nucleus, are used for transmission imaging in an analogous way to x rays, but the nature of their interactions with

matter is different. In contrast to x rays, neutrons interact weakly with electrons in a material. They instead interact mainly with atomic nuclei, with a likelihood that depends on the nuclear structure. Hence, neutron transmission images can provide high contrast between materials of low or similar atomic number, and even between isotopes of the same element [28].

The focus of this work is a fundamentally different form of radiation imaging: *emission imaging*. In contrast to radiography, where one is interested in the intervening materials, the goal of emission imaging is to measure the spatial distribution of radiation emissions themselves. For example, in nuclear medicine, a patient may be injected with a gamma-ray-emitting radiotracer to observe its uptake within the body. The subsequently-detected gamma rays are then used to infer the rate of emitted particles per unit volume of space within the body. While thermal neutrons are not suitable for use in nuclear medicine for a number of reasons, a thermal neutron emission image is also a map of emission density.

Neutrons at thermal equilibrium with their surroundings at room temperature (290 K) are considered thermal neutrons. Their energy distribution is Maxwellian, with most probable energy 25.3 meV and velocity 2200 m/s. Thermal neutrons are not emitted directly via nuclear processes, which generally result in the emission of fast (MeV-range) neutrons. Instead, fast neutrons may slow down to thermal energies via nuclear collisions in a process referred to as moderation. A thermal neutron emission image therefore shows the distribution of slowed-down neutrons leaving a moderator rather than a map of their original source. According to scattering kinematics, a neutron loses energy most efficiently via collisions with similar-mass nuclei. Hydrogen is most efficient since a neutron and proton have nearly equal mass, making hydrogenous materials such as H_2O very good moderators. Hence, a bottle of water near a source of fast neutrons would appear bright in a thermal neutron image.

It follows that thermal neutron imaging can be used to find hydrogenous ob-

jects within nonhydrogenous media, such as finding plastic landmines underground or identifying plastic explosives in cargo. In these applications, a source of fast neutrons is introduced to interrogate an object, and its return emissions are observed. Other applications such as warhead counting, nuclear smuggling detection, and radiation protection involve a source of neutrons near shielding or moderating material. Thermal neutrons have a mean free path (MFP) in air of about 20 m, and stand-off detection techniques have been demonstrated for distances up to 60 m [26]. Imaging also allows detection systems to overcome fluctuations in background over time due to cosmic rays to find very weak sources, especially those that are far away [27]. To form a thermal neutron image from any of these objects, an appropriate imaging device must be developed.

1.2 Overview of Thermal Neutron Imaging

An image of visible light is formed using a conventional camera by focusing light onto a focal plane with one or more refracting lenses. Interestingly, a neutron's wave nature causes the particle to exhibit optical behaviors analogous to light when its wavelength is comparable to the atomic spacing of materials it encounters. The path of a thermal neutron, which has wavelength 1.8 Å at 25.3 meV, can therefore be manipulated by means of refraction, reflection, and diffraction. In addition, a neutron has magnetic moment equal to -1.9 μ_N, where $\mu_N = 3.15 \times 10^{-8}$ eV/T is the nuclear magneton, meaning its path can be deflected by magnetic field gradients. These physical properties of slow neutrons gave rise to the development of focusing neutron optics [29]. Unfortunately, the acceptance angles for these techniques are physically limited to order 1° or less at thermal energies, so their use is mainly limited to focusing already-collimated neutron beams. Optical methods are not considered practical for this work's motivating applications that require an imaging field of view (FOV) of order 10°.

Like thermal neutrons, high-energy photons are also difficult to focus using traditional optics because of their short wavelength. Coded aperture imaging was proposed as a way around this problem in 1961 by Mertz and Young [30]. The concept was developed further by Dicke [31] and Ables [32], giving rise to the multi-pinhole approach used in several high energy x-ray and gamma-ray telescopes today [33]. The technique is equivalent to pinhole imaging, but rather than use a single pinhole, a pattern of many holes is used to achieve higher counting efficiency without sacrificing spatial resolution. Much work has been done on the selection of patterns to achieve the best image quality for various applications. There are several comprehensive reviews on coded aperture imaging that outline its development over the years [11, 34, 35, 36].

Coded apertures offer high throughput with large field of view, making them well suited for thermal neutron emission imaging. Thermal neutron imaging using a coded aperture was originally proposed in 1995 by Vanier, Forman, and Selcow of Brookhaven National Laboratory [20]. In this proof-of-principle work, a Cd slit collimator with an array of position-sensitive ^{3}He tubes was used to demonstrate crude directionality to a moderated ^{252}Cf source, with a contrast ratio of 3.5. The following year, Vanier and Forman reported results from a high-resolution position-sensitive neutron detector [21]. The device was originally developed for use in low-energy neutron scattering studies and consisted of cathode and anode wire arrays suspended in high pressure ^{3}He. This position sensitive detector achieved 300 μm spatial resolution with excellent uniformity, making it an ideal device for coded aperture imaging.

This initial coded aperture device featured a 31×29 pattern of holes referred to as a uniformly redundant array (URA) [37] and was made from a sheet of less than 1-mm-thick Cd metal. Several 2-D thermal neutron emission distributions of moderated neutrons were imaged, including a single source from 20 m away as well as 2, 3, and 4, sources within the imaging FOV at 3 m distance. Lastly, a ^{252}Cf source was used to interrogate a 1-in-thick chunk of polyethylene buried beneath 3 cm sand. The

resulting images indicated the correct location of the respective sources with varying degrees of image quality.

Although there has since been some development of long-range (50 to 100 m) collimated thermal neutron detectors for stand-off detection [25, 38], these systems look in one direction at a time and so do not fall within the category of multi-directional imagers most relevant to this work. The original group at Brookhaven National Lab has led the effort in the development of thermal neutron emission imaging since its inception. In 2002, Vanier and Forman reported additional measurements with their original coded aperture system, with analysis on the statistical behavior of resulting images and the attenuation of thermal neutrons as a function of distance from a thermal source [26].

A new device based on the same principles was introduced one year later, this time with larger sensitive area and several MURA-based mask patterns of various order up to 47×47 [39]. Notably, the complex shape of two moderators were resolved, an on-axis view of a triangular- and circular-framed area of a polyethylene moderator. There has been additional work demonstrating this device for use in thermal neutron backscatter imaging [22], stand-off detection [27], and active interrogation [40]. More recently, a new pad-based ^{3}He detector was developed to replace the wire-based technology that has higher efficiency, less mass, and a lower gas pressure for field applications [41, 42]. Stereo coded aperture imaging of multiple sources was successfully demonstrated using this new device.

Time-modulated thermal neutron imaging was demonstrated in 2009 using a rotating modulated collimator (RMC) by Boyce, Kowash, and Wehe [43]. The traditional RMC design consists of two grids of parallel wires or slits that rotate in unison between a source and detector. The shadow of the front-most grid falls on the grid closest to the detector, and their overlapping attenuation pattern creates a time-varying signal that depends on the 3-D position of the source [44]. They demonstrated imaging

of a point-like PuBe source using both ^{3}He and BF_3 detectors along with Cd and borated epoxy masks. No moderator was used to thermalize the source in this case, as a small fraction of neutrons are emitted from the (α,n) reaction below the Cadmium cutoff at 0.5 eV. Although this system was possibly the first implementation of time-modulated imaging for thermal neutrons, the RMC is not the best choice here because it generally does not utilize detector position information or exhibit the flat sidelobe response of coded imaging, which can provide high SNR images of extended sources in the presence of high background or low source counts.

1.3 Mechanism for Thermal Neutron Detection in CdZnTe

Thermal neutron detectors generally rely on exothermic nuclear reactions for detection since thermal neutrons themselves are uncharged and not directly ionizing. Hence, common reactions used for thermal neutron detection all result in the production of one or more energetic charged particles, such as a recoil nucleus, proton, alpha particle, or fission fragments [45]. Included in these are some of the most popular reactions for thermal neutron detection: $^3\mathrm{He}(n,p)$, $^{10}\mathrm{B}(n,\alpha)$, and $^6\mathrm{Li}(n,\alpha)$. Each of these target isotopes has a large absorption cross section for neutrons at thermal energies: 5333 b, 3835 b, and 940 b, respectively [46]. A larger absorption cross section implies higher neutron absorption probability, which generally leads to a more efficient detector.

The isotope ^{113}Cd has an extraordinarily high thermal neutron capture cross section, equal to 20 600 b. Its abundance in naturally-occurring Cd is roughly 12% and is a major constituent of CdZnTe radiation detectors which commonly have composition $Cd_{1-x}Zn_xTe$, typically with $0.05 \leq x \leq 0.2$ [47]. These detectors cannot sense the capture event directly, however the resulting excited ^{114}Cd nucleus decays promptly

via gamma-ray cascade, as expressed in the following nuclear reaction:

$$^{113}_{48}\mathrm{Cd} + ^{1}_{0}\mathrm{n} \rightarrow ^{114}_{48}\mathrm{Cd}^{*} \rightarrow ^{114}_{48}\mathrm{Cd} + ^{0}_{0}\gamma \;\; 9.043 \text{ MeV}. \tag{1.1}$$

Nuclear deexcitation is a stochastic process, leading to a number of possible gamma-ray lines and multiplicities from a single reaction. The sum energy of ^{113}Cd capture cascade gamma rays is always equal to the reaction's Q-value, 9.043 MeV, however the precise multiplicity and energy distribution is not known completely [48]. Internal conversion also occurs and is detectable by CdZnTe, but is only favored for low-energy transitions which are relatively rare for this reaction.

Despite a large number of deexcitation paths, about 74% lead to the emission of a 558 keV gamma ray [10] that is detectable via its subsequent interactions in CdZnTe. In that sense, a CdZnTe crystal acts as both the conversion and detection material for thermal neutrons. This was first demonstrated in 1996 by McGregor, Lindsay, and Olson using a 10 mm $\times$ 10 mm $\times$ 3 mm crystal that achieved 3.7% efficiency at 558 keV [18]. It should be noted that the Cd cascade was previously used for thermal neutron detection in CdTe [49, 50]. For Cd(Zn)Te thickness on the order of 1 mm or more, detection efficiency is mainly a function of the probability that a cascade gamma ray is absorbed and increases with larger crystal size [51].

Although CdZnTe is not the most efficient choice of neutron detector, simultaneous neutron detection and gamma ray spectroscopy at room temperature can provide unique capabilities for certain applications. For instance, a 10 mm $\times$ 10 mm $\times$ 3 mm coplanar-grid CdZnTe detector was found to be adequate for neutron and gamma-ray dosimetry when used near medical accelerators [52]. Furthermore, dual neutron/gamma-ray detection capability in one portable instrument can be useful for situations such as the black box problem described in the opening remarks of this chapter. Extending this capability to imaging, however, presents a new set of

engineering challenges.

The 558 keV gamma ray has a mean free path of about 2 cm in CdZnTe. Since the gamma-ray emission is also isotropic, information about the original absorption position of the neutron is severely degraded. Still, it's possible to recover some position information for a fraction of measured events using Compton imaging. This was demonstrated in 2008 by the GammaTracker group at Pacific Northwest National Lab [53]. GammaTracker is a pixelated CdZnTe array system based on technology developed at the University of Michigan. The system contained 18 detectors, each 15 mm $\times$ 15 mm $\times$ 10 mm, with a calculated thermal neutron detection efficiency of 9% at 558 keV. Because the mean free path of thermal neutrons in CdZnTe is only about 300 μm, incident neutrons are always captured very near the detector surface. Hence, some basic directionality is possible if neutron absorptions are localized to their respective crystal surfaces since the surfaces facing a neutron source will be most illuminated by 558 keV emissions.

However, the surface illumination technique does not provide enough information to discern the detailed shape of objects. If one were to instead use a coded aperture, the recorded pattern would be severely blurred by the dispersal of 558 keV gamma rays. The blur's extent is on the order of the size of most CdZnTe arrays, so the image from a stationary coded aperture would generally have spatial resolution on the order of the FOV size. Apart from accepting additional statistical noise to improve spatial resolution, e.g., by means of deblurring, this limits images to very coarse and simple shapes. Given the low count rates typically involved in thermal neutron emission imaging, increased statistical noise is generally not an acceptable requirement to achieve images of reasonable detail.

On the other hand, the timing of a neutron's capture in CdZnTe is known accurately compared to the length of time taken for a typical measurement. Dominated by the drift time of electrons in CdZnTe, timing uncertainty is on the order of 100s

of ns compared to minutes of measurement time. This means that a very detailed time pattern may be recorded over the course of a typical measurement. While fluctuations in the neutron background over time due to cosmic rays are a concern to imaging detection systems looking for very weak sources and operating on the order of days [27], here we desire an imager to operate near much brighter sources measured on the order of minutes to hours. These basic facts helped motivate the decision to investigate time coding for thermal neutron imaging with CdZnTe.

1.4 Introduction to Time-Encoded Imaging

In emission imaging, time encoding refers to modulating the flux of particles incident from a certain direction according to a time-varying pattern that is measured or known a priori. Detected particles affected by the modulation will induce a count rate that fluctuates in time according to the pattern. Hence, the magnitude of the pattern present in the recorded signal is proportional to the number of detected particles from that modulated direction. This relation satisfies the fundamental requirement for radiation imaging: to associate a measurement with an intensity of particles from a specific direction or spatial location.

To measure emission rates from multiple directions simultaneously, distinct patterns must be used to encode the flux of particles from each direction. Neglecting nonlinear effects such as detector dead time, these signals combine linearly when recorded by a detector. Statistical fluctuations aside, coding patterns are preferably uncorrelated so that one pattern's presence does not hinder the detection of another. More rigorously, the set of patterns is ideally a complete set of mutually orthogonal functions [54]. This allows for the best separation of recorded patterns in the presence of statistical noise that comes naturally from both nuclear decay and detection processes. In other words, a mutually orthogonal set of patterns provides image information with maximum SNR.

Figure 1.1 is an illustration of the time encoding concept. There are three point-like sources emitting particles isotropically, a rotating disk with a single hole that lets radiation through, and a simple radiation counter. The lines of sight between the sources and detector indicate which source's particles may pass through unattenuated to the detector for counting. The three sources form an object vector with emission rates $\vec{x} = [x_1, x_2, x_3]^T$ that emit particles subsequently counted by the detector d_1 at each of the three disk positions. The number of counts recorded during the time spent at each position result in the measurement vector $\vec{y} = [y_1, y_2, y_3]^T$.

The relationship between $\vec{x}$ and $\vec{y}$ in this example can be described by the binary encoding matrix $\boldsymbol{T} = (t_{ij}) \in \{0, 1\}^{3\times3}$. Ignoring counts from background, $\vec{y} \propto \boldsymbol{T}\vec{x}$ if equal time is spent at each disk position and all detector-source distances are the same. Each column of this matrix uniquely identifies the signal from one object direction, where $t_{ij} = 1$ indicates the hole is aligned between the detector and the source at θ_j, and $t_{ij} = 0$ indicates the source is blocked at that angle. In this simple example, the three column vectors are $\boldsymbol{T}_{*1} = [1, 0, 0]^T$, $\boldsymbol{T}_{*2} = [0, 1, 0]^T$, $\boldsymbol{T}_{*3} = [0, 0, 1]^T$. The collection of vectors is indeed a mutually orthogonal set, and represents a very simple time-based encoding scheme. Since $\boldsymbol{T}$ is the identity matrix in this case, the estimate for relative intensities of each source is very straightforward.

The utility of the code used in this example can also be intuitively understood by making some basic observations. The disk, with motion either known a priori or measured directly, essentially blocks emissions from all directions except one. In this case there is a one-to-one correspondence between detection time (or equivalently, rotational angle) and a particle's direction. The relative intensities of each source can then be inferred from the number of counts recorded while the hole was facing that respective direction. This is essentially a scanning pinhole, and is analogous to the well-known stationary pinhole with position-sensitive detector. Contrastingly, the one-to-one correspondence in that case is shared between detected *position* and

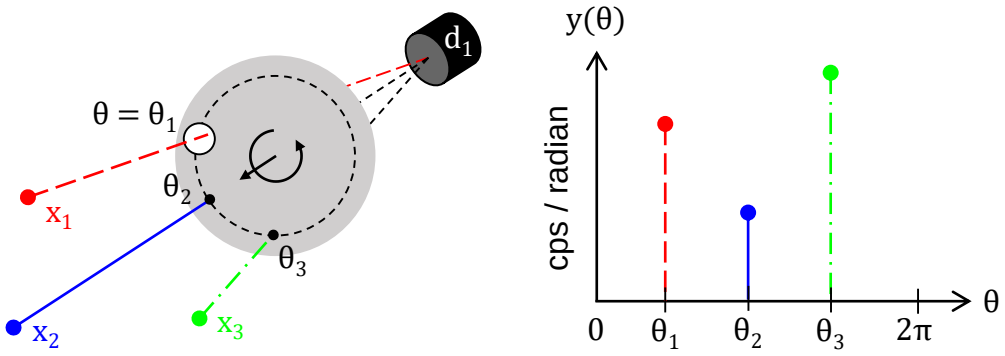

(a) (b)

Figure 1.1: Illustration of time coding, as described in the text. (a) Three point-like sources emit particles isotropically in front of a single detector, with a counter-clockwise-rotating disk between them that blocks incident radiation except through a single hole. (b) Measured signal versus disk angular position.

direction rather than detected time and direction.

Despite having one-to-one correspondence, a scanning pinhole has very low throughput. As it turns out, if coding patterns are selected cleverly (instead of all zeros and a one as before), one can achieve a much higher throughput while maintaining a so-called "ideal" imaging response, i.e., a sharp peak with flat response everywhere else. Special binary patterns referred to as cyclic difference sets have this property when using a matched filter [37], which is statistically optimal in contrast to other reconstruction techniques that require inverse filtering [55]. Another set of patterns which share this property are binary random patterns of infinite extent, where the ideal response can be approached using a large but finite length pattern [56].

As evidenced by the previous example, time-encoded imaging does not require a position-sensitive detector. However, position sensitivity, i.e., multiple detector elements, can still provide additional imaging information. This includes 3-D imaging for tomography, as illustrated by Figure 1.2. The two sources induce the same time pattern in detector d_1 and are therefore seen as a single, larger-intensity source. However when viewed from the perspective of detector d_2, a distinction can be made

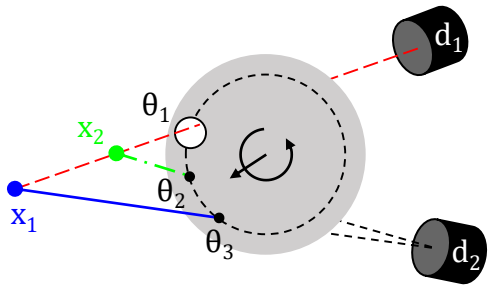

Figure 1.2: Two detectors viewing two sources. The perspective from d_2 provides the distance and intensities of the two sources away from d_1, a demonstration of the utility of parallax in the near field.

since a distinct pattern is recorded for each source. The result is the ability to resolve location in depth away from the detectors in addition to angle, θ. This is only possible in the near-field, where the separation between detectors is at least comparable to the distance from detector to source, i.e., where there is nonzero parallax.

Position sensitivity can also reduce the complexity of coding necessary to differentiate a given number of image directions. In other words, adding detectors can increase the number of resolvable image pixels, enhancing spatial resolution or enlarging the imaging FOV. For instance, the coded imaging problem can be seen as a system of linear equations. To determine the intensity of N sources without ambiguity, one must acquire at least N measurements to form N independent equations relating them. Figure 1.3 on the right shows how $N = 4$ sources may be distinguished using measurements at only two rotational positions of the disk. It's easy to see that each detector acts as a separate imager, independently viewing two sources and distinguishing their intensities using knowledge of hole's rotational position at either θ_1 or θ_2. While there are only two angular positions, there are also two detectors, making $2 \times 2 = 4$ independent equations to determine the four source intensities. The result is again a one-to-one correspondence like a pinhole, but this time it's between

source intensity and the *combined* information of detected position and time.

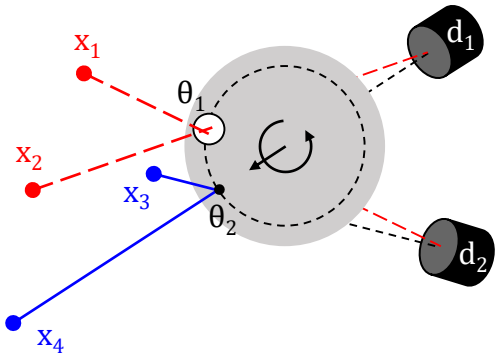

Figure 1.3: Two detectors viewing four sources. Only measurements at two angular positions, θ_1 and θ_2, are needed to resolve all four source intensities.

When using many detector elements, the number of vantage points may be sufficient to forgo the requirement for time modulation. This approach is known as coded aperture [34], and is the spatial analogue of time coding. In fact, given the same code and idealized measurement setup, the two approaches provide identical information for imaging. The key difference is that rather than modulate incident flux in time, a coded aperture provides the code in the spatial domain by casting the shadow of an attenuating pattern onto a position-sensitive detector plane. The part of the pattern that is recorded by the detector changes as a function of source position, and hence, each direction has an associated code. When designed appropriately, the measured code is distinct and uncorrelated for a given set of directions, equivalent to the aforementioned requirements for time coding. The signal processing necessary to form an image from the measured patterns is also equivalent.

It is important to note that the two methods are identical only for an idealized measurement. What is considered ideal, however, is fundamentally different for the two cases. For time coding, ideality requires a uniform background and detector response as a function of time. On the other hand, the ideal coded aperture measurement has uniform background and detector response as a function of position.

Perhaps the most interesting observation is to note that time coding is essentially *immune* to spatial nonuniformities in the same way that spatial coding is immune to temporal nonuniformities since those measurements are integrated over time. The quality of images produced in either case is heavily influenced by fluctuations in the domain where the pattern was encoded. Therefore, the design choice of coding in time, space, or both can be utilized to minimize or even avoid fluctuations that are inherent to the code's measurement in one domain or the other.

1.5 History of Time-Encoded Imaging

The first instance of extracting imaging information from a fluctuating time signal was reported in 1964 by Oda [57]. The device consisted of two stacked attenuating grids of wires whose shadows generated an oscillatory time signal on a detector as an astronomical x-ray source moved across its field of view. The modulation amplitude depended on the angular size of the object such that the source's 1-D size could be determined very accurately, to within about 10 arcmin. This initial work led to the development of the modern RMC, with pioneering work by Mertz [58]; Schnopper, Thompson, and Watt [59]; and Bradt et al. [60]. The design has been successfully used in a number of astrophysics missions and also studied for use in medicine [61], source search and localization [62], and neutron-stimulated emission computed tomography [63].

Image artifacts are inherently present in RMC images, which require inverse filtering for reconstruction. These artifacts appear as nonzero fluctuations around the peak of a point-source image that is additive in the presence of another source. Hence, this effect can obscure relatively weak or extended sources. Sidelobes can be reduced, e.g, by having multiple front-facing grid sizes to sample different parts of the Fourier spectrum, which allows one resolve more complex source distributions [64]. Another approach that utilizes a spinning aperture is the rotating slit [65, 66]. Here, the re-

construction is analogous to that of transaxial tomography, where an inverse filter is applied to remove the 1/r component from the image.

Time modulation using cyclic difference sets produces the ideal imaging response when using a matched filter, i.e., its autocorrelation consists of a single peak with flat sidelobes [37, 67]. Furthermore, it can be shown that matched filtering is statistically optimum with regard to quantum noise, in contrast to inverse or mismatched filtering methods which remove imaging artifacts but amplify noise [55]. The early literature on time coding generally refers to sequences with ideal response as pseudonoise or pseudorandom with two-valued autocorrelation, however these are equivalent to those generated by cyclic difference sets [68]. A method for using these 1-D sequences for scanning 2-D pictures was first demonstrated in 1968 by Gottlieb [68].

That approach was later utilized for gamma-ray imaging with stochastic apertures, formulated in 1974 by May, Akcasu, and Knoll [54, 56]. Distinct from apertures based on cyclic difference sets, stochastic apertures encode a scene using random binary sequences which approach orthogonality as sequence lengths approach infinity. For finite-length codes, however, stochastic apertures cause coding error, i.e., a peak with fluctuating sidelobes. To avoid this error, the actual implementation of stochastic apertures was realized by shifting a cyclic difference set through the 2-D FOV [69], similar to the approach of Gottlieb [68].

The previous work was done in collaboration with members of the University of Michigan Medical School Department of Internal Medicine, Division of Nuclear Medicine. The advantages of time-encoded imaging over pinhole imaging for nuclear medicine were clearly demonstrated in a 1975 publication by Koral, Rogers, and Knoll [70]. Notably, these include smooth focus and defocus for tomography without coherent artifacts, uniform resolution across the FOV, and immunity to unmodulated background that is constant in time. The approach was investigated for single-photon tomographic imaging of the heart [71] and thyroid [72], with promising results.

The University of Michigan group also investigated time encoded imaging with multiplexed apertures for use in transaxial single photon emission tomography, an effort pioneered by Williams and Knoll [73, 74]. The Single Photon RINg Tomograph (SPRINT) system consisted of 78 NaI(Tl) detectors spaced evenly around a 15.9 cm radius, 1 mm thick Pb ring with slits spaced according to a ($v = 156$, $k = 31$, $\lambda = 6$) cyclic difference set [75]. This approach improved SNR compared to non-multiplexed imagers for small emitting objects, but the major advantage of time coding for imaging in this application was the suppression of effects from uncorrelated background and highly-penetrating gamma rays [76].

Nonetheless, the future of time coding in nuclear medicine was inevitably limited due to its statistical nature [77]. One of the fundamental shortcomings of the technique was that regions of low activity have diminished SNR compared to regions of high activity, which can obscure important low-intensity structures for diagnosis. This disadvantage is shared with stationary coded apertures and other multi-pinhole-based approaches, and is a result of overlapping projections at the detector plane. However, some improvement may be achieved by optimizing the mask design when the source extent is known [78, 79, 80].

Until recently, the use of time-coded imaging has been relatively limited since its investigation for use in nuclear medicine during the 1970s and early 1980s. Developments in time-coded imaging of SNM have been underway at Sandia National Laboratories in Livermore, CA. 1-D gamma-ray and fast neutron imagers for standoff detection were initially investigated in 2010 [81, 82]. The LIGHTHOUSE device consisted of a single liquid scintillator surrounded by rotating, vertical high-density polyethylene (HDPE) bars arranged according to a ($v = 31$, $k = 15$, $\lambda = 7$) cyclic difference set. The more efficient Portable Rotating Imager using Self Modulation (PRISM) device consisted of three liquid scintillators placed adjacent two each other, forming a triangle. All of the detectors rotated about the central axis so that each detector's

count rate was modulated by its neighbor. Both imagers were able to find point-like sources using the maximum likelihood (ML) expectation maximization (EM) algorithm [83].

2-D fast neutron imagers have also been under investigation by the same group, including the more exotic time-encoded imager with bubble-based aperture [84]. The proposed devices consists of a liquid scintillator detector surrounded by liquid-filled tubes through which injected air rises in the form of bubbles. These bubbles are intended to form a pattern of gaps in the scattering liquid to modulate the incident neutron flux in time. Experimental results show that this technique is feasible, however there are some challenges related the non-ideal nature of the bubbles and deviation from orthogonality of patterns. Another 2-D imager was successfully demonstrated by this group in 2015, which imaged a circular source of ^{252}Cf using a 10-cm-thick rotating HDPE mask around a liquid scintillator, again employing the ML-EM algorithm [85].

FitzGerald, Burggraf, Kowash, and Hull designed and demonstrated a novel time-modulated imager in 2013 [86]. The liquid metal known as AIM-70 was used as the attenuating mask material and was distributed in a 10×10 grid of 5 mm $\times$ 5 mm square columns. The mask pattern was altered by evacuating or filling the various chambers with the liquid, allowing arbitrary mask patterns to be generated. Improvements in image SNR were observed by combining measurements from different mask patterns.

Time coding has in some sense come full circle, back to its roots in x-ray astronomy. As part of the Energetic X-ray Imaging Survey Telescope (EXIST) project in 2004, Grindlay and Hong of the Harvard College Observatory showed that a coded aperture mask which scans across the sky in 2-D has drastically-improved sensitivity compared to a pointing imager [87]. The advantages come mainly from the averaging of systematic detector noise. Rather than moving the attenuating mask to create the

time code, the emitting objects move across the FOV, shining through different parts of the mask at different times. When the entire 2-D mask is traversed, each source is modulated by the complete mask pattern. This approach is actually very similar to the one pursued here for thermal neutron imaging; the main difference is that the mask is moved rather than the source.

1.6 Contributions and Summary of this Work

In this work, we successfully demonstrated thermal neutron imaging using pixelated CdZnTe detectors and a proof-of-principle time-encoding system. The system achieved roughly 4° angular resolution by scanning a BN-based coded aperture mask across a 50° FOV. The resulting images also exhibited smooth defocusing in depth, a result of the parallax offered by the two separate pixelated CdZnTe detector arrays. Chapter VIII presents these thermal neutron imaging results, which include both single and two-moderator images.

The methods developed en route to this objective also have significant value for nuclear imaging and detection, especially for large volume, pixelated CdZnTe detector systems. First of all, our analysis of experimental thermal neutron data in Chapter IV demonstrates that there is rich information provided by pixelated CdZnTe about Cd capture events. This includes the spatial and energy distributions of coincident cascade gamma rays that can help differentiate Cd cascade from background gamma rays. To further gauge CdZnTe's usefulness for thermal neutron detection, we experimentally verified calculations on the detection efficiency of a CdZnTe array to thermal neutrons using both ^{3}He and BF_3 detectors.

The approach to time coding described in Chapter VI is also novel, most similar to the scanning coded aperture by Grindlay and Hong [87]. The technique reduced the mask's mass and form factor compared to other 2-D planar implementations at the cost of increased mechanical complexity of the mask positioning system [70]. Any

2-D or folded 1-D pattern may be used for the mask in this system.

The system was first tested experimentally using a W mask with ^{57}Co and ^{235}U gamma-ray sources. The resulting image quality from simple correlation was excellent; 0.28° angular resolution within a 22° fully-coded FOV was shown with almost-negligible image artifacts due to systematics for near-point sources. Chapter VII presents time-encoded gamma-ray imaging results. We observed some artifacts for large, extended sources; their origin is still under investigation. The gamma-ray imaging progress described here marks a considerable improvement in image quality over traditional coded aperture using pixelated CdZnTe [88, 89]. Furthermore, the coding technique is not limited to pixelated CdZnTe; it can be applied to any counting detector. Its application to thermal neutrons came next, with several added complexities introduced by the nature of thermal neutron detection in CdZnTe. This is discussed in Chapter VI.

Chapter V provides a formal treatment of time-encoded imaging along with its relation to code aperture. Chapter II is an overview of gamma-ray detection and imaging using pixelated CdZnTe, and the opening sections of Chapter III provide an introduction to neutron thermalization and the physics of neutron detection in CdZnTe. These discussions are meant to provide an outline and review of the physical basis for this work.

CHAPTER II

Overview of Pixelated CdZnTe Detectors

CdZnTe is a wide-bandgap semiconductor material that was invented during the early 1990s [90]. Its high atomic number ($Z_{eff} \approx 50$) makes it an attractive material for x- and gamma-ray detection. Since then, novel electrode configurations have enabled single-polarity charge sensing in CdZnTe, overcoming the material's low hole mobility and improving energy resolution. Notably, the pixelated anode design can provide the depths of interactions [91], and in effect, the 3-D positions of interactions within a single CdZnTe crystal. This approach has led to considerable improvements in the gamma-ray spectroscopic and imaging performance of large-volume CdZnTe.

This chapter introduces the basic physical process of gamma-ray detection and spectroscopy in pixelated CdZnTe followed by an overview of gamma-ray imaging using the 3-D positions and energies of interactions. The last section enumerates and describes detector limitations as they relate to coded imaging. Its purpose is to motivate the use of time-encoded imaging with pixelated CdZnTe arrays.

2.1 Detection of Ionization Events

Radiation detectors typically require ionizing events to occur within a sensitive detector volume, where election-hole pairs are created and detected using sensitive readout electronics. Charged particles such as α and β particles produce paths of

ionized particles as they slow down in a material and have relatively short range. Hence, they are easy to detect as they pass through a detector's sensitive volume, but equally easy to shield. Neutral particles such as gamma rays and neutrons, on the other hand, pass through many materials with a much lower probability of interaction. This makes these particles good signals for detection in applications such as nuclear security, which intends to find deliberately-hidden nuclear materials, which are possibly obscured by shielding.

However, a gamma ray or neutron traversing a detector's sensitive volume does not necessarily free any charge. These neutral particles must interact within or nearby the detector material and generate energetic charged particles. These secondary particles must then slow down and induce further ionizations in the sensitive region as the α and β particles described before. The three most common interactions of gamma rays with matter produce charged particles, which include photoelectric absorption, Compton scattering, and pair production. The relative probability of each interaction in CdZnTe as a function of gamma-ray energy can be determined from the plot of attenuation coefficient, μ in Figure 2.1, which assumes a nominal mass density of 5.78 g/cm^3 [2]. The reciprocals of each attenuation coefficient are the mean distance between photoelectric, scattering, and pair-production interactions, respectively. The reciprocal of the total attenuation coefficient is the mean distance between any two interactions, commonly referred to as the gamma-ray MFP.

The probability that a gamma ray of energy hv is photoelectrically absorbed in a material of atomic number Z is proportional to $\mathrm{Z}^n(hv)^{-3.5}$, where n varies from 4 to 5 [45]. Here, the gamma-ray interacts with an atom, which absorbs the gamma ray and ejects an energetic electron, most likely from one of its inner shells. The electron has kinetic energy $hv - E_b$, where E_b is the binding energy of the electron. Shortly following emission, electrons from the atom's outer shells transition to lower energy via characteristic x-ray and Auger electron emission. Given that these rela-

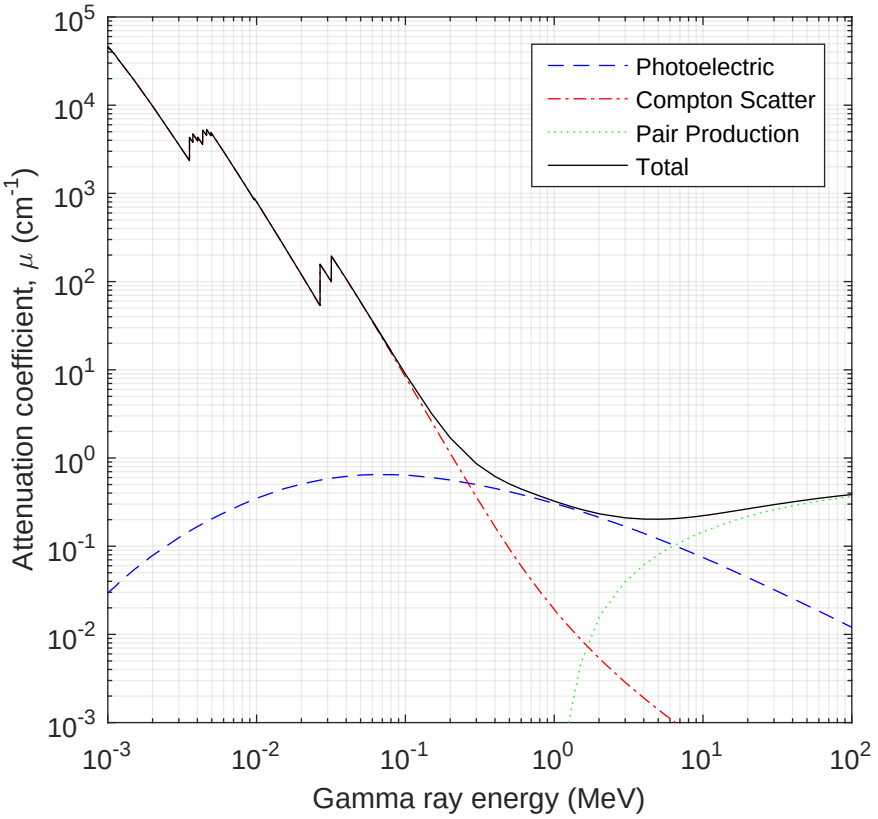

Figure 2.1: Attenuation coefficients for gamma-ray interactions in $Cd_{0.9}Zn_{0.1}Te$ as a function of gamma-ray energy. Each curve is the product of the mass attenuation coefficients tabulated by NIST in cm^2/g [1] and CdZnTe mass density 5.78 g/cm^3 [2].

tively short-range particles are all collected within the detector's sensitive volume, the total deposited energy is roughly proportional to $h\nu$. For this reason, photoelectric absorption is the preferred interaction for gamma-ray spectroscopy.

Compton scattering is an interaction between a gamma ray and an electron in a material. The gamma transfers some fraction of its momentum to the recoil electron, and leaves the interaction with energy

$$h\nu' = \frac{h\nu}{1 + \frac{h\nu}{m_0c^2}(1 - \cos\theta)}, \tag{2.1}$$

where m_0c^2 is the rest mass energy of an electron and θ is the deflection angle of the

gamma ray from its original path. The electron then acquires kinetic energy $hv - hv'$, which slows down in the material, causing ionizations.

Pair production only occurs for $hv \geq 2m_0c^2 = 1.022$ MeV, and becomes a prominent interaction mechanism at several MeV. Here, a gamma ray interacts in the Coulomb field of a nucleus, is absorbed, and is replaced by an electron-positron pair. The kinetic energy shared between the pair is $hv - 2m_0c^2$. The electron slows down and creates ionizations while the positron typically annihilates before slowing down completely. The result is an additional pair of 511 keV annihilation photons which will go on to interact elsewhere, possibly escaping the detector's sensitive volume.

Some charged-particle-producing neutron interactions include (n,α), (n,p), and elastic scattering, which generates ionized recoil nuclei. Radiative capture and inelastic scattering of neutrons in materials do not produce charged particles directly, but gamma rays that can be detected via interaction mechanisms described above. This includes the ^{113}Cd$(n,\gamma)^{114}$Cd reaction, which is the primary means for thermal neutron detection in CdZnTe [18]. Further discussion of neutron interactions as they relate to thermal neutron detection is provided in Chapter III. The focus of this section is mainly on the detection of gamma-rays in pixelated CdZnTe, which enables the detection of thermal neutrons.

2.1.1 Charge Generation

As an energetic charged particle, e.g., a photoelectron, slows down in a semiconductor material, some of its energy is transferred to bound electrons in the crystal lattice. These electrons are effectively freed from their bound state, or promoted from the material's valence to conduction band. The result is a trail of electron-hole pairs created along the original particle's slowing-down path. A hole is the lack of an atomic electron in the crystal lattice where one should otherwise be, which effectively creates a local positive charge equal in magnitude but of opposite polarity to

Table 2.1: Comparison of selected semiconductor characteristics [14].

	Si	**Ge**	**$Cd_{0.8}Zn_{0.2}Te$**
Z	12	32	48/30/52
ρ (g/cm^3)	2.33	5.33	5.78
Operating Temp. (K)	295	77	295
Bandgap (eV)	1.12	0.72	1.6
W (eV/pair)	3.6	2.98	5.0
μ_e (cm^2/Vs)	1450	36000	1350
μ_h (cm^2/Vs)	450	42000	120

an electron's charge. In the presence of an electric field due to biased electrodes, the so-called "electron cloud" drifts towards the positively-charged anode, increasing in size as a result of diffusion and electrostatic repulsion [92, 93, 94, 95].

The average amount of energy lost by a slowing-down particle per electron-hole pair is given by its average ionization energy, W, which depends on the material and particle type. Values for CdZnTe and other common semiconductor materials are provided in Table 2.1 for electrons. As one might have intuitively guessed, W is a strong function of the energy difference between conduction and valence bands in a material [45]. This so-called *bandgap* energy is the energy required to promote an electron from the valence to conduction band in a material. A small bandgap implies small W, and hence, more electron-hole pairs created for a given amount of deposited energy. Although the number of electron-hole pairs generated is ideally proportional to the energy deposited, the exact number is subject to statistical fluctuation and, in some cases, other nonlinear effects. However, smaller W generally results in more charge carriers and a smaller relative standard deviation in the total freed charge. Hence, a semiconductor's bandgap fundamentally limits its energy resolution.

The bandgap energy for several semiconductors is given in Table 2.1. Ge's low bandgap is one reason for its excellent energy resolution and why it's still considered the gold standard for gamma-ray spectroscopy. However, the bandgap is so low that it must be cryogenically cooled to avoid leakage current (noise) from thermally-excited

electrons. CdZnTe's large bandgap, on the other hand, permits it to be operated at room temperature. Although Si can also be operated at room temperature, the low-Z material is generally only available in mm-thick wafers which limit its application to charged particle and x-ray detection. The crystals used in this work are some of the largest achieved for CdZnTe, and are considered relatively large volume: 2 cm $\times$ 2 cm $\times$ 1.5 cm.

CdZnTe, however, does not come without its challenges. Like many compound semiconductors, the mobility of holes, μ_h, is an order of magnitude lower than electron mobility, μ_e. This can cause the measured charge to depend on the location of interaction in a planar electrode geometry. Furthermore, charge trapping and imperfections in the crystal lattice such as Te inclusions can cause unwanted fluctuations in the amount of charge sensed with interaction position within the crystal volume. These problems have been addressed using single-polarity charge sensing, as discussed in the next section. By configuring the geometry of the electrodes in a certain manner, the response of the device to charge generated within the crystal's volume can be controlled and ultimately used to improve energy resolution and gain knowledge of a charge cloud's position.

2.1.2 Small Pixel Effect

One way to overcome the low mobility of holes in CdZnTe is to design the electrodes to be insensitive to the movement of holes relative to electrons. The result is a single-polarity charge sensing device. There are several configurations that achieve this effect, including the pixelated [96], coplanar grid [97], and virtual Frisch grid [98] designs. The focus of this discussion is the pixelated design, where the anode is divided into a number of pixels with dimension that is small compared with the total device thickness.

Radiation detectors sense charge via electrostatic induction, i.e., when negative

charge approaches an electrode, it causes electrons in the conductor to flow in the opposite direction. In the pixelated design, the induced signal is shared amongst many pixelated anodes as the electron cloud approaches from a distance that is far compared to the pixel pitch. This effectively dilutes the induced signal's magnitude until the electron comes within one pixel pitch of its collecting anode, where, due to proximity, the charge induction becomes concentrated on that anode. As the charge nears the collecting anode, in effect moving away from the others, non-collecting anodes experience a change in the direction of the flow of charge. These are often referred to as transient signals and are more pronounced for pixels nearest the collecting anode.

The primary effect of this electrode configuration is that the anodes are only sensitive to charge motion very near the anode surface. This is referred to as the *small pixel effect*, which enables single-polarity charge sensing in a pixelated device. Only holes created within one pixel pitch of the anode surface induce an appreciable signal as they travel towards the cathode, while nearly all electrons pass through this small sensitive region before reaching their collecting anode.

The Shockley-Ramo theorem provides a more rigorous model for charge induction in the device [99, 100]. A detailed discussion on the calculation and application of the theorem to semiconductor radiation detectors has been published previously [101]. In summary, the total induced charge on an electrode due to the motion of a charge carrier is given by

$$Q = q\Delta\varphi_0, \tag{2.2}$$

where q is the charge of the carrier, and $\Delta\varphi_0$ is the change in the so-called weighting potential before and after movement. φ_0 is a function of space and can be found by solving the Laplace equation, $\nabla^2\varphi = 0$, for the detector-electrode geometry under the following conditions: the potential of the electrode of interest is set to unity, all other electrode potentials are set to zero, and space charge, e.g., trapped charge, is ignored.

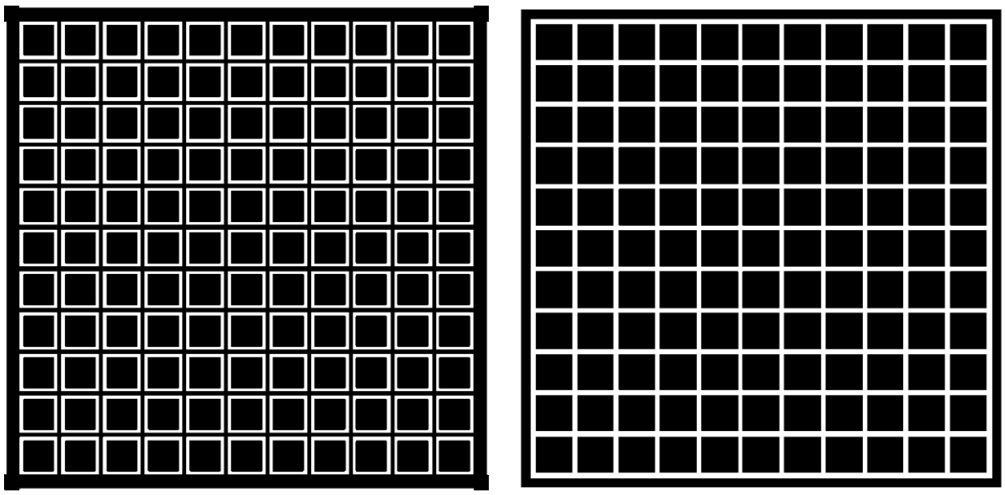

(a) (b)

Figure 2.2: Anode layouts for (a) gridded and (b) simple pixel detectors [3].

The two types of 11 × 11 pixelated anode designs used in this work are shown in Figure 2.2, each with a cross-sectional area of 2 cm × 2 cm. In both designs, the pitch between pixels is 1.72 mm. The grid between pixels and around the edge of the device pictured in Figure 2.2(a) is 0.1 mm wide and kept at bias lower than the anodes to steer electrons away from the gap between pixels. Although this can improve charge collection, this design can cause increased leakage current [3]. The simple pixel design of Figure 2.2(b) has larger pixels (and therefore smaller gap) to achieve adequate charge collection without the need for a steering grid. The size of these pixels is 1.66 mm as opposed to 1.22 mm in the gridded design. Note that in both cases, the cathode is planar, covering the entire 2 cm × 2 cm area of the device.

Weighting potentials were calculated using Ansoft's Maxwell 3D software along the 1.5 cm path from the center of the cathode to the center anode pixel in a 2 cm × 2 cm × 1.5 cm detector and plotted in Figure 2.3. The curves show the corresponding weighting potentials for the cathode, collecting (center) anode, and neighboring anode. Note that the value of the weighting potential at distances greater than about 2 mm from the anode is near zero for both the collecting and neighboring anode pixels. Equation 2.2 indicates that electrons which travel from the bulk of the

device to the collecting anode pixel experience a change in weighting potential close to unity, i.e., the induced charge on the collecting anode is $Q_a \approx Ne$, where N is the number of electrons and e is the electronic charge. Hence, the induced signal from electrons is independent of their initial location in the device.

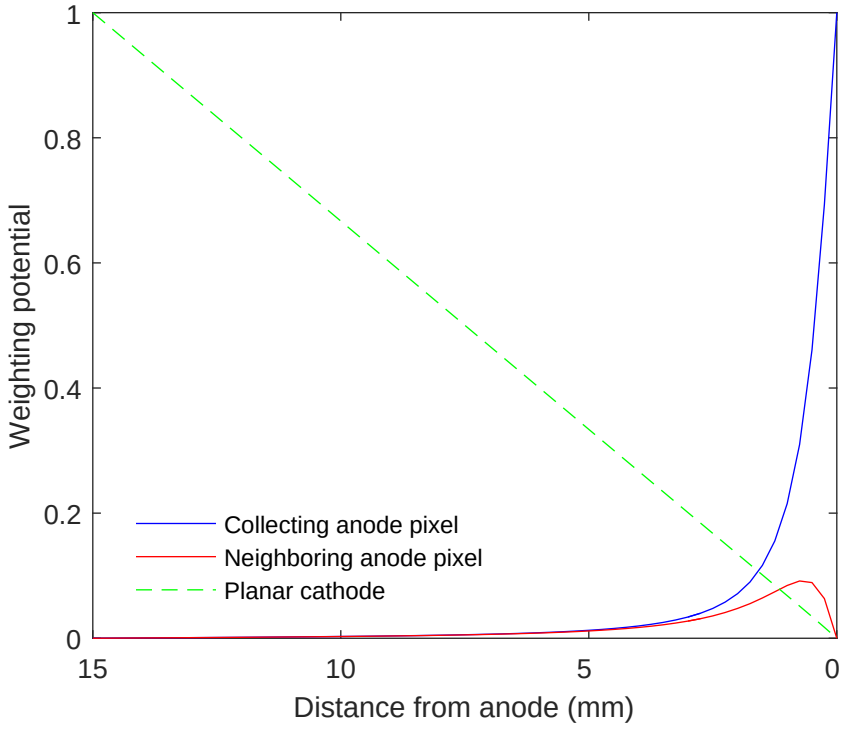

Figure 2.3: Weighting potentials calculated for the simple pixel detector geometry.

The drift velocities of electrons and holes are given by $v = \mu E$, where E is the electric field strength and μ is the carrier mobility, given in Table 2.1. In CdZnTe under a potential of 1000 V/cm, electrons travel roughly 1 cm/μs, while holes travel only 0.1 cm/μs. The slow movement of holes makes them subject to severe trapping, making their induced charge both slow to rise and dependent on the original ionization position within the material. Removing their contribution to the signal is therefore helpful for improving energy resolution and reducing pulse pileup. Holes are effectively ignored by pixelated anodes since the anode weighting potential slope is very shallow throughout most of the bulk and because they hardly move during the relatively brief

collection time of the electrons.

In a planar electrode geometry, the weighting potential is linear, as is the case of the planar cathode in Figure 2.3. $\Delta\varphi_0$ clearly depends on where the electrons begin their motion, and so, on the location of the original ionization event. The main implication for the planar cathode is that its induced charge $Q_c \propto Ne\,z$, where z is the distance of the ionization event away from the anode. This dependence for planar electrodes is obviously not attractive feature of spectrometers with both planar anodes and cathodes, and was the main motivation for single-polarity charge sensing in the first place. Note that if the holes moved as quickly as the electrons, their contribution would exactly complement the electron signal and render the signal independent of z.

The combination of pixelated anodes with a planar cathode, however, can offer an advantage beyond a depth-independent electron signal. Conveniently, the ratio of their signals $Q_c/Q_a \propto z$, provides the depth of interaction [91]. When the electric field in the device is roughly parallel from anodes to cathode, the identity of the collecting pixel, i.e., the one with the largest induced signal, provides the x and y position of interaction. Together with the ratio of cathode to anode signals, the device provides the 3-D position of an ionization event within its volume. For multiple, near-simultaneous ionizations, e.g., a Compton-scattered photon and subsequent photoelectric absorption, the individual depths can be determined by the drift time of each electron cloud [102]. Due to the nature of the pixelated electrode weighting potential, the cathode trigger time indicates when the electrons start moving, and the anode trigger times indicate when they reach their respective anodes. Their separate depths can then be determined, again assuming a parallel electric field.

The neighboring electrode's induced signal follows the red curve of Figure 2.3 as an electron travels from the cathode to center anode pixel. For charge created some distance from the cathode, the net induced charge is negative since $\varphi_0 = 0$ at the non-

collecting anode surface. This can be problematic for multiple-ionization events that are in neighboring pixels, for instance, since they both reduce the net induced charge on their respective anodes. A correction factor is often employed for reconstructing the energies of multiple-ionization events in practice [103]. Figure 2.3 shows that this effect is most prominent for interactions occurring within a few mm of the anode surface which undergo the largest magnitude $\Delta\varphi_0$.

On the other hand, transient signals can also be used for sub-anode-pixel position sensing in pixelated CdZnTe. The basic idea is that the charge will induce a larger signal on the neighbor pixel that it's closest to as it approaches collection. The difference in transient signal magnitude for neighbor pixels has been experimentally shown to improve position resolution from the 1.72 mm anode pixel pitch to around 230 μm at 662 keV [104]. It should be noted that this was possible using a digital readout. The analog Gamma-Medica-Ideas (GMI) application specific integrated circuit (ASIC)s used for detectors in this study, on the other hand, consist of simple peak-hold circuitry and are not capable of sub-pixel position resolution [94].

Perhaps most notably, the pixelated anode design allows for depth-dependent correction of gamma-ray spectra recorded with large-volume CdZnTe detectors. This is crucial for achieving good energy resolution in detectors with significant trapping and material nonuniformities. Since these position-dependent features do not change significantly with time, each voxel of the CdZnTe material can be calibrated separately and aligned during future measurements. This technique has led to 0.6% energy resolution at 662 keV for low-noise, digital readout systems [105] and 1% for analog readout systems [106] in large-volume, pixelated CdZnTe detector arrays. Example spectra at lower energies for both analog and digital readouts is shown in Figure 2.4. Each are measurements of gamma- and x-rays from the same HEU-metal sample during a visit to the Y-12 NDSTC. The limiting factor for pushing the energy resolution is still the electronic noise of the readout, so significant effort is being put forth to

design the next lower-noise generation of digital ASICs.

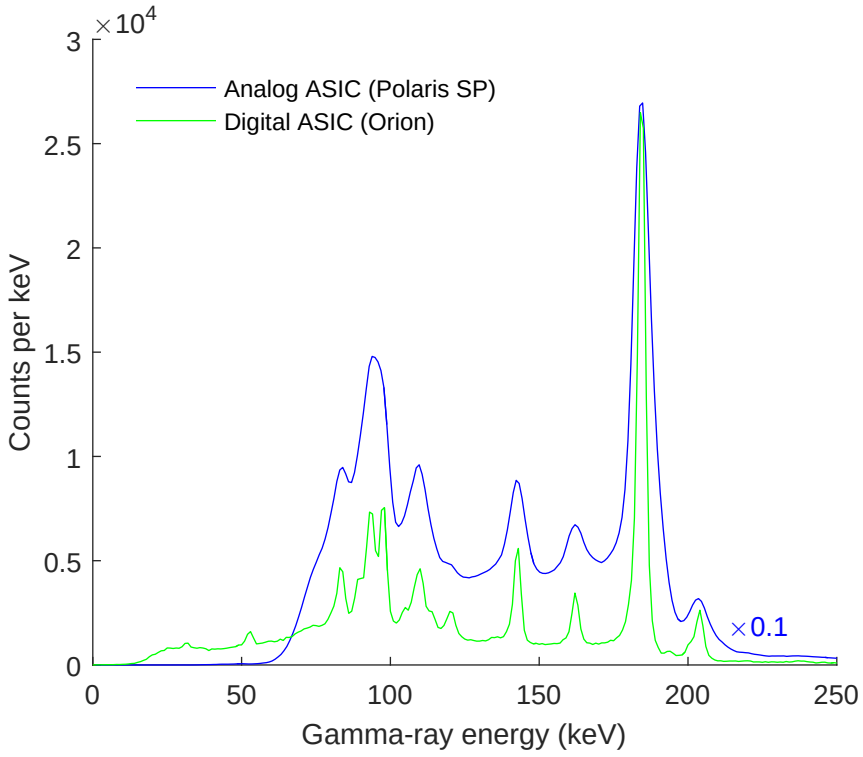

Figure 2.4: HEU gamma-ray spectra measured by the Orion 4-detector and Polaris SP 18-detector systems at the Y-12 NDSTC.

2.2 Gamma-Ray Imaging

The 3-D positions and energies of gamma-ray interactions in pixelated CdZnTe convey a great deal of information about the detector's radiation environment. Notably, it is sometimes possible to estimate which direction particles are incident from, and hence, discern the spatial distribution of their emissions. In other words, this information allows a single CdZnTe detector or array of detectors to act as a radiation imager. For instance, a simple pointer towards the direction of a gamma-ray source can be inferred from the attenuation of counts through the bulk of a large-volume CdZnTe detector [107]. More advanced techniques can not only point, but estimate complex spatial distributions of gamma-ray emissions.

2.2.1 Compton Imaging

Figure 2.1 indicates that Compton scatter is the dominant interaction mechanism for photons in CdZnTe at energies between about 300 keV and 6 MeV. Rearranging Equation 2.1 and defining the energy transferred to the free electron as $E_{e^-} = hv - hv'$, one can solve for the cosine of the change in direction of the photon as a result of a Compton scattering interaction:

$$\cos\theta = 1 - \frac{m_0 c^2}{hv} \frac{E_{e^-}}{(hv - E_{e^-})}. \tag{2.3}$$

Since the energetic electron is directly ionizing, it creates electron-hole pairs in CdZnTe material as it slows down. The quantity E_{e^-} may then be estimated from the amount of charge generated and subsequently induced on the detector's electrodes. The remaining unknown parameter is the photon's incident energy hv, which is only known if the photon is fully absorbed in the detector after its initial Compton scatter, i.e., via eventual photoelectric absorption. This can occur after one or more Compton interactions, where the last interaction in the sequence is photoelectric.

If the photon is fully absorbed, then sum of its deposited energies equals its incident energy, hv. In principle, photopeak events in a gamma-ray spectrum meet this requirement. Hence, if photopeak events are used for Compton imaging, hv is known and the photon's scattering angle θ can be estimated. Furthermore, since the 3-D positions of each interaction are known within a single crystal's volume, this scattering angle can be positioned with respect to the crystal's 3-D coordinates. The vector between the first and second interactions describes which direction the photon was traveling post-scatter, and θ limits the possible pre-scatter directions to the surface of a cone with vertex at the first interaction location, axis between the first and second interaction locations, and half opening angle θ. If the scattered angle of the electron was also known, this cone would be truncated to a single pointing

vector for that photon. This is difficult using the current configuration due to the combined effects of diffusion and the relatively large size of the pixelated electrodes, both of which tend to degrade the information of the electron's complicated path.

Since multiple interactions from a single gamma ray in CdZnTe occur much faster than the detector's timing resolution, currently on the order of 10 ns [108], the order in which the interactions occured is unknown. Generally, the correct sequence of interactions must be chosen to calculated the correct Compton cone for an event. For 2-interaction events, this can be done using the simple comparison method [102, 109]. In this algorithm, both possible sequences are first subject to the Compton edge test, which determines if either deposited energy is larger than the Compton edge calculated assuming full energy deposition. If one sequence fails, the other is chosen. If they both pass, then the interaction with larger deposited energy is chosen. This is because events that forward scatter and deposit little energy are more likely to escape the CdZnTe volume.

The ability to Compton image in 4π using a single large-volume pixelated CdZnTe detector was demonstrated in 2004 by Xu, He, Lehner, and Zhang [110]. Since then, that University of Michigan group has developed many new detection and imaging algorithms for pixelated CdZnte detector systems [102, 109, 111, 112, 113, 114]. An example back-projection Compton image of a point-like source of 662 keV gamma rays from ^{137}Cs is shown in Figure 2.5. The data was recorded using the Polaris II 18-detector array, the successor to the original Polaris developed in 2010 [106], and reconstructed using UMImaging, which was developed around the same time [13]. A study on the long-term stability of the Polaris systems has been published [115]. 2-, 3-, and 4-pixel interaction events with sum-energy within the 662 keV photopeak were used for this reconstruction.

The individual rings generated by the Compton cones in spherical coordinates can be faintly seen in the image of Figure 2.5, which consists of about 10^4 Compton-

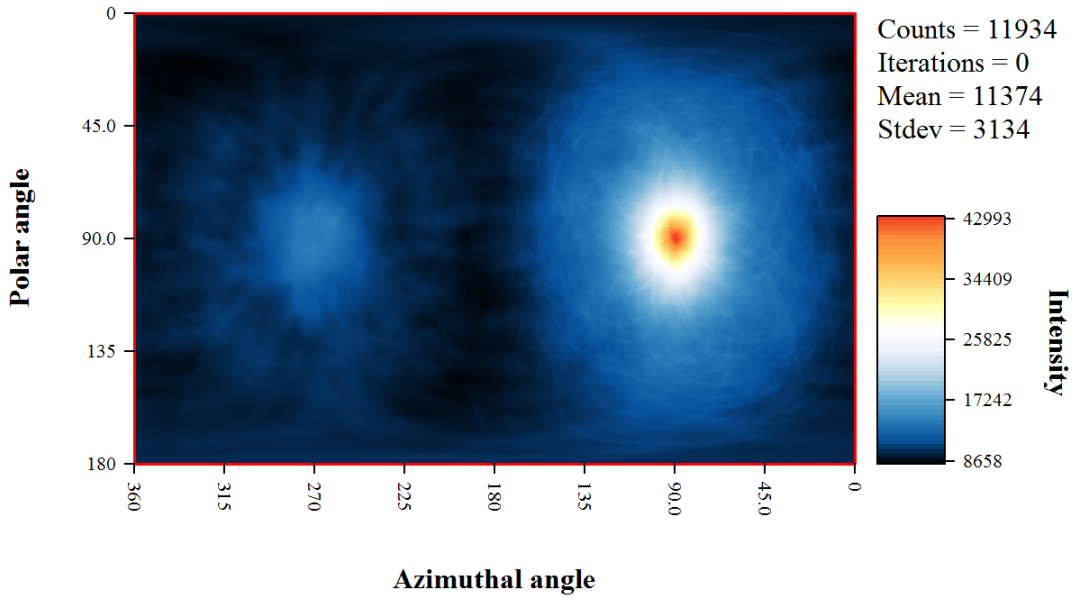

Figure 2.5: Back-projection Compton image of a point-like source of 662 keV gamma rays from ^{137}Cs using the Polaris II CdZnTe array and UMImaging software.

scatter events. The many overlapping rings generate a broad distribution in angular space, causing a full width at half maximum (FWHM) of about 30°. However, other methods such as filtered back-projection and list-mode ML-EM are able to deconvolve the cones from the image, and both are able to clearly separate two point-like ^{137}Cs sources 15° apart using a single CdZnTe crystal [110]. Today, this imaging technology has matured to the point of commercialization, and is used for a number of various imaging applications [116].

2.2.2 Coded Aperture Imaging

Figure 4.6 shows that photons below 300 keV mainly have photoelectric interactions in CdZnte. Therefore, CdZnTe detectors are intrinsically not efficient Compton imagers in this regime. The MFP of photons in the material post scatter also becomes very short, which tends to accentuate the negative effects of interaction posi-

tion uncertainties on spatial resolution [109]. Combined with the increasing effects of Doppler-broadening, the overall quality of Compton images at low energies degrades significantly.

The Polaris arrays have two 3 × 3 arrays of CdZnTe, each with 2 cm × 2 cm cross sectional area facing outward, as pictured in Figure 2.6(a). These detectors are spaced 2 mm apart such that the total cross sectional area, including the gaps between detectors, is 6.4 cm × 6.4 cm. Together, the cathode surfaces act as a position-sensitive detector plane due to the pixelated anode configuration, pictured in Figure 2.2. This is adequate for use of Polaris as a coded aperture imager, which relies only on the detected position of a single interaction.

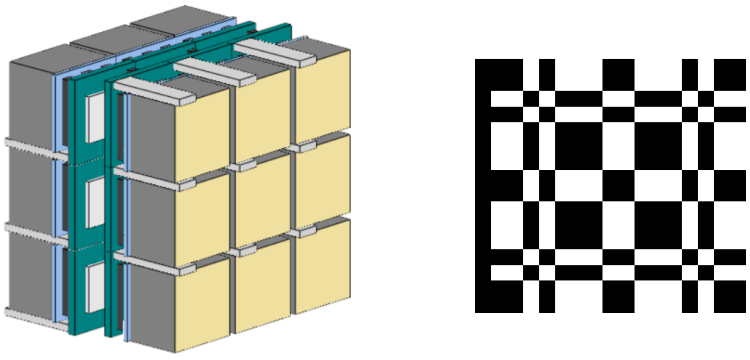

(a) (b)

Figure 2.6: (a) Polaris 18-detector CdZnTe array. (b) 17 × 17 MURA pattern.

A mathematical description of coded aperture is presented in Chapter V, however the method can also be understood intuitively. A coded aperture mask, which consists of a pattern of both attenuating and open elements, is placed between a radiation source and a position-sensitive detector plane. The trajectories of particles from the source essentially projects the attenuating pattern onto the plane, so that some subsection of the pattern is recorded by the detector. The key is that depending on the source's position, a different part of the pattern will be recorded, and ideally, this pattern is unique for some set of directions within the FOV of the detector-mask combination. One can then relate the detected pattern to the position of the source

by finding the pattern that matches and noting which direction it corresponds to.

In total, Polaris has 33×33 pixels per plane. The depth sensitivity of the pixelated CdZnTe also allows the sides of the crystals to act as position-sensitive detector planes, and therefore can facilitate coded aperture imaging [117]. This was initially demonstrated using simulation in 2008 and experiment in 2009 by Kaye, Kaye, and He [88, 118]. Both random and MURA masks have been used with Polaris. The 17×17 MURA pattern is shown in Figure 2.6(b), and a representative coded aperture pattern measured using Polaris II and a 1-mm-thick W mask arranged in this pattern is shown in Figure 2.7, along with its image from correlation. The nature of MURA patterns and their construction is described in Section 5.3.

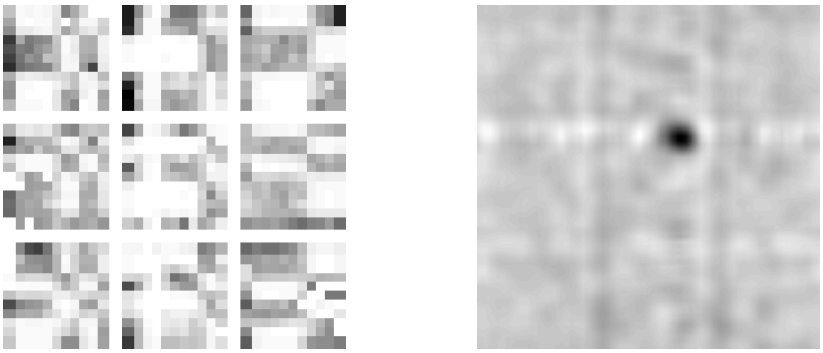

(a) (b)

Figure 2.7: (a) Map of counts on Polaris 3×3 CdZnTe detector array. (b) Image from correlation with MURA pattern pictured in Figure 2.6(b).

It is clear from Figure 2.7(a) that the detectors are not perfectly uniform, and so, the recorded pattern is distorted from its original form in Figure 2.6(b). The result is an image with nonzero sidelobes, or fluctuations outside the main peak in Figure 2.7(b). It has also been shown that a moving source with known trajectory significantly reduces systematic artifacts in a coded aperture image from pixelated CdZnTe [119]. This is analogous to the improvement demonstrated by Grindlay and Hong for scanning coded apertures in x-ray astronomy [87]. It is also the first evidence

for the advantage of time coding using pixelated CdZnTe, where moving the mask instead of the source essentially provides the same effect.

2.3 Limitations Related to Coded Imaging

Pixelated CdZnTe detectors provide a wealth of information about ionization events within their volume, however, like any measurement instrument, this information is never without uncertainty. The most important, intrinsic limitations of large-volume pixelated CdZnTe as they relate to coded imaging will be outlined here. Issues that arise only for a small fraction of events and do not contribute significantly to the quality of coded images will not be address. Also, problems that arise from operator error or otherwise malfunctioning equipment will not be discussed. The following imperfections exist even under the proper operating conditions.

2.3.1 Spatial

Pixel, Detector, and Array Dimensions

The 2 cm $\times$ 2 cm $\times$ 1.5 cm CdZnTe crystals used in this work are currently some of the largest-volume produced. To construct an imager with enough pixels to form a reasonably-detailed coded image, the detectors must be tiled in an array. The size of anode pixels may also be reduced, however, at the cost of spectroscopic performance. This is generally not an acceptable tradeoff. The number of sensitive pixels within that plane fundamentally limit the number of coded aperture elements that it can resolve, which directly limits the spatial resolution of a traditional coded aperture system. For time coding, each pixel acts as an independent imager, so the FOV is not dependent on the detector size. Furthermore, detector position resolution is not even necessary for time-encoded imaging, i.e., the number of sensitive elements can be as low as one.

Figure 2.2 shows that some anode pixels are near the edges of crystals. Since the

detectors are thick and their edges present a larger solid angle to radiation sources, particles that do not penetrate far into the CdZnTe will be preferentially collected on those pixels near edges. This results in a pixel-dependent efficiency that also depends on the direction to the source.

This can distort the measured coded aperture pattern in different ways for different source directions, which is difficult to deconvolve. The effect can be seen by inspecting the differences between the plots of flood irradiation by ^{57}Co from different angles in Figure 2.8(a) and Figure 2.8(b). The increased counts seen along vertical rows in Figure 2.8(b) correspond to detector edges which face the source placed at an angle. Notice there is also a dip in counts at roughly the same location on each detector; this is attenuation from a capacitor that is repeated for each detector on the high voltage distribution board very near the cathodes.

The gaps between the detectors present a further problem. If a single, continuous pattern is projected onto an array, there will be parts of it missing in the recorded pattern due to the gaps. The effect of the gaps can be seen as a #-shaped pattern in Figure 2.7(b). This can be overcome using several small masks, at the cost of FOV, or by cleverly arranging the detectors and mask pattern such that the full pattern is still acquired from anywhere within FOV. These artifacts can also be reduced in software, for instance, by setting the gap's value to the measured pattern's average instead of leaving it zero. Time-encoded imaging overcomes each of these geometric problems by allowing each detector pixel to act as an independent imager.

Pixel Jumping

The pixelated CdZnTe geometry can be thought of as a square box with columns of sensitive area between each anode pixel and the cathode surface, and ideally each pixel is sensitive to ionization events within its respective column. However, this is not always the case. Pixel jumping occurs when the interaction recorded in one pixel

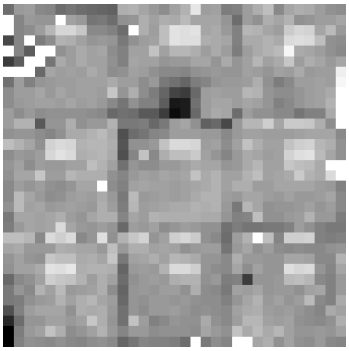

(a) 122 keV, perpendicular

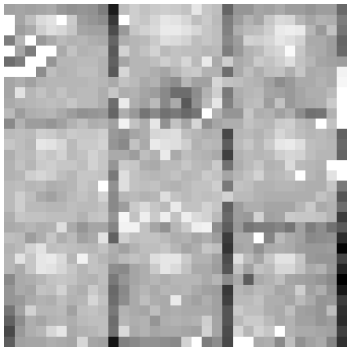

(b) 122 keV, angled

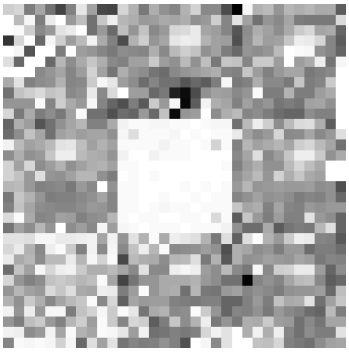

(c) 80 keV, perpendicular

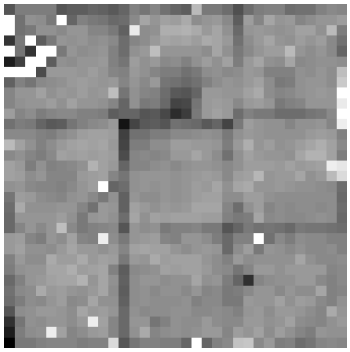

(d) 356 keV, perpendicular

Figure 2.8: Counts on each pixel of Polaris II due to a flood irradiation of gamma rays at different energies and incident angles. "Perpendicular" refers to a far field source centered with the array cathodes, and "angled" is a far field source offset towards the right from the plane's centerline into the page.

is actually due to an ionization event in another pixel's sensitive region. This can occur when electric field lines in a pixelated CdZnTe detector between cathode and anode are not parallel somewhere in the bulk of the crystal.

This effect has been studied using a collimator, and degrades the quality of coded aperture images because it distorts the measured pattern [89]. In time coding, this can cause image blurring, but does not induce systematic artifacts as long as the behavior does not change during the measurement.

Readout Electronics

Electronic noise is inherent in any detector system, which determine the low-energy threshold for electrodes. In particular, the anode low-energy threshold can affect uniformity, and its effect can be seen very clearly in Figure 2.8(c). The center detector is noisier than the rest, requiring its thresholds to be above the 80 keV gamma-ray from ^{133}Ba. There is also speckled zeroing of counts from varying anode threshold in the rest of the detector. This will obviously harm the quality of coded aperture images taken at this energy, but for time-coded imaging only efficiency is lost.

Further spatial nonuniformity can be caused by "dead" anode pixels, which are often unusable because of electrode fabrication issues. The effect can be seen, for example, in Figure 2.8(d), where the white pixels have zero counts. Gain deficit can also occur due to poor contact between the electrode and substrate, which reduces the signal relative to noise and requires a higher low-energy threshold. On some anodes, the noise is high enough such that it must be disabled to prevent excessive triggering.

There are also dead layers, about 2 mm near the anode and a small (on the order of 100 μm) region near the cathode. The latter has basically no effect for gamma-ray energy photons, however the anode dead layer significantly reduces sensitivity. This dead layer is the result of the weighting potential near the anode, plotted in Figure

2.3. Electrons generated in that region experience a change in weighting potential significantly less than unity, and so less charge is induced and there less signal above electronic noise. Generally, this only degrades efficiency, but this can also cause nonuniformity in anode response, as the size of this region is not necessarily even across all anodes. Again, this is not a concern for time coding because each pixel acts independently.

2.3.2 Temporal

A fluctuating count rate in time during a time-coded measurement is analogous to a spatial pattern recorded during a coded aperture measurement, like the one pictured in Figure 2.7(a). Like its spatial counterpart, quality and detail of the recorded pattern in time is limited in pixelated CdZnTe systems. To begin, the time sampling of the pattern is analogous to the spatial sampling by anode pixels; both of which have finite extent and number.

System Dead Time

The rise time of a signal in 1.5-cm-thick CdZnTe under 3000 V bias is on the order of 100 ns, and the best-achievable timing resolution at 511 keV was found to be approximately 10 ns using waveform analysis [108]. Although higher count rates have been achieved in more recent readout systems, the 18-detector Polaris systems with GMI ASICs have a nominal dead time of about 410 μs, meaning the highest output count rate is about 2400 cps. Hence, the dead time is the main limitation on the number of pattern elements one can resolve given a certain length of measurement time.

Dead time can also affect the quality of the measured time signal if it changes during the measurement. This is quite possible, for instance, if blocking elements reduce the incident number of particles significantly such that the percent dead time

increases when they are open. However, dead time is typically a correctable problem as long it has been characterized. Note that any irregularities in time are also not a concern for coded aperture, as long as the net effect is the same for every sensitive detector element, since the measurement is integrated over time.

For measurements in this work, only a small portion of the total gamma-ray energy spectrum was modulated by the mask, so the overall count rate and percent dead time remained roughly constant, even while the mask moves. Figure 2.9 shows the count rate versus time for a measurement of K_α x-rays from DU were recorded using Polaris SP for about 45 min while a 2-mm-thick W mask moved in front of the array. The total count rate at all gamma-ray energies was 215 cps. The rate of detected x-rays appears constant except for statistical fluctuations, and the signal's DFT suggests the same. Like all MURA patterns, the ones used in this work were designed such that the same fraction of gamma-rays pass through its open elements and reach the detector, regardless of its position. So, dead time fluctuations are not an issue for the system in this work.

Other Irregularities in Time

Uniformity of the signal in time is analogous to the spatial uniformity measured and plotted in Figure 2.8. However, given the collection of measurements recorded as part of this work, it is not obvious that any nonuniformities intrinsic to the pixelated CdZnTe or its readout plays a significant role. 400 s of measured counts at 511 keV from ^{22}Na is shown in Figure 2.10, where the count rate at all energies was about 1 000 cps.

The data again appears uniform in time for each plane and its detectors, except for what should ideally be Poisson counting noise from the nuclear decay process of ^{22}Na. Indeed, when an individual detector's count rate is arranged in a histogram, the data from a single detector appears to follow the theoretical Poisson trend, shown

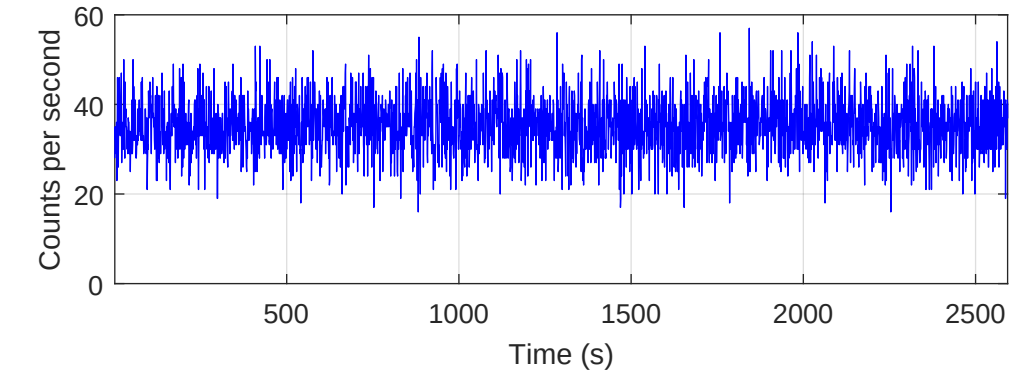

(a)

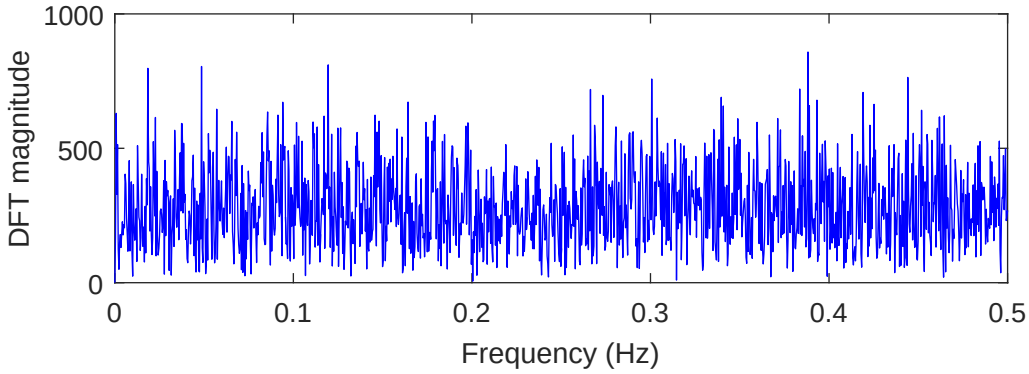

(b)

Figure 2.9: Time behavior of uranium K_α x-ray count rate (95 keV and 98 keV) during DU measurement using Polaris SP. (a) Counts versus time for plane B, the only working detector plane. (b) DFT of count rate with its mean (DC) value subtracted.

in Figure 2.10(c) for example. Even when choosing an outlier pixel from the array, e.g., the one with the very most counts during the measurement, Figure 2.10(d) shows that its count rate distribution corresponds well with the predicted distribution from Poisson emission of particles. A more thorough study on uniformity in time should be done, especially at longer time scales, which is part of future work described in Chapter IX. At time scales relevant to this work, however, Poisson statistics appears to be the main limiting factor for time-coded image uniformity with these systems. In a way, this implies that the time domain is an otherwise blank canvas for recording coded imaging patterns.

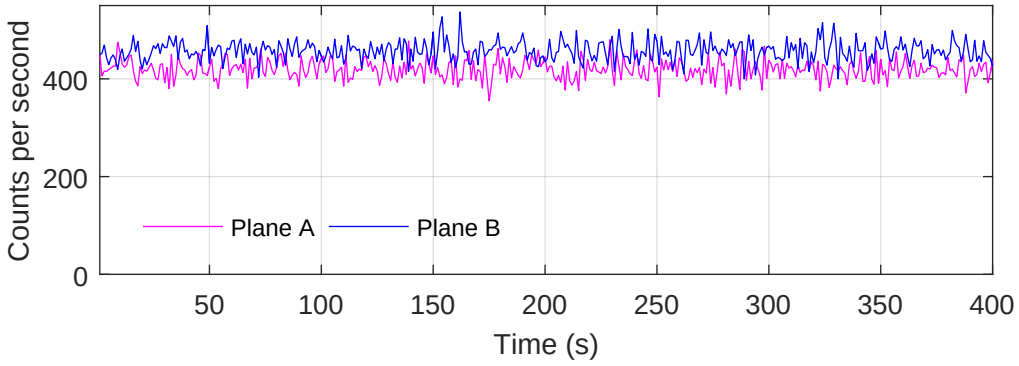

(a)

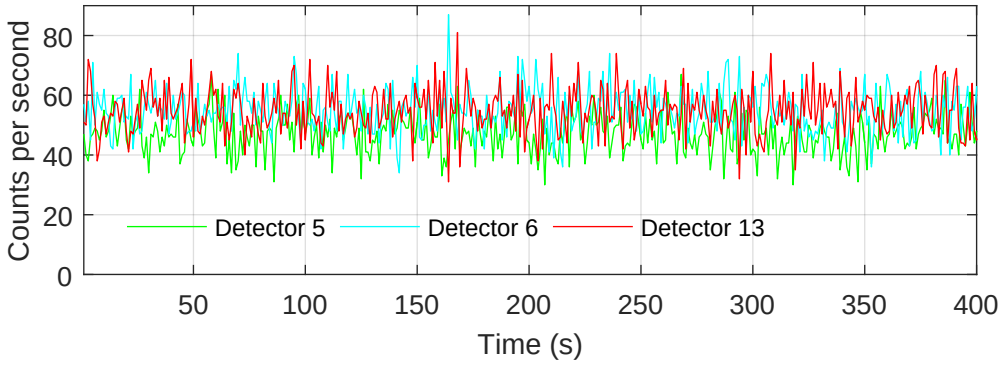

(b)

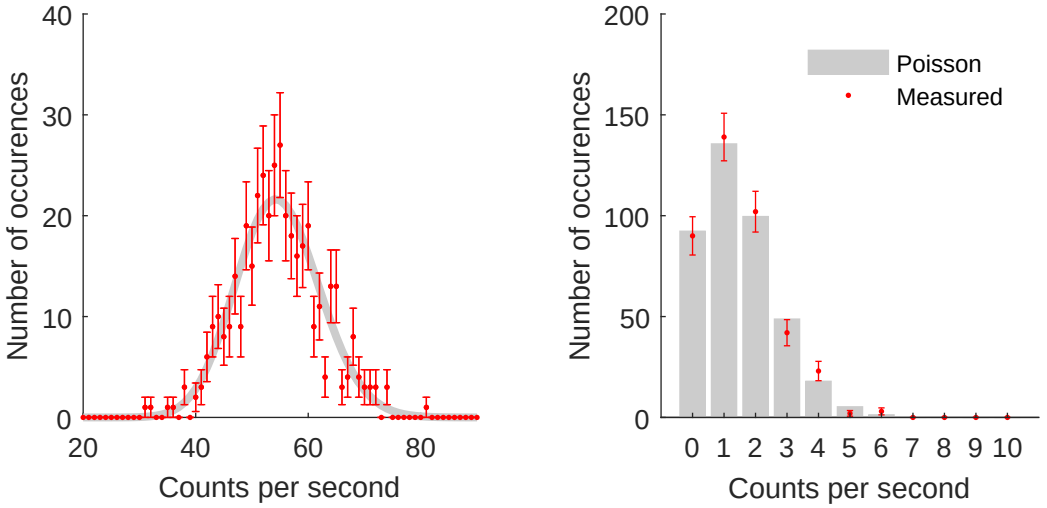

(c) (d)

Figure 2.10: Statistical behavior of 511-keV photopeak count rate over time during uniform ^{22}Na irradiation of Polaris SP. (a) Counts versus time for each plane, each with nine detectors. (b) Counts versus time for three representative detectors. (c) Distribution of count rates for detector 13. (d) Distribution of count rates for channel 98 of detector 13, the pixel which recorded the most counts.

CHAPTER III

Thermal Neutron Emission and Cd Capture

CdZnTe is not sensitive to thermal neutrons directly, but relies on the $^{113}\mathrm{Cd}(n,\gamma)$ reaction to convert incident neutrons to detectable gamma rays. Hence, it acts as both the conversion and detection material for thermal neutrons, placing it amongst a number of semiconductor-converter materials [120]. The physical process of thermal neutron detection in CdZnTe is described here, from the basics of neutron thermalization and emission to Cd capture, gamma-ray cascade, and interaction in CdZnTe. The mechanism for detection of gamma-ray interactions in pixelated CdZnTe is outlined in Chapter II. Experimental results for thermal neutron detection using pixelated CdZnTe is provided in Chapter IV.

3.1 Nature of Thermal Neutron Emissions

3.1.1 Energy and Velocity Distributions

Thermal neutrons are unbound neutrons with kinetic energy comparable to the thermal motion of nuclei in a material at room temperature. The Maxwell-Boltzmann distribution is widely used to describe the velocity and energy distribution of neutrons in thermal equilibrium with a medium, and more generally the distribution of particles in an ideal gas. It's based on the kinematics of a collection of particles moving freely within a volume which transfer their energy and momentum via collisions. Here,

the collisions occur between free neutrons and some material's atomic nuclei. The Maxwell–Boltzmann distribution in energy can be written as [4]

$$M(E) \equiv \frac{2\pi}{(\pi kT)^{3/2}} \sqrt{E} \exp\left(-\frac{E}{kT}\right), \tag{3.1}$$

which is the probability distribution function for the kinetic energy of a collection of particles at temperature T, where the Boltzmann constant is $k = 8.6173 \times 10^{-5}$ eV/K. Using the nonrelativistic expression for kinetic energy, $E = \frac{1}{2}mv^2$, i.e., $dE = mv\,dv$, the corresponding Maxwell–Boltzmann velocity distribution is

$$M(v) \equiv \left(\frac{m}{2\pi kT}\right)^{3/2} 4\pi v^2 \exp\left(-\frac{mv^2}{2kT}\right), \tag{3.2}$$

where m is the neutron mass ($m \approx 1$ u).

Neutron flux is defined as the number of neutrons passing through a unit area per unit time, or

$$\phi = n\,v, \tag{3.3}$$

where n is the number of neutrons per volume, and v is their velocity. Hence, the neutron flux distribution for neutrons in thermal equilibrium with a medium at temperature T is

$$\phi_M(E) \equiv n_0\,v\,M(E) = \frac{2\pi}{(\pi kT)^{3/2}} \left(\frac{2}{m}\right)^{1/2} E \exp\left(-\frac{E}{kT}\right), \tag{3.4}$$

where n_0 is the total neutron number density. Equation 3.4 is plotted in Figure 3.1(a) for $n_0 = 1.0$ cm^{-3} at $T = 290$ K. The maximum neutron flux occurs at $E = kT$, which is 25 meV at 290 K. This is the neutron energy at which many thermal neutron reactions are measured and tabulated.

It's often of interest to calculate the reaction rate for a population of neutrons incident on some material, e.g., a radiation detector. For a beam of neutrons incident

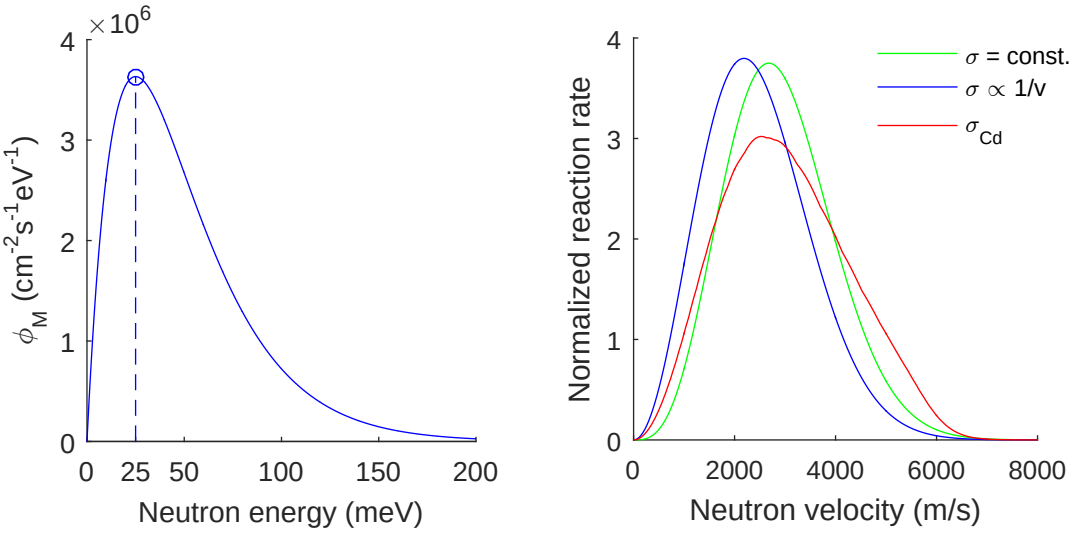

Figure 3.1: Characteristic energy and velocity distributions for neutrons in thermal equilibrium at room temperature. (a) Neutron flux distribution in energy. (b) Reaction rate distributions in velocity normalized to their integrals for $1/v$ materials and Cd.

on a thin target,

$$R \equiv \sigma N_A \phi \tag{3.5}$$

where R is interaction rate in $\mathrm{cm}^{-2}\,\mathrm{s}^{-1}$, σ is microscopic cross section in cm^2, and N_A is the number of target nuclei per cross-sectional area of the beam in cm^{-2}. Microscopic cross section has units of area and is proportional to the probability that a neutron will interact with an atomic nucleus. The reaction rate distribution for a population of thermal neutrons as a function of neutron velocity is then

$$R_M(v) \equiv \sigma N_A \phi_M(v) = \sigma N_A n_0 v M(v). \tag{3.6}$$

For some materials, σ at low neutron energies very closely follows the amount of time a neutron spends within interacting range of a nucleus, i.e., $\sigma \propto 1/v$. This is true for several nuclides commonly used for neutron detection, including those plotted in Figure 3.4(a) and discussed further in Section 3.2. For materials exhibiting this $1/v$

behavior, $R_M(v) \propto n_0\, M(v)$. Hence, the integrated count rate for a perfectly-$1/v$ detector is directly proportional to the density of neutrons, regardless of their energy.

Figure 3.1(b) shows plots of normalized $R_M(v)$ for several material types at $T =$ 290 K. The Cd cross section was taken from ENDF/B-VII.1 evaluated nuclear data [5]. Note that the velocity of maximum reaction rate for $1/v$ materials is the so-called most probable neutron velocity, $v_p = \sqrt{\frac{2kT}{m}}$, or 2 200 m/s at 290 K. Detectors which absorb nearly 100% of incident thermal neutrons fall into the $\sigma =$ const. category of Figure 3.1(b). Since CdZnTe detectors sense thermal neutrons via Cd capture, the σ_{Cd} curve of Figure 3.1(b) corresponds to the distribution of neutron velocities detected by very thin CdZnTe, while CdZnTe with thickness > 2 mm can be approximated by the $\sigma =$ const. curve since the MFP of thermal neutrons in CdZnTe is about 300 μm.

3.1.2 Neutron Moderation Process

Unbound neutrons are generally born of nuclear processes and have kinetic energies in the MeV range. To reach thermal energies, on the order of 10 s of meV, a fast neutron can lose most of its kinetic energy in a material via multiple nuclear collisions. The slowing down process is referred to as *moderation*. There are three types of nuclear scattering interactions by which a neutron can lose some fraction of its kinetic energy: inelastic scattering, elastic resonance scattering, and potential scattering [4]. Each of these are represented in the plot of carbon's microscopic scattering cross section in Figure 3.2.

The total interaction cross section for a material can be broken into its scattering and absorption components, i.e.,

$$\sigma_t = \sigma_s + \sigma_a. \tag{3.7}$$

Here, σ_t is the total interaction cross section, σ_s is the scattering cross section, and

σ_a is the absorption cross section. The absorption cross section can also broken down further into a sum of all neutron-absorbing reactions including capture, fission, and (n,α). For the purpose of this discussion on moderation, however, they will remain grouped together as σ_a. Similarly, σ_s can be broken down:

$$\sigma_s = \sigma_e + \sigma_{in}, \tag{3.8}$$

where σ_e is the elastic scatter cross section including both elastic resonance and potential scatter, and σ_{in} is the inelastic scatter cross section. Figure 3.2 is a plot of carbon's nuclear scattering cross section at room temperature, which serves as an example of the nature of neutron scattering within a low-Z material. The solid lines are evaluated nuclear data from ENDF/B-VII.1 [5], and the lines with data points are measured data using graphite [6]. Figure 2-9 of the textbook by Duderstadt and Hamilton [4] provides a similar plot. Save for neutron energies above about 10 MeV, $\sigma_t \approx \sigma_s$, which indicates that carbon is mainly a neutron scatterer.

A free neutron born from nuclear processes generally has kinetic energy of order 1 MeV, near $\boxed{4}$ in Figure 3.2. In this energy range, the neutron has kinetic energy near the low energy levels of the ^{13}C compound nucleus, causing resonances in σ_e, or sharp fluctuations in the elastic scatter probability. In an elastic resonance scatter, a neutron is absorbed by the ^{12}C nucleus and promptly reemitted, returning the target nucleus to its ground state. Kinetic energy is conserved during an elastic scatter. Neutrons at energies greater than 10 MeV have very short de Broglie wavelength, defined as

$$\lambda = \frac{h}{p} = \frac{h}{\sqrt{2mE}}. \tag{3.9}$$

Hence, when a neutron's wavelength is small compared to the length scale of the nucleus as in $\boxed{5}$ its interaction probability decreases as $\mathrm{E}^{-1/2}$.

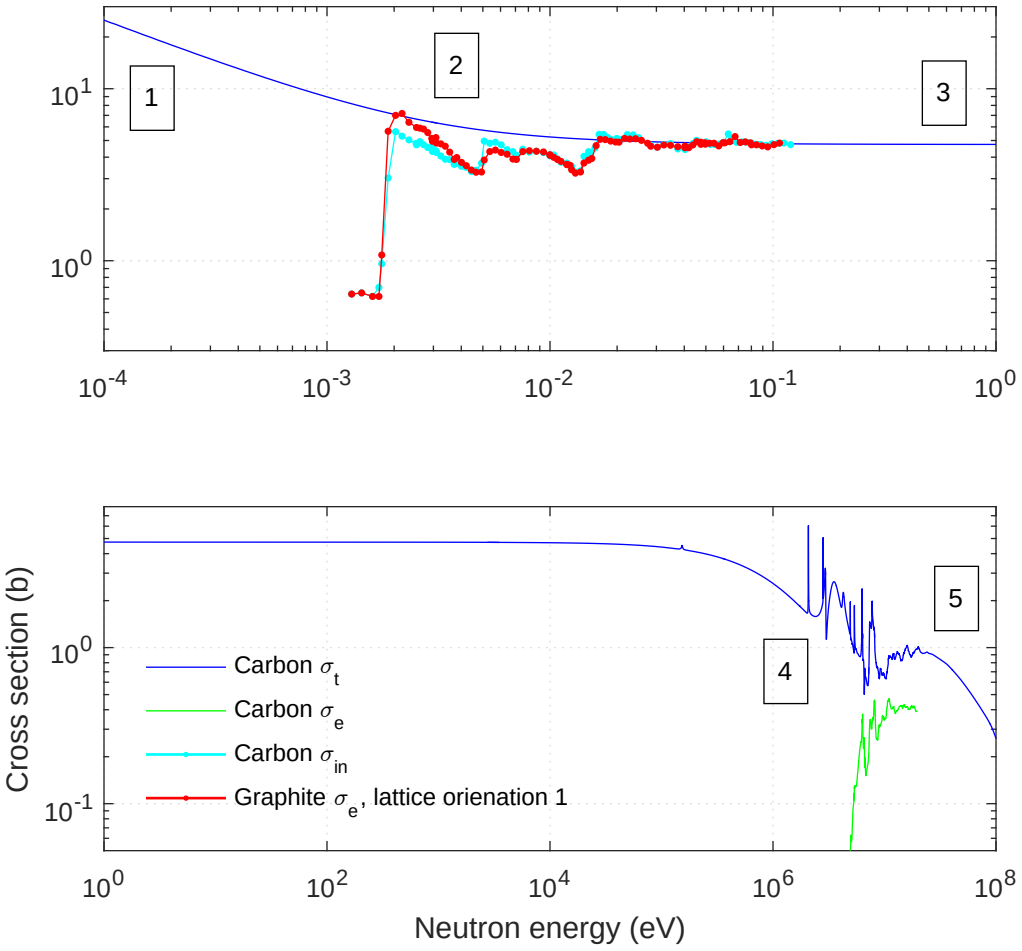

Figure 3.2: Plot of carbon cross section versus neutron energy, adapted from [4]. Solid lines are from ENDF/B-VII.1 [5] and lines with data points are from the XFOR library [6]. Boxed numbers are labeled cross section features described in the text.

Other types of threshold reactions are likely to occur at fast neutron energies, including inelastic scattering. During an inelastic scatter, a neutron with energy exceeding the lowest energy level of the target's compound nucleus is absorbed and reemitted, leaving the residual nucleus in an excited state. As a result, the neutron changes direction and transfers some momentum to the nucleus. The recoil nucleus later relaxes via gamma-ray emission. Kinetic energy is not conserved during an inelastic scatter. Notably, this reaction is detectable in CdZnTe, e.g., at fission neutron energies of several MeV, since it produces gamma rays in the range of 100 s of keV from in Cd, Zn, and Te isotopes [19].

On the other hand, an elastic scattering event can be modeled as a simple two-body collision problem between an energetic neutron of mass number unity and a relatively motionless nucleus of mass number A. Defining the constant

$$\alpha = \left(\frac{A-1}{A+1}\right)^2, \tag{3.10}$$

the leftover kinetic energy of the neutron after an elastic collision is

$$E_f = \frac{1}{2}\left[(1+\alpha) + (1-\alpha)\cos\theta_C\right] E_i. \tag{3.11}$$

In the above formula, $\cos\theta_C$ is the cosine of the center-of-mass scattering angle, and E_i is the neutron's incident energy. An important implication from Equation 3.11 is that a neutron loses the most kinetic energy when the target nucleus has atomic mass near unity. Maximum energy transfer for any nucleus occurs during a backscatter, where $\theta_C = 180°$ and $E_f = \alpha E_i$. For instance, a neutron can lose all of its kinetic energy during a backscatter collision with hydrogen, but only 2% of its energy with ^{238}U. CdZnTe is therefore not a good moderator, since the atomic numbers of its constituents are $\{48, 30, 52\}$, however, the small amount of energy (few keV) transferred to recoil nuclei from backscattered MeV-energy neutrons is

Table 3.1: Slowing down parameters of commonly-used moderators, adapted from Table 8-1 of [4].

Moderator	A	α	ξ	ρ (g/cc)	$\langle \# \rangle$	1-$\bar{\mu}_0$*	$\xi\,\Sigma_s\,(\mathrm{cm}^{-1})$	$\xi\,\Sigma_s/\Sigma_a$
H	1	0	1	gas	14	0.3386	–	–
D	2	.111	.725	gas	20	–	–	–
H_2O	–	–	.920	1.0	16	0.676	1.35	71
D_2O	–	–	.509	1.1	29	0.884	0.176	5670
He	4	.360	.425	gas	43	0.8334	.000016	83
Be	9	.640	.209	1.85	69	0.9259	0.158	143
C	12	.716	.158	1.60	91	0.9444	0.060	192
^{238}U	238	.983	.008	19.1	1730	0.9972	0.003	.0092
HDPE	–	–	.950	0.95	15	–	†2.10	99‡

*From Appendix A of [4]
†Value for unirradiated HDPE [122]
‡Calculated using σ_a for CH_2 [123]

detectable using a low-electronic-noise digital ASIC [19].

The change in a neutron's trajectory as a result of an individual scatter is a random process that follows the differential scattering cross section, provided elsewhere [4, 121]. Average values of scattering cosines for common moderators in the lab frame, $\bar{\mu}_0 \equiv \cos\theta_L$, are provided in Table 3.1, along with several other important parameters. The lab and center-of-mass frame scattering angles are related by

$$\tan\theta_L = \frac{\cos\theta_C}{A^{-1} + \cos\theta_C}. \tag{3.12}$$

It can be seen from Table 3.1 that neutrons typically scatter forward from heavy nuclei but scatter at larger angles from light nuclei.

Since moderation of fast neutrons to thermal energies involves energy loss of more than six orders of magnitude, it is convenient to define the unitless number *neutron lethargy*,

$$u \equiv \ln\frac{E_0}{E}, \tag{3.13}$$

where E_0 is the maximum neutron energy in the system of interest. Furthermore, one can define the average lethargy gain for a material, which corresponds to the average logarithmic energy loss of a neutron following a collision with a nucleus:

$$\xi \equiv \langle u \rangle = 1 + \frac{\alpha}{1-\alpha} \ln \alpha. \tag{3.14}$$

One can then calculate the mean number of scattering interactions necessary to moderate a neutron from 2 MeV to 1 eV, for instance: $\langle \# \rangle \equiv u/\xi = ln\left(2 \times 10^6\right)/\xi = 14.5/\xi$. Values of ξ and $\langle \# \rangle$ are provided in Table 3.1. Given the values $\langle \# \rangle$ and $\bar{\mu}_0$ for each material, its clear that neutrons generally require many scatters to reach thermal energies, and as a result, their angular distribution is roughly isotropic.

An effective moderating material slows down neutrons with few collisions and within a small volume. The macroscopic scattering cross section is defined in terms of the number density of nuclei in a material, N:

$$\Sigma_s \equiv \sigma_s N, \tag{3.15}$$

where the average distance between scatters in a material material is Σ_s^{-1}. One can then use this measure to define the figure of merit

$$\text{Moderating power} \equiv \xi \Sigma_s. \tag{3.16}$$

However, Equation 3.16 is not sufficient to describe an effective moderator, which does not absorb a large fraction of neutrons as they slow down. Low σ_a also means that thermalized neutrons may eventually exit a material without being absorbed, allowing for their emission. In this sense, another figure of merit for measuring the

effectiveness of a moderator is

$$\text{Moderating ratio} \equiv \frac{\xi \, \Sigma_s}{\Sigma_a}, \tag{3.17}$$

where Σ_a is the macroscopic absorption cross section. The cross section used for this calculation is the one which a neutron mainly experiences as it slows down, referred to as the *epithermal* energy range. The cross section is roughly constant in this range for most nuclei, marked by 3 in Figure 3.2. Table 3.1 provides a summary of common moderating materials used in practice. Included in this table is the plastic material HDPE, which, according to Equations 3.16 and 3.17, is a moderator comparable to water. This material is used in the experimental part of this work to generate thermal neutrons from fast neutron sources, described in Chapter VIII. In contrast, if graphite (C of Table 3.1) was used as a moderator, Equation 3.17 suggests that relatively large volumes of the material would be required for moderation, despite Equation 3.17 indicating that fewer neutrons would be captured in the process.

As a fast neutron loses energy via scattering, it reaches the epithermal energy range from eV to keV. In Figure 3.2, the scattering cross section for carbon is roughly constant in the region of 3. Interactions here are dominated by potential scattering, where a neutron scatters off the nuclear potential rather than forms a compound nucleus. The cross section here is approximately constant and roughly corresponds to the geometric cross-sectional area of the nucleus. Heavier nuclei have lower energy states, of order 10 keV, so nuclear resonances can dominate the cross section in this energy range.

Neutrons that avoid absorption during the slowing down process and remain within the moderating material eventually reach the low-energy regions of 1 and 2 in Figure 3.2. These neutrons have energy on the order of the thermal motion of nuclei at room temperature. Equation 3.11 describing elastic scatter of a fast neutron

must then be corrected to include the momentum of the target nucleus for a thermal neutron. Notably, this may result in a boost in energy for the neutron. The overall effect is that neutrons reaching this low energy at room temperature within a material may eventually reach equilibrium with its nuclei. The resulting neutron energy and velocity distribution is in principle Maxwellian, as described in Section 3.2.

In practice, neutrons leaving a moderator near a fast neutron source have an energy spectrum with a few other distinct features. Figure 3.3 shows calculated neutron spectra from ^{252}Cf, a spontaneous fission source, moderated by a polyethylene sphere. The spectrum is provided in flux per unit lethargy, a common unit for visualizing neutron slowing-down spectra. The sphere surrounds the point-Cf source, with inner diameter 3 in. The calculation was done using the Monte Carlo transport code MCNP5 [124]. Notice that the Watt spectrum emitted by the bare source is attenuated by the presence of HDPE, while the thermal component of the spectrum grows. There is also a relatively flat epithermal range between 1 eV and 100 keV. $1/v$ detectors tend to be sensitive at the lower-end of this range, but Cd-based detectors are relatively insensitive since the Cd cross section falls off rapidly around 0.5 eV.

Once a neutron reaches thermal energies, its wavelength is on the order of the atomic spacing in materials. This causes neutrons to interact with collections of nuclei rather than individual nuclei. For example, a neutron may diffract as it travels through a crystal lattice, causing a sharp dependence on neutron energy at integer numbers of lattice spacing. Evidence of this behavior is seen in the jagged cross section curve near $\boxed{2}$ in Figure 3.2 for two lattice orientations of a crystalline graphite sample placed in a neutron beam [6].

Neutrons at sub-thermal energies denoted by $\boxed{1}$ can be generated using moderators at temperatures cooler than room temperature such as liquid hydrogen or deuterium. Cold neutrons can have negligible speed compared to a nucleus in thermal motion at room temperature. Hence, the thermally-averaged cross section at

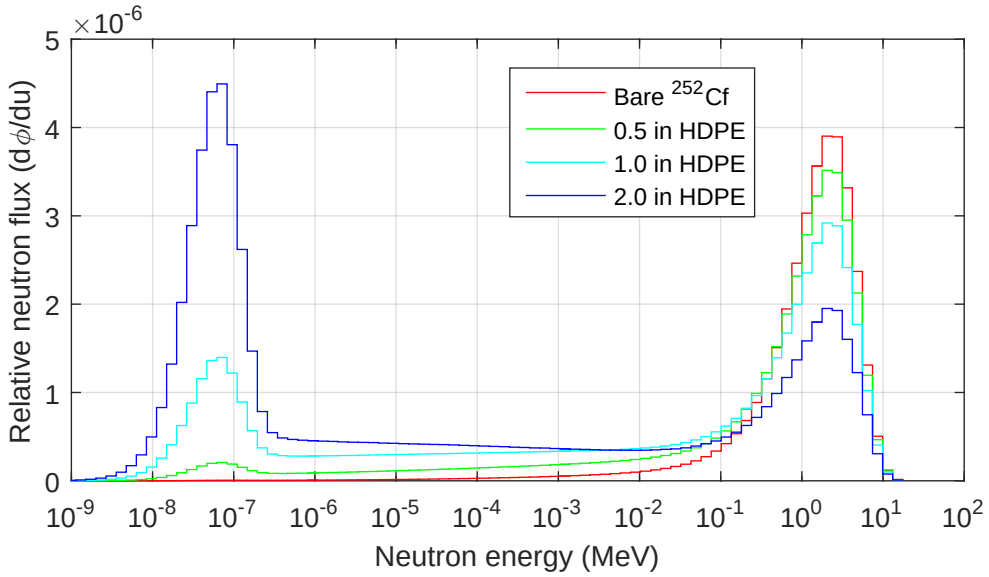

Figure 3.3: Calculated neutron spectra leaving ^{252}Cf surrounded by spherical polyethylene of various thicknesses. Sphere inner diameter was 3 in.

these energies is inversely proportional to the neutron speed, or proportional to the time spent within the interaction range of a nucleus.

To summarize, fast neutrons tend to slow down in low-Z materials via nuclear collisions. Some fraction of these neutrons may reach thermal equilibrium with the material before they are absorbed or leak from its volume in a process called moderation. A good moderator will generate a large population of thermal neutrons within a small volume. Since many scattering interactions are required to reduce a neutron from fast to thermal energies, thermal neutron emissions from moderators are generally isotropic. Thermal neutrons leaving a material can then travel a long distance through air before interaction as their mean free path is about 20 m.

3.2 Cd Capture in CdZnTe

Since thermal neutrons have kinetic energy less than 1 eV, they are not directly ionizing; therefore, they have to be measured indirectly. Most thermal neutron detectors rely on exothermic nuclear reactions that produce one or more charge particles.

Common examples include (n,α) and (n,p) reactions. Several cross sections for reactions commonly utilized for this purpose are plotted in Figure 3.4(a) and all exhibit the $1/v$ behavior discussed in Section 3.1.1. Equation 3.6 shows that rather conveniently, the reaction rate for $1/v$ detectors and hence the count rate is directly proportional to the number density of incident neutrons, regardless of their velocity distribution. This is, of course, only accurate at energies where the cross section follows the $1/v$ trend, which is true below about 100 keV for the materials of Figure 3.4(a).

For heavy nuclides, gamma-ray emission is most likely following thermal neutron capture [125]. Cross sections for the radiative capture reaction are plotted in Figure 3.4(b) for several heavy non-fissile nuclides of interest. These particular isotopes have exceedingly high capture cross sections, ^{113}Cd included. At 25 meV, the ^{113}Cd capture cross section is 20 600 b, beyond even the cross sections of common neutron detectors from Figure 3.4(a). This is one reason that natural Cd is frequently used for shielding thermal neutrons. In addition, the sharp drop off in cross section around 0.5 eV allows transmission of neutrons at higher energies. This feature is commonly referred to as the Cd cutoff.

As a result of the large ^{113}Cd cross section, the MFP of a 25 meV neutron in $Cd_{0.9}Zn_{0.1}Te$ is a mere 300 μm. By definition, the kinetic energy of a thermal neutron is on the same order as the thermal motion of the ^{113}Cd nuclei at room temperature. This means the small initial transfer of momentum to the compound ^{114}Cd* nucleus from thermal neutron capture is not directly detectable in room-temperature CdZnTe detectors. However, as Equation 1.1 suggests, the compound nucleus relaxes by emitting a cascade of gamma rays with sum energy 9.043 MeV. The final product of this reaction is the ^{114}Cd nucleus in its ground state.

By conservation of momentum, even if a single 9.043 MeV gamma-ray is emitted during relaxation, the recoil ^{114}Cd nucleus would have kinetic energy less than 0.4

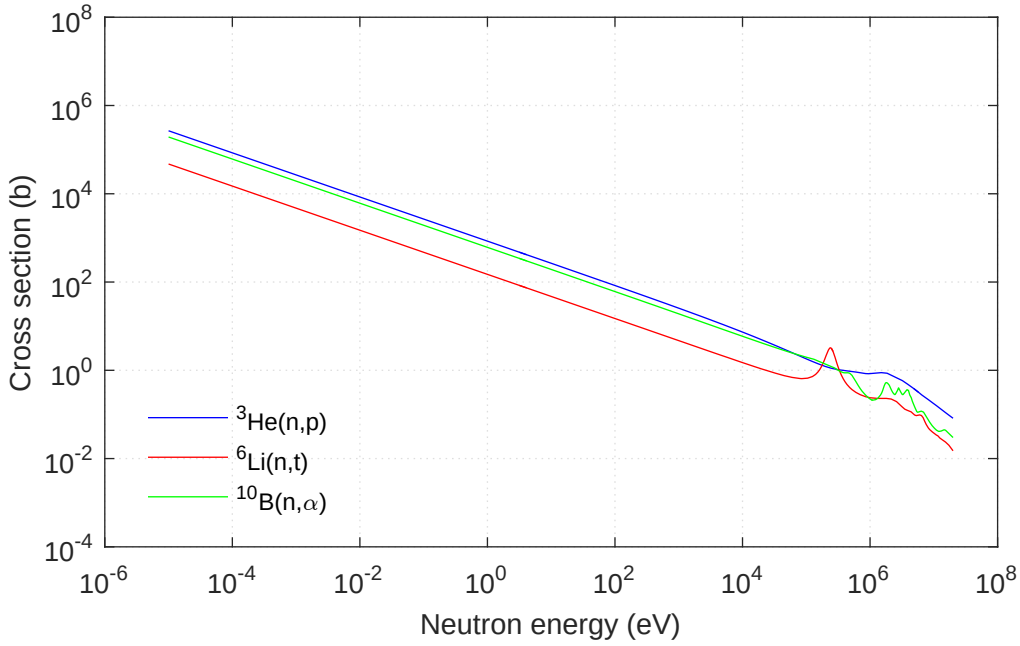

(a)

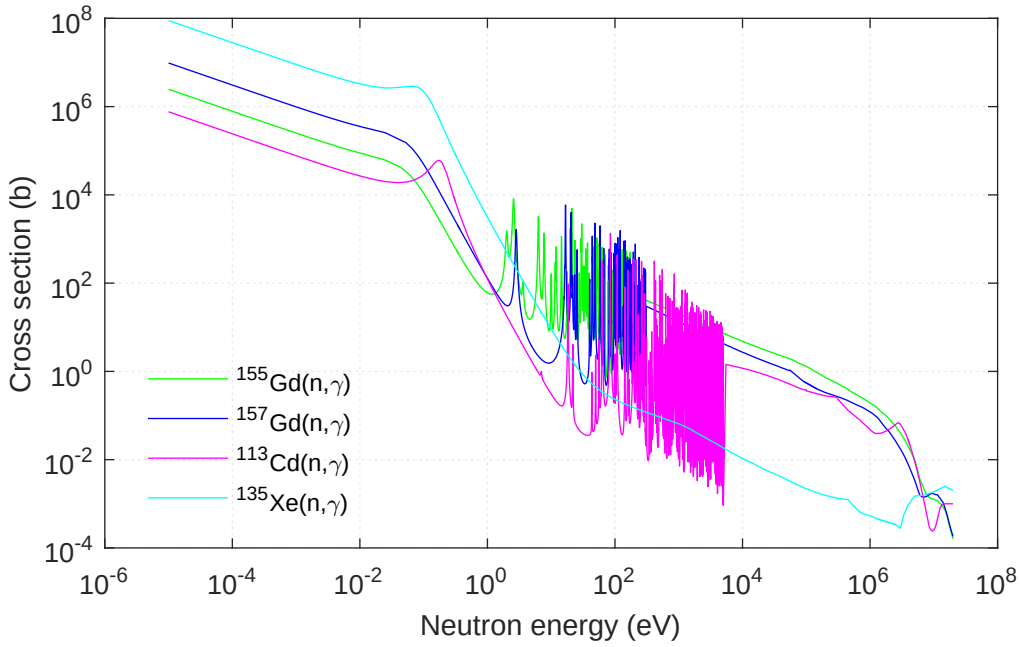

(b)

Figure 3.4: (a) Cross sections for reactions with several low-Z nuclides used commonly in neutron detection. (b) Exceptionally high radiative capture cross sections exhibited by several common nuclides. All cross sections were taken from ENDF/B-VII.1 evaluated nuclear data [5] except for ^{135}Xe(n,γ), taken from the JEFF-3.1 Nuclear Data Library [7].

keV. This is below the current electronic noise threshold in CdZnTe. Furthermore, the most frequent thermal neutron capture events actually result in emission of multiple, lower-energy gamma rays which can cause the recoil nucleus to have even lower kinetic energy. Hence, ^{113}Cd(n,γ)^{114}Cd reactions in CdZnTe must be sensed via secondary interactions of these cascade gamma rays or internal conversion electrons, as discussed in the following sections.

3.2.1 Energies and Multiplicity of Cascade Gamma Rays

Following ^{113}Cd capture, the compound ^{114}Cd* nucleus exists in a 9.043 MeV excited state before decaying to ground. The many possible quantum states of the ^{114}Cd nucleus permits a large number of decay paths for each capture event. As it decays, the nucleus briefly exists at a number of intermediate energy levels, with half-lives on the order of fs to ns. At the moment of transition from one level to the next, a gamma ray is released to carry away the corresponding difference in energy. The result is a number of various combinations of gamma rays emitted during each capture event each with sum energy 9.043 MeV.

Figure 3.5 shows levels for ^{114}Cd that are below 1365 keV, only a small fraction of possible transitions [8]. This plot also shows all transitions observed using CdZnTe as part of this work, as reported in Chapter IV. It is interesting to note the pairs and triplets of transitions that are expected to occur in near-coincidence; the half-lives of these states are given and on the order of a few ps to ns. These simultaneous transitions include the pairs 725 keV and 558 keV, 806 keV and 558 keV, 576 keV and 558 keV, and the triplet 96 keV, 651 keV, and 558 keV; all of which were observed and reported in Chapter IV. The probabilities of frequent gamma-ray transitions following ^{113}Cd capture have also been measured and tabulated [10], and the values are plotted in Figure 3.6. Notice that the gamma-ray lines are widespread in energy and many are in the MeV-range. The most likely transition is by far 558 keV, the

second-to-last transition for many deexcitation paths.

Gamma-ray emission always competes with the process of internal conversion during nuclear transition. In this transition, a closely-bound electron (most likely K-shell) interacts with the nucleus, ejecting it from its bound state. The energetic conversion electron then carries away the transition energy less the electron binding energy. Characteristic X-rays and/or Auger electrons follow as the resulting vacancy is filled by the higher-level electrons of the atom. The probability of gamma-ray emission versus internal conversion for a given transition is quantified by the ICC, equal to the ratio of internal conversion to gamma ray transition probabilities.

Figure 3.5 also provides the angular momentum and parity of each ^{114}Cd state below 1365 keV. The difference in nuclear spin and parity between levels determines the gamma-ray multipolarity for that transition, which affects the ICC [125]. The dominating multipolarities and corresponding ICCs are provided in Table 3.2 for all transitions with greater that 1% probability of emission during ^{113}Cd capture. Here, electric and magnetic multipolarity is indicated by {E1, E2, ...} and {M1, M2, ...} respectively, were a + sign indicates a mixture of two types. Gamma ray emission is not possible for E0 transitions, where internal conversion is the primary mode of decay. Note that ICCs are less than 0.005 for every transition except at 96 keV. The ICC decreases rapidly with gamma-ray energy, and therefore, most transitions from ^{113}Cd capture result in the emission of one or more gamma rays.

In terms of detection efficiency, gamma rays are much more difficult to stop than conversion electrons of the same transition. Unfortunately, the only transition with reasonably high ICC (96 keV) occurs with relatively low probability. On the other hand, Table 3.2 shows that 558 keV is emitted during 74.4% Cd capture events. The MFP of the resulting gamma ray in CdZnTe is 2.1 cm, while others are also on the order of cm. For this reason, large-volume CdZnTe detectors with thickness on the order of cm are necessary to achieve reasonable detection efficiency. As mentioned

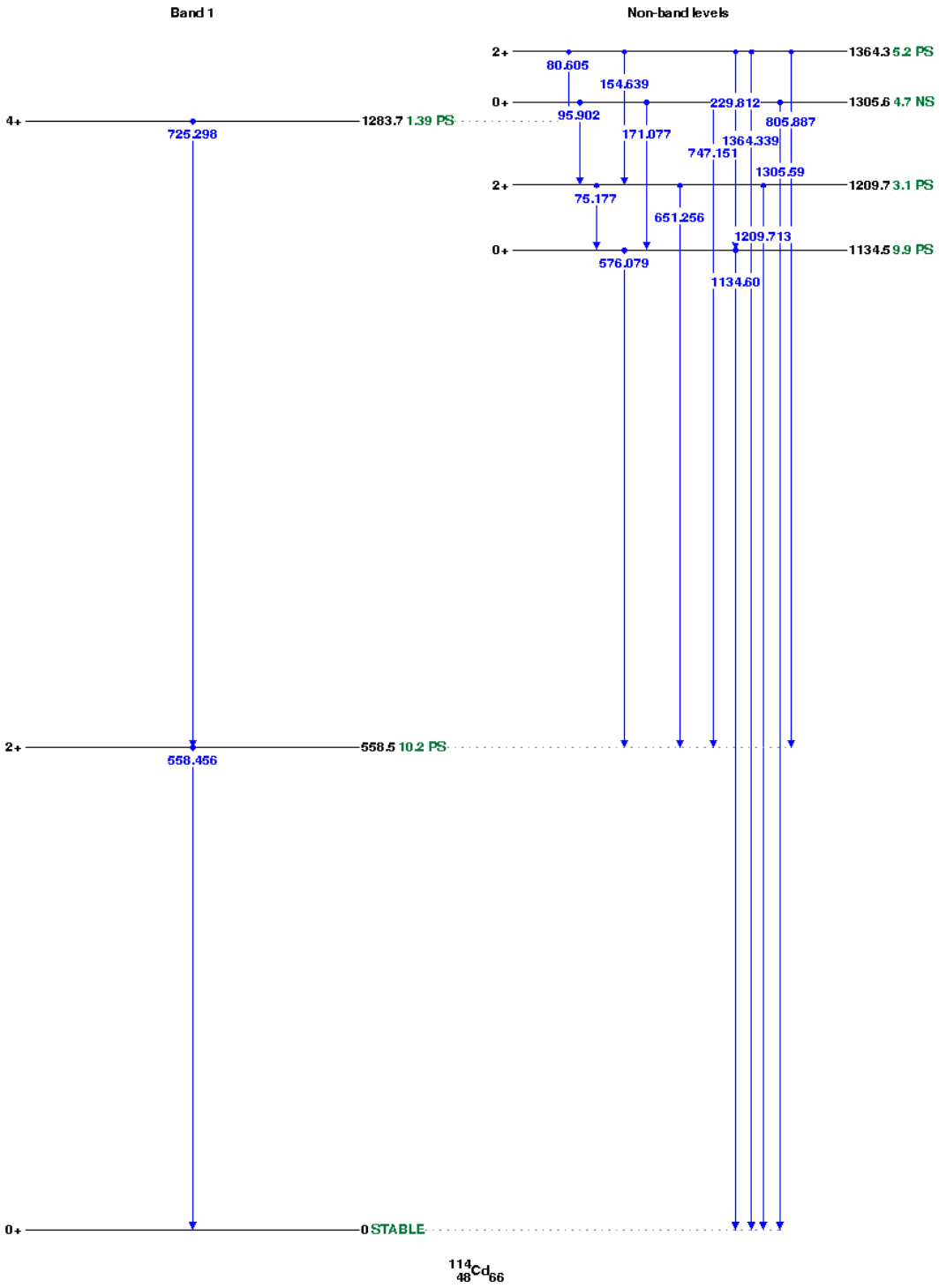

Figure 3.5: ^{114}Cd nuclear level scheme for levels below 1365 keV only [8], with chart generated using the NNDC website [9]. The black text provides each level energy in keV as well as spin-parity, the green text indicates the half life for each level, and the blue text is the gamma-ray energy in keV corresponding each transition. The vertical separation of levels is proportional to their energy difference. Levels on the left correspond to the ground state rotational band.

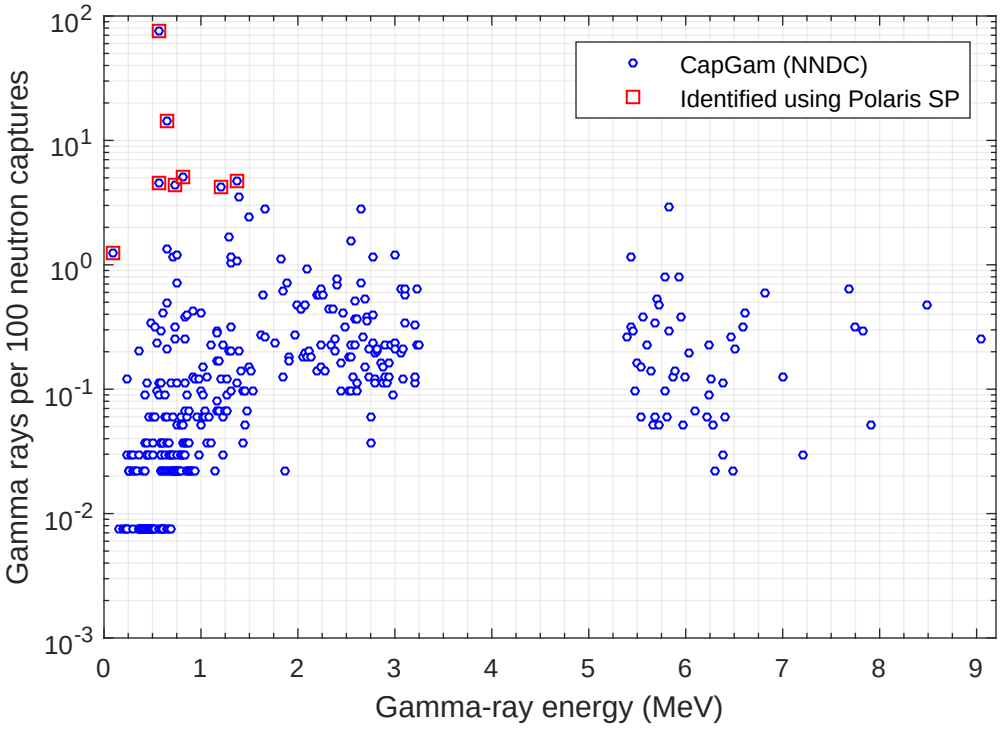

Figure 3.6: Yield of gamma rays from ^{113}Cd capture, downloaded from CapGam of NNDC [10]. Uncertainties also reported there. Gamma-ray lines identified in gamma-ray spectra recorded using the Polaris SP pixelated CdZnTe array as part of this work are indicated with red boxes.

before, capture events occur very near the CdZnTe surface, so half of cascade gamma rays are lost to the 2π solid angle facing away from the crystal.

The number of gamma rays emitted per capture was measured for neutrons at the 0.2 eV resonance by Rusev et al. in 2013 [48]. Coincident gamma-ray spectra were reported for gamma-ray multiplicities from 2 to 7, which peaked in intensity at a multiplicity of 4. It is important to note that the sum energy from the simultaneous interactions of several gamma rays, which vary in energy from one capture to the next, does not result in a photopeak, but instead a continuum that is difficult to separate from gamma-ray background [120]. Although multiplicity will reduce the photopeak efficiency of traditional spectrometers using the Cd reaction, Chapter IV demonstrates experimentally that pixelated CdZnTe can overcome this problem by

Table 3.2: Transitions of intensity $\geq 1\%$ for the excited compound ^{114}Cd nucleus as a result of ^{113}Cd capture, organized by intensity. Parameters given are the transition energy, intensity expressed in percent of ^{113}Cd captures [10], gamma-ray multipolarity [8], and total ICC [15]. Multipolarity information was not available for transitions above 5 MeV.

E (keV)	**I (%)**	**γ Mult.**	**ICC**	**E (keV)**	**I (%)**	**γ Mult.**	**ICC**
558.46*	74.4	E2	0.0049	2550.1	1.53	E1	0.0011
651.26*	14.1	M1+E2	0.0034	654.55	1.33	M1+E2	0.0033
805.89*	5.11	M1+E2	0.0020	95.90*	1.25	E2	1.735
1364.3*	4.64	E2	0.0006	748.39	1.21	E1	0.0009
576.08*	4.47	E2	0.0045	2999.7	1.18	E1	0.0013
725.30*	4.46	E2	0.0024	707.42	1.16	E2	0.0026
1209.7*	4.15	E2	0.0008	5433.1	1.16	–	–
1399.6	3.45	E1	0.0004	1305.8	1.14	E0	–
5824.6	2.95	–	–	2767.5	1.14	E1	0.0012
1660.4	2.79	M1+E2	0.0006	1826.3	1.10	E1	0.0007
2660.1	2.77	M1+E2	0.0008	1370.6	1.08	E1	0.0004
1489.6	2.38	M1+E2	0.0006	1301.2	1.03	E2	0.0007
1283.5	1.69	E2	0.0007				

* Identified using Polaris SP pixelated CdZnTe array as part of this work.

reading out coincident interactions separately rather than the collective signal.

3.2.2 Spatial Distribution of 558 keV Interactions

The ultimate objective of this work goes beyond detection and seeks to image thermal neutron emissions. The approach taken here is one of time-coded apertures, which intrinsically does not require position sensitivity. However, if a large array is used to achieve higher detection efficiency, the size of the array can limit the imager's spatial resolution. This effect can be mitigated if the position of each ^{113}Cd capture site can be localized to a scale smaller than the detector array dimensions using either a known gamma-ray or internal conversion electron.

Internal conversion is clearly preferable in terms of position resolution due to the short range of conversion electrons. The 96 keV transition of Table 3.2 is in principle a good imaging signal for this reason, and the MFP of its associated gamma ray is

also only 1.0 mm. In practice, however, the gamma-ray background and Compton continuum from higher-energy gamma rays combine at these lower energies in large-volume CdZnTe detectors, which can generate a prohibitively high background level of counts at 96 keV. This can be witnessed in gamma-ray spectra reported in Chapter IV, e.g., Figure 4.1. Unmodulated gamma-ray background causes degradation in the statistical SNR of a coded image, making the 96 keV line unattractive for the purposes of this work.

On the other hand, the same spectrum of Figure 4.1 also shows that the prominent transition of 558 keV has high enough energy to avoid the low-energy rise in gamma-ray background. As a result, the 558 keV peak has inherently better statistical SNR for imaging. SNR is a key characteristic when imaging with few counts or in the presence of high gamma-ray background; each of these are commonly-encountered conditions when imaging thermal neutron emissions in practice. However, the MFP of 558 keV gamma rays is relatively large, about 2 cm. The resulting spread in 558 keV interactions away from the absorption site due to the gamma ray's isotropic emission must be understood to make best use of its signal for imaging.

As mentioned previously, thermal neutrons have very short MFP in CdZnTe; more than 99% are absorbed within the first 1.5 mm of the crystal surface. Cascade gamma rays are therefore emitted from very near the CdZnTe surface, and since their emission is isotropic, the combined effects of geometric and mass attenuation govern their spatial distribution. The flux of gamma rays from the capture site then falls off with intensity according to

$$\varphi_\gamma(r) = \frac{e^{-\mu r}}{4\pi r^2}, \tag{3.18}$$

where r is distance from the capture site and μ is the attenuation coefficient of CdZnTe at the gamma-ray energy of interest. Figure 3.7(a) shows Equation 3.18 for 558 keV gamma rays, numerically integrated over all x and y, where $r^2 = x^2 + y^2 + z^2$, for a

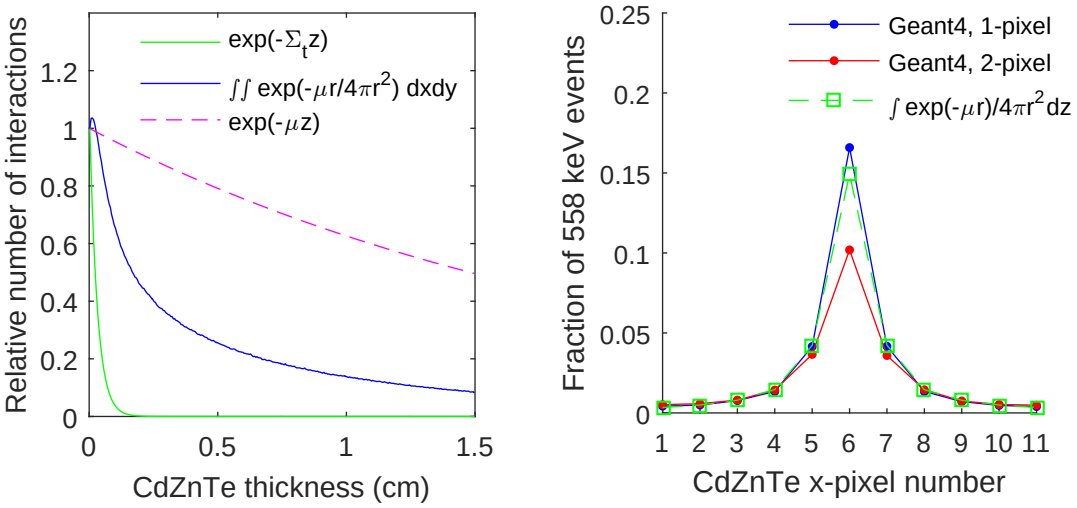

(a) (b)

Figure 3.7: (a) Exponential attenuation of thermal neutrons in CdZnTe, the resulting 1-D interaction distribution of 558 keV cascade gamma rays according to Equation 3.18, and attenuation of 558 keV gamma rays from a far-field source for comparison. (b) Comparison between 558 keV interaction distributions in the x direction for a 1.5-cm-thick pixelated CdZnTe detector, predicted by Equation 3.18 and calculated using Geant4, as described in the text.

distribution of Cd capture sites that follows the exponential attenuation of thermal neutrons in CdZnTe, i.e. $\exp(-\Sigma_t z)$, where z is depth into the crystal. The result is the theoretical interaction distribution of 558 keV gamma-rays for a flood irradiation of thermal neutrons at the surface of a large CdZnTe array. Note that this distribution falls off faster than exponential attenuation, which is expected for a source of 558 keV gamma rays much farther away from the CdZnTe surface.

Figure 3.7(b) shows the lateral distribution of interactions generated by Equation 3.18 for neutrons incident on the cathode side of a 2 cm $\times$ 2 cm $\times$ 1.5 cm CdZnTe crystal and absorbed within the center pixel of the 11 $\times$ 11 pixel array. The detector's electrode geometry is described in more detail in Section 4.1. Geant4 simulation [126] agrees well with the predicted fraction of 558 keV photopeak interactions in each pixel for 1-pixel events except at the center pixel. This is likely due to backscattered-then-absorbed events in the center (emitting) pixel that are counted as 1-pixel events,

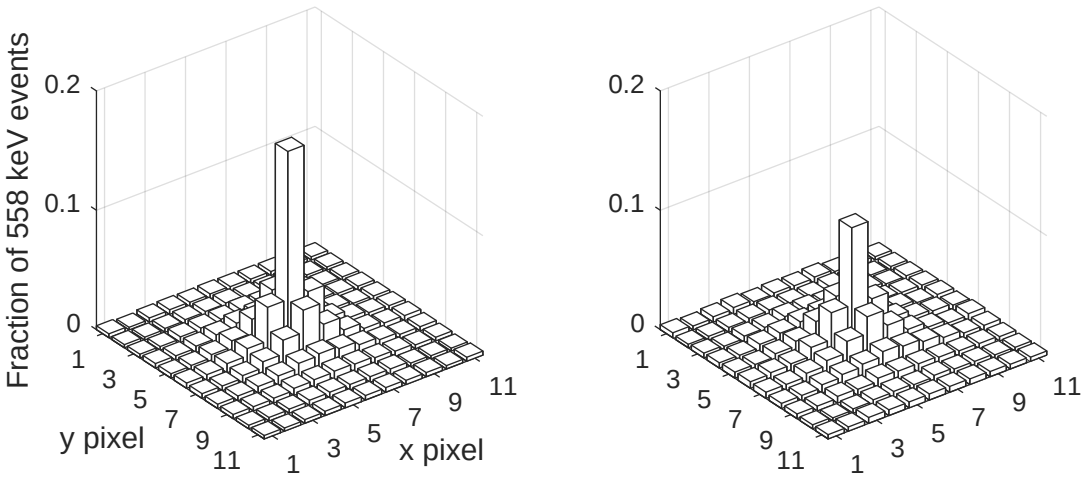

Figure 3.8: Calculated interaction distributions of 558 keV gamma rays in a single 2 cm × 2 cm × 1.5 cm CdZnTe crystal for (a) one- and (b) two-pixel events due to a pencil beam of thermal neutrons incident at the center x and y pixel (6,6) above. Two-pixel event locations were chosen according to the first interaction, where the sequence was chosen using the simple comparison method. Calculated using Geant4.

though they include two interactions.

The 2-pixel interaction distribution calculated by Geant4 is also shown in Figure 3.7(b), using the first interaction pixel as the binned position. The simple comparison method was used to sequence these events, however this method does not always choose the correct sequence, as discussed in Section 2.2.1. Incorrect sequencing is likely the main reason for the reduced fraction of events attributed to the pixel where capture occurs. For a 3 × 3 array of CdZnTe detectors of the same size, the fractions of 558-keV photopeak events categorized as 1-, 2-, and 3-pixel from a thermal neutron flood irradiation at the cathode surface were calculated using Geant4 and found to be 0.53, 0.40, and 0.05, respectively.

The distributions in x and y provided by Geant4 are also shown in Figure 3.8 for 1- and 2-pixel events. These histograms are essentially the probability distributions of 558 keV photopeak events for neutron captures that occur within the center pixel of the 11 × 11 pixelated CdZnTe detector, which cover its 2 cm × 2 cm cross-sectional

area. Hence, it is the combined blur induced by 558 keV photons and detector pixels. 2-pixel interactions of 558 keV photons, however, may be back-projected to their original location using Compton imaging [53, 127], as described in Section 4.3. This blur is a limiting factor on the size of coded aperture elements in both time-coded and coded aperture imaging. Section 6.3 further discusses its effect on the design of the time-coded aperture in this work.

CHAPTER IV

Measured Thermal Neutron Detection Performance

Neutron detection via the Cd capture reaction is considered to be inherently sub-optimal due to the combined effects of gamma-ray multiplicity and the fact that there are hundreds of possible transitions from the cascade. The concern is that frequent, simultaneous interactions from several gamma rays of varying energies do not generate photopeak counts. Rather, their sum energy produces a continuum that is not easily discernible from gamma-ray background, as described in a review by Bell, et al. [120]. It was also noted that the collection of previously-reported CdZnTe and CdTe detector efficiencies measured via photopeak areas do not appear to be in mutual agreement.

The experimental results presented here demonstrate pixelated CdZnTe's ability to address this problem, mostly due to its pixelated anode readout. Since multiple, coincident gamma-ray interactions are read out by separate anode pixels, each can be separated and added back to its respective photopeak. The large MFP of most Cd-cascade gamma rays causes their interactions to be spatially separated well beyond a single pixel pitch. Section 4.2 shows that this procedure returns the photopeak efficiency at 558 keV to very near its theoretical value without multiplicity losses. In total, about one third of 558 keV events occurred in coincidence with other gamma

rays.

The ability to resolve coincident capture gamma-rays using the pixelated CdZnTe readout is demonstrated in Section 4.1.2. In total, the seven most-probable gamma-ray lines were identified, in addition to the lower-energy 96 keV line, as listed in Table 3.2. Further separation of Cd capture events from gamma-ray background based on their interaction locations is also shown. Finally, the inherent directionality of CdZnTe from surface illumination is demonstrated in Section 4.3.

4.1 Measurement of Cascade Gamma Rays at NARS

The first demonstration of thermal neutron detection using CdZnTe was provided in 1996 by McGregor, Lindsay, and Olsen [18]. In that work, a 10 mm $\times$ 10 mm $\times$ 3 mm $Cd_{0.8}Zn_{0.2}Te$ commercial detector was used to measure a twice-diffracted beam of thermal neutrons from the Ford Nuclear Reactor at the University of Michigan/Phoenix Memorial Laboratory. A spectrum recorded for 9.5 h at $4\,100 \pm 2\,100$ $cm^{-2}s^{-1}$ clearly showed the 558 keV and 651 keV gamma-ray lines, as well as 576 keV, 651 keV, 725 keV, and 806 keV.

In April of 2015, a set of thermal neutron measurements were taken with the Polaris SP system at the NARS laboratory as part of this work. The facility houses an external beam line from the 500 kW Ohio State University Research Reactor (OSURR). The beam is a small, 30-mm-diameter opening that provides a clean thermal neutron flux controllable by adjusting reactor power [128]. The Polaris SP system consists of two separate planes of 20 mm $\times$ 20 mm $\times$ 15 mm pixelated $Cd_{0.9}Zn_{0.1}Te$ detectors arranged in a 3×3 array, pictured in Figure 4.1(a). Not only does this system contain a significantly greater volume of CdZnTe for detecting cascade gamma rays, but the pixelated electrode design provides additional information about cascade events beyond the spectra provided in previous work.

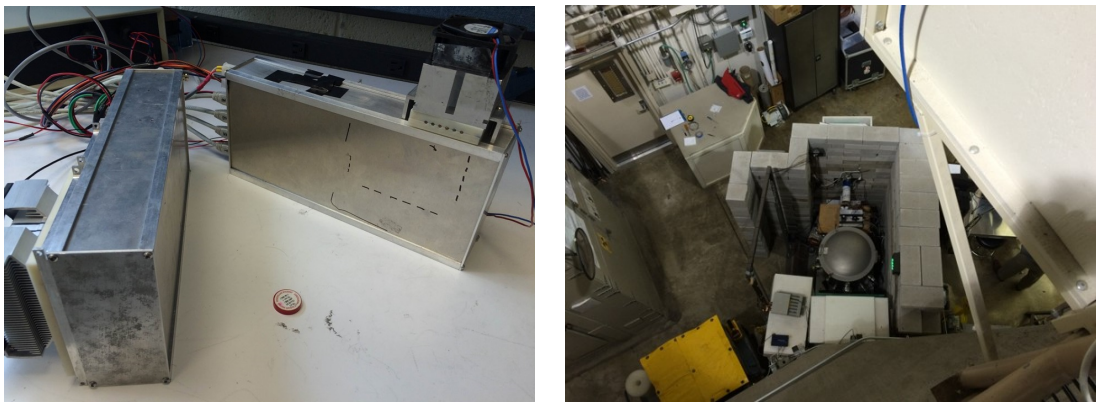

(a) (b)

Figure 4.1: (a) Polaris SP system with both plane's cathodes facing a button source of gamma rays. (b) Output of the beam port at the NARS laboratory. The beam was incident from the bottom of the picture, through the round sample chamber, and onto the cathodes of Polaris SP's plane B, positioned near the center of the photograph.

4.1.1 Modulation of Neutron Beam with ^{6}Li Glass Plate

The first measurement taken at the NARS laboratory was at 0.5 kW reactor power, resulting in a thermal neutron flux of about 2 500 $\mathrm{cm}^{-2}\mathrm{s}^{-1}$ at the output of the beam port. The beam was incident on the cathodes of Polaris SP's plane B for 15 min, with plane A placed directly behind as pictured in Figure 4.1(b). To compare the resulting gamma-ray energy spectrum with and without thermal neutrons present, the measurement was repeated with a ^{6}Li glass plate covering the beam line. The purpose of this plate was to absorb most thermal neutrons without creating additional capture gamma rays. The resulting count rates were 1 783 cps with and 2 170 cps without the ^{6}Li glass. A nominal 410 μs dead time was used to calculate the percent dead time during each measurement, which was 73% and 89%, respectively. The dead-time-corrected spectra for both measurements are shown in 4.2(a).

There is a clear difference between the two spectra of Figure 4.2(a). The unshielded beam spectrum shows some of the most prominent lines listed in Table 3.2, with relative intensities convolved with detector efficiency. These include the 96 keV, 558 keV, and 651 keV emissions. A small cascade gamma ray peak at 578 keV is also

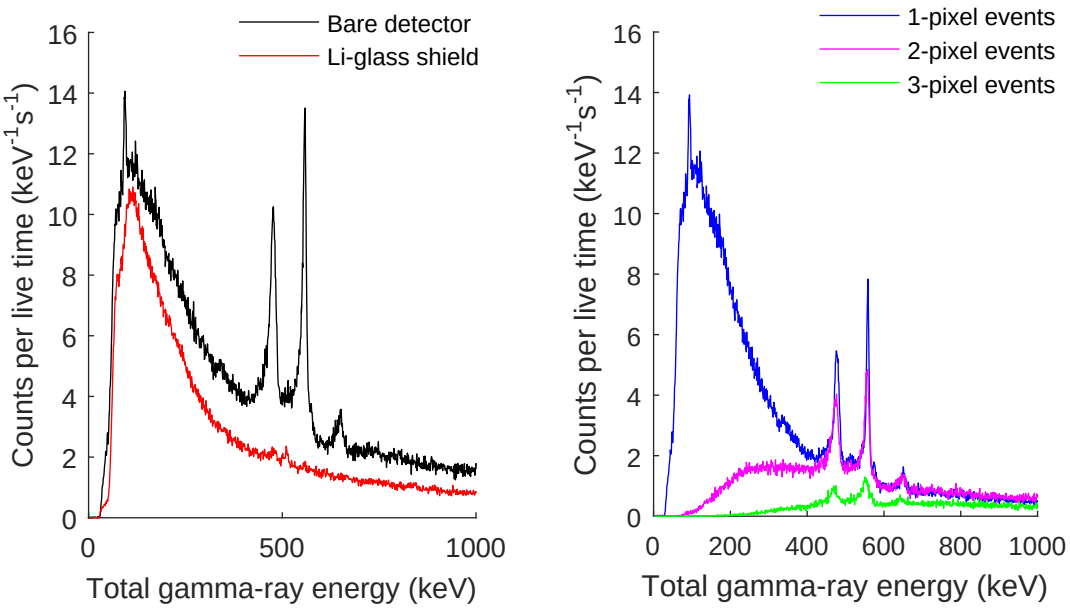

Figure 4.2: Gamma-ray energy spectra for thermal neutrons incident on Polaris SP CdZnTe array. (a) Spectra for unshielded neutron beam and shielded by ^{6}Li glass plate. (b) Unshielded spectrum separated by the number of triggered pixels per event.

present in the 1-pixel spectrum of Figure 4.2(b). The absence of these gamma-ray lines in the presence of the thermal-neutron-absorbing ^{6}Li glass plate is further evidence that the observed signal is the result of neutron capture. The peak at 478 keV is the Doppler-broadened gamma-ray emission from neutron capture on boron, which is present in the printed circuit board (PCB)s between the beam port and detector cathodes. The 511 keV peak is also produced from interactions outside the CdZnTe.

Figure 4.2(b) shows the unshielded beam spectrum of Figure 4.2(a) separated by the number of triggered pixels per event. As discussed in Section 3.2, multiple gamma rays are commonly emitted during the cascade. However, the 96 keV, 558 keV, and 651 keV peaks present in the 1-pixel spectrum are the result of photoelectric events of individual cascade gamma rays. Similarly, the 558 keV and 651 keV peaks present in the 2- and 3-pixel spectra are the result of individual gamma rays interacting multiple times. These peaks are present because some gamma rays from the cascade do not

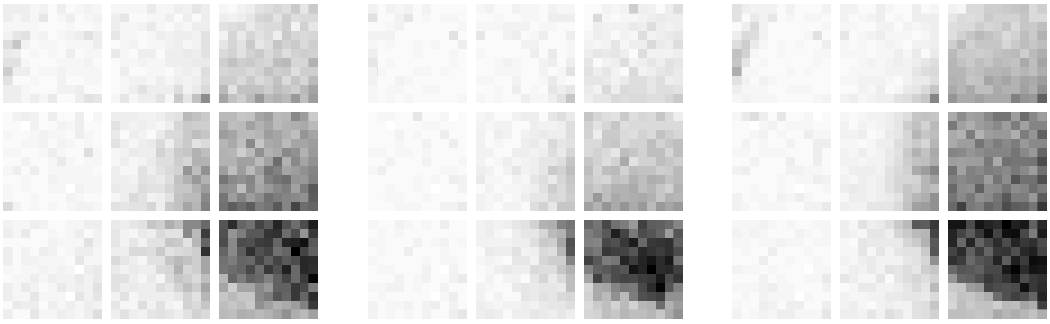

(a) 478 keV peak (b) 558 keV peak (c) 680 keV to 1000 keV

Figure 4.3: Spatial distribution of 1- and 2-pixel events for three different gamma-ray energy windows. The circular shape of the thermal neutron beam can be seen at the right side of the array. The ^{6}Li glass plate partially blocked the beam, leaving the bottom right detector most exposed to thermal neutrons.

result in a triggered pixel, e.g., they are emitted in a direction opposite the detector, their interaction does not exceed anode thresholds, or they simply transmit through the CdZnTe volume without interaction. More detail on detection of multiple gamma rays is provided in Section 4.1.2.

A third measurement was taken with the ^{6}Li glass plate partially blocking the thermal neutron beam. The plate covered the circular cross section of the beam except for a region roughly corresponding to the bottom third of the array. The relative number of counts for each pixel of the 3×3 array are plotted for 1- and 2-pixel events in Figure 4.3 for three different energy windows. For 2-pixel events, the interaction closest to the cathode was chosen. The plot of the locations of 558 keV events in Figure 4.3(b) clearly shows highest contrast between the unshielded and shielded regions of the beam. Since both lower-energy 478 keV events and higher-energy continuum events yielded lower contrast, the difference could not have been caused by the energy-dependent attenuation of gamma rays directly from the beam through the glass plate. In fact, a few additional observations can be made to show that this was actually a result of the modulation and subsequent absorption of thermal neutrons at the CdZnTe surface.

Continuum events in Figure 4.3(c) were likely caused by gamma rays directly from the beam that were weakly modulated by the low-Z glass plate. On the other hand, a large fraction of the 478 keV events shown in Figure 4.3(a) were induced by thermal neutrons strongly modulated by the ^{6}Li-loaded plate, yet those events yielded similar contrast to Figure 4.3(c). The difference is that these neutrons were captured by ^{10}B in the PCB, farther from the cathode surface of CdZnTe crystals. Therefore, these isotropically-emitted capture gamma rays were broadly distributed in space before reaching the detector. The resulting contrast between unshielded and shielded beam regions is therefore similar to the continuum events upon which the 478 keV peak rests. On the other hand, 558 keV events are most likely absorbed near their emission location as discussed in Section 3.2, providing the increased contrast seen in Figure 4.3(b).

4.1.2 Observation of Coincident Cascade Gamma Rays

Coincident cascade gamma rays may be used as a unique signal for detection of thermal neutrons since their interactions have energy and spatial distributions that are different from interactions of individual gamma rays. The unshielded measurement of thermal neutrons using Polaris SP at NARS was used to confirm that the expected coincident gamma ray lines from Cd capture were observed. Events with total energy equal to the sum of known coincident cascade pairs from Figure 3.5 are plotted in Figure 4.4. The blue histograms show individual energies of 2-pixel events, while the red histograms show every combination of energies from 3- and 4-pixel events that were assumed to be the result of either one or both gamma-rays at the listed energies Compton scattering before absorption. Double coincidence is clear in Figure 4.4 for each pair of lines expected to occur in coincidence. Interestingly, Figure 4.4(b) contains the $96 + 651$ keV pair of peaks along with $558 + 189$ keV peaks that likely correspond to events of 558 keV gamma-absorption with a coincident backscattered

gamma ray. The effect of backscattered gamma rays is also clear in the plot of Figure 4.4(a) among others.

For each of the double coincidence lines in Figure 4.4, there exists a substantial background from chance coincidence. The spatial separation of interactions may be used to further reduce this background. Figure 4.5 demonstrates this concept using spatial filters for 2-pixel interaction events. The pairs $558 + 725$ keV and $558 + 806$ keV are not shown because due to large statistical noise. Here, only interactions separated by at least 5 mm were plotted. Figures 4.4(a) and 4.4(b) have the additional requirement that the 96 keV gamma ray must have interacted within 2 mm of the cathode surface. When compared to Figure 4.4, it is clear that the chance coincidence level from non-cascade gamma rays was reduced. Events that include the 96 keV gamma will also provide excellent position resolution due to the short range of conversion electrons and low energy gamma ray. It should be noted that this analysis is also possible for the less-frequent triple coincidence signals, however the chance coincidence rate largely overwhelmed the triples rate here.

4.1.3 Spatial Discrimination of Neutrons and Gamma Rays

There will inevitably be some gamma-ray background beneath photopeaks from Cd cascade events. For both thermal neutron detection and imaging, it can be helpful to reduce the gamma ray background. The purpose of this analysis was to use the spatial information provided by pixelated CdZnTe to better separate cascade events from background gamma rays of the same deposited energy. The following analysis was done using data from the bare irradiation of Polaris SP's cathode surface at the NARS laboratory. The total energy spectrum is provided in Figure 4.2, which includes a significant background from non-cascade gamma-rays.

A 2-D representation of the Polaris SP array is also provided in Figure 4.6 to illustrate some characteristic spatial differences between cascade and background gamma

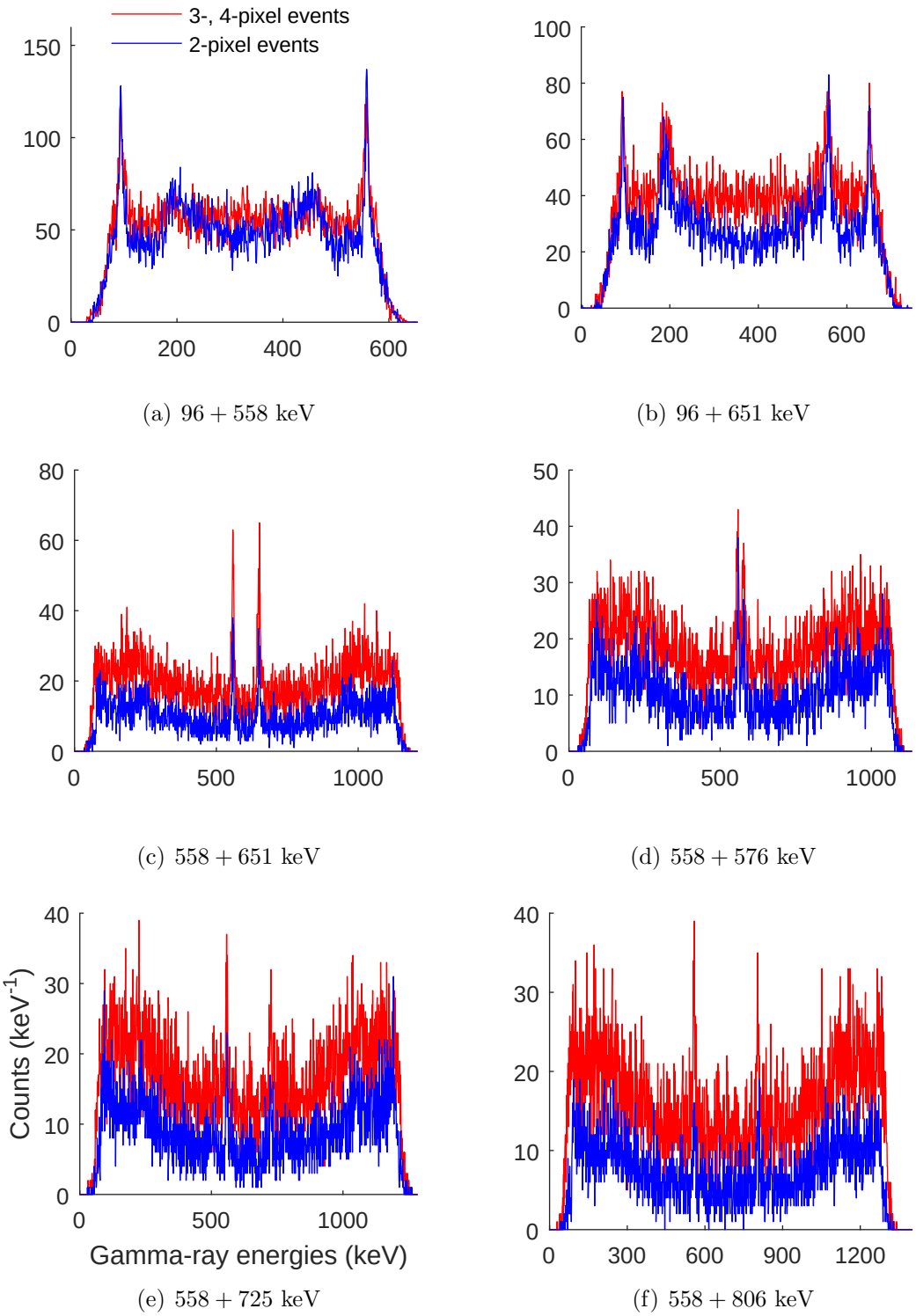

(a) $96 + 558$ keV

(b) $96 + 651$ keV

(c) $558 + 651$ keV

(d) $558 + 576$ keV

(e) $558 + 725$ keV

(f) $558 + 806$ keV

Figure 4.4: Coincidence energy spectra for events which fall within energy windows corresponding to the sum of two coincident cascade gamma rays from Cd capture. Measured using Polaris SP at the NARS laboratory.

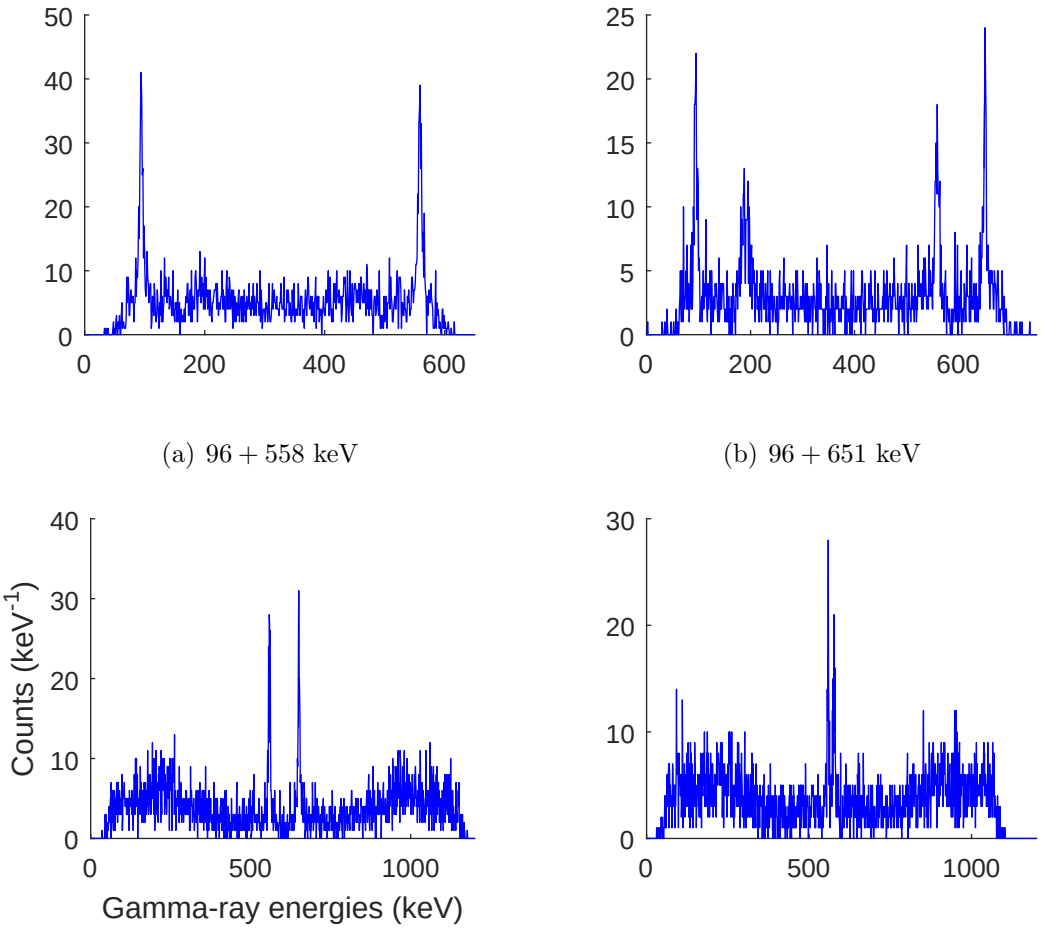

(a) $96 + 558$ keV

(b) $96 + 651$ keV

(c) $558 + 651$ keV

(d) $558 + 576$ keV

Figure 4.5: Selected coincidence spectra from Figure 4.4 with additional spatial filters as described in the text. Measured using Polaris SP at the NARS laboratory.

rays for 1-, 2,- and 3-pixel events during the measurement. Here, the spatial coordinates of interactions were used to construct *features* to classify cascade events. In machine learning, a feature is a measurable property that is used to describe some phenomenon to distinguish it from others. This analysis is meant to provide a few examples of quantities that could be used as features for more sophisticated algorithms such as statistical classification, a subject of future work as discussed further at the conclusion.

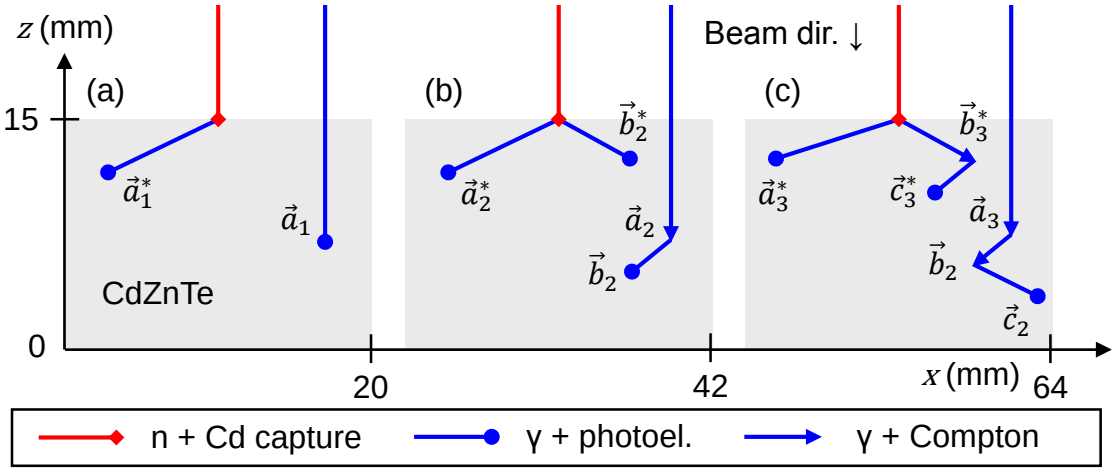

Figure 4.6: 2-D representation of Polaris SP detector array during cathode irradiation of a mixed thermal neutron and gamma ray beam at NARS. The beam is incident from the top of the page (-z direction) onto the cathodes, located at $z = 15$ mm (pixelated anodes at $z = 0$). (a) 1-pixel, (b) 2-pixel, and (c) 3-pixel interactions from both cascade and background gamma-ray events are illustrated along with vectors indicating their position coordinates, as described in the text.

1-Pixel Events

Since cascade gamma rays were emitted from the cathode side of the CdZnTe during the experiment, their interactions are expected to occur more frequently near the cathode surface. Their spatial distribution follows Equation 3.18, which falls off more rapidly from the cathode surface than exponential attenuation at the same energy. The difference is also illustrated in diagram (a) of Figure 4.6. Hence, a feature of 1-pixel cascade events might be interaction depth, i.e.,

$$f_d \equiv \vec{a}_1 \cdot \hat{z}. \tag{4.1}$$

Figure 4.7 shows depth-separated, 1-pixel spectra. Choosing 558 keV interactions nearer the cathode, for instance, increases the area of the photopeak relative to the continuum beneath it. Other cascade gamma rays exhibit similar behavior, including the 96, 651, and 576 keV lines. The 478-keV boron capture line does not exhibit such a large increase in area near the cathodes since it was not emitted very near the

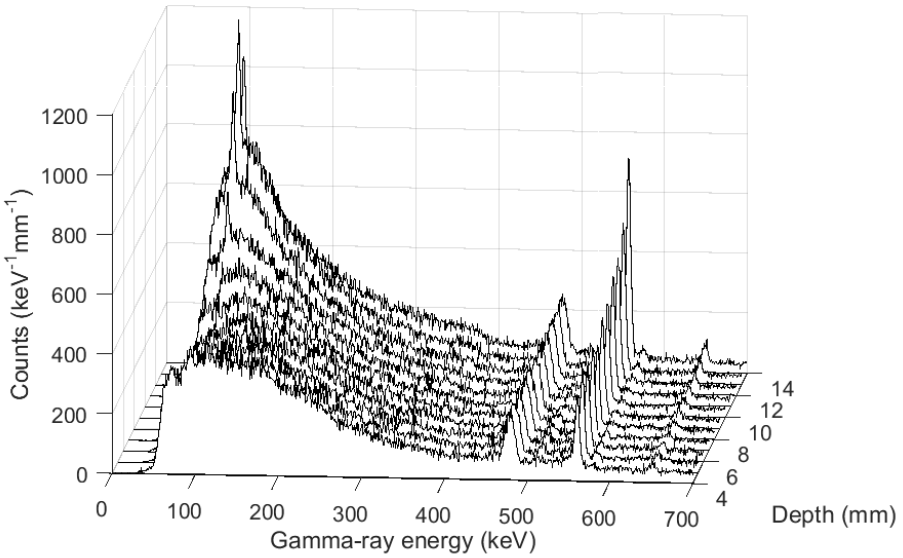

Figure 4.7: Depth-separated, gamma-ray energy spectra for all 1-pixel events measured by Polaris SP's plane B during thermal neutron irradiation of its cathodes. Depth, equivalent to f_d of Equation 4.1, is labeled as distance from anodes, i.e., the cathode's position was at 15 mm.

CdZnTe surface and therefore follows more normal exponential attenuation.

2-Pixel Events

2-pixel cascade events may also be selected based on their depth of interaction using feature f_d of Equation 4.1. Best performance is achieved when the depth of the first interaction is used, since a Compton-scattered gamma ray may deflect in any direction. Figure 4.8 shows the result when the event closest to the cathode is assumed to be first. Notice that the 558 keV line increases in area more rapidly than the 478 keV line near the cathodes using this simple logic. Better discrimination may be possible, for instance, when using Compton kinematics to sequence events as described in Section 2.2.1.

Cascade lines at 725 keV, 806 keV, and 1210 keV were also revealed, marked by arrows in Figure 4.8. The peak around 746 keV may be the result of coincident 96 keV and 651 keV cascade gamma rays combined with 558 keV and backscattered gamma

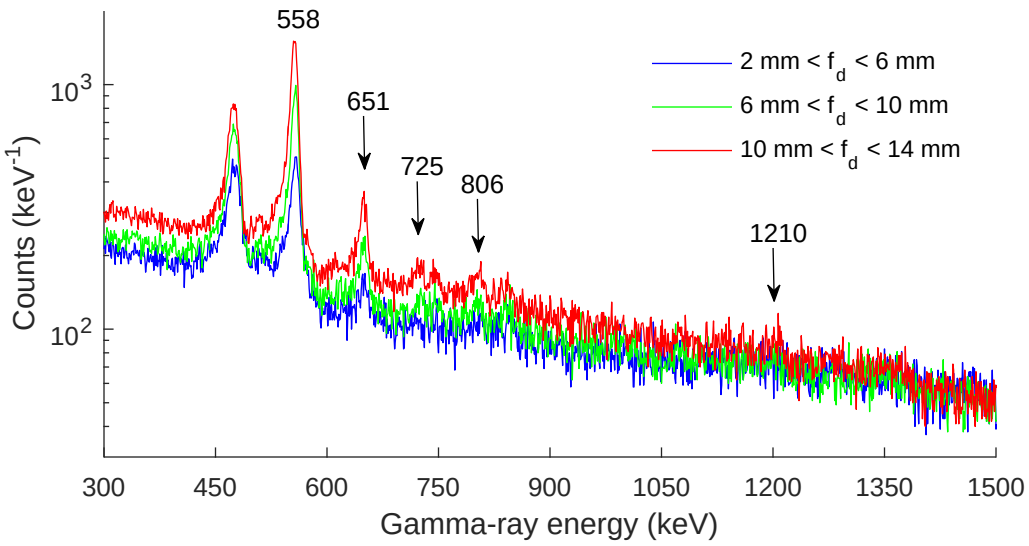

Figure 4.8: Depth-separated, gamma-ray energy spectra for all 2-pixel events measured by Polaris SP's plane B during thermal neutron irradiation of its cathodes. Cascade gamma ray lines are indicated by arrows.

rays, both of which were prominent in the coincidence spectra of Figures 4.4(b) and 4.5(b). Another peak around 844 keV may be the result of fast neutrons from the beam interacting in the aluminum housing of Polaris SP, which is pictured in 4.1(a). Activated ^{26}Al from the ^{27}Al(n,2n) reaction produces 843.8 keV gamma rays with 9.45 min half life [129].

During a cascade event, it is also possible that a gamma ray is photoelectrically absorbed while another interacts once at a different location. In principle, the distance between the two interaction locations should be larger on average for two cascade gamma rays than for a single, twice-interacting gamma ray. Hence, a simple feature of these cascade events is the spatial separation of interactions, or

$$f_s \equiv |\vec{a}_2 - \vec{b}_2|, \tag{4.2}$$

illustrated by the diagram (b) of Figure 4.6. Figure 4.9 shows distance-separated spectra for each individual gamma-ray interaction in the data set, as opposed to the

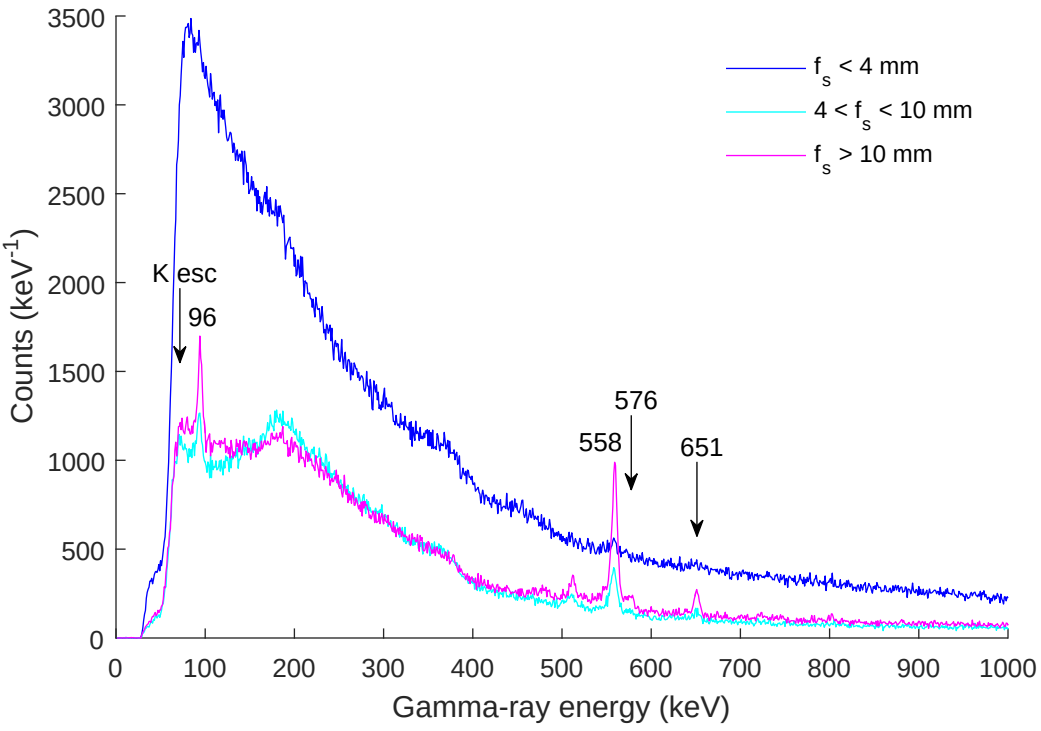

Figure 4.9: Individual gamma-ray energy spectra for all 2-pixel events measured by Polaris SP's plane B during thermal neutron irradiation of its cathodes. Here, events are classified by distance between interactions, or f_s of Equation 4.2.

typical sum energy for each event. The advantage for choosing events with separation $f_s > 10$ mm is clear since the cascade peaks are much more pronounced at these distances. The absence of a peak for interactions close together ($f_s < 4$ mm) demonstrates that this category of events is almost always from gamma ray background or charge-sharing events in neighboring pixels.

The weak 576 keV cascade line is highlighted more clearly in Figure 4.9. In addition, the combination of K x-ray escape lines from the 96 keV transition is discernable around 72 keV. These are likely from the combined effects of photoelectric absorption by Cd and Te as well as internal conversion by Cd directly following neutron capture very near the cathode surface.

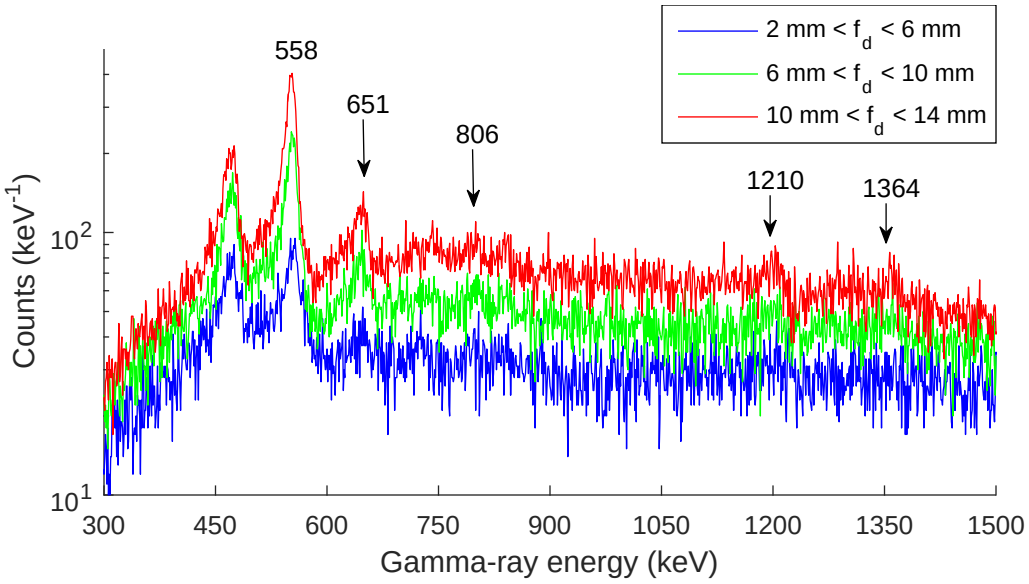

Figure 4.10: Depth-separated, gamma-ray energy spectra for all 3-pixel events measured by Polaris SP's plane B during thermal neutron irradiation of its cathodes.

3-Pixel Events

Discrimination of cascade events from background gamma rays is discussed here for three types of 3-pixel events. The first occurs when a single cascade gamma ray scatters twice before it is absorbed. As with 1- and 2-pixel events, the most straightforward way to discriminate cascade events with one interacting gamma ray from background gamma rays is to select based on depth of interaction, or feature f_d of Equation 4.1. Figure 4.10 shows depth-separated spectra, where the interaction closest to the cathode is used to categorize each event. Once again, a large increase in peak-to-background ratio is seen for cascade gamma ray peaks, and some of the higher energy cascade lines, namely 1210 keV and 1364 keV, are revealed.

A second type of 3-pixel event occurs when a cascade gamma ray is photoelectrically absorbed and the other two interactions were the result of one additional gamma ray. There are a number of ways one could discriminate these events from background. For example, one might recall that the distance between interactions from different gamma rays are large relative to those from a single gamma ray. The

mean distance between one interaction and the other two was the feature utilized in Figure 4.11, or

$$f_p \equiv \frac{|\vec{a}_3 - \vec{b}_3| + |\vec{a}_3 - \vec{c}_3|}{2}. \tag{4.3}$$

There are three combinations of interactions which yield different values of f_p. Here, the interaction $\vec{a}_3$ which yielded largest f_p was assumed to be the photoelectrically-absorbed cascade gamma ray. Figure 4.11 shows the distance-separated energy spectra for all 3-pixel events, binned by the energy of the photoelectric interaction. The cascade peaks again become prominent for larger interaction separations f_p.

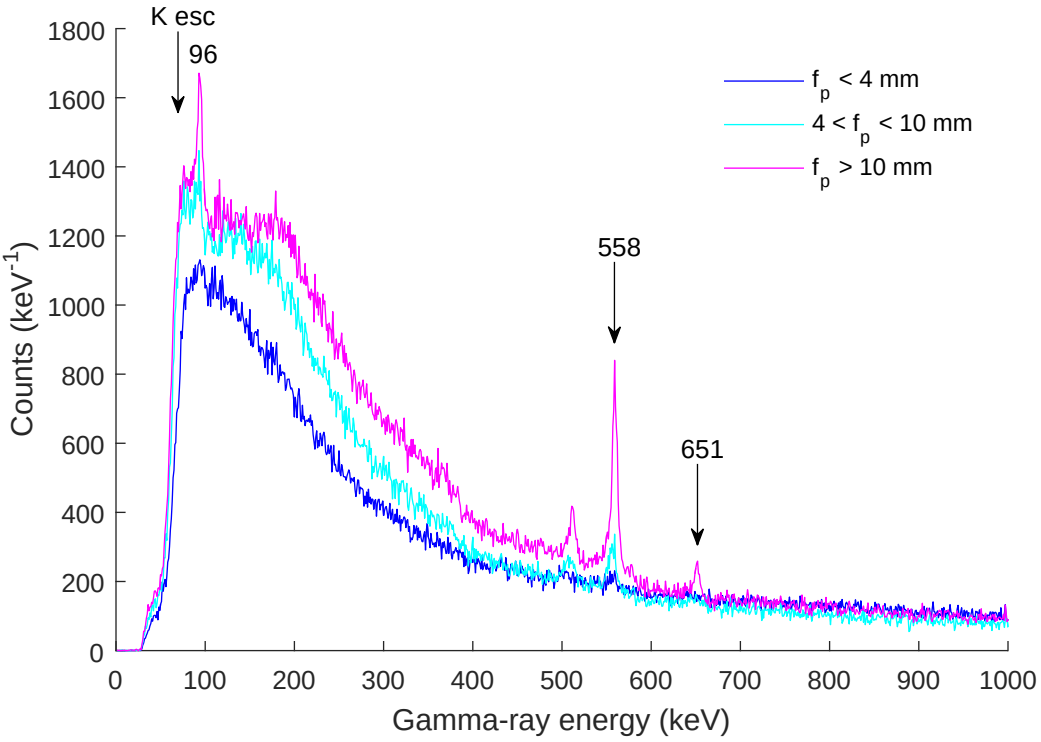

Figure 4.11: Gamma-ray energy spectra for all 3-pixel events measured by Polaris SP's plane B during thermal neutron irradiation of its cathodes. Here, cascade gamma rays that interact only once via photoelectric effect are classified by their separation distance from the other two interactions, i.e., f_p of Equation 4.3.

The final type of 3-pixel event discussed here is similar to the previous one, but

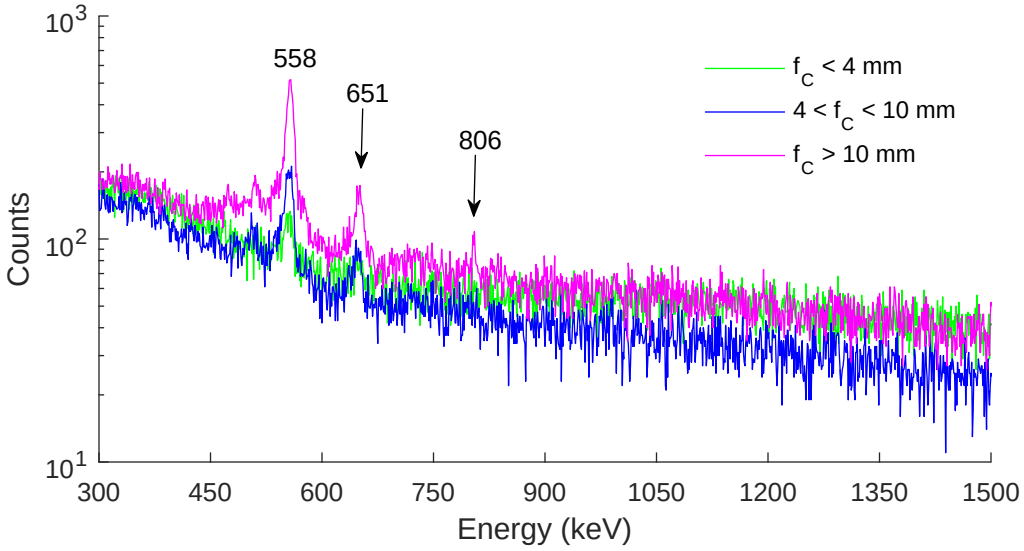

Figure 4.12: Gamma-ray energy spectra for all 3-pixel events measured by Polaris SP's plane B during thermal neutron irradiation of its cathodes. Here, cascade gamma rays that scatter once before absorption are classified by larger separation distance from a third interaction, described by feature f_C of Equation 4.4.

the focus is instead on the two interactions in close proximity. This occurs when a cascade gamma ray is scattered once then absorbed, while another gamma ray interacts elsewhere. The two interactions of the single gamma ray are most likely to occur in close proximity, while the second gamma ray's interaction occurs farther away. Hence, two out of three interactions sum to a cascade gamma ray energy. The feature used to select these events in Figure 4.12 is

$$f_C \equiv \ |\vec{a}_3 - \vec{b}_3| - |\vec{c}_3 - \vec{b}_3|, \tag{4.4}$$

or the difference in length between the farthest two and closest two interactions. The histogram shows the sum energy of the closest two interactions. Clearly, larger f_C provides better discrimination of cascade events.

Summary and Outlook

The 558 keV gamma ray is by far the most frequently emitted following neutron

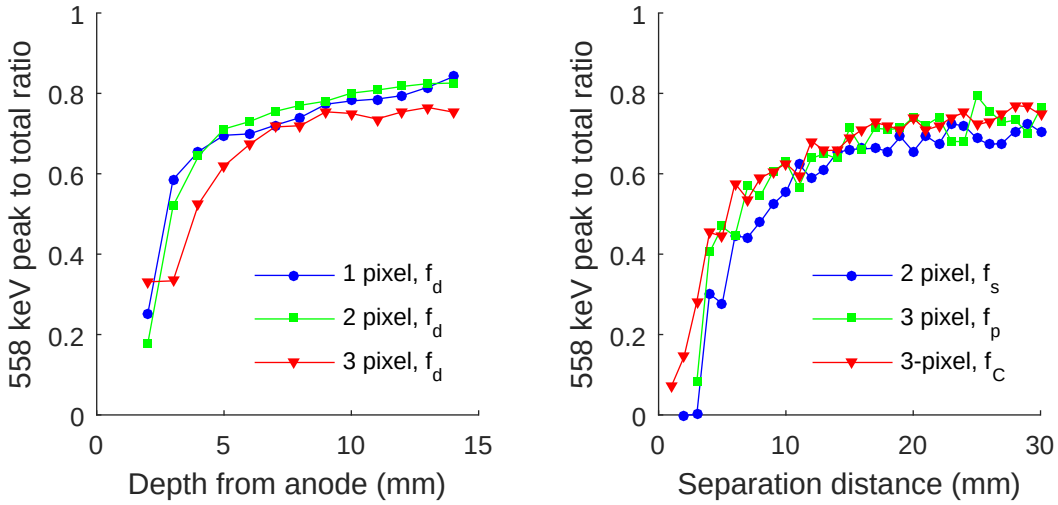

Figure 4.13: Ratio of background-subtracted 558-keV peak area to total area with background for (a) depth-separated and (b) distance-separated spectra.

capture on ^{113}Cd, and is of high enough energy so that it avoids the majority of gamma-ray background at low energies (< 300 keV). This makes the 558 keV photopeak signal a good candidate for thermal neutron imaging. The plots of Figure 4.13 show the ratio of peak counts to total counts within an energy window encompassing the 558 keV cascade gamma ray peak. Events nearer the cathode surface and/or separated by larger distance had higher ratio. The spatial features used for classification are based on physical characteristics of thermal neutron capture in CdZnTe: that thermal neutrons are captured near the crystal surface and that multiple gamma rays are emitted from the cascade, isotropically and in coincidence. They result in a signature for gamma rays in pixelated CdZnTe that allows for better separation from events from individual background gamma rays.

The methods employed in this section are not meant to provide the best-achievable classification of cascade events. Rather, simple features were used to demonstrate that there is indeed a measurable and significant difference between cascade and background gamma ray events of the same deposited energy in large volume pixelated

CdZnTe. More advanced techniques may be used to better optimize the fundamental tradeoff between bias and variance for event discrimination. Such methods include statistical classification, a subtopic of machine learning. For instance, the approach of support vector machines was successfully employed by Sanderson, Scott, Flaska, Polack, and Pozzi [130] for pulse shape discrimination of neutron and gamma ray events in organic scintillators. Hence, a feature-based classification scheme might benefit from the preceding analysis, utilizing the locations of interactions to construct features for discriminating thermal neutrons and gamma rays in pixelated CdZnTe.

4.2 Measured Detection Efficiency

Detection efficiencies reported for semiconductors using the Cd reaction are varied and do not necessarily agree [120]. To further complicate things, losses from gamma-ray multiplicity makes photopeak efficiencies difficult to calculate, especially considering that data on multiplicity distributions are relatively limited [48]. The approach here was instead to recover multiplicity losses experimentally and compare the result to calculations that excludes this effect. This technique was possible due to the CdZnTe's pixelated electrode configuration, described in Section 2.1.2, which can read out coincident interactions separately. Each coincident interaction can in principle be returned to its respective photopeak. Evidence of coincident photopeaks from Cd capture are provided in Section 4.1.2. Results indicate a good match between predicted and measured efficiencies, both about 10% at 558 keV for a 3×3 array of 2 cm $\times$ 2 cm $\times$ 1.5 cm CdZnTe.

Experimental Setup

Two thermal neutron detectors were used to verify the sensitivity of the Polaris II array to thermal neutrons using the 558 keV photopeak signal. Like Polaris SP, the Polaris II array also has two planes of 3×3 CdZnTe detectors. The first neutron

Table 4.1: List of parameters for both neutron detectors used in the experiment.

Detector	Diameter (in)	Active length (in)	Pressure (atm)	Bias (V)	Sensitivity (cps/nv)
BF_3	1.0	12.25	0.53	1300	6.4
^3He	1.0	5.9	4	1100	24

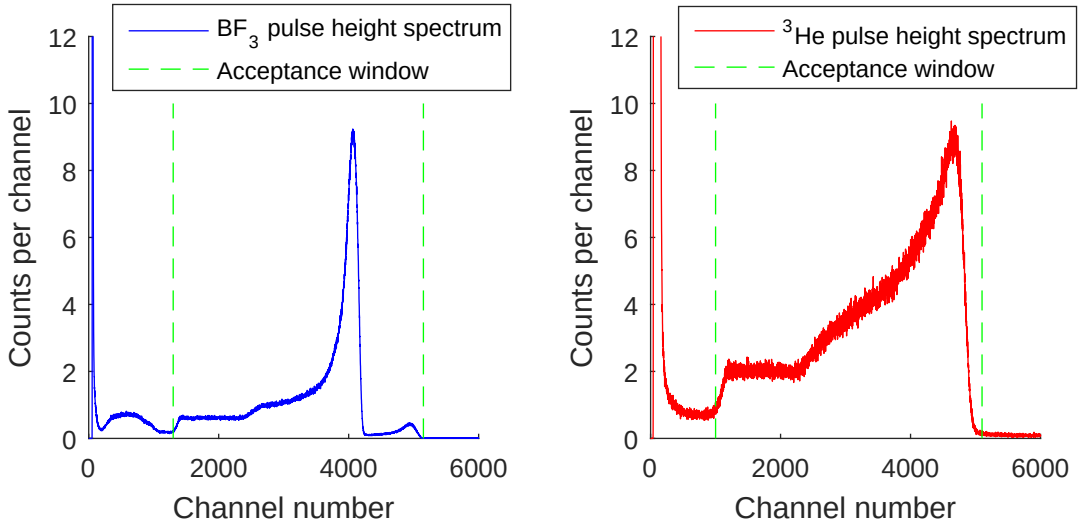

(a) (b)

Figure 4.14: (a) BF_3 and (b) ^3He (right) pulse height spectra. Vertical dashed lines indicate acceptance range for neutron-induced pulses during the experiment. The broad "bump" in counts between channels 100 and 1000 of the BF_3 spectrum is a known feature of this particular detector and is assumed to be noise.

detector used in this study was an LND, Inc. BF_3 tube model 2029 and the second was a ^3He tube manufactured by Harshaw Chemical Co. The neutron sensitivity of the BF_3 detector was given by its manufacturer, while the ^3He tube sensitivity was assumed to follow a nominal curve for 1 in ^3He given elsewhere [131]. The markings on the ^3He detector along with its operating voltage suggested that the gas pressure was 4 atm. The operating parameters of both detectors are summarized in Table 4.1, and their pulse height spectra given in Figure 4.14. The spectra were recorded inside a 42 cm $\times$ 42 cm $\times$ 42 cm paraffin block approximately 10 cm from a 1 Ci ^{239}PuBe neutron source, also inside the paraffin block. The setup was repeated for both detectors individually.

Figure 4.15 shows the experimental setup for verifying Polaris II's neutron sensi-

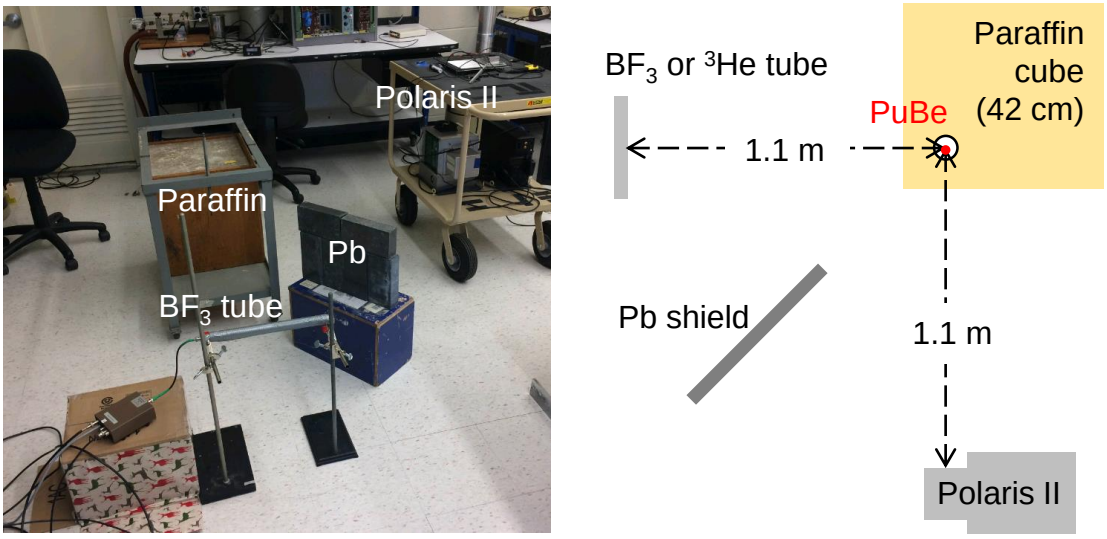

Figure 4.15: Experimental setup for efficiency measurement. (Left) Photograph. (Right) Diagram from top-down perspective.

Table 4.2: Experimental count rates from both neutron detectors and conversion to neutron flux.

Detector	Bare (cps)	Cd Covered (cps)	Difference (cps)	nv ($cm^{-2}s^{-1}$)
BF_3	19.69	0.69	19.00	2.97 ± 0.06
^3He	75.45	3.45	72.00	3.00 ± 0.05

tivity. The neutron detectors were placed one at a time in a position symmetric to Polaris II's, 1.1 m from the ^{239}PuBe source which was inside the paraffin block. The aim was to achieve identical neutron spectra and incident flux at the two positions to allow for comparison. There was about 10 cm of paraffin between the neutron source and the outer surface of the paraffin block, allowing for adequate moderation of the emitted fast neutron spectrum. The count rate at neutron energies below the Cd cutoff were measured using the Cd difference method with a Cd sleeve that fit snugly over the 1-in-diameter BF_3 and ^{3}He tubes. The results are presented in Table 4.2, with both detectors indicating a thermal neutron flux of about 3 $cm^{-2}s^{-1}$.

Predicted CdZnTe Count Rate

The cathode side of Polaris II's plane B, which faced the neutron source, has a total area of 36 cm^2 so according to the flux reported from Table 4.2, 108 ± 1.4 n/s were incident on the detector cathodes. However, the PCB used for high voltage distribution in front of the cathodes contained layers of woven E-Glass, which consist of 5-10% B_2O_3 [132]. Previous measurements of the PCB used for Polaris II showed that it attenuates $24 \pm 1.8\%$ of the incident thermal neutron flux from the moderated ^{239}PuBe source, reducing the neutron rate of neutrons incident on the CdZnTe in this experiment to 81 ± 6.1 n/s. The emission probability of 558 keV photons following absorption by ^{113}Cd is 0.744 gammas/neutron [10], so about 60 ± 4.5 γ/s were emitted from the cathode surface of the crystals. Geant4 simulations of 558 keV photons emitted near the cathode surface showed that 14.3% of these gamma rays then undergo photoelectric absorption in the CdZnTe crystals, resulting in 8.6 ± 6.5 predicted photoelectric events/s. Finally, system dead time is nominally 410 μs, so that the measured count rate of 925 cps induced 38% dead time, i.e., the predicted count rate of 558 keV photoelectric interactions was about 5.3 ± 0.4 cps.

Measured CdZnTe Count Rate

Figure 4.16 shows the measured gamma-ray energy spectrum from Polaris II between 300 and 700 keV. The blue spectrum is the combined 1-, 2-, 3-, and 4-interaction energy spectrum. As shown in Section 4.1.2, the gamma-ray cascade following Cd capture frequently results in simultaneous interactions of coincident gamma rays. The red spectrum includes all combinations of coincident 1-, 2-, 3-, and 4-pixel interactions in addition to those events shown in the blue spectrum. It is clear from Figure 4.16 that this approach causes an additional "chance coincidence" level for incorrect combinations of interactions, however correct combinations result in additional counts under the cascade photopeaks. Each sequence is attempted once, so

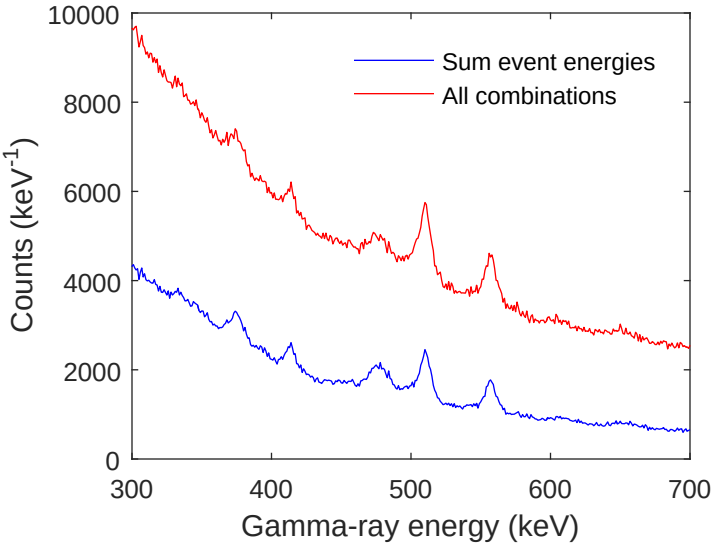

Figure 4.16: Gamma ray energy spectra using the sum-energy of each event and the energy of all combinations of interactions for each event.

each fully-absorbed, coincident gamma ray is counted only once. Including gamma-ray coincidence, the background-subtracted, 558-keV photopeak area was about 50% larger than its traditional sum-energy counterpart.

The gamma-ray background was then approximated as an exponential, fit from 624 keV to 642 keV and 670 keV to 750 keV and subtracted from the spectrum, shown in Figure 4.17(a). Polaris II's plane B response to 662 keV gamma-rays, measured in the lab following the experiment, was used to fit the 511 keV and 558 keV peaks. The fit function consisted of Gaussian and error functions for both low and high energy tails, accounting for the asymmetric shape of Polaris II's photopeak. A similar fit function including low energy tails is found in [133]. The fit to 511 keV and 558 keV photopeaks from the neutron measurement is shown in Figure 4.17(b). The area under the 558 keV curve above 400 keV is 5.1 cps. This range of energies included counts in the low-energy tail of the peak, but above the 558 keV Compton edge at 383 keV. Counts in this range are attributed to full-energy depositions from 558 keV gamma rays, however their energies were not completely reconstructed due

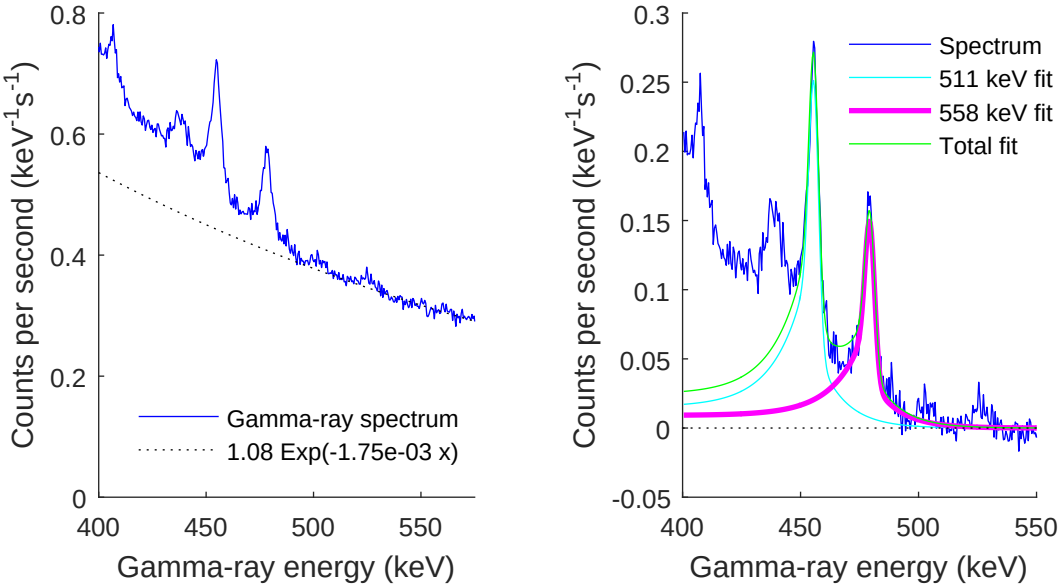

(a) (b)

Figure 4.17: (a) Exponential fit to gamma-ray continuum. (b) Background-subtracted spectrum with fits for 511 keV and 558 keV photopeaks.

to weighting potential losses or other charge-loss effects such as trapping or charge sharing between pixels.

Conclusion

The measured rate of photoelectric events (5.1 cps) in the experiment was reasonably close to its predicted value (5.3 ± 0.4 cps). Inaccuracies in the peak fitting procedure were considered by the author to be the main source of error in the measured rate. The same procedure achieved roughly 5% error for peak areas in spectra at lower energies (^{235}U gamma rays). Geant4 simulation of 558 keV interactions in CdZnTe did not include losses from weighting potential effects near the anode, which may have resulted in a small over prediction of the predicted count rate. However, the author believes that statistical uncertainty, mainly from the PCB attenuation measurement, was the primary source of error in the calculated rate.

Neglecting dead time and correcting for PCB attenuation, both measurement and

calculation roughly agree that the efficiency of the CdZnTe array at 558 keV was about 10 photopeak events per 100 incident thermal neutrons. The resulting sensitivity of Polaris II per unit area of CdZnTe facing the source, correcting for dead time, was 0.076 cps/nv/cm^2. The analogous per-area sensitivities for the 1-in-diameter ^{3}He and BF_3 tubes calculated from their nominal values were 0.63 cps/nv/cm^2 and 0.081 cps/nv/cm^2. When compared this way, which indicates detection efficiency in the far field, the Polaris instrument has similar efficiency to a 1-in-diameter BF_3 tube, per cross sectional area. However, since the 558 keV peak is typically found amongst considerable gamma-ray background, Polaris II will not be as effective as a BF_3 tube at detecting a thermal neutron source based on counting alone, even though it has similar sensitivity.

4.3 Directionality from Surface Illumination

There is inherently some directional information provided by Cd capture in large volume CdZnTe because thermal neutrons are captured near the crystal's surface. In the presence of a thermal neutron source, CdZnTe will detect cascade gamma rays emitted from the crystal surfaces that face the source. Hence, if cascade gamma rays are localized to their emission locations, the surfaces facing the source can be identified, and the direction to the neutron source can be estimated. The concept was first demonstrated using the GammaTracker system in 2008 by Seifert, Barnett, and Myjak [53] and later used with the Polaris II array to locate a thermal neutron source in 2013 by Brown, Boucher, Mann, Zhu, and He [127]. The array consists of eighteen 2 cm $\times$ 2 cm $\times$ 1.5 cm pixelated CdZnTe crystals arranged in two 3×3 arrays. The arrays are placed back-to-back separated by 4.4 cm, with cathodes facing out. The array is pictured in Figure 2.6(a). The following is adapted from the work presented in the author's aforementioned publication, to which the reader is referred for a more detailed description of the work.

Methods

In principle, intensity of neutron capture on each surface of the Polaris II array is proportional to the cosine of the angle between the surface normal vector and the vector pointing towards the source. The strongest detected signal from thermal neutron capture in CdZnTe is the 558 keV cascade gamma ray, whose primary mode of interaction in CdZnTe is Compton scatter. As discussed in Section 2.2.1, pixelated CdZnTe's 3-D position sensitivity allows for Compton imaging of gamma rays in this energy range. Hence, the emission distribution of 558 keV cascade gamma rays can be estimated to determine which surfaces of the CdZnTe array face a thermal neutron source.

Since Compton rings may overlap multiple detector surfaces, the imaging response to a thermal neutron source cannot be modeled accurately using geometry only. For this reason, the array's response to thermal neutrons from 4π directions was modeled using Monte Carlo simulation of both thermal neutrons and cascade gamma rays. The list-mode data from gamma-ray interactions generated by simulation was then reconstructed using Compton imaging and binned by incident neutron direction to construct a response matrix for the array. The least squared difference between simulated and measured response was taken as the best estimate of the neutron direction.

One challenge this method presents is the rejection of continuum counts beneath the 558 keV peak from both background and scattered gamma rays. The scattered component of the continuum comes from both inside and nearby the detector material. Although the methods described previously for identifying cascade gamma rays based on their spatial distribution in Section 4.1.3 does reduce this background, it does not remove it completely. To demonstrate the principle, a method that involves two separate measurements is presented. For the first measurement, a thermal neutron absorber was placed between the detector and neutron source. This effectively

reduces the thermal neutron component of the spectrum so that the reconstructed image consists mostly of background and scattered gamma rays. For the second measurement, the absorber is removed and the rest remains the same. Therefore, the difference between the image with and without the absorber leaves the image of neutron capture on the detector, effectively providing a background-subtracted signal.

The Polaris II array was positioned 1.1 m a 1 Ci ^{239}PuBe moderated by paraffin. The paraffin block was 42 cm $\times$ 42 cm $\times$ 42 cm, and the ^{239}PuBe source was located 10 cm within the front face of the block, centered vertically. The detector was positioned at eight different angular orientations relative to the source for each pair of measurements, where one was used for background subtraction.

To attenuate the thermal component of the neutron flux for background subtraction, a 1 in-thick, 5%-by-weight borated polyethylene slab was placed between the source and detector during one of the two measurements. This reduced the 558 keV photopeak count rate from 1.10 cps to 0.36 cps when the cathode side of the array faced the source. To verify that the change in photopeak count rate was due to a change in thermal neutron flux, measurements were also taken using an LND 2029 cylindrical BF_3 neutron detector. The detector was placed in the same location as the Polaris II array, and the Cd difference method was used to measure count rate below 0.5 eV. With the borated polyethylene sheet in place, the thermal neutron count rate was reduced by $69.1 \pm 0.4\%$, in agreement with the 67% experienced by Polaris II. The background-subtracted gamma-ray spectrum is shown in Figure 4.18, which shows an increase in low-energy counts with the borated-polyethylene present. This could be from additional gamma-ray scatter in the shield or from a reduction in the interaction rate of higher-energy cascade gamma rays that contribute to the continuum in that energy range.

The CdZnTe array's response to thermal neutrons was simulated using Geant4 release 4.9.4 [126]. In the simulation, neutrons of energy 25.3 meV were emitted

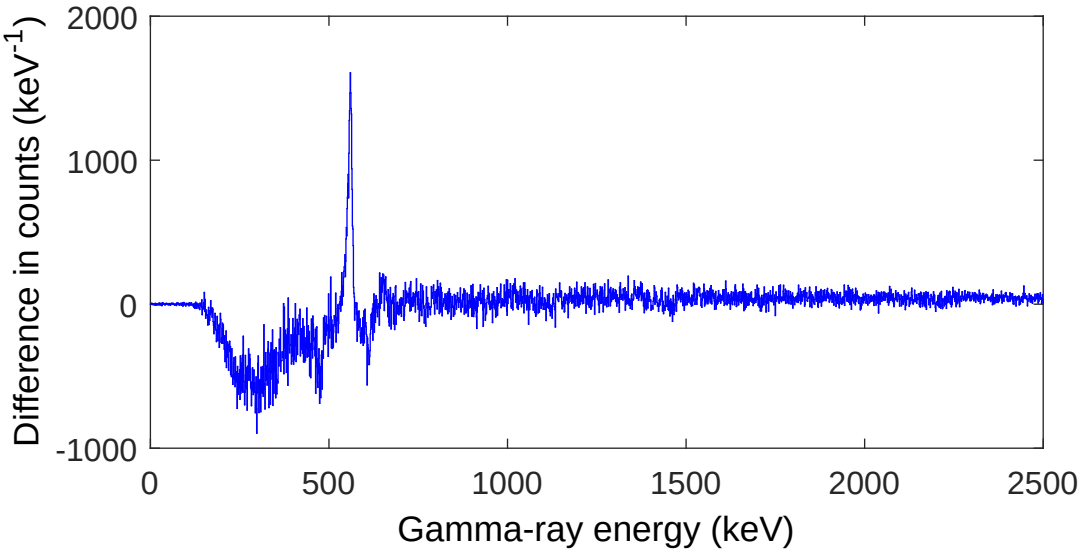

Figure 4.18: Background-subtracted CdZnTe gamma-ray spectra generated by thermal neutrons from 1 Ci PuBe in paraffin; measurement with 1 in borated polyethylene was subtracted from without.

isotropically from the surface of a 1.0 m radius sphere with the 3-D Polaris CdZnTe array at its center. In addition to the detectors, a 10.8 cm $\times$ 10.8 cm $\times$ 0.4 cm layer of ABS plastic used for structural support between the two 3 $\times$ 3 detector planes was also included in the geometry.

The G4NDL3.14 neutron cross section library was used as well as the Livermore library for photon transport. This model includes Doppler broadening for Compton scatter [134]. The 3-D position and energy of interactions were output in list mode along with their corresponding emission positions. These positions were recorded in order to bin the detector response by initial neutron direction. The emission positions were binned on a geodesic grid of size 162 so that each angular bin subtended approximately the same solid angle to balance simulation variance amongst bins. The angular distance between points on the grid was about 30°.

Gaussian energy broadening corresponding to 1% energy resolution was applied to the energy deposition events along with 0.5 mm Gaussian blur in the depth direction.

Depth corresponds to distance from interaction location to anode pixel surface, or z direction. A uniform electric field within the CdZnTe detectors was assumed so that x and y positions were stored as the anode pixel numbers under which the interaction occurred. It should be noted that multiple scatters under the same pixel were combined into a single recorded interaction since the analog ASIC used in the experiment cannot distinguish these events.

The reconstruction of the Compton-scattered gamma rays from both simulation and measurement was calculated using UM Imaging, a code developed at the University of Michigan [111]. The image space onto which cones were back projected was defined as the outward-facing surfaces of the CdZnTe array, binned by 1 mm $\times$ 1 mm image pixels. Compton cones were back projected onto the array surface for each scatter event, with multiple cones if the event had more than one possible interaction sequence, weighted by that sequence's probability.

Thus, the intensity contributed to each image pixel from a single Compton-scattered gamma ray was weighted by the probability the gamma ray originated from that pixel and then experienced its sequence of interactions. The width, or thickness, of each cone surface was scaled relative to the uncertainty in scatter angle contributed by position and energy uncertainty. Doppler broadening was not considered in the spread of the cones. The width of the ring created by the cone's intersection with the detector surface was then determined by this thickness. Finally, the weight of each pixel intersected by the ring was given by Equation 3.18. A lower limit on the ring width was set to two times the pixel diagonal length so that interactions close to the surface did not contribute all their weight to only one pixel, causes large variance in the result.

Images were reconstructed this way for both simulated and measured events. For the measurement data, difference between the images with and without the borated polyethylene sheet was taken, leaving the relative intensities of thermal neutron ab-

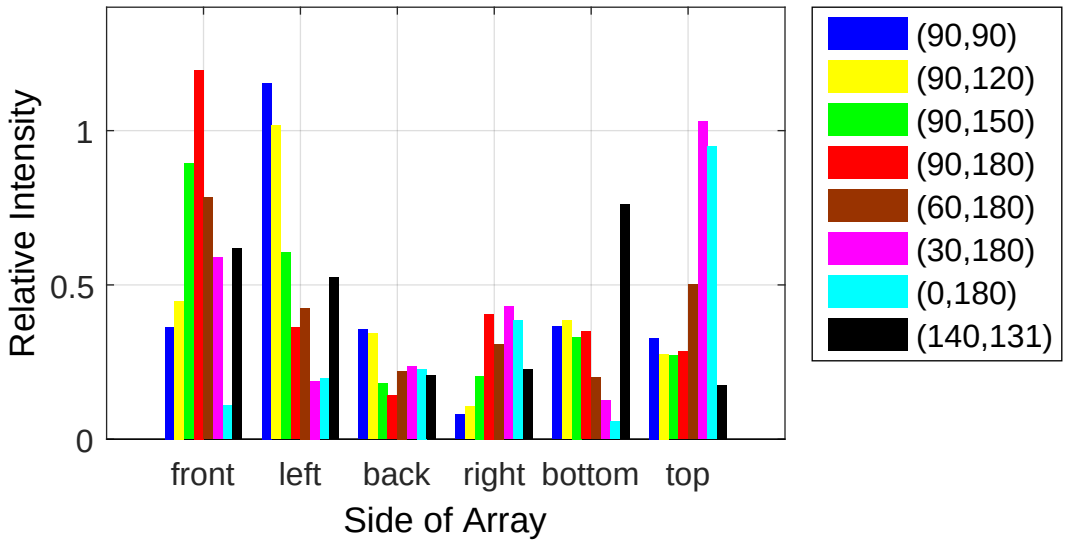

Figure 4.19: Intensity attributed to each side of the array via Compton imaging for each orientation. The legend provides the (polar,azimuthal) angle to the source in degrees.

sorption on the array sides. The total intensity for each of the six sides of the array was then calculated, and the results from both simulation and measurement compared.

Results

The background-subtracted, relative intensities of thermal neutron capture per unit surface area measured by the 3-D Polaris CdZnTe detector array are shown in the bar graph of Figure 4.19. Further details on the results background subtraction are provided in the original publication [127]. One can clearly see the change in intensity of capture on each surface as a function of neutron source direction. The coordinates of each face of the array is shown in Table 4.3. As expected, there is a higher intensity of neutron capture on a surface when it is more directly facing the source. Cones that overlap multiple surfaces and cones projected from an incorrect sequence of interactions will contribute some residual intensity on surfaces facing away from the source.

A representative comparison between simulation and measurement is given in

Table 4.3: Coordinate system assigned to the array, corresponding to Figures 4.19 and 4.21. Left and Right are outward-facing directions normal to the cathodes of each plane.

	Front	**Left**	**Back**	**Right**	**Bottom**	**Top**
Polar direction (degrees)	90	90	90	90	180	0
Azimuthal direction (degrees)	180	90	0	270	–	–

Figure 4.20. It shows the estimates of relative neutron capture rates via Compton imaging from simulation and measurement for the case of cathode irradiation of the Polaris II array. Clearly, there is a mismatch between the regular pattern produced by simulation, and the irregular one from measurement. Model mismatch can be attributed to a number of sources, including detector limitations discussed in Section 2.3 and the incomplete Geant4 model, which excluded things such as the thermal-neutron-absorbing PCB boards. Furthermore, the background subtraction method was not perfect, since the gamma-ray environment changed with the presence of the borated polyethylene shield and the background induced by higher-energy cascade gamma rays was reduced along with the thermal neutron flux.

Figure 4.21 shows a map of the squared error between simulated and measured response for each of the eight measurements in 4π angular space. The simulated response was calculated at each pixel center using linear interpolation within the triangular space between geodesic grid points. The + symbol shows the direction given by the maximum point of the Compton image of 2.2 MeV ^{1}H capture occurring within the polyethylene block. The *o* symbol shows the direction given by the minimum least squared error. Table 4.4 is a numerical summary of these results.

Conclusion

The mean difference between the true and estimated neutron directions was 11.4 degrees, with a standard deviation of 4.6 degrees. The response matrix was binned on a relatively coarse geodesic grid with 162 grid points, each separated by about

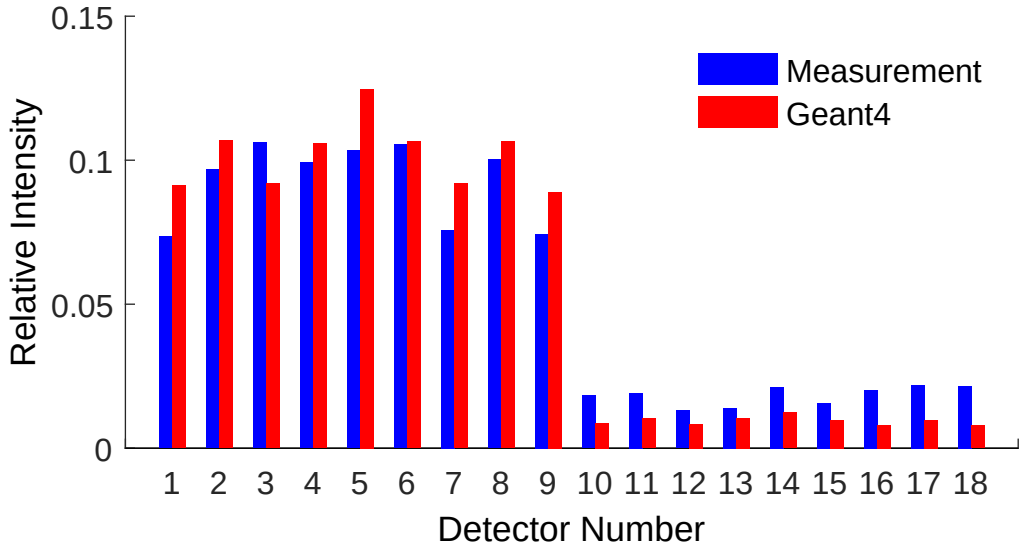

Figure 4.20: Representative comparison between simulation and measurement showing relative 558 keV counts amongst detectors. This plot is for the left-side-facing, or (90°,90°) orientation of the source relative to the detector array.

30 degrees. Accuracy of this method would be improved if a finer mesh was used, at the cost of statistical error. In addition, model mismatch between simulation and measurement caused a biased estimate of the capture rate on each detector surface, influencing the direction estimates. It should be noted that more advanced deconvolution of the Compton cones, such as an ML-based method, might avoid Monte Carlo simulation by reducing the problem to a geometric one. This could prevent the need for a simulated response. Overall, the work here demonstrates that the direction to a single, far-field thermal neutron source can be roughly estimated using a pixelated CdZnTe array.

4.4 Discussion and Conclusion

Taken as a whole, the experimental results from this section indicate pixelated CdZnTe's utility as a thermal neutron detector. Its ability to overcome multiplicity losses inherent to Cd-based detectors is key, and was shown to recover about a third

Table 4.4: Comparison of thermal neutron source directions estimated from the centroid of the 2.2 MeV H capture line and Cd capture. All values in degrees.

2.2 MeV γ	**Cd capture**	**Separation**
$(91, 90)$	$(92, 87)$	3
$(91, 122)$	$(100, 106)$	18
$(89, 151)$	$(100, 157)$	13
$(89, 180)$	$(100, 184)$	12
$(61, 184)$	$(60, 166)$	16
$(29, 181)$	$(25, 198)$	9
$(0, 181)$	$(9, 305)$	9
$(131, 140)$	$(137, 154)$	11

of all 558 keV photopeak events. The resulting efficiency for a 3×3 array of 2 cm $\times$ 2 cm $\times$ 1.5 cm CdZnTe at 558 keV was about 10%, confirming its calculated value. Per cross-sectional area, the array's efficiency was comparable to a 1-in-diameter BF_3 tube for neutrons below the Cd cutoff.

Furthermore, multiplicity of Cd capture events offers more than just a problem; based on their spatial interaction distribution, one can actually start to tease them apart from background gamma-rays. Section 4.1.2 offers a starting point for this effort, which demands more rigorous attention. The ability to discriminate thermal neutron capture events from gamma-ray background could drastically reduce counting times for both detection and imaging of thermal neutrons. The shape of the receiver-operating characteristic curve will tell more about any particular method's efficacy.

The work provided here on thermal neutron directionality could be improved. Better deconvolution of the Compton rings could remove the need for a simulated neutron response for the pointer, making the algorithm analytical rather than dependent on Monte Carlo transport. This technique could be used for CdZnTe arrays or individual crystals. It utilizes data that is naturally available from a pixelated CdZnTe detector in the presence of thermal neutrons, and so, it can be viewed as a software update to existing data processing code.

Initial measurements demonstrating the feasibility of thermal/epithermal neutron

spectroscopy were not shown here, however they are interesting to mention for future work. The PCBs near the CdZnTe crystals in the Polaris arrays have significant quantities of ^{10}B, hence the 478 keV peak in many spectra from this chapter. Its corresponding capture cross section follows the $1/v$ behavior, which is somewhat sensitive to the epithermal part of the neutron spectrum, below about 100 eV. This is in contrast to the ^{113}Cd cross section, which is relatively insensitive above 0.5 eV. Since the ratio of thermal- to epithermal-range neutrons changes as a function of moderator thickness, as seen in Figure 3.3, it is in principle possible to observe this difference by measuring the difference in peak areas of the 478 keV to 558 keV peaks in Polaris. The result may be able to measure information about a thermal neutron source, such as what type or how much moderator is around it, and is related to the commonly-used Cd ratio [135]. Initial measurements suggested this is true, however more convincing measurements should be taken to confirm this capability.

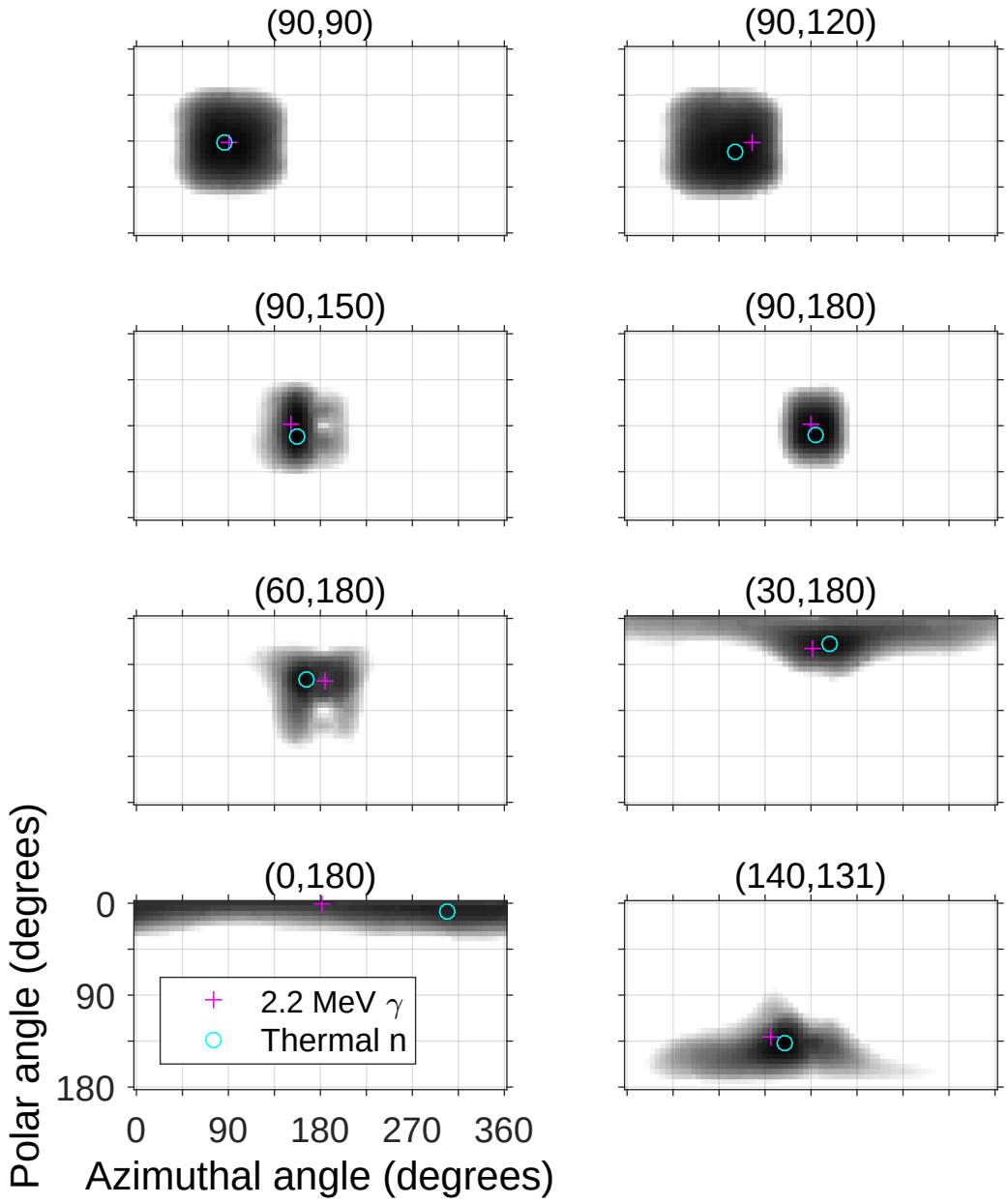

Figure 4.21: Maps of squared difference between simulation and measurement as a function of neutron emission direction from around the CdZnTe array for each measurement. Dark areas have lower squared difference, with a ceiling of 0.3 set to white to better compare each shape. The least squared difference for each measurement is indicated by the ∘ symbol. This is the estimated direction from thermal neutron capture. The + symbol indicates the direction estimated by the centroid of the Compton image of 2.2 MeV H capture in the paraffin.

CHAPTER V

Time-Encoded Imaging Theory

This chapter focuses on the basic principles of time-encoded imaging using a multi-element detector. It presents a general formulation for coded imaging to facilitate the comparison of time-encoded imaging to its spatial counterpart, coded aperture imaging. The differences between these closely-related techniques are mainly the result of systematic imperfections in the measured signal. Hence, this model includes fluctuations in the recorded signal that exist as a result of an imperfect detector, which excludes Poisson statistics. Rather than limit the discussion to patterns from cyclic difference sets, the encoding and decoding process was derived for any arbitrary piecewise-constant, binary pattern. Compared to more general patterns, these are often simpler to implement in practice and are known to provide optimal SNR [54]. An overview of patterns generated from cyclic difference sets was also given along with the resulting image SNR for (M)URA-based patterns.

5.1 Measurement Setup for Planar Coded Imaging

Figure 5.1 shows the time-encoding geometry for a planar mask and detector, similar to the coded aperture geometry found elsewhere [11]. A 2-D slice through an emitting object is described by the coordinates $\vec{r}_o = (x_o, y_o)$, positioned at a perpendicular distance, z, from the detector plane that has coordinates $\vec{r}_d = (x_d, y_d)$.

Spatial locations at the mask plane are given by $\vec{r}_m = (x_m, y_m)$, where there exists attenuating material with thickness ζ at $(\vec{r}_m, t) \in \mathbb{M}$, where $\mathbb{M}$ is the set of 3-D coordinates in space and time, t, where the attenuating material is present. In this general model, the object and detector coordinate systems are laterally offset (within their respective planes) by 2-D relative position as a function of time, $\vec{r}_\Delta(t)$. This vector may be used to incorporate the motion of an emitting object passing by in a vehicle, or a detector moving laterally to increase parallax during the measurement of a stationary near-field source.

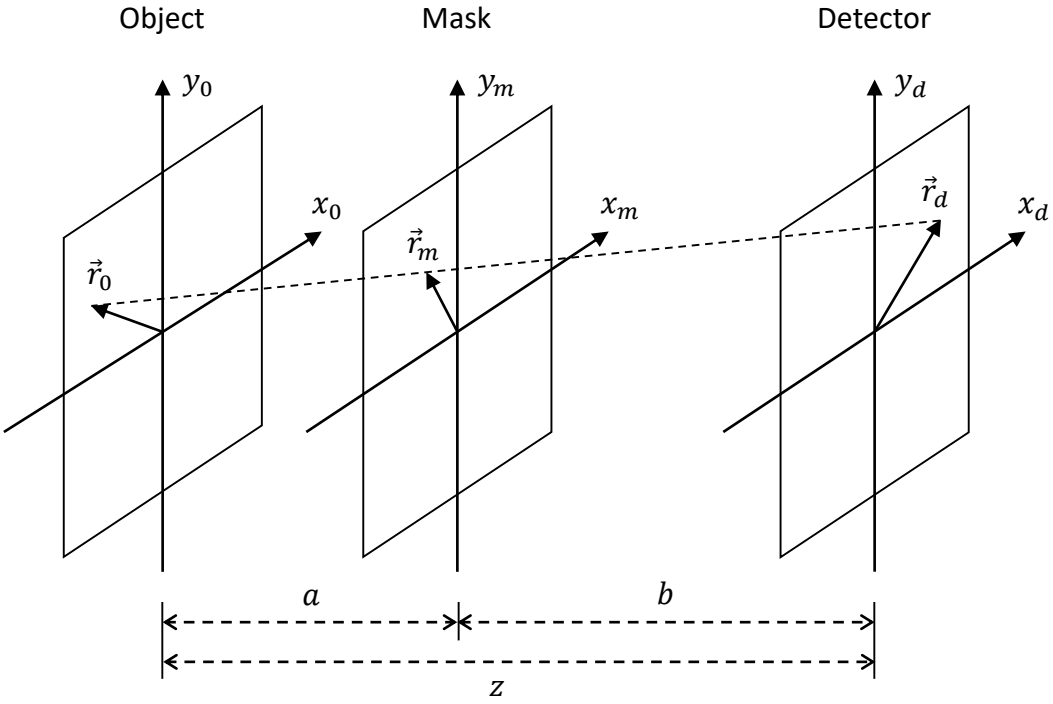

Figure 5.1: Planar coded imaging geometry, adapted from [11].

Neglecting air attenuation and self-attenuation of the source, the flux of particles at $\vec{r}_d$ and time t due to the isotropic emission of particles at the object plane is

$$\phi(\vec{r}_d, t) \equiv \iint_{\vec{r}_o} \frac{x(\vec{r}_o)}{4\pi z^2} \exp\left(-\frac{\mu\zeta}{\cos\theta}\,\chi_{\mathbb{M}}(\vec{r}_m, t)\right) \cos^3\theta \, d^2\vec{r}_o, \tag{5.1}$$

where $x(\vec{r}_o)$ is the 2-D emission rate distribution with units emissions per time, and

$\chi_{\mathbb{M}}(\vec{r}_m, t)$ is the indicator function that equals 1 if $(\vec{r}_m, t) \in \mathbb{M}$ and 0 otherwise. Theta is the incident angle of particles from $\vec{r}_o$ on $\vec{r}_d$ at t, found from geometry:

$$\theta(\vec{r}_d, \vec{r}_o, t) \;=\; \arctan\left(\frac{|\vec{r}_d - \vec{r}_o + \vec{r}_\Delta(t)|}{z}\right). \tag{5.2}$$

The $\cos^3\theta$ term of Equation 5.1 comes from both the inverse power law and the definition of flux through the detector's surface [11].

It's convenient to model the emitting object as a collection of J point-like sources, each with intensity

$$x_j \;\equiv\; \iint\limits_{\vec{r}_o} s(\vec{r}_o)\,\delta(\vec{r}_o - \vec{r}_j)\,d^2\vec{r}_o, \tag{5.3}$$

where $\vec{r}_j$ is the jth source location, $j \in \mathbb{J} \equiv \{1, \ldots, J\}$, and $\delta(\vec{r})$ is Dirac's impulse. Here it is also assumed that $\chi_{\mathbb{M}}(\vec{r}_m, t)$ is constant over time intervals of duration τ, and that the total measurement time consists of N such intervals. Time during the measurement can then be indexed by $n \in \mathbb{T} \equiv \{1, \ldots N\}$, where $t_n \in [(n-1)\tau, n\tau)$.

Particles during the n time interval from $\vec{r_j}$ incident on the detector at some position $\vec{r}_i$, belonging to a collection of I detector elements where $i \in \mathbb{I} \equiv \{1, \ldots, I\}$, are then modulated by the binary pattern element

$$\omega_{inj} \equiv 1 - \chi_{\mathbb{M}}\left(\frac{a}{z}\vec{r}_i + \frac{b}{z}\vec{r}_j, t_n\right) \in \{0, 1\}. \tag{5.4}$$

This model assumes that the particle's travel time from source to detector is negligibly short. The effect of the thermal neutron speed distribution is addressed in Section 6.3.2. The total flux incident from all point sources $j \in \mathbb{J}$ at location $\vec{r_i}$ on the detector plane during the nth time interval is then

$$\phi(\vec{r}_i, t_n) \;=\; \frac{1}{4\pi z^2}\sum_{j=1}^{J} x_j\,\exp\left(-\frac{\mu\zeta}{\cos\theta_{inj}}\,(1 - \omega_{inj})\right)\cos^3\theta_{inj}, \tag{5.5}$$

where $\theta_{inj} \equiv \theta(\vec{r}_i, \vec{r}_j, t_n)$.

To convert flux to expected counts, Equation 5.5 is multiplied by detector element area, α, measurement duration, τ, and detector efficiency. Including an additive background term, the expected number of counts measured by the ith detector element during the n time interval is

$$\mathrm{E}\left[y_{in}\right] = \frac{\alpha\tau}{4\pi z^2} \sum_{j=1}^{J} x_j \exp\left(-\frac{\mu\zeta}{\cos\theta_{inj}}\left(1-\omega_{inj}\right)\right) \cos^3\theta_{inj}\, \varepsilon_{inj} + \mathrm{E}\left[\beta_{in}\right], \tag{5.6}$$

where $\varepsilon_{inj} \in (0, 1]$ is the spatially- and time-varying detection efficiency averaged over the nth time interval for particles emitted from $\vec{r}_j$ and incident at the ith detector element. Here, we assume that the number of counts is Poisson distributed, i.e., $y_{in} \sim \mathrm{Poisson}(\bar{y}_{in})$ where $\bar{y}_{in} \equiv \mathrm{E}\left[y_{in}\right]$. Similarly, β_{in} is the number of counts during interval n due to spatially- and time-varying background at the ith element, also Poisson-distributed.

Note that this formulation assumes the particle flux is roughly constant over the extent of a detector element, which is valid, e.g., if the extent of the projected element at the detector plane is much larger than the mask pixel pitch, i.e., the magnification $m \equiv (1 + b/a) \gg p_d/p_m$. Lengths p_d and p_m are the detector and mask element pitches, respectively, for a system with elements of uniform size as seen in Figure 6.4.

The aforementioned assumption is for simplicity, to ensure that only one element of the pattern ω_{inj} is recorded by each detector element, during each time interval, and for each object direction. Detector elements which record multiple parts of the pattern when exposed to a point-like source at position $\vec{r}_j$ with intensity x_j, e.g., relatively large detector elements, can be modeled without much extra effort. A large element's signal is simply the linear sum of many smaller elements that meet the previous small-element criteria. When combined, the result is a signal identical to a small element witnessing multiple neighboring sources, with summed intensity equal

to x_j. Therefore, the result of applying the image reconstruction methods found here on large detector elements will be one with blurred point spread function (PSF).

If $\zeta / \cos\theta_{inj} \gg \mu^{-1}\ \forall (i,j) \in \mathbb{I} \times \mathbb{J}$, where $\times$ is the Cartesian product, then the mask is said to be perfectly attenuating. Furthermore, collimation effects from finite mask thickness can be neglected in some cases, for instance, if the mask element pitch $p_m \gg \zeta \tan\theta_{inj}\ \forall (i,j) \in \mathbb{I} \times \mathbb{J}$. Additionally ignoring nonlinear effects such as detector dead time, the expected number of counts at the ith detector element during the nth time interval is

$$\mathrm{E}\left[y_{in}\right] = \frac{\alpha\tau}{4\pi z^2} \sum_{j=1}^{J} x_j\, \omega_{inj} \cos^3\theta_{inj}\, \varepsilon_{inj} + \mathrm{E}\left[\beta_{in}\right]. \tag{5.7}$$

5.2 Encoding-Decoding Process Using Imperfect Detectors

Each measurement, y_{in}, is binned by spatial index, i, and time index, n. The collection of measurements can then be organized in a matrix $\boldsymbol{Y} = (y_{in}) \in (\mathbb{Z}^+)^{I \times N}$, where $\mathbb{Z}^+$ is the set of all positive integers. Given a multi-element detector with time-varying transmission pattern, the code used to distinguish particles from each object direction, indexed by j, can be measured in either the time domain, spatial domain, or both. All else equal, the choice of domain for encoding depends on which provides the best image quality upon reconstruction. Decoding via correlation is employed here for image reconstruction and presented as a matrix-vector product. This is a generalized version of the traditional periodic correlation used for image decoding. Hence, any arbitrary code may be used rather than only those based on cyclic difference sets, which are described in Section 5.3.

The collection of pattern elements, each defined by Equation 5.4, can be arranged in a 3-D binary array $\boldsymbol{\Omega} = (\omega_{inj}) \in \{0,1\}^{I \times N \times J}$, referred to here as the encoding array. In practice, detector nonuniformities prevent the code from being recorded perfectly. This was modeled using varying detector efficiencies, ε_{inj}, and particle

incidence angles, θ_{inj}. The resulting imperfect measured pattern is referred to as the recorded encoding array, defined as $\tilde{\boldsymbol{\Omega}} = (\omega_{inj}\varepsilon_{inj}\cos^3\theta_{inj}) \in \mathbb{R}^{I\times N\times J}$. The recorded encoding array can then be used to rewrite Equation 5.7 to more easily demonstrate the encoding-decoding process. Whether this process occurs in the time, spatial, or combined domains has important implications for the final image that depend on the nature of the aforementioned uniformities. The encoding-decoding process was described separately for each domain for comparison.

5.2.1 Time Domain (Time-Encoded Imaging)

The encoding-decoding process for time-encoded imaging occurs in the time domain only. When using a multi-element detector system, this means that a complete code is recorded separately by each detector element during the measurement. The encoding step may be achieved, for instance, via motion of the coded mask, object, or detector during the measurement. Each detector element's time-varying signal is then decoded separately and then combined to form a composite image from all detector elements. In effect, this renders time-encoded images immune to nonuniformities amongst detector elements, as long as those uniformities are consistent throughout the duration of the measurement.

Let $\boldsymbol{Y}_{i*} \equiv \mathrm{col}_i \boldsymbol{Y}^T \in (\mathbb{Z}^+)^{N\times 1}$ be the ith detector element's time varying signal. In the time domain, it is most convenient to define a 2-D slice of the 3-D encoding array at the ith index, described by matrix $\boldsymbol{T}_i \equiv \boldsymbol{\Omega}_{i**}$, and likewise, $\tilde{\boldsymbol{T}}_i \equiv \tilde{\boldsymbol{\Omega}}_{i**}$. These are referred to here as the 2-D time encoding and recorded time encoding matrices for the ith detector element, respectively. The relative expected number of counts derived from Equation 5.7 can then be written:

$$\mathrm{E}\left[\boldsymbol{Y}_{i*}\right] \propto \sum_{i=1}^{I} \tilde{\boldsymbol{T}}_i \vec{x} + \mathrm{E}\left[\boldsymbol{B}_{i*}\right], \tag{5.8}$$

where $\boldsymbol{B} = (\beta_{in}) \in (\mathbb{Z}^+)^{I\times N}$ is the matrix of measured background counts.

If $\boldsymbol{T}_i$ is left invertible, there exists a decoding matrix $\boldsymbol{T}_i^{-L} \equiv (\boldsymbol{T}_i^T \boldsymbol{T}_i)^{-1} \boldsymbol{T}_i^T$ that is its left inverse, i.e., $\boldsymbol{T}_i^{-L} \boldsymbol{T}_i = \boldsymbol{I}_J$ where $\boldsymbol{I}_J$ is the $J \times J$ identity matrix. An estimator for the relative intensity can then be formulated using the decoding matrix, $\hat{\vec{x}}_{time} \equiv \sum_i \boldsymbol{T}_i^{-L} \boldsymbol{Y}_{i*}$, which has expected value

$$\mathrm{E}\left[\hat{\vec{x}}_{time}\right] \propto \sum_{i=1}^{I} \boldsymbol{T}_i^{-L} \tilde{\boldsymbol{T}}_i \vec{x} + \boldsymbol{T}_i^{-L} \mathrm{E}\left[\boldsymbol{B}_{i*}\right]. \tag{5.9}$$

Note that each time encoding matrix should be chosen carefully such that multiplication of its left inverse with the Poisson-distributed data vector does not greatly amplify measurement noise. In other words, it is best to choose a set of encoding patterns such that $\boldsymbol{T}_i$ is well conditioned. Patterns based on cyclic difference sets fit this criterion and are described further in Section 5.3.

The estimator of Equation 5.9 does not always preserve the relative intensities of the true object, $\vec{x}$. There are, however, certain measurement conditions where indeed $\mathrm{E}\left[\hat{\vec{x}}_{time}\right] \propto \vec{x}$, and others where simple adjustments to the estimator can also achieve proportionality. For strict proportionality with no corrections, there must be negligible background as well as $\tilde{\boldsymbol{T}}_i \propto \boldsymbol{T}_i$. Incidence angle, θ_{inj}, and detector efficiency, ε_{inj}, must then be functions of detector element index, i, only so that $\tilde{\omega}_{inj} = \cos^3 \theta_i \, \varepsilon_i \omega_{inj}$. This means that only nonuniformities in the spatial domain are tolerated. Despite these somewhat restrictive requirements, there are some other common scenarios that cause the estimate to be nearly proportional to the true intensity distribution, or proportional except for some easily-removable bias.

For instance, during some measurements it is reasonable to assume that the background rate is constant in time. It is also common that the sum of each row of $\boldsymbol{T}_i$ is the same, i.e., the ith detector element is exposed to the same mask open fraction during each time interval. Under these conditions, nonzero background contributes only a flat DC term to the object estimate, i.e., $\boldsymbol{T}_i^{-L} \mathrm{E}\left[\boldsymbol{B}_{i*}\right] \propto \vec{1}$, where $\vec{1}$ is the

all-ones vector. This DC term can easily be subtracted from the final image.

It is also common for particle incidence angle, and sometimes detector efficiency, to change significantly as a function of object direction but remain constant in time. For instance, this occurs for an extended object in the near field using an array of thick detectors. In this case, $\tilde{\boldsymbol{T}}_i = \boldsymbol{T}_i \operatorname{diag}(\vec{s}_i)$ where $\vec{s}_i \equiv (\varepsilon_{i1} \cos^3 \theta_{i1}, ..., \varepsilon_{iJ} \cos^3 \theta_{iJ})$ is the detector element-wise sensitivity vector, such that the encoding and decoding matrices of Equation 5.9 cancel as intended, leaving only the diagonal matrix, $\operatorname{diag}(\vec{s}_i)$. If the detector sensitivity is known, and the background rate is negligible, then this is easily corrected via multiplication of each summand by $\operatorname{diag}^{-1}(\vec{s}_i)$. This procedure amounts to a sensitivity correction, which is commonly used in imaging.

Even if these ideal criteria are not met, the summation over all detector elements in Equation 5.9 effectively averages the bias from each element with the others. If the resulting average bias is nearly constant for each object direction, then it becomes a removable DC term. This is most helpful for detectors with many elements since the imaging response is averaged over a large number of detector elements.

5.2.2 Spatial Domain (Coded Aperture Imaging)

In conventional coded aperture, the measurement can be modeled by setting the number of time bins N to unity since the system is stationary throughout the measurement. However, it is possible to have a purely spatially-encoded measurement with some motion, e.g., tracking an object in a moving vehicle such that its position within the imaging FOV does not change. The composite image is then a summation of N snapshots of the object. To keep this example general, the n index for time interval will not be dropped. Notably, for spatial coding, time-varying fluctuations do not affect the reconstructed image as long as they are consistent across all detector pixels.

Here, the vector $\boldsymbol{Y}_{*n} \equiv \operatorname{col}_n \boldsymbol{Y} \in (\mathbb{Z}^+)^{I \times 1}$ is the number of counts indexed by

detector element at the nth time interval. Analogous to the time-encoding case of the previous section, it is then convenient to define a 2-D slice of the 3-D encoding array at the nth index, defined here as the spatial encoding matrix $\boldsymbol{S}_n \equiv \boldsymbol{\Omega}_{*n*}$ and recorded spatial encoding matrix $\tilde{\boldsymbol{S}}_n \equiv \tilde{\boldsymbol{\Omega}}_{*n*}$. The relative expected number of counts for each detector element during the nth time interval can then be written as

$$\mathrm{E}\left[\boldsymbol{Y}_{*n}\right] \propto \sum_{n=1}^{N} \tilde{\boldsymbol{S}}_n \vec{x} + \mathrm{E}\left[\boldsymbol{B}_{*n}\right]. \tag{5.10}$$

Like the time encoding case, if $\boldsymbol{S}_n$ is left invertible, then the following decoding matrix exists: $\boldsymbol{S}_n^{-L} \equiv (\boldsymbol{S}_n^T \boldsymbol{S}_n)^{-1} \boldsymbol{S}_n^T$. The analogous estimator $\hat{\vec{x}}_{space} \equiv \sum_n \boldsymbol{S}_n^{-L} \boldsymbol{Y}_{*n}$ can then be formulated, which has expected value

$$\mathrm{E}\left[\hat{\vec{x}}_{space}\right] \propto \sum_{n=1}^{N} \boldsymbol{S}_n^{-L} \tilde{\boldsymbol{S}}_n \vec{x} + \boldsymbol{S}_n^{-L} \mathrm{E}\left[\boldsymbol{B}_{n*}\right]. \tag{5.11}$$

Again, only under certain measurement conditions does $\mathrm{E}\left[\hat{\vec{x}}_{space}\right] \propto \vec{x}$. Much like the time encoding case, there must be negligible background as well as $\tilde{\boldsymbol{S}}_n \propto \boldsymbol{S}_n$. Incidence angle, θ_{inj}, and detector efficiency, ε_{inj}, must then be functions of time index, n, only so that $\tilde{\omega}_{inj} = \cos^3 \theta_n \, \varepsilon_n \omega_{inj}$. This means that only nonuniformities in the time domain are tolerated without introducing image artifacts.

Of course, there are more flexible conditions for which proportionality can be achieved using a simple adjustment to the estimator. These echo the analogous conditions for time-encoded imaging. If the background rate is flat over all detector elements and the sum of each row of $\boldsymbol{S}_n$ is the same, i.e., each detector element is exposed to the same mask open fraction during the nth time interval, then nonzero background contributes only a flat DC term to the object estimate. Under these conditions, the bias from background can easily be subtracted from the final image.

The tracked moving source example described at the start of this section is one scenario where particle incidence angle, and sometimes detector efficiency, can change

significantly as a function of object direction but remain constant over all detector elements. For example, this happens for extended objects moving in the far field with respect to a thick detector array. In this case, $\tilde{\boldsymbol{S}}_n = \boldsymbol{S}_n \operatorname{diag}(\vec{s}_n)$ where the time-varying sensitivity vector is $\vec{s}_n \equiv (\varepsilon_{n1} \cos^3 \theta_{n1}, ..., \varepsilon_{nJ} \cos^3 \theta_{nJ})$. Again, the encoding and decoding matrices of Equation 5.11 cancel, leaving only the diagonal matrix, $\operatorname{diag}(\vec{s}_n)$. If the detector sensitivity is known, and the background rate is negligible, then this is easily corrected via multiplication of each summand by $\operatorname{diag}^{-1}(\vec{s}_n)$. Regardless of these ideal conditions, the summation over time in Equation 5.9 effectively averages the bias from each time interval with the others. If the average bias is nearly constant for all object directions, then it becomes a removable DC term.

5.2.3 Combined Time and Spatial Domains

Coded imaging is not restricted to either the time or spatial domains; the encoding-decoding process may occur in both domains together. For example, a position-sensitive detector might be used to record regions or patches of the shadow from an over-sized coded aperture mask pattern, moving the detector or mask between successive measurements to record the entire pattern. The result is that the full code exists in neither time nor spatial domains exclusively. This approach does not benefit from complete immunity to nonuniformities in the time or spatial domains, as does spatial- or time-encoded imaging, however it has other advantages. Mainly, fewer measurements are needed to record a code of a given length as compared to purely time or spatial coding. Furthermore, the fraction of the code measured in time versus spatial domains could be optimized in principle, e.g., by using more time steps to better average out detector nonuniformities.

Although the combined encoding-decoding process follows almost trivially from the process in either domain described previously, it is outlined here for completeness. A new measurement vector, $\vec{y} \in (\mathbb{Z}^+)^{IN \times 1}$, is defined here which contains the number

of counts from all detector elements during all measurement intervals. This vector can be arbitrarily arranged from the elements of the previously-defined measurement matrix, $\boldsymbol{Y}$. In this example, the measurement vector is defined as the concatenated columns of $\boldsymbol{Y}$ ordered by time index: $\vec{y} \equiv [\boldsymbol{Y}_{*1}^T, ..., \boldsymbol{Y}_{*N}^T]^T$. The 3-D encoding array is similarly rearranged into a 2-D encoding matrix, i.e., $\boldsymbol{O} \equiv [\boldsymbol{\Omega}_{*1*}^T, ..., \boldsymbol{\Omega}_{*N*}^T]^T = [\boldsymbol{S}_1^T, .., \boldsymbol{S}_N^T]^T \in \{0,1\}^{IN \times J}$ which is just the spatial encoding matrices stacked vertically in order of time index. Likewise, the associated recorded encoding matrix $\tilde{\boldsymbol{O}} \in \mathbb{R}^{IN \times J}$ is arranged in the same manner.

The expected value of the relative measured counts is then

$$\vec{y} \propto \tilde{\boldsymbol{O}}\vec{x} + \vec{\beta}, \tag{5.12}$$

where the background vector is defined as $\vec{\beta} \equiv [\boldsymbol{B}_{*1}^T, ..., \boldsymbol{B}_{*N}^T]^T$. Given that $\boldsymbol{O}$ is left invertible, the corresponding decoding matrix $\boldsymbol{O}_n^{-L} \equiv (\boldsymbol{O}^T\boldsymbol{O})^{-1}\boldsymbol{O}^T$ can be used to provide an object estimate $\hat{\vec{x}}_{combo} \equiv \boldsymbol{O}^{-L}\vec{y}$ that has expected value

$$\mathrm{E}\left[\hat{\vec{x}}_{combo}\right] \propto \boldsymbol{O}^{-L}\tilde{\boldsymbol{O}}\vec{x} + \boldsymbol{O}^{-L}\mathrm{E}\left[\vec{\beta}\right]. \tag{5.13}$$

For $\mathrm{E}\left[\hat{\vec{x}}_{combo}\right] \propto \vec{x}$, there must be negligible background and $\tilde{\boldsymbol{O}} \propto \boldsymbol{O}$, i.e., $\tilde{\omega}_{inj} = \varepsilon \cos\theta \omega_{inj}$. This means that the estimate is sensitive to nonuniformities in both the time and spatial domains.

However, if background is flat over all time bins and detector elements and the rows of $\boldsymbol{O}$ have equal sums, i.e., each detector element at each time interval is exposed to the same open fraction, then nonzero background produces an easily-removable DC term in the final image. Of course, a sensitivity correction is possible when background is small, under the additional condition that $\tilde{\boldsymbol{O}} = \boldsymbol{O}\mathrm{diag}(\vec{s})$, where $\vec{s} \equiv (\varepsilon_1 \cos\theta_1, ...\varepsilon_J \cos\theta_J)$. A simple sensitivity correction following reconstruction, i.e., multiplication by $\mathrm{diag}^{-1}(\vec{s})$, will then result in an unbiased estimate.

Using the same total number of measurements, IN, longer codes may be recorded using both domains rather than either time or spatial domains only. Given the same number of object elements, J, longer codes are in general more tolerant of measurement error since the encoding matrix $\boldsymbol{O}$ effectively becomes better conditioned. So, a long code measured in both domains may achieve higher image quality than a short code measured exclusively in one domain, especially one where nonuniformities exist. Alternatively, the longer code may be used to reconstruct an image with more elements, since left invertibility of $\boldsymbol{O}$ requires $J \leq IN$. This is in contrast to $J \leq N$ for $\boldsymbol{T}_i$ and $J \leq I$ for $\boldsymbol{S}_n$. Hence, better spatial resolution and larger FOV size is achievable using both the time and spatial domains for encoding.

5.3 Coded Imaging Using Cyclic Difference Sets

Although some coded apertures are based on random or non-redundant arrays [11, 35], cyclic difference sets are particularly useful for generating coding patterns because of their near-ideal imaging properties using a finite number of elements. A cyclic difference set is a collection of nonnegative integers $\{d_1, ..., d_k\}$, where $d_i \in \{0, ..., N-1\}$, such that all possible differences between them modulo N, i.e., $(d_i - d_j) \bmod N \ \forall i \neq j$, occur a constant number of times, λ [67]. "Modulo N" simply means that if $(d_i - d_j) < 0$, then the difference becomes $(d_i - d_j + N)$. The essential property of a (N, k, λ)-cyclic-difference set can also be illustrated using a difference table [136], shown for example in Table 5.1.

5.3.1 One-Dimensional Codes

1-D sequences based on cyclic difference sets are binary and consist of elements $a_n \in \{0, 1\}$, where $a_n = 1$ if the number n belongs to the cyclic difference set, and $a_n = 0$ if not. The vector containing these sequence elements $\vec{a}$ then has the property

Table 5.1: Difference table for the $(11, 5, 2)$-cyclic-difference set $\{1, 3, 4, 5, 9\}$. Due to the special properties of the cyclic difference set, each difference between the 5 numbers in the top row and left column modulo 11 appears precisely 2 times.

	1	**3**	**4**	**5**	**9**
1	0	2	3	4	8
3	9	0	1	2	6
4	8	10	0	1	5
5	7	9	10	0	4
9	3	5	6	7	0

that its periodic autocorrelation is two-valued. That is,

$$(\vec{a} \otimes \vec{a})_q \equiv \sum_{n=0}^{N-1} a_n \, a_{(n+q) \bmod N} = \begin{cases} k & \text{if } q \bmod N = 0 \\ \lambda & \text{otherwise,} \end{cases} \tag{5.14}$$

where $\lambda = k(k-1)/(N-1)$ [55]. For coded imaging, each open element of a mask would correspond to elements $a_n = 1$ and each closed one to $a_n = 0$. When the mask consists of at least two consecutive cycles of this pattern, a source at object index $j \in \{1, .., N\}$ will project the pattern $\vec{a}$ cyclically shifted by $j-1$, referred to here as $\vec{a}^{\,j-1}$, onto the detector elements with intensity proportional to the source's intensity, x_j. In other words, the measurement vector for counts from the jth image direction is $\vec{y}^{\,j} \propto x_j \, \vec{a}^{\,j-1}$ where the total measurement is the sum from each direction, $\vec{y} = \sum_j \vec{y}^{\,j} + \vec{\beta}$ and $\vec{\beta}$ is the vector of counts due to background. The resulting pattern may be recorded in the time, spatial, or both domains as described in Section 5.2. Figure 5.1 provides a 1-D diagram of the setup used in this work.

The same encoding process can be described using a $J \times J$ encoding matrix that has jth column equal to $\vec{a}^{\,j-1}$, i.e., $\boldsymbol{O}_{\vec{a}} \equiv [\vec{a}^{\,0}, ..., \vec{a}^{\,J-1}]$. Ignoring background, the measurement vector can be written $\vec{y} \propto \boldsymbol{O}_{\vec{a}} \vec{x} + \vec{\beta}$, which is the perfect-detector version of Equation 5.12. If the encoding matrix is based on an (N, k, λ)-cyclic-difference set, Equation 5.14 stipulates that $\boldsymbol{O}_{\vec{a}}^T \boldsymbol{O}_{\vec{a}} = (k-\lambda)\boldsymbol{I}_J + \lambda \mathbf{1}$, where $\mathbf{1}$ is the all-ones matrix. Hence, substituting $\boldsymbol{O}_{\vec{a}}^T$ for $\boldsymbol{O}_{\vec{a}}^{-L}$ as the decoding matrix in Equation 5.13 only adds

an easily-removable DC background level to the reconstructed image.

In general, the inverse matrix operation suffers from noise amplification, while the transpose does not; so with regards to SNR, cyclic-difference-set-based patterns are desirable for coded imaging. The reconstruction employed here is also equivalent to applying a matched filter, or periodic correlation of the measurement with the basic pattern: $\hat{\vec{x}} = \boldsymbol{O}_{\vec{a}}^T \vec{y} = \vec{a} \otimes \vec{y}$. Alternatively, the left inverse for these encoding matrices can be used to avoid the DC background and can be computed easily and without loss of precision. The decoding matrix in this case is $\boldsymbol{O}_{\vec{a}}^{-L} \equiv (k-\lambda)^{-1}(\boldsymbol{O}_{\vec{a}}^T - k^{-1}\lambda \mathbf{1})$.

5.3.2 Two-Dimensional Codes

The 1-D sequences generated from cyclic difference sets are typically folded into 2-D arrays for use in spatial coding (coded aperture imaging) of 2-D objects. The folding procedure is described in detail elsewhere [11]. These special 2-D arrays provide the near-ideal, two-valued response for any cyclic shift of the array in both x and y directions. This is described by the 2-D periodic autocorrelation function [55], a matrix with pqth element

$$(\boldsymbol{A} \circledast \boldsymbol{A})_{pq} \equiv \sum_{m=0}^{M-1} \sum_{n=0}^{N-1} a_{mn}\, a_{m'n'} = \begin{cases} k & \text{if } p \bmod M = 0 \text{ and } q \bmod N = 0 \\ \lambda & \text{otherwise,} \end{cases} \tag{5.15}$$

where $m' = (m+p) \bmod M$ and $n' = (n+q) \bmod N$, and M and N are the dimensions of matrix $\boldsymbol{A}$. This formula is analogous to the 1-D version in Equation 5.14. For 2-D coded aperture masks, the pattern of holes denoted by the 1's in $\boldsymbol{A}$ is often arranged in a 2×2 mosaic such that each column of the encoding matrix, termed weighing matrix in the review by Caroli et al. [35], becomes a 2-D cyclically shifted version of $\boldsymbol{A}$ with elements arranged in vector form.

The resulting encoding matrix $\boldsymbol{O_A}$ has analogous properties to its 1-D counterpart, i.e., $\vec{y} \propto \boldsymbol{O_A}\vec{x} + \vec{\beta}$ and $\boldsymbol{O_A}^T \boldsymbol{O_A} = (k-\lambda)\boldsymbol{I}_J + \lambda \mathbf{1}$ when using a (N, k, λ)-cyclic-

difference set. A similar estimator can then be used, $\hat{\vec{x}} = \boldsymbol{O}_{\boldsymbol{A}}^{T}\,\vec{y}$, that is equivalent to the result from 2-D periodic correlation commonly used for image reconstruction in coded aperture, $\hat{\boldsymbol{X}} = \boldsymbol{A} \otimes \boldsymbol{Y}_{2D}$, arranged into a vector, where $\boldsymbol{Y}_{2D}$ is the recorded pattern, $\vec{y}$, arranged in a matrix to correspond with the basic 2-D code.

A cyclic-difference-set-based code was used for the time-encoding system in this work. Each column of the encoding matrix $\boldsymbol{T}_i$ is a cyclic shift of the others, so moving the source simply causes a 1-D shift in the time-varying count rate that is recorded by the detector. Hence, there is no need for codes applied in the time domain to retain the 2-D periodic autocorrelation properties of coded apertures, even when imaging 2-D objects. In fact, many time-encoded systems have used 1-D codes to image in 2-D, which included those based on cyclic difference sets [70, 75] and stochastic apertures [56]. In principle, any dimension code may be used for time coding as long as the data is subsequently arranged to correspond to the dimension where it has its special correlation properties.

The code used in this work is the 2-D MURA pattern, which, among other properties, has 50% open elements with equal and prime dimensions, i.e., both $M = N$ are prime numbers. They are derived from a specific class of cyclic difference sets called quadratic residues [137]. MURA arrays are commonly used in practice, and the reader is referred to the seminal paper on the topic for information on how to generate them from 1-D sequences [138]. The procedure is similar to that of construction for the URA, which is another well-known 2-D pattern that is instead derived from twin-prime Hadamard arrays [137]. URAs can be arranged to form various open fractions, but with limited choice in dimensions M and N, which cannot be equal.

Notably, URA patterns are 2-D arrays satisfying Equation 5.15. Although MURAs are also derived from cyclic difference sets, they do not have this property. However, the difference is very small. Changing the element a_{11} of $\boldsymbol{A}$ from 0 to 1 generates $\tilde{\boldsymbol{A}}$, where $\tilde{\boldsymbol{A}} \otimes \boldsymbol{A}$ is indeed two-valued. Furthermore, the decoding matrices for MURAs

are very similar to that of URAs and hence, they have nearly-identical SNR properties close to that of a matched filter.

5.3.3 Signal-to-Noise Ratio of (M)URAs

In coded imaging using multi-pinhole apertures, the estimate of intensity in one direction may be obscured by Poisson fluctuations in the recorded counts from other directions. This inherent disadvantage heavily contributed to the demise of time-encoded imaging for medical applications, where discerning low-intensity structures amongst strong ones can sometimes be crucial [77]. However, Equations 5.14 and 5.15 show that when using cyclic-difference-set-based patterns, all reconstructed image pixels share the same DC background level due to the collective sources that is proportional to λ, implying that the directions with large intensity will have higher-than-average SNR.

Since the applications of interest here are mainly focused on finding the shape or location of the brightest source within the FOV, lower-intensity structures or objects are, generally speaking, not as important as strong ones. This makes coded imaging statistically advantageous for some, but not all, situations. Regardless, the statistical nature of coded imaging is pervasive and governs the length of counting time necessary to resolve an object. It therefore requires close attention during the design phase of an imager and special consideration during measurements of objects that have very different intensity distributions.

Time coding and spatial coding techniques utilize essentially equivalent data, i.e., a set of Poisson-distributed counts in some space and time interval. They also utilize the same reconstruction techniques from that data, i.e., periodic correlation or matrix-vector product with decoding function. Therefore, ignoring detector nonuniformities or other nonidealities, each method is statistically equivalent given that the same encoding and decoding matrices are used.

The SNR for coded imaging systems has been derived in a number of studies [11, 37, 65, 70, 139], however the expression for MURAs and URAs from Accorsi, Gasparini, and Lanza is used here [80]. That work also has detailed derivation of SNR for other patterns as well as the general case. As alluded to previously, and can be seen from Equation 5.15, the SNR for the intensity in each image direction is different and depends on the intensity distribution in all other directions. Hence, SNR_{pq} is defined for each pqth image direction and is the ratio of the net signal in that direction to the statistical fluctuations in that direction. The statistical fluctuations included in this model are the combined effects from the signal itself, the DC offset of Equation 5.15, transmission through the mask, and uniform unmodulated background. Furthermore, detector nonuniformities are not considered, collimation effects from the mask are neglected, and the projected pattern line up exactly with detector elements as before.

The following expression is for SNR of images from (M)URA arrays and is directly from [80] with slightly-adjusted notation:

$$\mathrm{SNR}_{pq} = \frac{\sqrt{\rho\, C}\sqrt{(1-\rho)}(1-f)\psi_{pq}}{\sqrt{(1-f)(\rho+(1-2\rho)\psi_{pq})+t+\xi}}, \tag{5.16}$$

where C is the expected total counts from the source with no mask, summed over all detector elements and time intervals; ρ is the open fraction of the mask; $f = \exp(-\mu\zeta)$ is the probability that a particle streams through the mask, where ζ is the nominal mask thickness; $\psi_{pq} = C_{pq}/C$, where C_{pq} is the expected counts from the pqth direction; and finally, $\xi = \sum_{in} \mathrm{E}\left[\beta_{in}\right]/C$ is the expected fractional number of background counts. As mentioned earlier $\rho \approx 0.5$ for MURAs, so a simpler expression is obtained for SNR of patterns used in this work:

$$\mathrm{SNR}_{pq}\left(\rho = 0.5\right) = \frac{\sqrt{C}(1-f)\psi_{pq}}{\sqrt{2(1+f)+4\xi}}, \tag{5.17}$$

which is directly proportional to the fractional object intensity ψ_{pq}. Notice that for

a point source without background or transmission through the mask; i.e., $\psi_{pq} = 1$, $f = 0$, and $\xi = 0$; both Equations 5.16 and Equation 5.17 simplify to $\text{SNR}_{pq} = \sqrt{C/2}$, or the square root of the total number of measured counts. This makes intuitive sense because the intensity estimate in the point-source direction in that case is simply the sum of the measured counts.

5.4 Summary

This chapter provided a mathematical description of time-encoded and coded aperture imaging, juxtaposed to highlight their similarities and differences. It defined coded imaging in a general sense, such that any arbitrary binary code can be modeled for coded imaging in the time, spatial, or combined domains. Notably, the analysis showed that patterns measured in the time domain (time-encoded) are immune to nonuniformities in the detector's spatial domain, while patterns measured in the spatial domain (spatially-encoded or coded aperture) are immune to nonuniformities in the time domain. Further discussion showed that cyclic difference sets are particularly useful for generating patterns in coded imaging since they circumvent the need for matrix inversion and therefore generally provide high image SNR. Lastly, an expression for image SNR using (M)URA codes was provided that is useful for predicting the imaging performance of the time encoding system used in this work.

CHAPTER VI

Time-Encoded Imaging System Design

6.1 Mask Positioning System

To provide time-varying patterns of attenuating material for time-encoded imaging, we built a programmable mask positioning system. The so-called "Mira" system also enables repeatable placement of a single Polaris SP plane on a stage facing the mask and can align the cathodes of the array between about 12 cm and 60 cm from mask plane. The Mira system is pictured in Figure 6.1 with a single plane of Polaris SP. Most components are made of Al, except (most notably) the vertical and horizontal ball screws and vertical support rods that are made of steel. The ball screws are each connected to a stepper motor that is wired to a driver and controlled using an Arduino Uno board.

The two degrees of freedom offered by the perpendicular ball screws allow for x, y positioning of a coded aperture mask within a 17 in $\times$ 17 in area, the extent of the ball screw range. The range ends are monitored by limit switches that inform the Arduino that the mask is traveling out range when contact is made. A simple block diagram of the setup is provided in Figure 6.2.

A laptop was connected to the Arduino board to program the device and receive real-time output of the mask's position versus time. The computer was also connected to Polaris SP to receive gamma-ray interaction data. The laptop's system clock was

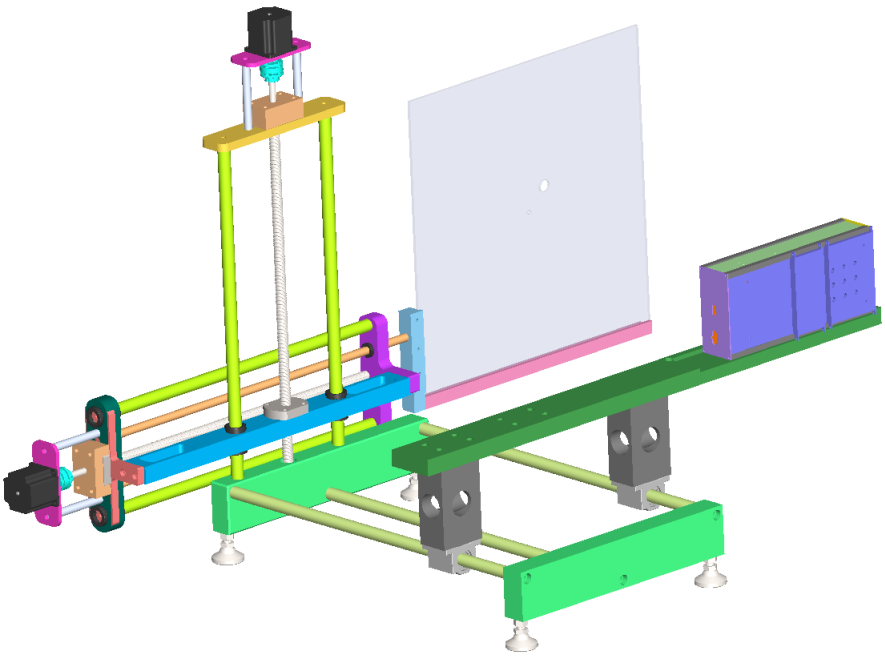

(a) Angled view of Mira and Polaris SP

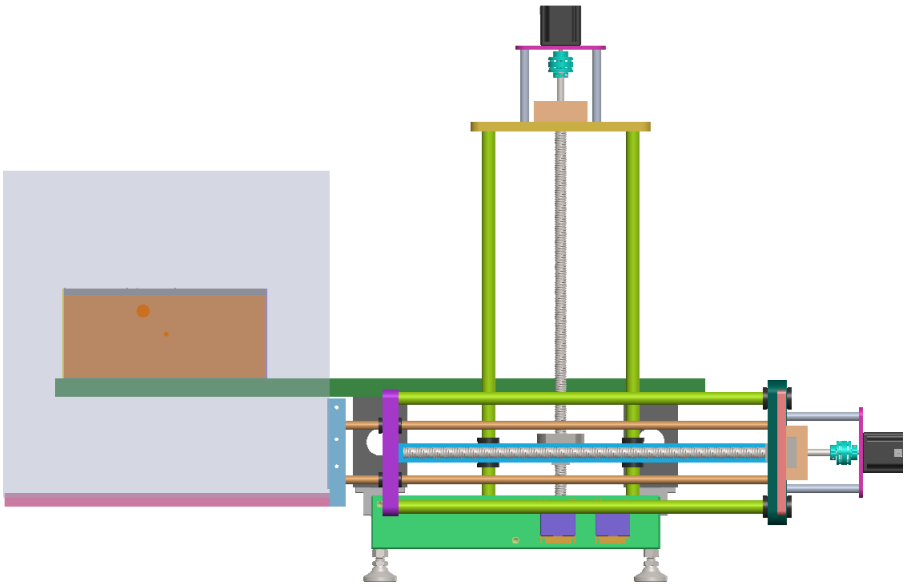

(b) Perspective from object plane

Figure 6.1: Screen captures of Mira system design from Solidworks CAD software. A single plane of Polaris SP was positioned on detector stage, pictured with purple backing in (a), and orange front face in (b). Stepper motors are pictured in black at the ends of the vertical and horizontal ball screws for x and y movement of the mask between object and detector.

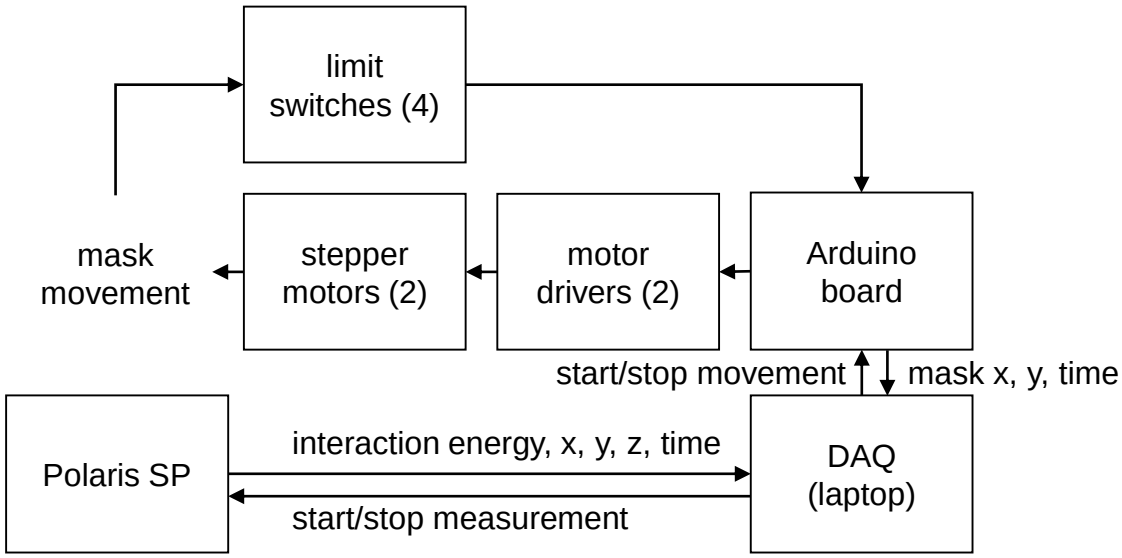

Figure 6.2: Block diagram for a time-encoded measurement using Mira and Polaris SP.

used to synchronize timing data from Polaris SP and the Arduino and were recorded to a precision of 1 ms. Timing accuracy on the order of about 10 ms is sufficient to resolve mask dwell times on the order of 1 s.

The timing information for gamma-ray interactions was determined from the reset time of the field-programmable gate array (FPGA) on the detector, which occurs directly following each triggered event. To test if gamma-ray arrival time could be approximated by the FPGA reset time, times between FPGA resets for a lab background measurement were arranged in a histogram, and a line was fit to the logarithm of the counts in each 1 ms bin, as shown in Figure 6.3. The slope and intercept both corresponded to the detector count rate corrected for dead time, indicating that timing information from the PFGA reset was indeed Poisson-distributed with the correct average rate.

The positional accuracy of the system was measured using a dial indicator over many repeated mask movements. It was found that the standard deviation of the

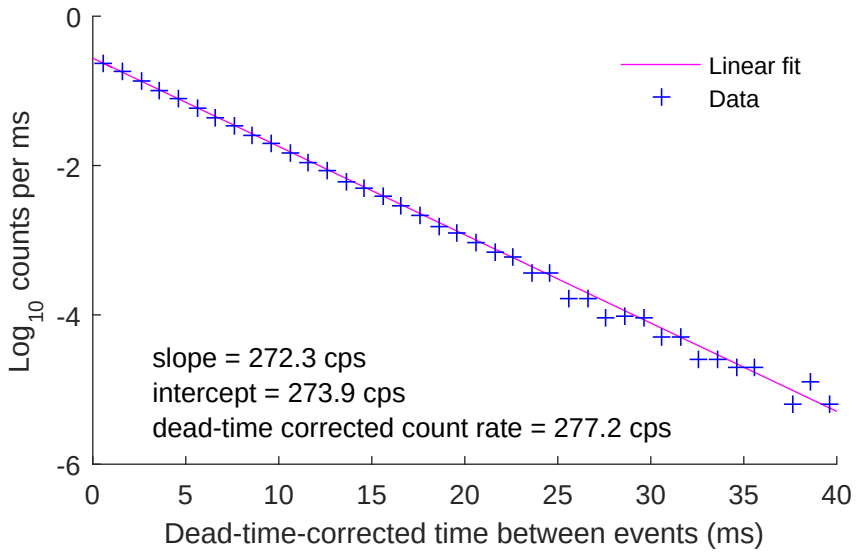

Figure 6.3: Evidence for Poisson distribution of time between events during a laboratory background measurement, indicating the acquisition of proper event timing information from the FPGA on board Polaris SP.

position of the mask relative to its reported position was less than 30 μm for several trials at different positions. The conversion between motor steps to position was also found to be very consistent for both forward and backward movements. Its measured value on the along the x axis was $12.67 \pm 0.02\,\mu$m/step.

A 1-D representation of the measurement geometry is provided in Figure 6.4. A single square cycle of the MURA pattern has side length $(N-1)p_m$, where N is the square root of the number of elements in the cycle, and p_m is the mask pitch. At the image plane, the diverging, square, and uniform-sensitivity FOV has side length $F_u = \left(1 + \frac{a}{b}\right)(N-1)p_m$. One extra cycle of the mask must be available for shifting through FOV, as pictured on the left of Figure 6.4 If multiple detectors are used, there must be extra elements to ensure that the entire FOV is modulated by the mask for every detector element, as pictured at the right. Note that the mask's movement outside the FOV may cause partial modulation of emissions in this region, which can cause artifacts.

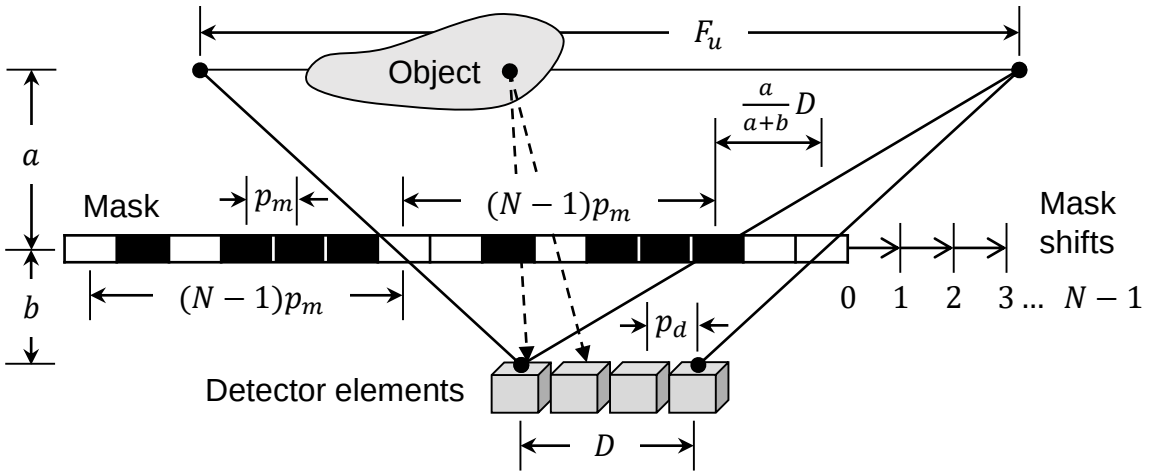

Figure 6.4: 1-D representation of geometry and mask movement scheme utilized for time-encoded imaging. The example mask pattern is based on a (7,3,1)-cyclic-difference set.

Each line of sight from detector to object within the FOV passes through a particular element in the mask plane. The attenuating material at this position is then modulated according to the mask's code by incrementally shifting the mask through its cycle, one element at a time. Hence, at the end of the cycle, each line of sight between the detector and object will have been modulated by the whole code. Note that neighboring elements receive the same time code shifted by one time bin. In this work, the movement is done discretely for simplicity of the model, and data recorded while moving the mask between positions is not used for reconstruction.

The extension to 2-D is straightforward. In this work, the MURA mask was cycled through each location with in the FOV by scanning the mask through each row. Hence, the mask moves back and forth through the entire pattern in a "snake" pattern. The same movement routine was used for all time-encoded measurements found in this work. The Arduino code is provided in Appendix B. Note that more than 2×2 mask cycles are required due to the Polaris SP's spatial extent, as pictured in Figure 6.4.

6.2 Gamma-Ray Mask

Pixelated CdZnTe response to gamma rays is well understood, so gamma-ray sources were used with Mira as a test bed for the new imaging system. A W-metal coded aperture mask was constructed with the aim of obtaining high spatial resolution with many image elements to demonstrate that detector position resolution and size do not limit spatial resolution in time-encoded imaging. The mask was not designed for any specific object, so a MURA pattern was chosen because it allows a high fraction (50%) of gamma-rays through, which is favorable for high-background scenarios.

The MURA pattern is not self-supporting, so 0.42-mm-wide tungsten connectors were used at the corners of each tile in mask. This causes small holes to become rounded at mask pitches less than about 1 mm. Furthermore, about 2 mm of W is needed to absorb 95% of 186-keV gamma rays from ^{235}U, which is of interest to this work. Given these constraints, the mask pitch was chosen to be 1.4 mm. The manufacturer of the W mask pattern was also limited to a square piece of less than 12 in $\times$ 12 in. In the end, this left room for a 79×79 MURA pattern, with the actual mask consisting of 200×200 elements to account for movement and detectors size. The base pattern and W mask are pictured in Figure 6.5. The photograph is a single 0.25-mm-thick sheet of the mask, of which there are 12, totaling 3 mm. These can be stacked and arranged to trade off between mask transparency and collimation effects from the mask thickness at different gamma-ray energies.

6.3 Thermal Neutron Mask

The ceramic material BN was chosen for the mask because it attenuates about 96% of thermal neutrons at 0.0253 eV within 1 mm and emits only one gamma-ray line at 478 keV, which is lower than the 558 keV signal used here for thermal neutron detection. The overall mask design goal is to achieve good image SNR within

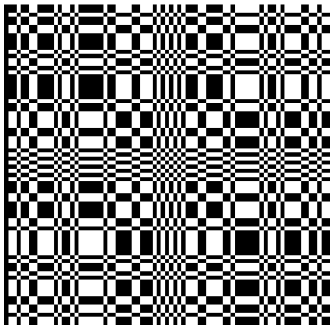

(a) 79 × 79 MURA array

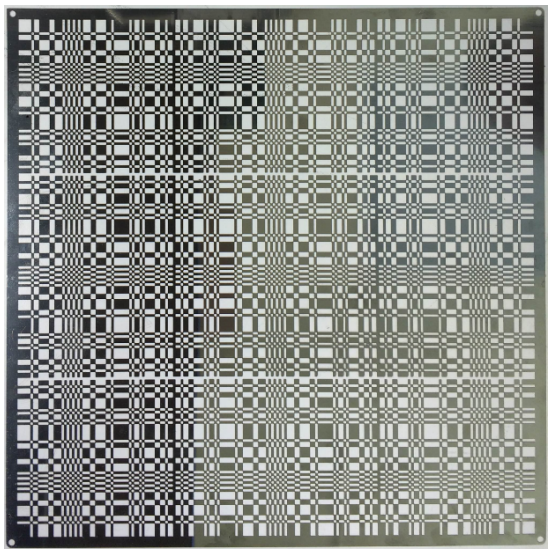

(b) 0.25-mm-thick W mask layer

Figure 6.5: Basic pattern and mask used for time-encoded gamma-ray imaging.

reasonable measurement time. Thus, the size of objects to be imaged, their emission rates, detector efficiency, and detector position resolution all must be considered.

The MURA pattern was used due to its high open fraction ($\rho = 0.5$), which enhances the thermal neutron signal amongst gamma-ray background. The total number of mask elements do not affect image SNR, as seen in Equation 5.16, therefore the most elements will be used to maximize imaging FOV. The Cramer-Rao approach to design optimization [140, 141] was initially considered for this work, however SNR for coded aperture images are relatively straightforward to calculate. In this section, we applied the SNR model of Equation 5.17 to thermal neutron imaging with CdZnTe using some minor adjustments.

6.3.1 Signal-to-Noise Ratio

For this work, configurations of fission sources with low-Z reflectors are of greatest interest. The Be-Reflected Plutonium (BeRP) ball is a 4.5 kg α-phase, weapons-grade Pu sphere fabricated by LANL in 1980 and is commonly used for benchmarking neutron and photon transport calculations [142]. Access to this source by research

groups is permitted for academic purposes, and for this reason it was used to represent the size, shape, and activity of typical neutron sources available for measurement by the imager. This serves as the design basis for the neutron mask, to achieve good image quality for low-Z reflectors surrounding fission sources similar to the BeRP ball.

Measurements of the BeRP ball were taken at the DAF during July 2016 using two 2 cm × 2 cm × 1.5 cm CdZnTe detectors in the Orion prototype digital system. When the BeRP ball was surrounded by 2 in of HDPE, there was clear evidence of thermal neutrons. Subtracting background, the 558 keV peak had 0.174 cps at 2.3 m from the source. When extrapolated to 18 detectors, the count rate of about 1.5 cps would still be roughly one order of magnitude lower than BNLs ^{3}He system with a comparable-intensity, moderated Cf-252 source at 2.3 m [26]. The background under the peak had roughly the same area, meaning a source-to-background ratio of about 1 was experienced. For the SP system, this ratio would be worsened to about 0.5 due to the roughly 2× degradation energy resolution from increased electronic noise. This is a conservative estimate since the peak's low-energy tail was ignored. Using the Orion digital system's measurement as a benchmark, the estimated 18-detector count rate for the SP system is then about 1.5 cps with a source-to-background ratio of 0.5 when measuring the BeRP ball from 2.3 m away.

Choosing a mask pattern which maximizes SNR is critical for this application because of the low count rates involved. This work is also subject to low source-to-background ratios relative to other applications such as medical imaging. The optimal open fraction for (M)URA patterns approaches 0.5 for any type of source, point or extended, when the source-to-background ratio goes to zero [80]. In fact, the optimal open fraction is always between 0.4 and 0.6 for source-to-background ratios greater than 1. For this reason, the MURA pattern was chosen, which has open fraction 0.5. It should also be noted that the SNR does not change as a function of the number of

mask elements, so in principle choosing a higher order mask pattern will not reduce SNR.

The SNR for coded aperture is well established for an idealized imaging system, as discussed in Section 5.3.3. However in this work, 558 keV gamma rays cause leakage of counts outside projected mask elements at the detector plane. For this reason, the recorded pattern is a blurred shadow of the mask. To account for signal leaking out of projected mask elements, a correction factor was used.

The correction factor, η, is the fraction of interactions that occur within the correct mask element's shadow on a 6.4 cm $\times$ 6.4 cm CdZnTe detector plane that is 1.5-cm-thick. This is the size of the 3×3 detector plane used in this work, excluding the gaps between detectors. The array is assumed to be centered with the element's shadow so that when the element shadow pitch is > 6.4 cm, $\eta = 1$. Equation 3.18 was numerically integrated to calculate η and plotted in Figure 6.6 as a function of projected element pitch, $mp_m = \left(1 + \frac{b}{a}\right) p_m$. Note that m refers to magnification, while the subscript m denotes "mask" in mask element pitch, p_m.

As a result, the count rates estimated from flood irradiation may be used for Equation 5.17 provided it is multiplied by η. Note that this assumes that 558-keV gamma rays leaking from the correct pixel are lost and do not contribute to the imaging signal. This correctly models the SNR at the affected pixel for a point source, but for an extended source the leaking signal can contribute to a neighboring pixel, and vice-versa. Hence, the correction factor is inherently conservative because it ignores some counts that would otherwise contribute to the signal.

The design goal of the neutron mask was to form an image of an object similar in size and emission rate to the 2-in, HDPE-reflected BeRP ball in reasonable time. Here, reasonable time is about 6 hours, or one working day accounting for setup and teardown times. The quality of these count-starved images will generally be limited by statistical SNR governed by Equation 5.17. For the purposes of this work, SNR

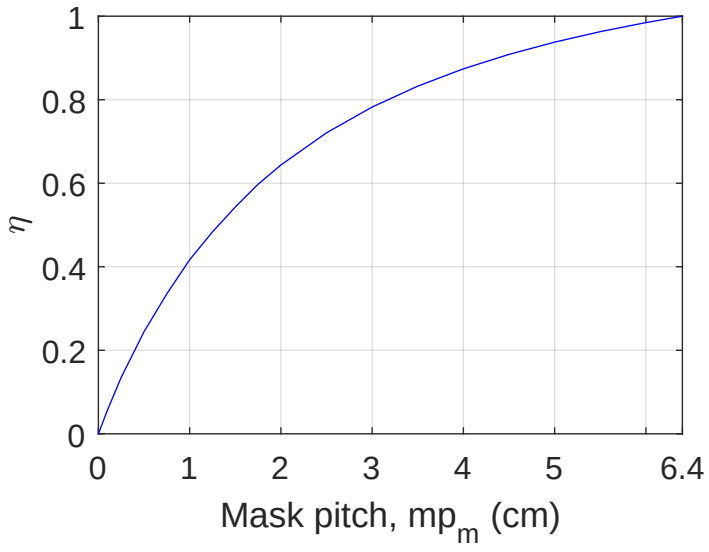

Figure 6.6: Plot of correction factor, η, versus projected (magnified) mask element pitch, mp_m, at the detector plane.

≥ 10 is desirable.

Figure 6.7 shows the mean SNR for one hour measurement of the BeRP ball surrounded by 2 and 4 in of HDPE reflector using the 18 CdZnTe Polaris SP system, predicted by Equation 5.17. The relative difference in count rates between the two configurations were calculated using MCNP5 [124], and the count rate was assumed to scale as inverse square of distance between object and detector. The object's intensity was assumed to be uniformly distributed across its 2-D extent within the imaging FOV, which in this case is a circle. 96% attenuation of thermal neutrons through the mask materal was assumed, corresponding to the theoretical value for 0.0253 eV neutrons attenuated by 1 mm of BN.

For these plots, the mask pitch was $p_m = 1.6$ cm. This pitch provided an appropriate trade off between image resolution and SNR for the BeRP ball configuration. The size of the elements was mainly limited by the spread of the signal at the detector plane, which effectively caused image blur. The result was that both 2-in and 4-in reflected geometries may be imaged up close (mask-object distance < 50 cm) to resolve

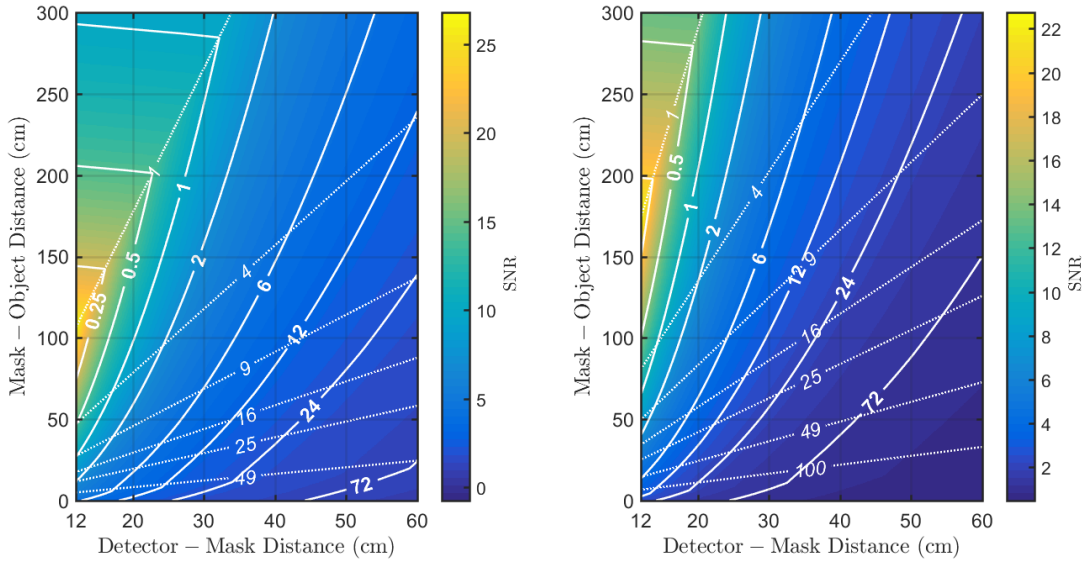

(a) 2-in polyethylene reflector

(b) 4-in polyethylene reflector

Figure 6.7: Predicted SNR of object pixels in an image of the BeRP ball reflected by polyethylene after one hour measurement using a coded aperture mask with element pitch $p_m = 1.6$ cm. SNR is plotted for a range of distances between the detector, mask, and object. Dotted contour lines indicate the number of image pixels subtended by the source at each configuration. Solid contour lines show the number of hours required to achieve SNR of 10.

their shape in under 6 hours. This can be seen by the dotted-line contours of equal object extent between 9 and 25 pixels that intersect with imaging times between 2 to 6 hours near the bottom-left of the each map. In the case of measurement times 1 h or less, images will be limited to near-point source configurations of the BeRP ball between about 1 to 3 m.

Following the decision to use 1.6-mm-pitch mask elements, 1-mm-thick BN tiles were used to create a 19×19 MURA pattern used for the mask. This rank was chosen because it is the largest size that is reasonable to transport for experiments. It also approaches the largest size Mira can handle without any problems with support or movement of the mask. Again, the idea was to maximize the FOV since adding elements does not reduce SNR in principle.

The overall mask pattern was rectangular rather than square since both 3×3

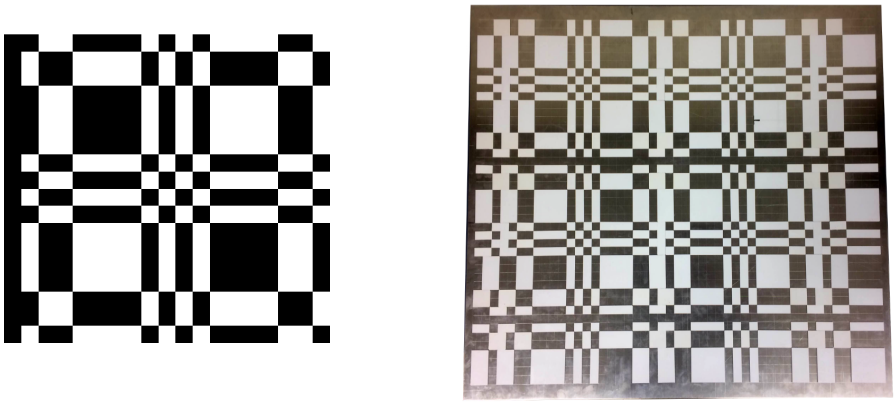

(a) 19 × 19 MURA array (b) BN mask with Al backing

Figure 6.8: MURA pattern and actual mask used for time-encoded thermal neutron imaging. Note that dark elements in (a) correspond to light-colored BN tiles in (b).

detector planes of Polaris SP positioned side-by-side were needed to view the source and maximize efficiency. Figure 6.4 illustrates the reason extra mask is needed span the FOV for all detectors in the array. A 30 in × 32 in, 2-mm-thick Al sheet was used as the backing to the tiles, onto which they were glued. A square grid was machined into the Al sheet's surface to guide tile placement. The sheet was noticeably curved due to the way the material was stored prior to being cut, with a bend on the order of mm. However, the arc was within tolerances for the experimental work done here.

6.3.2 Effect of Neutron Speed Distribution

A neutron's travel time from aperture to detector causes a delay in the recorded signal. For a monoenergetic collection of neutrons, this would merely cause a shift in the signal, which can be easily corrected. However, thermal neutrons have a significant spread in energy, which also causes the recorded signal to be blurred. Figure 3.1(b) gives the speed distribution of thermal neutrons at 290 K detected by several thin materials, described by velocity-dependent reaction rate $R(v)$ of Equation 3.6.

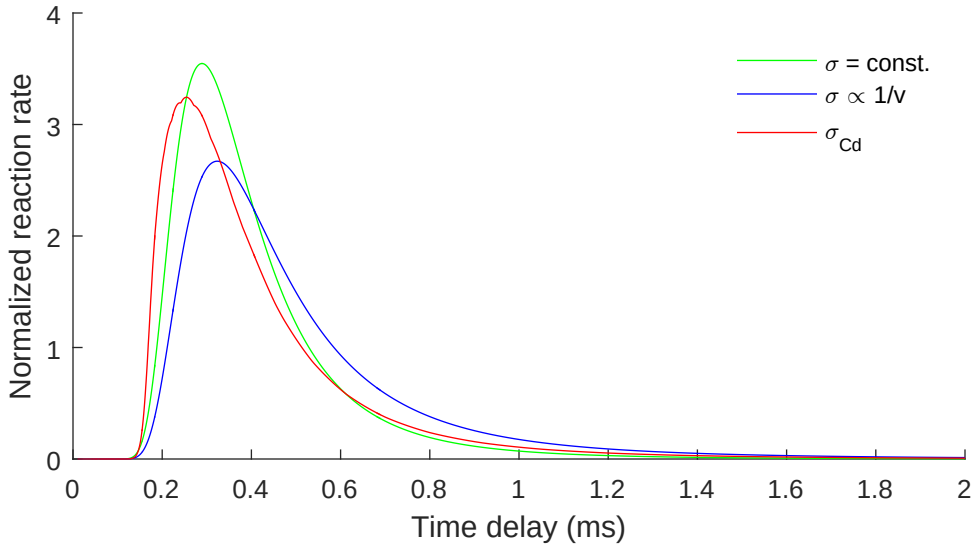

Figure 6.9: Reaction rate time distributions in time for thermal neutrons at $T = 290$ K traveling 1 m between a perfectly-attenuating time-coded aperture and thin detector of various σ.

A neutron's travel time from mask to detector separated by distance b is $t \equiv b/v$. Hence, the time-dependent reaction rate distribution from an impulse flux of thermal neutrons is

$$R_M(t;b) \equiv \sigma\, N_A\, n_0\, b^2\, t^{-3}\, M(b/t), \tag{6.1}$$

where σ, N_A, and n_0 are the cross section, number of nuclei per unit area of the thin detector material, and number density of neutrons, respectively. $M(v)$ is the Maxwell-Boltzmann distribution in velocity and is given by Equation 3.2. Most coded aperture masks are made such that their transmission probability is small, making their impulse response close to Equation 6.1. Figure 6.9 shows Equation 6.1 plotted for several different detector materials. Note that $\sigma = $ const. corresponds to the case where the detector is 100% efficient at all neutron energies.

Figure 6.9 shows that neutrons traveling between a mask and detector separated by 1 m are detected about 0.3 ms after they pass the mask, with a spread of about 1.0 ms. $R_M(t;b)$ is stretched in time for different mask-to-detector distances so that both

the delay and spread of detection times are scaled proportional to b. Hence, a system with mask-to-detector separation of 10 m would experience a delay in detected signal of about 3 ms with a spread of 10 ms. For most applications, including the one here, the delay of neutrons on this time scale is negligible. However, a spinning aperture, for instance, may operate at high rpm to suppress artifacts in time-varying background environments. For systems such as these, it's advantageous to keep the rate of change of the code low enough to avoid the blurring effects from the distribution of thermal neutron speeds.

CHAPTER VII

Gamma-Ray Imaging Performance

Two sets of time-encoded gamma-ray imaging measurements were recorded and are presented here. First, several ^{57}Co sources were used to test imaging performance of the Mira system with Polaris SP. The objective was characterize the image quality and 3-D capability provided by the system. Images of spatially-extended uranium metal objects stored at the Y-12 facility and available to the academic community are presented in Section 7.2.

Throughout this work, coded image reconstruction was done via correlation to measure the intrinsic imaging response of the system. The procedure is similar to back-projection and is identical in the case of correlation with the mask pattern itself; the simple Matlab function for image reconstruction from Polaris SP data is provided in Appendix C. While more advanced algorithms such as ML-EM [83] or stochastic origin ensembles (SOE) [143] would likely improve image quality, they tend to deconvolve the system response from an image. In that sense, the focus here is more on the quality of the imaging data rather than the algorithm chosen for reconstruction.

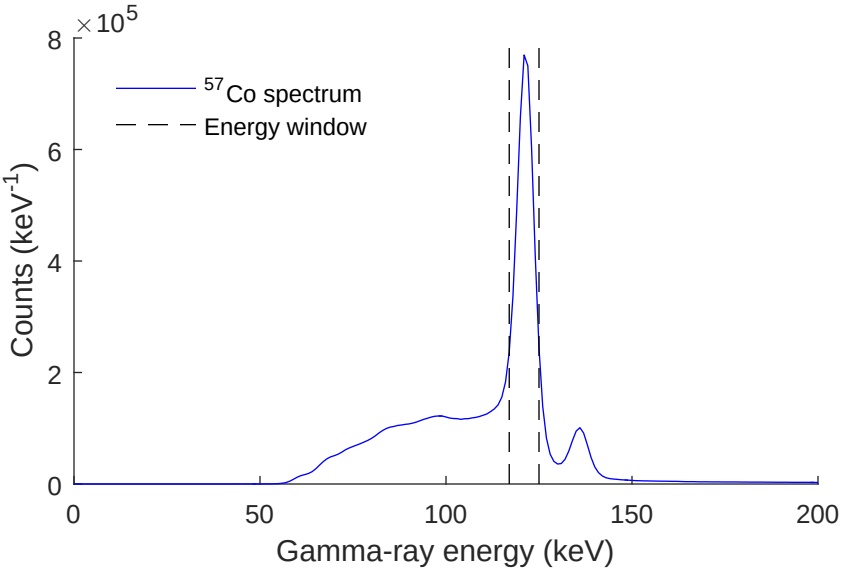

Figure 7.1: ^{57}Co gamma-ray energy spectrum measured using Polaris SP.

7.1 ^{57}Co Measurements

7.1.1 Check Source, Close to Mask

The first gamma-ray emitter used to investigate imaging performance of the time encoding system was 53 μCi ^{57}Co. The source contained a 5-mm-diameter active element within a 1-in-diameter plastic disk [144]. The disk was placed 1 cm from the mask which was positioned 28 cm from the cathode surfaces of Polaris SP's plane B. 1 mm of W was used for the mask, which absorbs roughly 99% of incident 122 keV gamma rays. The measurement was taken for about 2.5 h, with total count rate 1365 cps. The measured gamma-ray energy spectrum is plotted in Figure 7.1, showing there was very little background compared to counts from the source at 122 keV. A window around the 122 keV photopeak was used for imaging.

A 1.2 s mask dwell time was used at each of the 79^2 locations during the measurement, taking 0.28 s to move between positions. As explained in Chapter VI, only data taken while the mask was still was used here. However, it should be noted that data acquired during the mask's travel could in principle be used for imaging.

The magnification in this case was $m \approx 29$, so the projected mask pitch at the detector plane was about 4 cm. When the detector element size is small compared to the projected mask pitch, the spatial resolution at the object plane can be estimated from geometry [70]. Here, spatial resolution $R \approx (1+\frac{a}{b})p_m = 1.45$ mm, or roughly half the diameter of the source's active element. Although source is slightly extended, the measured pattern of counts versus time is clearly visible in the data from the entire array pictured in Figure 7.2(a). However, note that the 4 cm projected mask pitch is still smaller than the array itself, which spans 6.4 cm $\times$ 6.4 cm. Therefore, both the recorded time and location of each event were used to position counts within the patterns of Figure 7.2, as seen in the algorithm of Appendix C.

Figure 7.2 demonstrates time-encoded imaging using data from the entire 3×3 detector array, a single detector, as well as a single anode pixel. Although the pattern is not discernible from the anode pixel data alone, reconstruction via correlation was able to recover the source's location, albeit with substantial statistical noise. The images using the detector and array appear nearly uniform, with a very faint cross-shaped artifact centered on the source location and spanning the entire image, only visible in the two images with more counts. As a reminder, the extent of the hot spot corresponds to the 5-mm-diameter extent of the source, as each image pixel is only 1.45 mm on a side. So, the PSF of the system is actually tighter than what is suggested by these images of a small ^{57}Co disk.

The statistical fluctuations in the DC level of the individual anode's image is modeled well by a normal distribution, as seen in Figure 7.3. Its standard deviation is very near the square root of total counts measured by the anode, or 56.1, consistent with the noise term predicted by Equation 5.16. However, the number of counts underpredicted the standard deviation of the DC levels by 20% and 40% for the detector and array images, respectively. This is indicative of the small systematic artifacts noticed previously. The source of these artifacts has not yet been identified

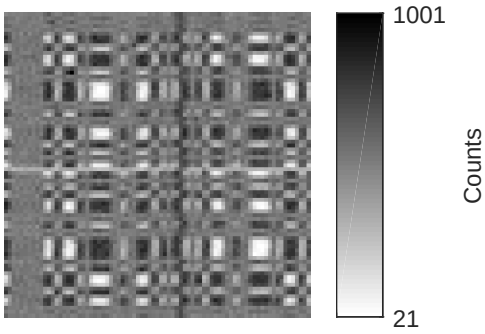

(a) Pattern from entire array

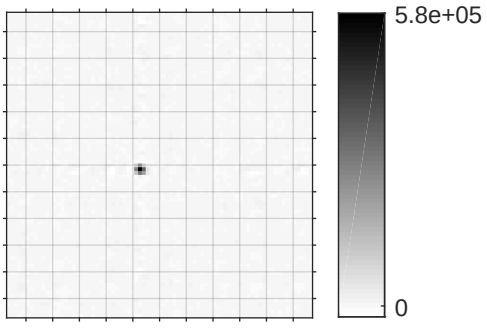

(b) Image from array, 3.3×10^6 counts

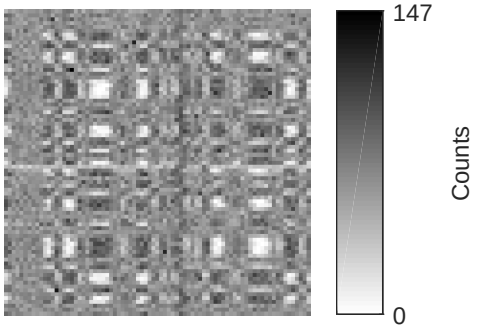

(c) Pattern from center detector

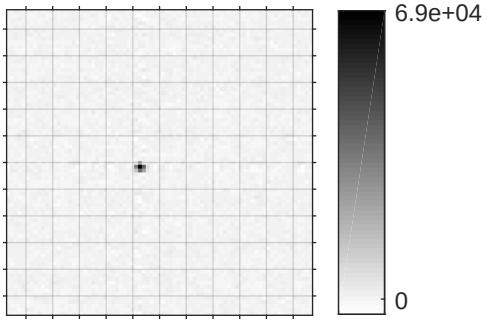

(d) Image from center detector, 3.9×10^5 counts

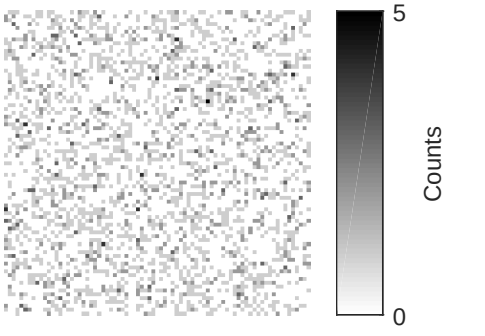

(e) Pattern from center anode pixel

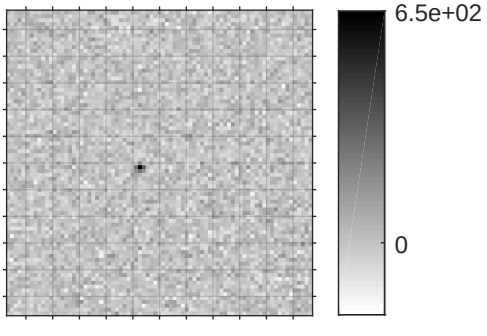

(f) Image from center anode, 3.1×10^3 counts

Figure 7.2: Measured patterns and images reconstructed via correlation with the mask pattern. Each image pixel is 1.5 mm on a side. The data used was either from the entire array, center detector, or center anode pixel. Image grid lines have 1 cm pitch.

by the author.

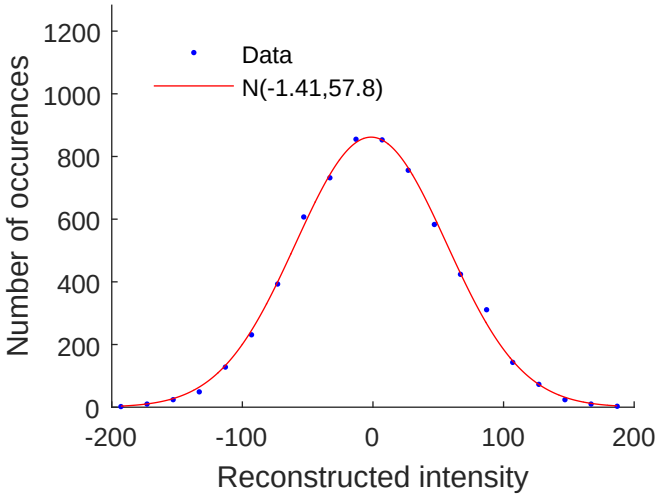

Figure 7.3: Distribution of intensities outside the peak in Figure 7.2(f).

7.1.2 Check Source, Away from Mask

The same ^{57}Co source was placed at 7.5 cm from the mask while the distance from mask to detector remained at $a = 28$ cm to observe the effect of parallax. The source was again measured for 2.5 h at an average count rate of 1190 cps. Figure 7.4 shows images reconstructed at planes stepping away from the mask, beginning at the mask plane. In Figure 7.4(a), the intensities contributed by each of the 3×3 detectors can be clearly seen. These separate hot spots eventually converge at the source's true position in Figure 7.4(c). This is further evidence of each detector acting as an independent imager.

Note the color scales in Figure 7.4; the intensity of the focused image is much higher than the unfocused images. If there was another source with comparable intensity also present at an out-of-focus plane, it would be brighter than the diffuse distribution of the other. In contrast, conventional coded aperture imaging introduces systematic artifacts at distances other than the one at proper magnification.

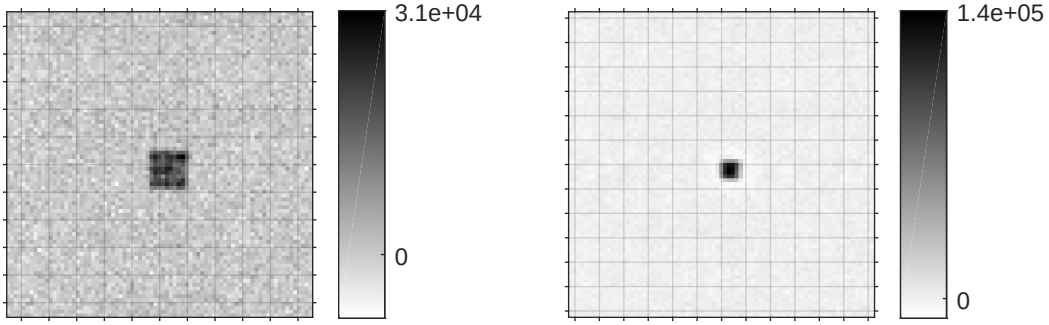

(a) $a = 0$ (b) $a = 3.75$ cm

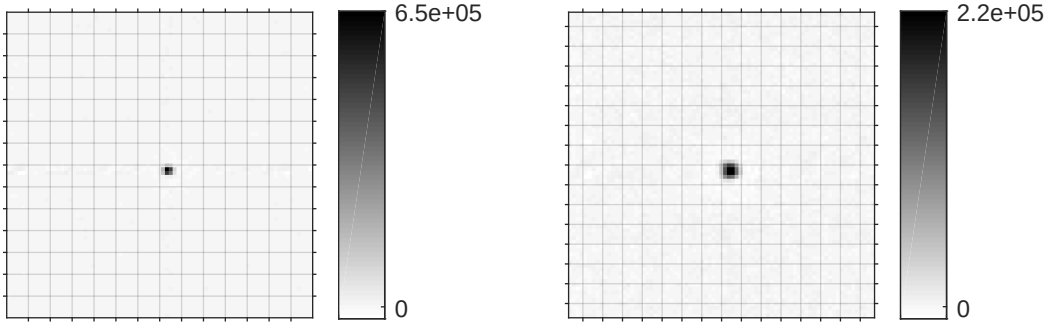

(c) $a = 7.5$ cm, true distance (d) $a = 11.25$ cm

Figure 7.4: Effect of parallax at several image planes reconstructed using different distances from the mask, where the true distance was $a = 7.5$ cm. Each image uses 2.8×10^6 counts.

One can also use parallax to measure the distance between source and mask. Figure 7.5(a) shows the distribution of intensity in distance, a, through the maximum intensity pixel in 3-D space. The maximum corresponds well to the true distance, 7.5 cm, with FWHM of roughly 5 cm. The discontinuities in this distribution are the result of grouping counts into 79^2 discrete locations prior to correlation for reconstruction. The smooth defocusing effect is also clearly seen in Figure 7.5(b) and Figure 7.5(c). Note that the parallax from edge to edge of the array in this case was a mere 10°, whereas a larger array or farther-separated detectors would likely achieve better depth resolution.

7.1.3 Flexible Marker, Coiled

The purpose of this next experiment was to demonstrate the imaging system's ability to reconstruct extended objects. The source used in this experiment was 85 μCi ^{57}Co in solution within a 50-cm-long plastic tube. The inner diameter of the tube containing the solution was 0.8 mm with outer diameter of 2.4 mm. The source was coiled in a circular shape and placed within a standard CD case, which was designed to hold a CD of 12 cm diameter, pictured in Figure 7.6(a).

The case was then positioned perpendicular to the mask and 2 cm from the mask so that the imager could view the circular outline of the source. The detector was again positioned 28 cm from the mask. The 50 cm tube length exceeded the circumference of the circle, so the extra length was used to convey the image's spatial resolution. The tube was pressed up against itself on the right side of the CD case pictured in Figure 7.6(a) so that the edges were touching. The tube gradually diverged away from this position to provide a range of tube separations.

The object was measured for 9 h at 1720 cps. Again, about half an hour of this time was spent moving the mask and not used for imaging. The reconstructed image is shown in Figure 7.6(b). The recorded pattern was oversampled by 10× prior to

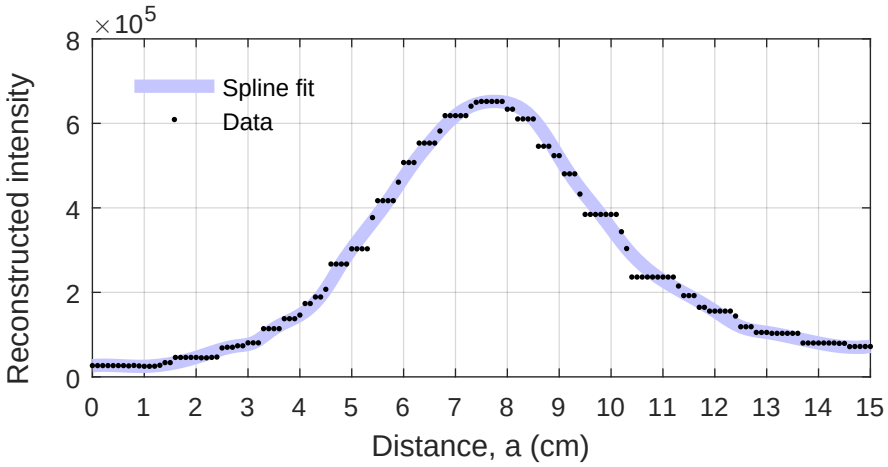

(a) Depth distribution of intensity through maximum-intensity pixel

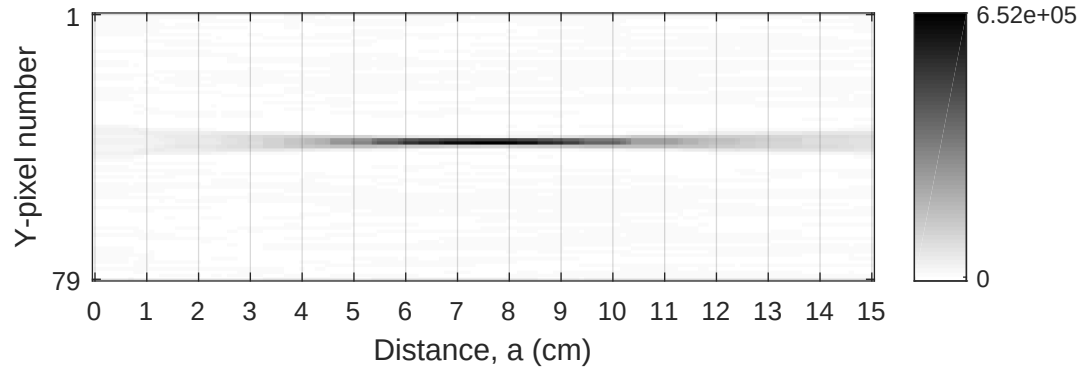

(b) Vertical slice through maximum-intensity pixel

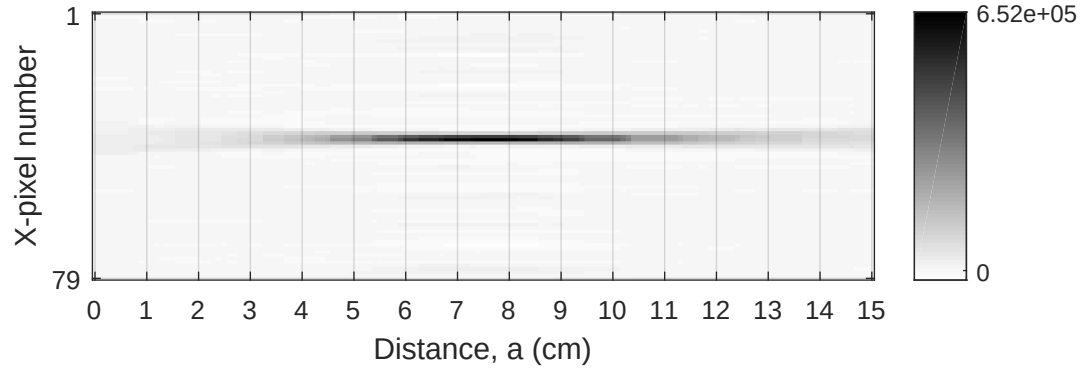

(c) Horizontal slice through maximum-intensity pixel

Figure 7.5: Reconstructed intensities at 122 keV as a function of distance from the mask, where true distance was $a = 7.5$ cm. Each image uses 2.8×10^6 counts.

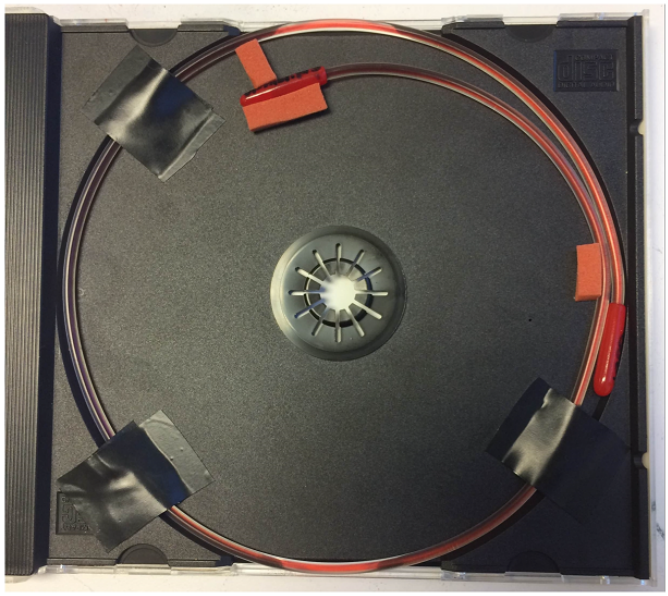

(a) ^{57}Co-filled flexible marker in a standard CD case

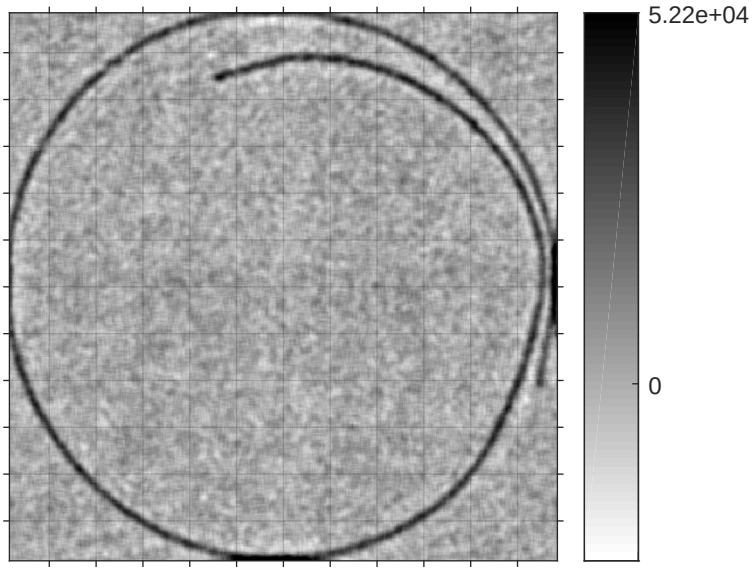

(b) Reconstructed image from 1.7×10^7 counts at 122 keV

Figure 7.6: Reconstructed image with photograph for reference. The tube containing ^{57}Co solution has inner diameter of 0.8 mm and outer diameter of 2.4 mm. Grid lines have 1 cm spacing, and color scale maximum is set at maximum pixel value outside aliased areas on right and bottom of edges image.

correlation, or $ns = 10$ in the algorithm given in Appendix C, allowing for more accurate interaction position information to be used. For the rest of the images in this chapter, the detector pixel positions were simply rounded to the nearest pattern element on a 79^2 element grid before correlation ($ns = 1$). Notice that the noise in the image now appears statistically correlated, a result of the smoothing effect from correlation of the measured pattern with the kronecker product between the decoding matrix and a 10×10 matrix of ones.

Since the magnification of the pattern is large ($m \approx 15$), the spatial resolution at this distance should roughly correspond to the pixel pitch at the image plane, or about 1.5 mm. The physical separation of the inner surface of the tubes containing the fluid at the right side of the image is about 1.6 mm, and is well-separated in the image. Figure 7.7 shows horizontal and vertical slices through the image, zoomed to view the tube. Notice that one peak is roughly twice the size; this is due to aliasing. Unfortunate placement of the source meant it was actually slightly larger than the FOV at that plane, which was about 11.8 cm on a side. This meant that vertical and horizontal edges of the tube were coded with the same time pattern, making their signals ambiguous.

The result was that the four vertical and horizontal edges of the circle overlapped with the opposite side, summing their intensities. The FWHM of the large peaks in both vertical and horizontal slices are 1.77 and 1.68 mm, respectively. Assuming the diameter of the tube broadens this peak in quadrature with the image PSF, the average spatial resolution was 1.53 mm FWHM. This agrees well with the intrinsic system resolution predicted from geometry.

It should be noted that simple reconstruction by correlation does not approach the true limits of the system's spatial resolution. Parallax offered by each detector pixel adds a slightly-shifted view of the source, which is sufficient information to achieve super resolution [145]. By deconvolving the many overlapping, low-resolution images,

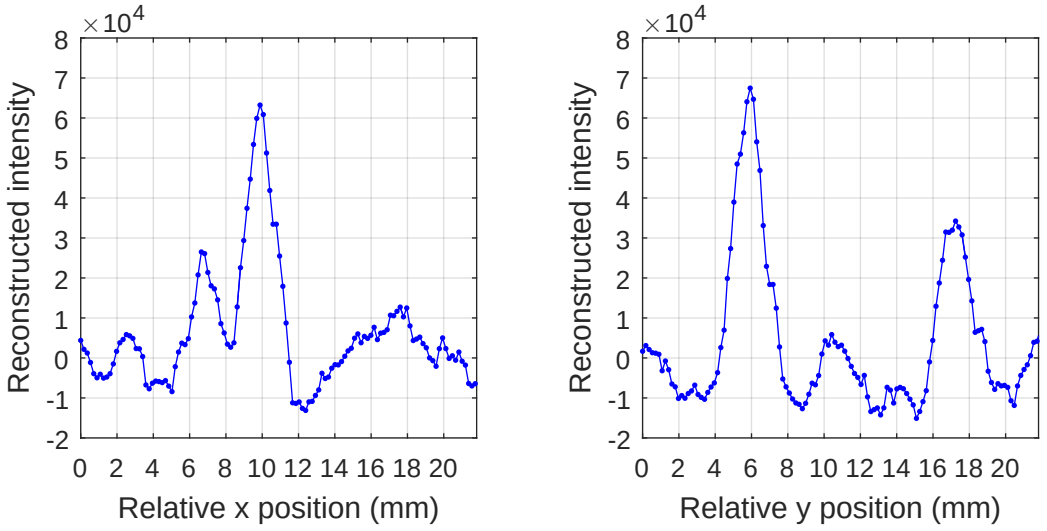

(a) Horizontal center slice of Figure 7.6(b)

(b) Vertical center slice of Figure 7.6(b)

Figure 7.7: Separation between peaks from ^{57}Co solution within tubes, which have inner diameter 0.79 mm and outer diameter 2.38 mm. The higher peaks are aliased, i.e., they are the result of two overlapping parts of the tube.

much higher resolution is achievable.

The complex, extended source also defocuses smoothly, as shown in Figure 7.8. These images were reconstructed at 1-cm intervals from the mask plane. Note that there appears to be a very faint, broad, cross-shaped artifact with a vertical cold and horizontal hot band that is centered in the image. The symmetric nature of this feature may be the result of the circular distribution of the source.

7.2 Uranium Metal Measurements

7.2.1 Highly Enriched Uranium Metal Disks

Uranium metal was measured at Y-12's NDSTC using the Mira system and Polaris SP. The first objects measured were 3-cm-diameter, 3-mm-thick U-metal disks used as enrichment standards at the facility. Two disks were positioned with circular surface facing the mask, one of 54% ^{235}U, and the other 70% ^{235}U. The 54% disk was positioned 3.6 cm away from the mask while the 70% disk was 6.9 cm away. The

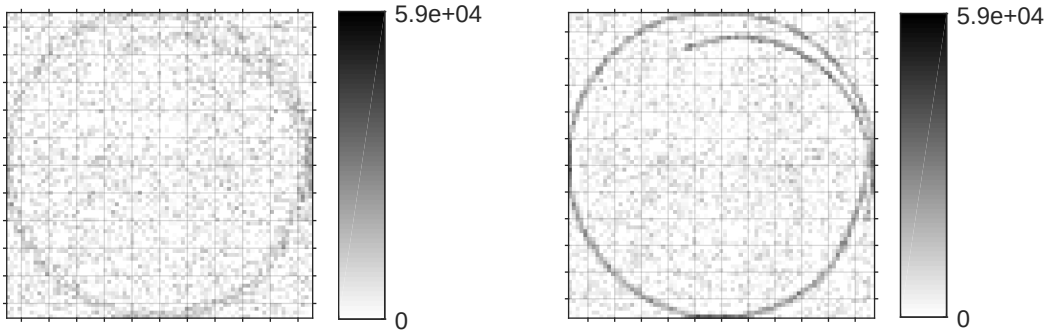

(a) $a = 0$ (b) $a = 1$ cm

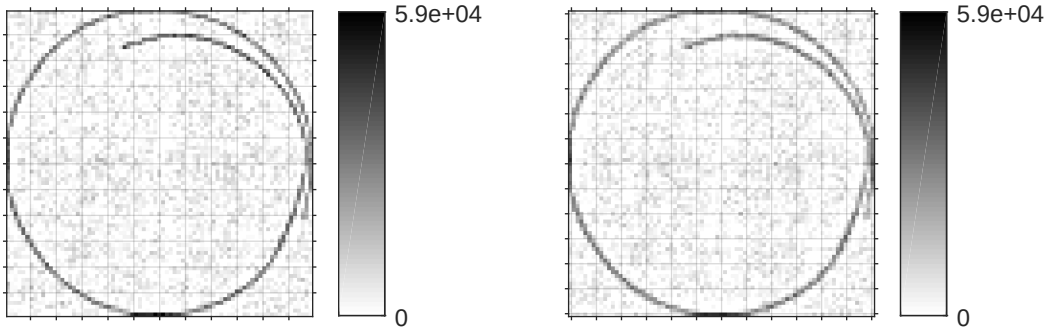

(c) $a = 2$ cm, true distance (d) $a = 3$ cm

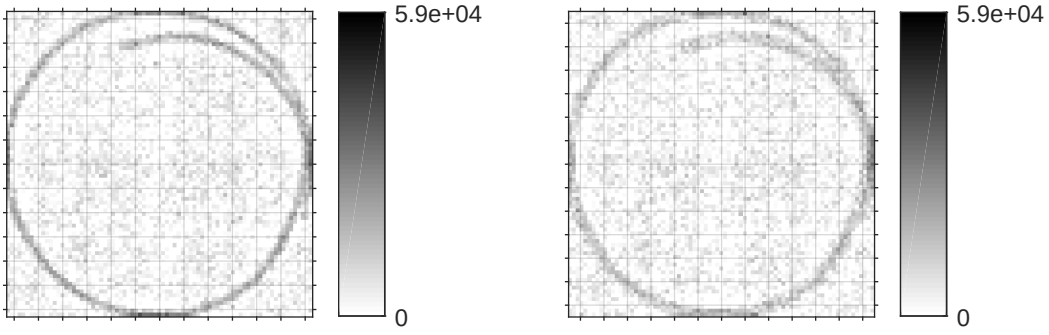

(e) $a = 4$ cm (f) $a = 5$ cm

Figure 7.8: Reconstructed images using 1.7×10^7 counts at 122 keV for different source-to mask distances, where the true distance was $a = 2$ cm. Color scale is cut off at zero to improve contrast. Grid lines have 1 cm spacing.

mask was 28 cm from the detector, which consisted of 2 mm of W to block 186 keV gamma rays from ^{235}U.

Two 2 h measurements were acquired and summed, including 30 min of mask travel time during each. The count rate was 670 cps, and the measured gamma-ray energy spectrum resembled the one plotted in Figure 2.4, which is dominated by the low energy HEU x- and gamma-ray lines from 205 keV and below.

All 1-pixel events below 215 keV were used for the reconstructions of Figure 7.9. These images are at planes stepping away from the mask at 3.3 cm intervals. Notice that the outline of each disk becomes sharpest at the plane where it was actually positioned. The relative intensities of each source also indicate the difference in enrichments. The key to obtaining correct estimates of enrichment from image pixel intensities is to achieve uniformity in response across the image. Given an artifact-free image, simply summing the intensities of pixels within the disk at 186 keV and subtracting DC background would provide the ratio of enrichments, provided the detector and source geometries are also accounted for.

There is, however, noticeable structure in the background of these images. This is possibly due to the same small artifacts witnessed in the previous tests using ^{57}Co, which became more apparent for these relatively large, extended objects. It could also be due to changes in gamma-ray background due to movement within the room and outside the FOV over the 4 h measurement. Localized sources of background from scatter may have also been partially modulated by the mask. The reason for this structure should be identified and corrected before attempting to estimate enrichment as a function of spatial location with time-encoded imaging.

7.2.2 Natural and Depleted Uranium Metal Disks

An overnight measurement was taken for 15 h using NU and DU enrichment standard disks. The configuration was similar to before, except that the DU disk was

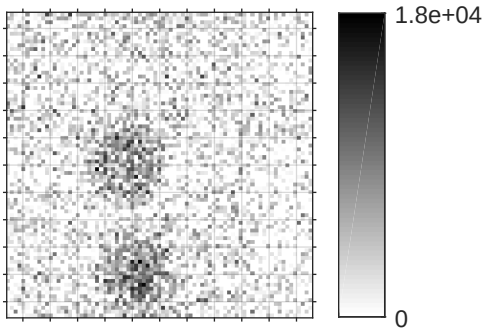

(a) $a = 0.3$ cm

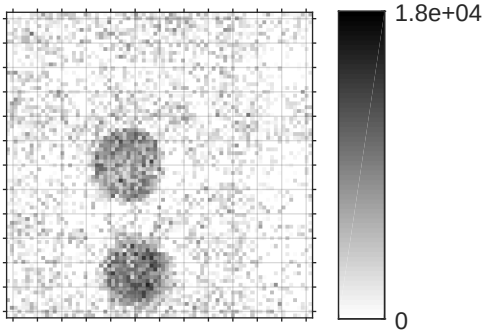

(b) $a = 3.6$ cm, 54% enriched true distance

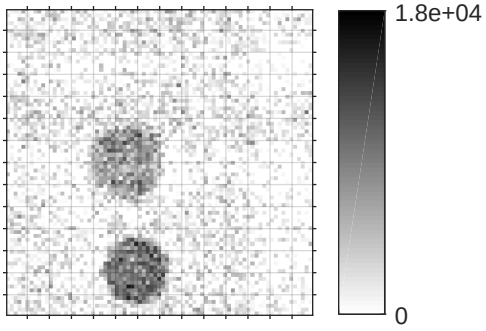

(c) $a = 6.9$ cm, 70% enriched true distance

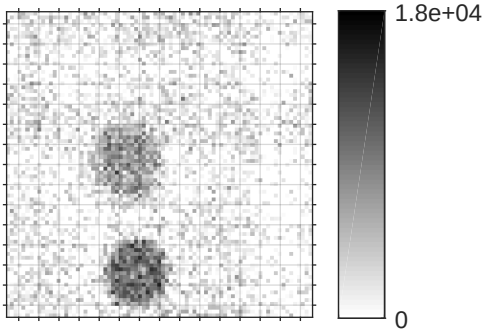

(d) $a = 10.2$ cm

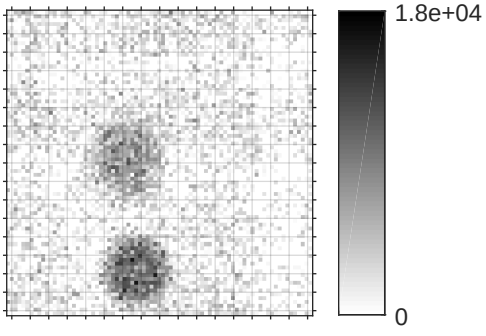

(e) $a = 13.5$ cm

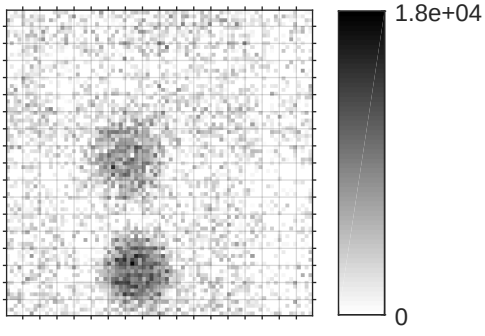

(f) $a = 16.8$ cm

Figure 7.9: Reconstructed images of 3-cm-diameter, 54% (top) and 70% enriched (bottom) HEU metal disks at different source-to-mask distances, a. In total, 5.6×10^6 1-pixel counts between 80 keV to 215 keV were used. Color scales are cut off at zero to improve contrast, and grid lines have 1 cm spacing.

4.3 cm from the mask plane and the NU disk was 7.1 cm from the mask. The low enrichment of the sample meant that the ^{235}U lines were not prominent, so the U K x-rays around 95 and 111 keV were used for imaging.

The total count rate was only 215 cps during the measurement, including 30 mins of mask movement. Figure 7.10 shows the measured gamma-ray spectrum, with substantial gamma-ray background beneath the x-ray photopeaks. The low count rate and large background contributed to the statistical noise found in the reconstructed images. Despite the noise, the sources are still discernible using their x-ray emissions.

7.2.3 Radiation Signature Training Device

The RSTD was designed to emulate the gamma-ray spectrum emitted from a significant quantity of HEU. It consists of a 12.6-cm-outer diameter shell of Al-U metal alloy, with a DU metal sphere at the center. The concept is that only the outer layer of HEU metal is measurable on an actual device due to the short MFP of the ^{235}U gamma rays, while the ^{238}U gamma rays come from farther within the material. The RSTD is designed such that gamma rays from both isotopes experience roughly the same number of MFPs, close to their infinite thickness. The device is pictured in Figure 7.11.

In the experiment, the RSTD was placed in the near field with its front edge only 1.7 cm from the mask, while the mask-to-detector distance was 14.8 cm. The objective was to determine if the hollow nature of the Al-U alloy shell was discernible from the time-coded image of ^{235}U gamma-ray emissions. The reasoning was that close proximity would enhance parallax and accentuate defocusing at the object's front plane to reveal a gap in intensity behind it.

The count rate in this setup was very high, about 1900 cps. Data from three measurements over a total of 6 h were combined. This equates to about 4.5 h of imaging data after subtracting mask movement time. The resulting images at the

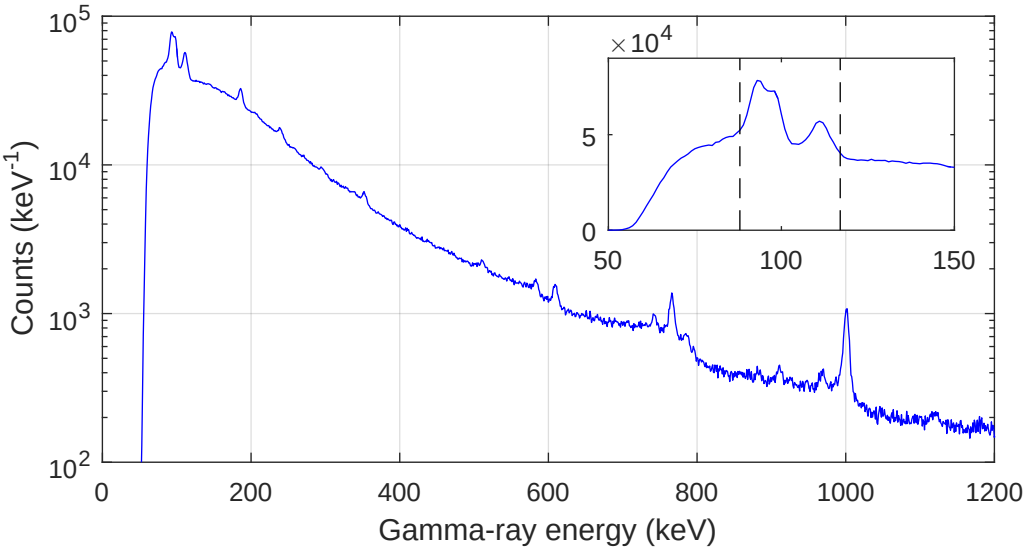

(a) 1-pixel gamma-ray energy spectrum and energy window

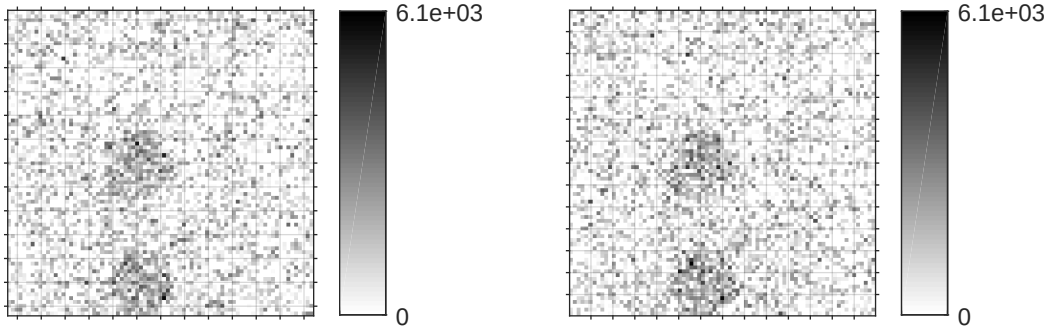

(b) $a = 4.3$ cm, DU true distance (top)

(c) $a = 7.1$ cm, NU true distance (bottom)

Figure 7.10: Reconstructed images and spectrum from 3-cm-diameter, DU (top disk) and NU (bottom disk) metal disks at different distances from mask, a. In total, 1.6×10^6 1-pixel counts between 90 keV and 117 keV were used. Color scale is cut off at zero to improve contrast, and image grid lines have 1 cm spacing.

Figure 7.11: Photograph of two RSTDs [12]. One has top hemisphere removed, revealing its DU core at center. The outer layer consists of an Al-HEU alloy enclosed in a thin Al shell.

front plane and at the centerline of the object are presented in Figure 7.12. Clearly, the image is dominated by statistical noise, even as the sphere comes into focus. The object subtended a very large solid angle from the perspective of the detector due to its proximity, and its intensity was spread across many image pixels. Equation 5.17 shows that SNR is proportional to the fractional intensity belonging to a pixel, which is quite small in this case.

The artifacts also appear prominently in Figure 7.12. Notably, this points to artifacts independent of background, since the relative background rate was negligibly small during the experiment. On the other hand, the artifacts pointed out in the initial ^{57}Co experiments are expected to worsen with source extent. This reinforces the need to determine the source of these artifacts. The distribution of intensity does appear to outline a circular shape of the correct size, but it is difficult to draw firm conclusions regarding its hollow structure due to these systematic artifacts and statistical fluctuations.

On the other hand, the 1001 keV line from ^{238}U provided data for Compton imaging of the DU core. The back-projection result is shown in Figure 7.12(c) with the outline of a circle with radius 6.3 cm centered at the hotspot centroid to show relative size. Note that Compton images are plotted as a function of angle and are not aligned to the time-encoded images. The hot spot of the Compton image is broad with FWHM on the order of 35°, consistent with the PSF of a point-like source of gamma rays. Furthermore, 25 iterations of the ML-EM algorithm also causes the intensity to localize to a much tighter area than what would be expected for emissions distributed throughout the entire sphere. This is consistent with the small size of the DU core within the larger RSTD sphere.

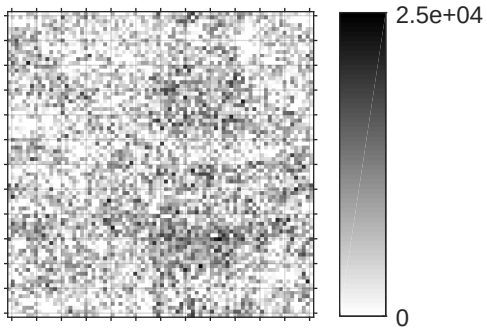

(a) $a = 1.7$ cm

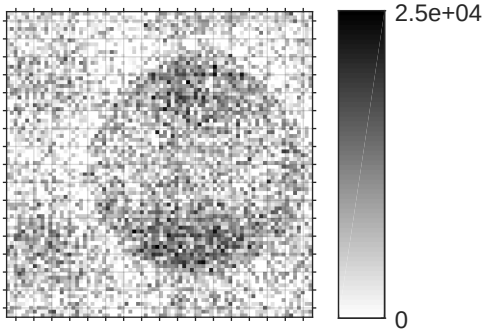

(b) $a = 8.0$ cm, centerline of RSTD

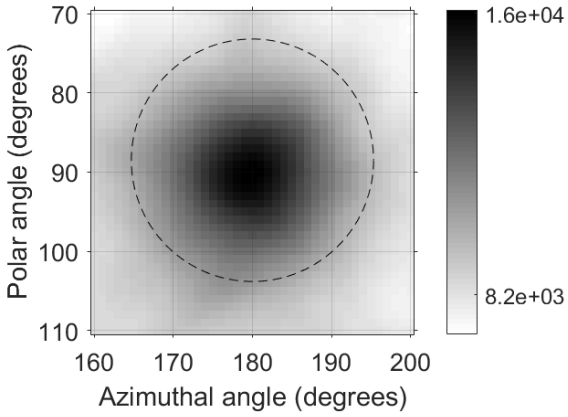

(c) Back-projection Compton image

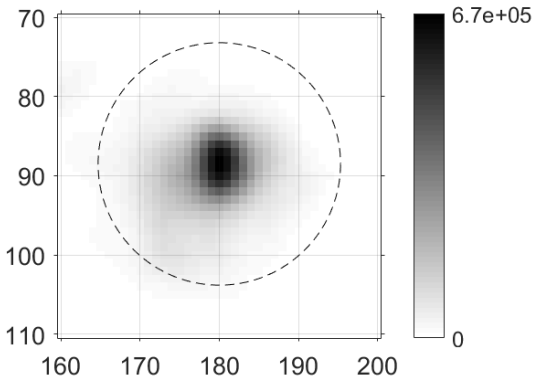

(d) ML-EM Compton image, 25 iterations

Figure 7.12: Reconstructed images of HEU (top, from 80 keV to 215 keV) and DU (bottom, at 1001 keV) portions of RSTD sphere. Dotted line on Compton images are circles centered at the maximum pixel with radius equal to RSTD's (6.3 cm or about 15°), centered at $a = 8.0$ cm. For time coded images, 2.7×10^7 1-pixel events were used, color scale is cut off at zero to improve contrast, and grid lines have 1 cm spacing.

7.3 Discussion and Conclusion

These initial time-encoded imaging results mark a substantial improvement over previous imaging capabilities for CdZnTe at low energies. The system's measured spatial resolution was consistent with predictions from geometry, and is controlled by adjusting the distance between the detector and mask. Detailed images of point-like and complex, extended objects were reconstructed with small artifacts only becoming an issue at very large source extent. The source of these artifacts is not yet understood. The 3-D distributions of objects were also successfully reconstructed and corresponded well with their true physical locations.

Furthermore, the utility of combined information from time coding and Compton imaging distinguished the RSTD object from a solid HEU metal sphere. Specifically, the time-coded image determined the HEU's size and shape, while the Compton image determined that there was a concentrated region of DU at its center. It should be noted that the imager could determine the same information from outside a so-called "black box", which is of particular interest to the nuclear security community.

The problem of artifacts appearing in images of very large, extended objects should be addressed in future work. For instance, it is often desired to get up close to an object to obtain more detail about its shape. Optimizing a mask for large objects might also be of interest since the 50% open MURA pattern used here is not optimal for large extended sources. In addition, throwing away the data during the mask travel time was done here for simplicity, however this data should be incorporated into future measurements. In fact, moving the mask continuously may be desirable for obtaining super resolution data in the far field where there is no parallax. Finally, more experiments should be performed using more advanced, statistical reconstruction algorithms to probe the spatial resolution limits of this device. In principle, spatial resolution is limited by the uncertainty of the mask positioning system, which was reported in Section 6.1 to be on the order of 10s of μm.

CHAPTER VIII

Thermal Neutron Imaging Performance

Two thermal neutron imaging experiments were performed inside the teaching laboratory at the University of Michigan, which has concrete floors, walls, and ceiling. Diagrams of each experimental setup is provided in Appendix A. To shield from room return, Polaris SP was placed inside a 1-in-thick, 5% borated polyethylene box with a 10 in $\times$ 12 in opening to allow thermal neutrons through the imaging FOV only. The opening was such that the detector's FOV tilted upward, away from the floor and out a large window to limit room return from within the FOV. The mask was about 1 in from the opening of the borated polyethylene window, and 35 cm from the detector cathodes. The setup was 30 in from the floor on a steel table. Both CdZnTe planes were operating during these experiments, with cathodes aligned in a plane and facing towards the source. The center of each 3×3 detector array was spaced 12.8 cm apart so that their Al housings were nearly touching. A photograph of the detector and borated polyethylene box is pictured in Figure 8.1(a).

The neutron source was 3.9 mCi ^{252}Cf (1.7×10^7 n/s), placed within an HDPE moderator during both experiments. The moderator was a 5-in-tall, hollow cylindrical tube, with 3-in-inner diameter and 7.75-in-outer diameter. A 3 in $\times$ 2 in cylindrical HDPE puck was used to plug the bottom of the moderator. The source was at the tip of a steel rod positioned inside the hollow opening from above using a ring stand.

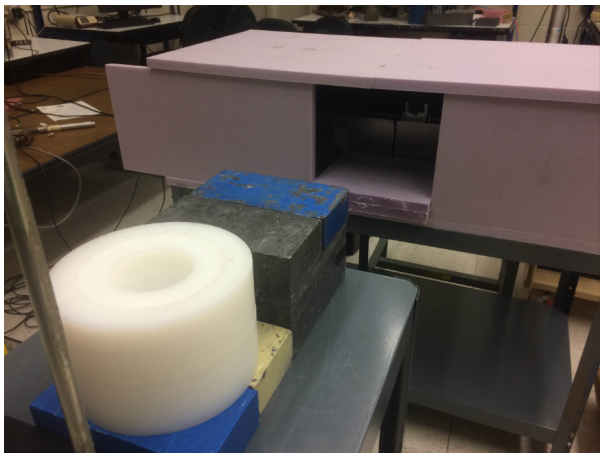

(a) Source and detector configuration

(b) Detector's perspective

Figure 8.1: Photographs of first experimental setup.

Approximately 8 in of Pb was used to shield gamma rays and fast neutrons from the direct line of sight from the source to the detectors. Two inches of Pb was used beneath the source, between the moderator and floor. The source, moderator, and shielding were all placed on a steel table 36 in above the floor. A photograph of the source from the perspective of the detectors is provided in Figure 8.1(b). Note that in practice, one should expect higher gamma-ray background with CdZnTe directly in the line of sight of ^{252}Cf with only low-Z moderator between them.

8.1 Single Moderated ^{252}Cf Source

For this initial experiment, the moderator was roughly aligned with the centerline between the two Polaris SP planes, with distance from detector to front surface of moderator about 100 cm. The moderator and shielding are pictured in Figure 8.1, where the opening to the moderator was 2 in $\times$ 4 in. A total of eight 1-h-long measurements were recorded and combined. One hour does not include the extra time taken to shift the mask between positions, which accounted for about 10 min. Count rate during the measurements was about 1640 cps, corresponding to 67% dead time.

The measured gamma-ray spectrum from one of these measurements is shown in Figure 8.2, along with a zoom on the 558 keV line used for imaging. Notice the prominent 478 keV line from boron capture in the borated polyethylene box surrounding Polaris SP. The 558 keV line is prominent for both 1- and 2-pixel events, with only slightly-degraded peak-to-background ratio for the latter. Both of these event types were used for imaging. Each neutron interaction was assumed to occur at the cathode side of the CdZnTe crystal, opposite of the anode pixel that was triggered by the 558 keV event. Two-pixel events were sequenced according to the simple comparison method described in Section 2.2.1, and the first interaction was used for event localization. Periodic correlation using the MURA pattern's decoding array was used in each case.

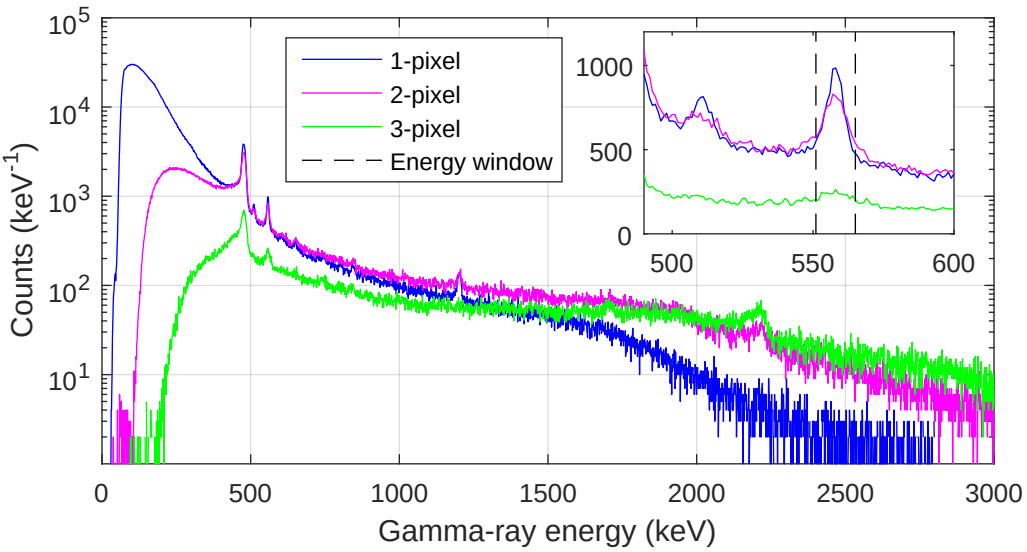

Figure 8.2: Gamma-ray energy spectra from 1 h imaging data separated by number of anode pixel triggers. Inset plot is a zoom-in on the 558-keV peak and energy window, using a linear y scale.

The first measured pattern from 8 h of data is shown in Figure 8.3(a). Upon close inspection, the pattern visually corresponds to the cyclically-shifted MURA pattern pictured in Figure 6.8(a) and used for the thermal neutron mask. The most prominent

features are the dark horizontal row of pixels centered about 6 pixels from the top of the image, and the diagonally-opposed dark spots below it, on the left and right of the pattern, the latter centered at the very bottom. The pattern is not clear because of statistics and the fact that it was projected by a slightly extended source. The reconstructed image of Figure 8.3(b) shows the correct position corresponding to the source during the measurement, and has roughly the correct size, which is wider than it is tall. On the image, the opening to the moderator should correspond to about 1×2 grid elements since they are spaced by 10 cm.

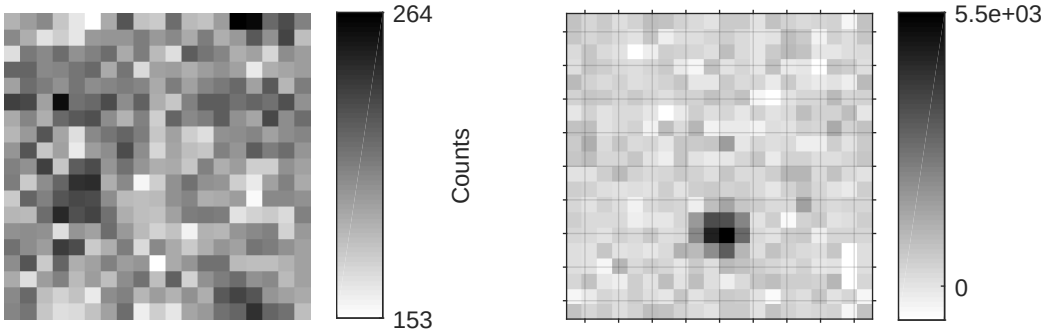

(a) Measured MURA pattern (b) Reconstructed image

Figure 8.3: Pattern and image at 558 keV from 8 h measurement, or 1.4×10^5 counts. Grid lines have 10 cm pitch.

One- and two-pixel data were then used to reconstruct images separately using the oversampling technique used for Figure 7.6. The result is shown in Figure 8.4 with comparable results, indicating both of these event types are useful for imaging. The parallax offered by the separation between CdZnTe planes offered information regarding the distance to the source. Figure 8.5 shows reconstructed images at intervals separated by 70 cm, beginning with the true mask-to-object distance $a \approx 70$ cm. The object defocuses smoothly, similar to the behavior demonstrated by the 3-D gamma-ray images of Chapter VII. Notice the defocusing occurs primarily in the direction of detector separation, or horizontally.

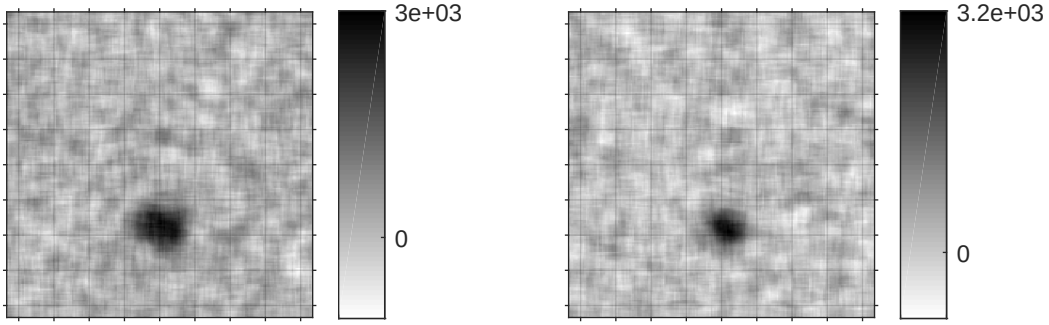

(a) 1-pixel interactions, 7.3×10^4 counts (b) 2-pixel interactions, 7.1×10^4 counts

Figure 8.4: Reconstructed, over-sampled images at 558 keV. Grid lines have 10 cm pitch.

The distance-to-source information is more plainly seen in Figure 8.6. Vertical and horizontal slices through the 3-D reconstructed image were taken at the maximum-intensity pixel. The 1-D profile through this pixel in depth was also plotted, showing a maximum near the correct mask-to-object distance at around 60 cm. This distance is actually within the lead shielding in front of the moderator, where some thermal neutrons are also being emitted. The apparent bending and smearing of intensities in the vertical and horizontal image planes is due to the nature of the pixelated intensities at the mask plane, and the fact that the true x and y image coordinates increase as a function of depth due to the diverging FOV. Hence, the y-axis label is not absolute position, but image-pixel number.

In Section 4.1.3, it was demonstrated that thermal neutron capture events can be separated from gamma-ray background based on their depth of interaction. Furthermore, Equation 3.18 shows that the spatial distribution of 558 keV interaction locations spreads out as a function of distance from the cathode. So, selecting events near the cathode for imaging should increase the ratio of neutron to gamma-ray background events selected for imaging and improve spatial resolution of the image. Of course, there is a statistical tradeoff since some neutron events are thrown away as a

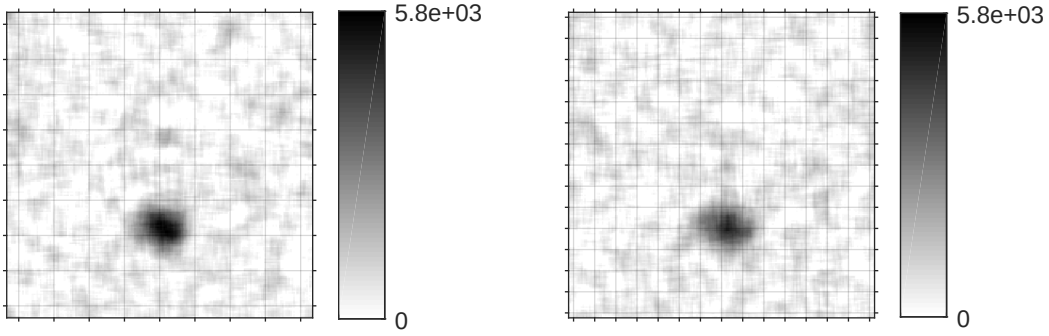

(a) $a = 70$ cm, true distance

(b) $a = 140$ cm

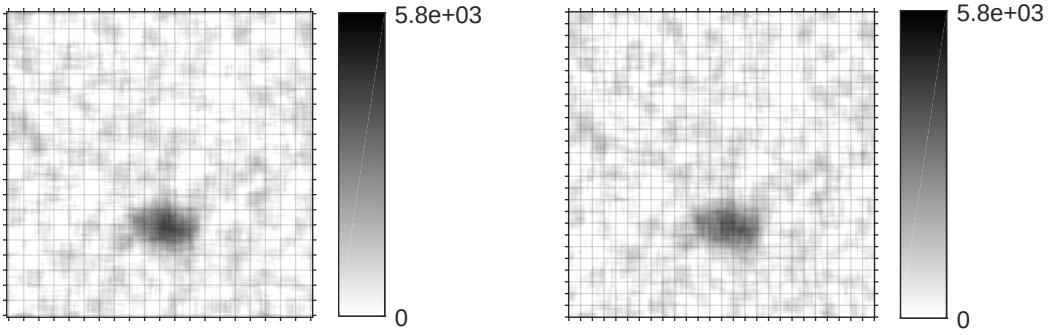

(c) $a = 210$ cm

(d) $a = 280$ cm

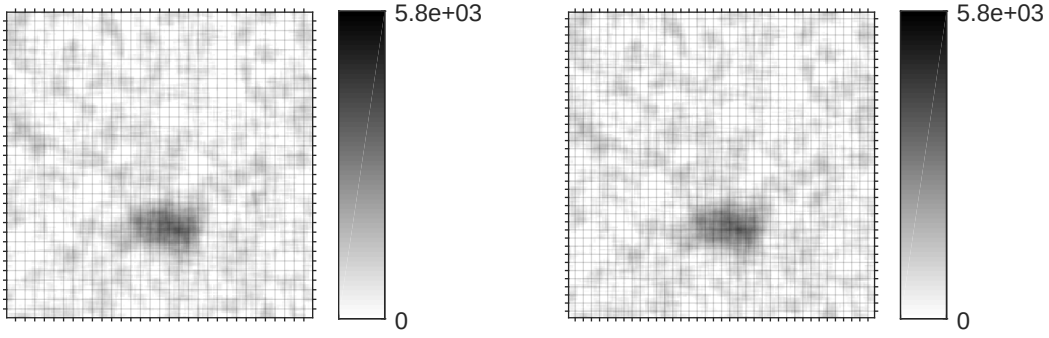

(e) $a = 350$ cm

(f) $a = 420$ cm

Figure 8.5: Reconstructed images at different object distances away from the mask, a. Both 1- and 2-pixel, 558-keV interactions were used for each image, in total 1.4×10^5 counts. Color scaled is cut off at zero to improve contrast. Grid lines have 10 cm pitch.

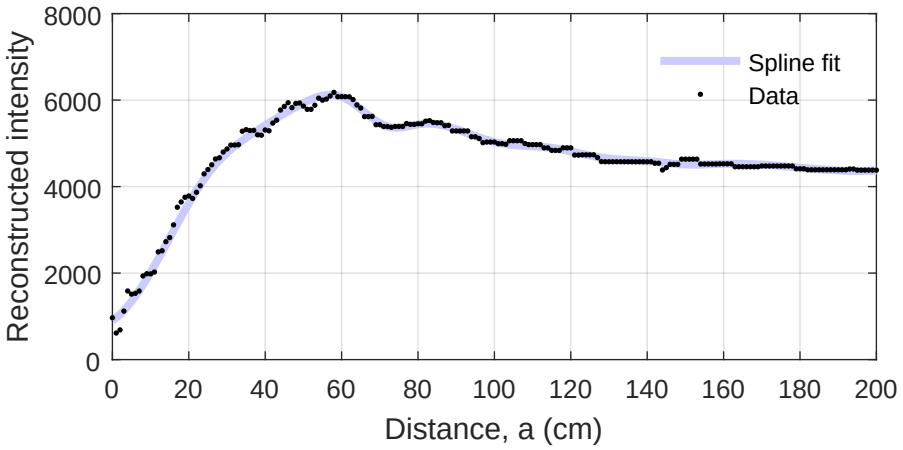

(a) Depth distribution of intensity through maximum-intensity pixel

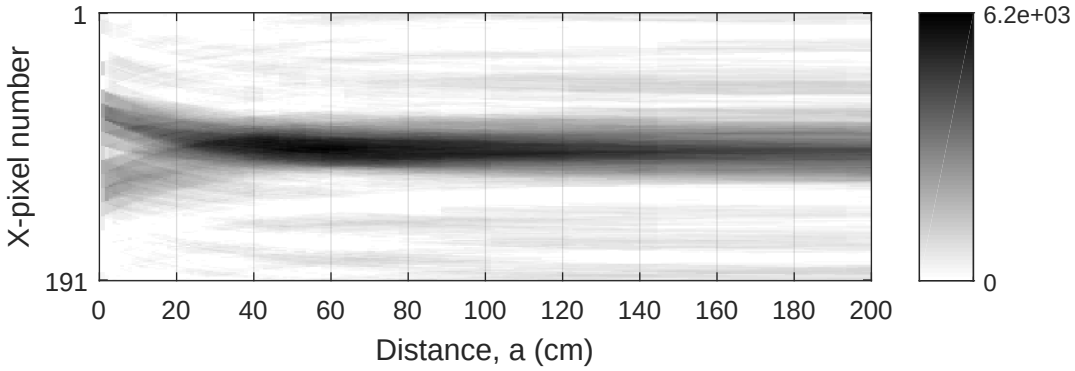

(b) Vertical slice through maximum-intensity pixel

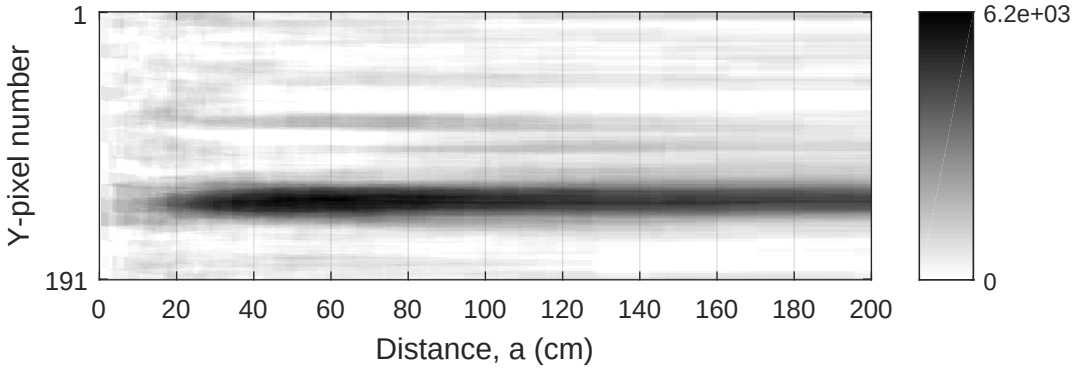

(c) Horizontal slice through maximum-intensity pixel

Figure 8.6: Reconstructed intensities at 558 keV as a function of distance from the mask, a, using 1.4×10^5 counts. White dashed lines intersect maximum intensity pixel.

result of event filtering.

However, only modest improvements in spatial resolution should be expected at this distance. The projected size of the mask pattern, which has element pitch p_m = 1.6 cm, scales with the magnification of the setup, which is $m = 1 + b/a \approx 2$ in this case. So, the projected mask element pitch is about 3.2 cm, and according to Figure 6.6, only about 20% of the measured 558 keV imaging signal is lost to neighboring elements. Given the noisiness of the image in Figure 8.3(b), it is unlikely that a reduction in this signal's already-modest spread would be visually noticeable.

The images of Figure 8.7(a) and Figure 8.7(b) are similar in terms of spatial resolution, but the SNR using interactions between 10 to 14 mm from the anode is clearly higher. Furthermore, vertical image slices in Figure 8.7(c) and horizontal slices in Figure 8.7(d), which are normalized to total counts, confirm that there was larger relative intensity attributed to the hot spot for events closest to the cathode. Figure 8.7(e) also shows that larger peak-to-background ratio was achieved for the 558 keV peak for events closest to the cathode, suggesting that neutron-gamma discrimination provided the improvement.

The FWHM of the 10 to 14 mm peak in Figure 8.7(c) and Figure 8.7(d) are 10.4 and 11.5 cm, respectively. Assuming that the actual emission distribution corresponded to the 2 in $\times$ 4 in window to the moderator in the Pb shield and the width of this distribution summed in quadrature with spatial resolution, the spatial resolution in the vertical and horizontal directions were 9.1 cm and 5.4 cm, respectively. The mismatch is likely due to the statistical fluctuations that underly the image, however both are likely overestimates due to the diffuse shape of the actual source due to leaking neutrons from the shield. The average spatial resolution is 7.3 cm, or roughly 4°.

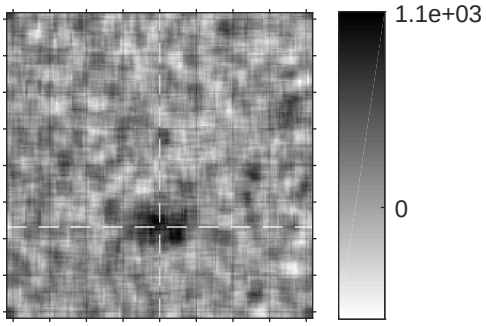

(a) Depths 2 to 6 mm, 3.6×10^4 counts

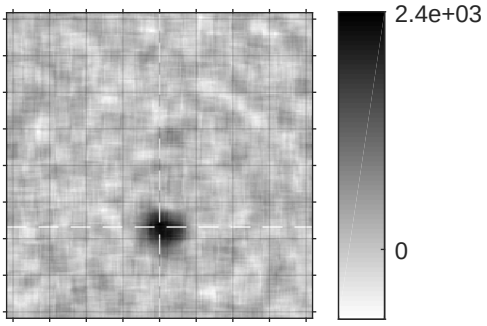

(b) Depths 10 to 14 mm, 3.9×10^4 counts

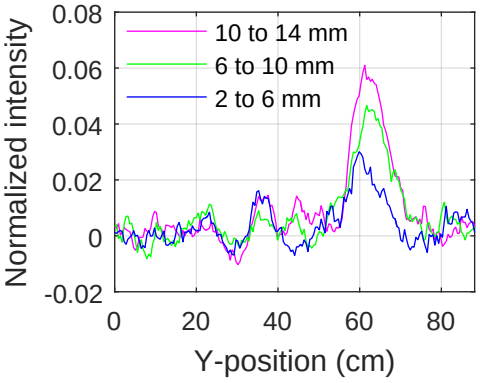

(c) Vertical slices through hot spots

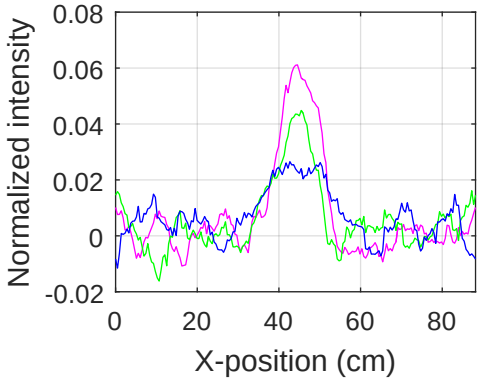

(d) Horizontal slices through hot spots

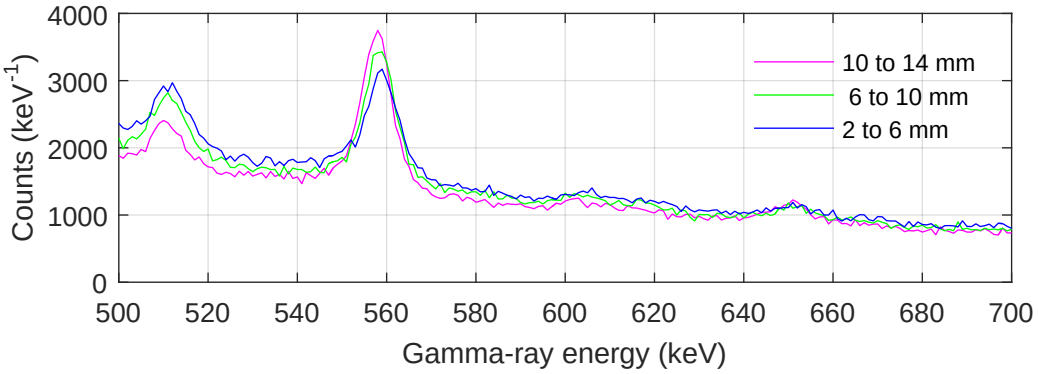

(e) Measured gamma-ray energy spectra

Figure 8.7: Images at 558 keV reconstructed via correlation using events from different depths away from the anode. (a) Between 2 mm to 6 mm from anode. (b) Between 10 mm to 14 mm from anode. (c) Vertical image slices. (d) Horizontal image slices. (e) Energy spectra for different depths. White dashed lines in (a) and (b) mark locations of image slices for (c) and (d). Grid lines in (a) and (b) have 10 cm pitch.

8.2 Two Moderators and ^{252}Cf Source

The goal of the next experiment was to show that it is possible to separate and count multiple sources within the imaging FOV. The setup was similar to that of Section 8.1, except that there were two moderators with shielding. The same ^{252}Cf source was used at each location, one at a time, and the results summed. Both moderators and shielding, however, were present during each measurement. A photograph of the setup is provided in Figure 8.8(a) and a diagram is provided in Appendix A. One moderator was approximately 100 cm from the detector plane, similar to the first experiment, and the other was about 70 cm away. They were separated by 26°, each roughly the same angular distance from the center of the FOV, or about 13°. As a point of reference, the angular extent of a single square mask element was about 2.6°, and the entire FOV was roughly 50° on a side.

In an attempt to reduce the solid angle of the sources, the Pb shielding was arranged such that the windows to the moderators were smaller than the first experiment. A photograph was taken with the camera lens positioned roughly at the center point between the two detectors, looking through the opening in the borated polyethylene box. The photograph is provided Figure 8.8(b), in which the 2 in × 2 in regions of exposed moderator can be seen.

The nearer source was raised 8.3 cm higher than the other source on a hollow aluminum box. The higher elevation was meant to provide a more interesting variety of emission locations within the FOV, however there were some possible side effects. The MFP of thermal neutrons in Pb exceeds 1 in, while each Pb brick was 2 in × 4 in × 8 in. It's possible that the nearer perspective exposed the detector to a greater solid angle of leaking neutrons, beyond the intended 2 in × 2 in region of moderator.

Images reconstructed separately for each source are shown in Figure 8.9. The count rate while the source was in the far moderator was 1430 cps, compared to 1714 cps in the near moderator. This led to a ratio of live times of about 1.4. To balance

(a) Moderator configuration (b) Detector perspective through FOV

Figure 8.8: Photographs of second experimental setup.

the number of counts from each measurement so their summed data corresponds to their simultaneous measurement, 8 h of measurement was taken on the left side, and 11 hours on the right. Each was split into 1 h measurement intervals, excluding the mask movement time.

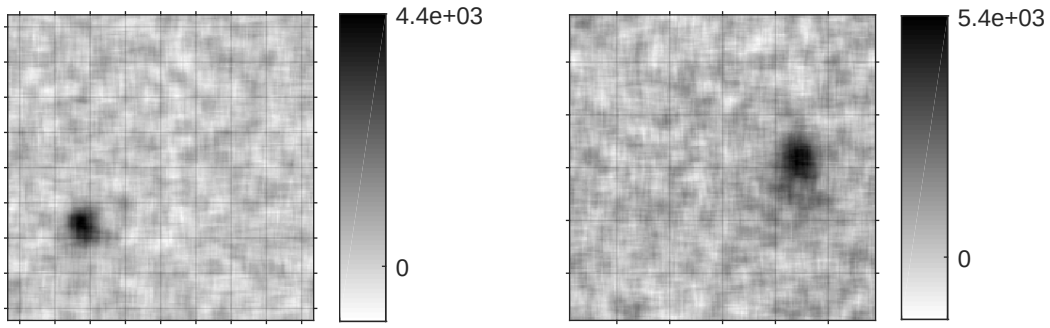

(a) Source in far moderator, 1.0×10^5 counts (b) Source in near moderator, 2.1×10^5 counts

Figure 8.9: Images reconstructed from separate data from near and far moderators, each using the 558 keV gamma-ray signal. Image grids have 10 cm pitch.

The combined reconstructions are shown in Figure 8.10. The sources are brightest in their correct, respective planes away from the mask. The defocusing effect is also somewhat smooth and without significant additional artifacts. A more advanced reconstruction algorithm such as ML-EM or SOE may be able to deconvolve these

objects in the depth dimension to more accurately determine their 3-D distribution, as their distribution from correlation alone is still very broad.

For comparison, a back-projection Compton image at 2.2 MeV (^{1}H capture in HDPE) was reconstructed and plotted using UMImaging with default settings [13]. The image using 2-, 3-, and 4-pixel events is shown in Figure 8.11. Only events from plane B were used because plane A performed significantly worse, however there are enough counts that statistical fluctuations are minimal. The sources are physically separated by about 26°, however the spatial resolution of each hot spot is about 35° FWHM. The result is that the near source overwhelms the far source, and the far source is barely noticeable as an asymmetry to the near source's hot spot, to its upper right.

Although the spatial resolution is significantly worse than the thermal neutron image, much of the background is directed away from the cathode-facing directions, removing it from the directions of interest. The background is seen as the orange vertical and horizontal bands at the extremes and center of the image. The contrast within the region of interest would be improved by ignoring this background region, and a more advanced deconvolution algorithm such as ML-EM or SOE may reveal the second source at the cost of additional statistical fluctuations. Hence, the worth of the 2.2 MeV image relative to the thermal neutron image for determining the shape of a hydrogenous moderator is uncertain.

8.3 Images from ^{3}He Tube

To corroborate the imaging results from CdZnTe, a ^{3}He tube was placed inside the box near Polaris SP during the second set of experiments. ^{3}He was chosen since it is relatively insensitive to gamma rays. The spectrum from the tube was saved every 1 s for each 1 h measurement, during which the mask paused for about 10 s at each position. Hence, the 1 s integration time added a small, but insignificant amount of

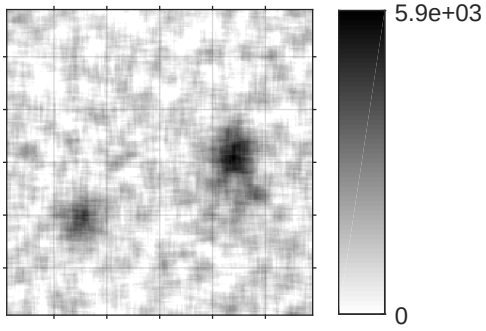

(a) $a = 35$ cm, right source true distance

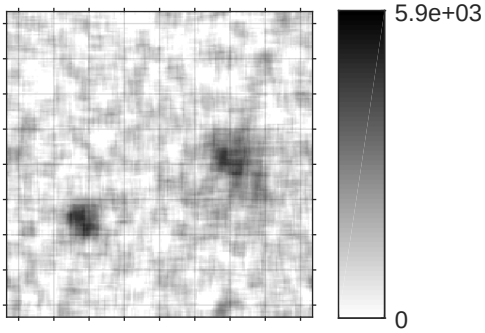

(b) $a = 70$ cm, left source true distance

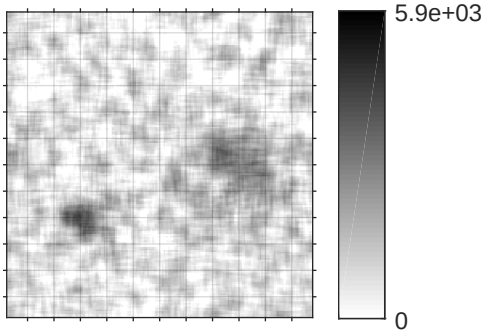

(c) $a = 105$ cm

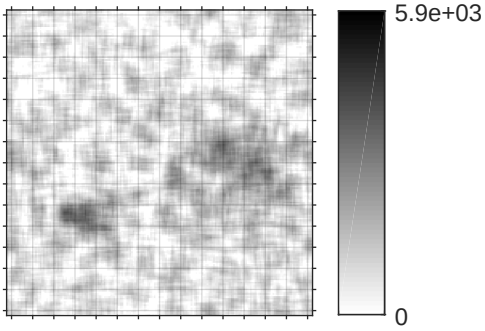

(d) $a = 140$ cm

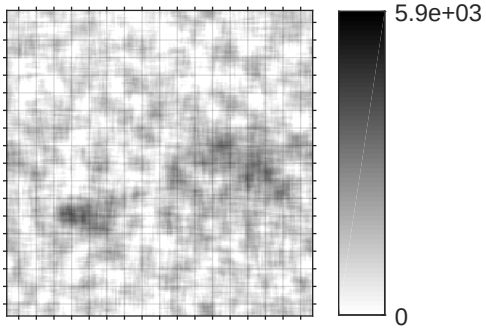

(e) $a = 175$ cm

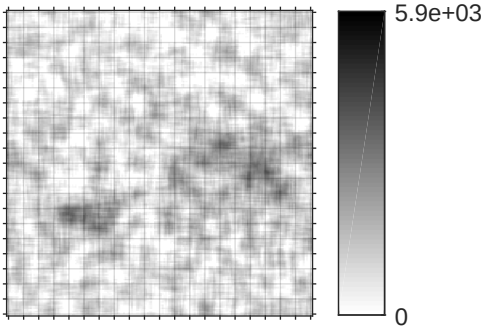

(f) $a = 210$ cm

Figure 8.10: 558-keV images reconstructed at different distances from the mask, a, using 3.2×10^5 counts. Color scale is truncated at zero to improve contrast, and grid lines have 10 cm pitch.

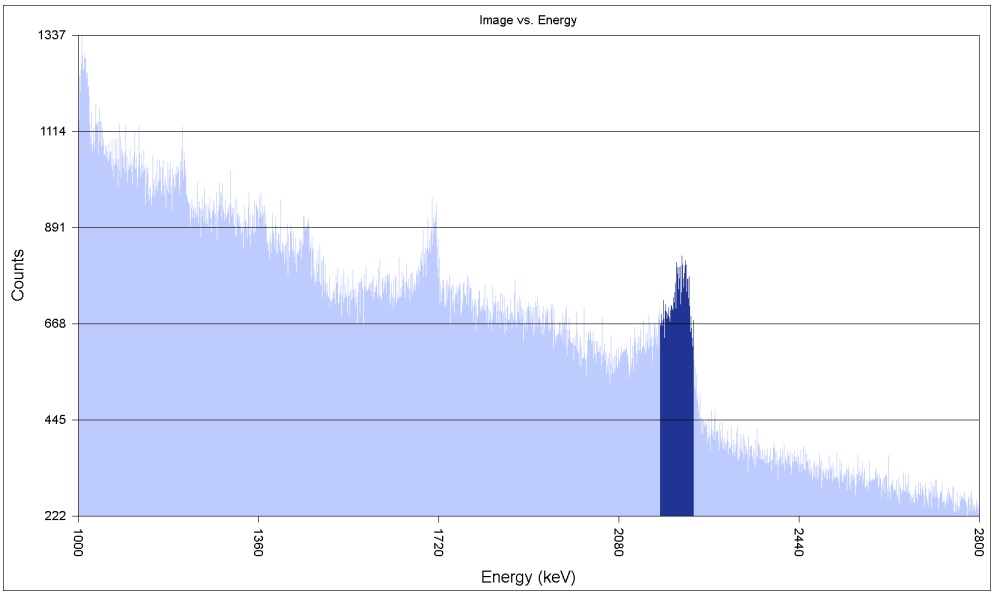

(a) Gamma-ray energy spectrum with imaging window

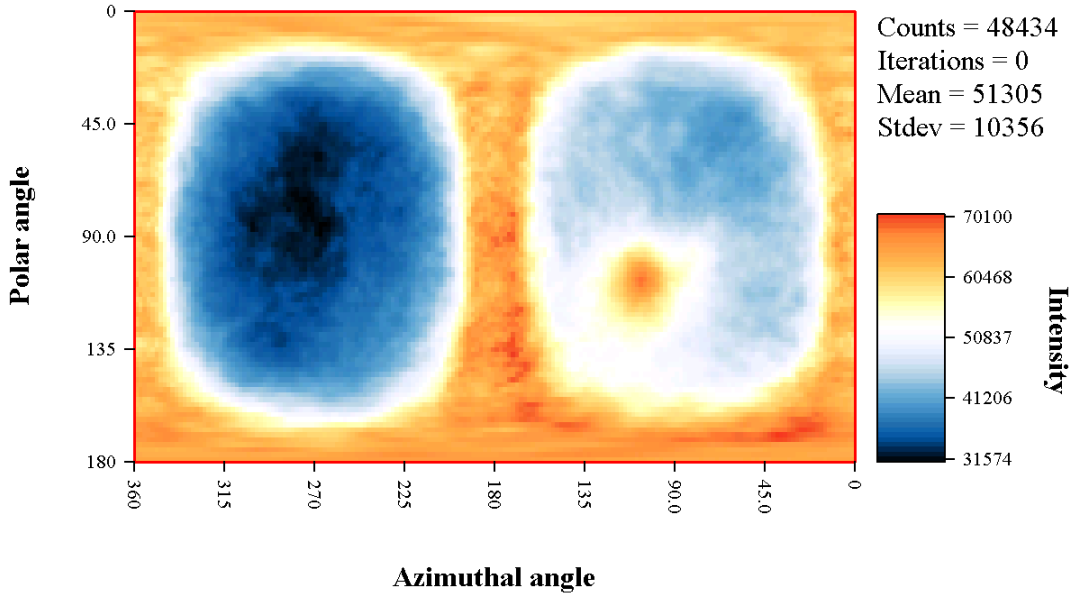

(b) Back-projection Compton image at 2.2 MeV

Figure 8.11: (a) Gamma-ray energy spectrum and (b) back-projected Compton image at 2.2 MeV from UM Imaging [13]. Sources are centered at about 100° azimuthal and 110° polar. Note that in this plot, 180° polar is straight up from the detector and 0° polar is down, so the image appears to be vertically flipped relative to the neutron images.

blur to the resulting image. In total, 8 h of data from each of the two source positions was used since the detector dead time in each case was comparable.

The ^{3}He tube was the same one used for the efficiency experiment in Section 4.2, and operated at the same settings from Table 4.1. The tube had 1 in active diameter, and 5.9 in active length. Figure 8.12 shows the He-3 tube and Polaris SP before the borated polyethylene box was constructed. The ^{3}He tube was positioned roughly perpendicular to the cathode planes of Polaris SP, clamped above using a ring stand on its side, as shown in Figure A.3. The moderators were at angles of about $\pm 13°$ from perpendicular, such that the sides of the tube were exposed to the sources. The blur added to the image from the tube's active length was likely the most important factor for image blur in the result.

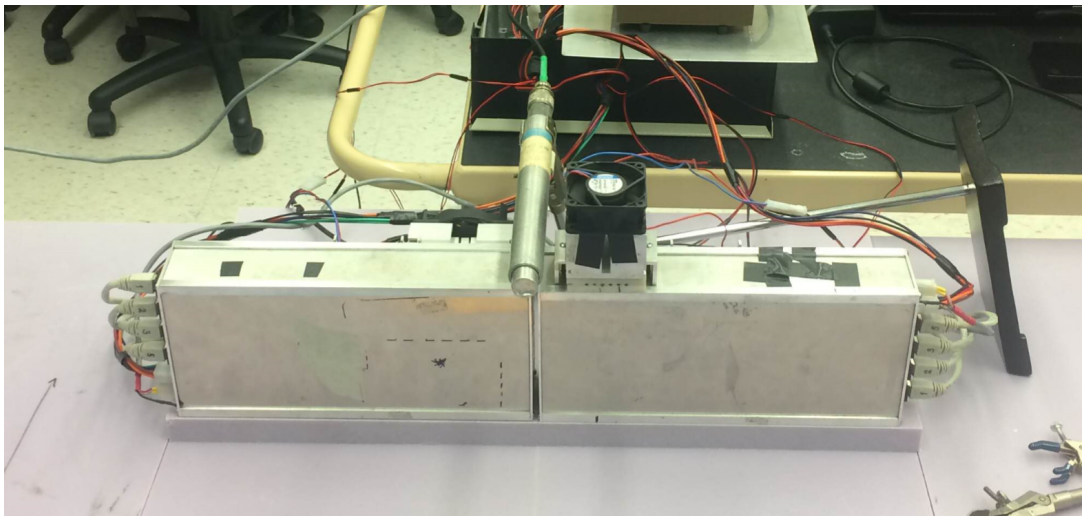

Figure 8.12: Polaris SP and ^{3}He tube positioned above. Photograph was taken prior to constructing the borated polyethylene box for the second experiment.

The recorded patterns and reconstructed images of Figure 8.13 correspond well to measured results from CdZnTe. During the measurements of the near source, the temperature inside the borated polyethylene box was steadily increasing, apparently causing a drop in count rate in the temperature-sensitive ^{3}He tube. The resulting vertical artifact on the right of the image was not present in the later measurements,

after an AC unit was introduced and the temperature stabilized. Overall, the ^{3}He image has better SNR compared to CdZnTe because of its higher detection efficiency and insensitivity to gamma rays.

Interestingly, the near source has a larger size than the far source and diffuse shape, similar to that of Figure 8.9(b). The near source also has larger solid angle due to its proximity; the ratio of solid angles 1.5, which corresponds well to the relative sizes of the objects in the image. This result also suggests that the difference in size of the objects in the images of Figure 8.9(b) is primarily from the actual distribution of thermal neutrons rather than blur from CdZnTe.

Furthermore, it is unlikely that the relative sizes of the sources is attributable to the ^{3}He tube's extent. Both sources are positioned at roughly equidistant angles away from the ^{3}He tube's axis, so the detector has the same aerial exposure to each. The source that is farther away has magnification $m = 1.5$, while the nearer source has magnification $m = 2.0$, corresponding to projected element pitches of 2.4 in and 3.2 in at the detector plane, respectively. If geometric blur from the detector is significantly contributing to each source's extent, the farther source should be blurrier, because its projected pattern is 25% smaller than the nearer source. The nearer source is only at about 3° degrees inclination from the ^{3}He tube, so vertical blur should be relatively small.

8.4 Signal-to-Noise Ratio

SNR was calculated as a function of measured counts for the first data set (single moderator) and for second data set using only data from the farther moderator. In both of these, the source was roughly the same distance away and in the same setup, but the actual measurements were taken about two weeks apart. Furthermore, in the first data set, the source was centered in the FOV, while in the second data set, the source was toward the left side of the FOV. See Appendix A for more details on the

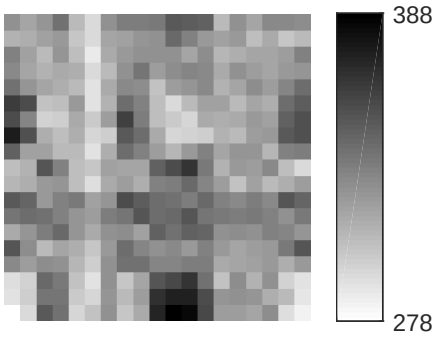

(a) Far source pattern, 1.2×10^5 counts

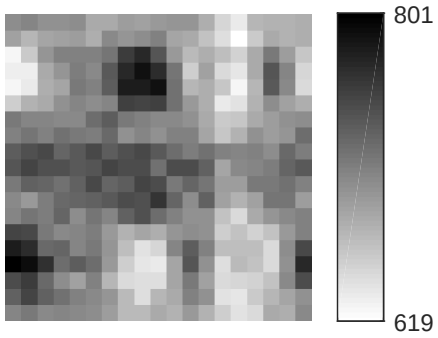

(b) Near source pattern, 2.5×10^5 counts

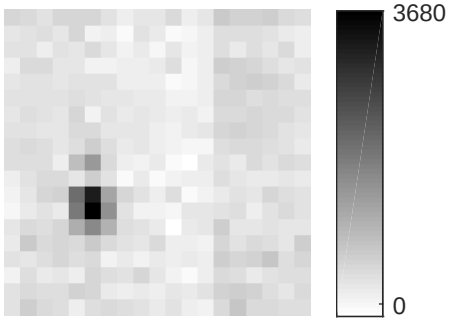

(c) Far source image

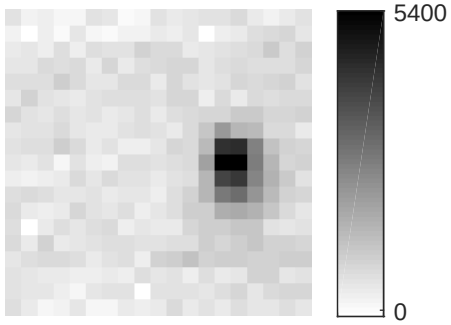

(d) Near source image

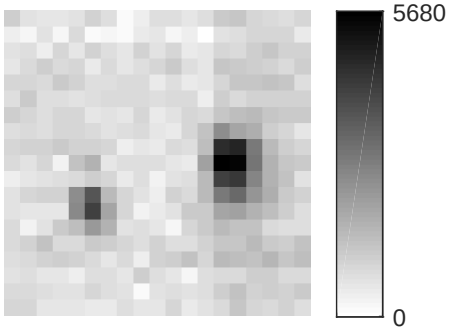

(e) Combined image, 3.7×10^5 counts

Figure 8.13: Measured patterns and reconstructed images using ^{3}He tube during measurements of Section 8.2. Each image pixel subtends a $2.6° \times 2.6°$ solid angle.

experimental setups.

In both cases, the 19×19 pixel image was divided into signal and noise regions. The signal region was defined as the pixels within two pixels vertically and horizontally of the hot spot, while the noise region was all other pixels. The broad signal area accounted for both the nonzero extent of the source and blurring from 558 keV gamma rays in CdZnTe. The image signal was then defined as the sum of intensities within the source region minus the average level of the noise region. The image noise was defined as the standard deviation of the noise region, and image SNR was the ratio of the two values.

The result is plotted in Figure 8.14. For both measurements, 8×1 h data sets were recorded, so the SNR and number of counts were averaged at 1, 2, and 4 h such that there was no double-counted data for any data point in Figure 8.14(a). In other words, the eight individual, 1-h data set SNRs were averaged for the first data point (lowest number of counts), then each 1 h data set was placed into pairs to form four unique 2-h SNRs, then two 4-h SNRs. Including the 8 h data set, this generated four data points to fit each curve. Notably, the trend of SNR $\propto \sqrt{\text{counts}}$ indicated by Equation 5.17 fits well with the observed data.

To examine whether the magnitude of measured SNR agrees with expectation, there must be a background estimate. While preparing for the first measurement, the FOV was covered with a 1-in-thick sheet of borated polyethylene. Including the borated polyethylene box, Polaris SP was completely surrounded with borated polyethylene, with only a small crack (< 1 cm) to let wires in through the back. The count rate within the 558 keV window (551 to 565 keV) in this configuration was $R_{\text{encl}} = 11.9$ cps, reduced from $R_{\text{open}} = 28.5$ cps with the FOV open. By observing the reduction in the continuum level with the added shielding, it was also estimated that $R_{\gamma\text{encl}} = 1.54$ cps from gamma rays were blocked. An additional measurement was taken by placing the borated polyethylene sheet (12 in $\times$ 12 in) in front of the

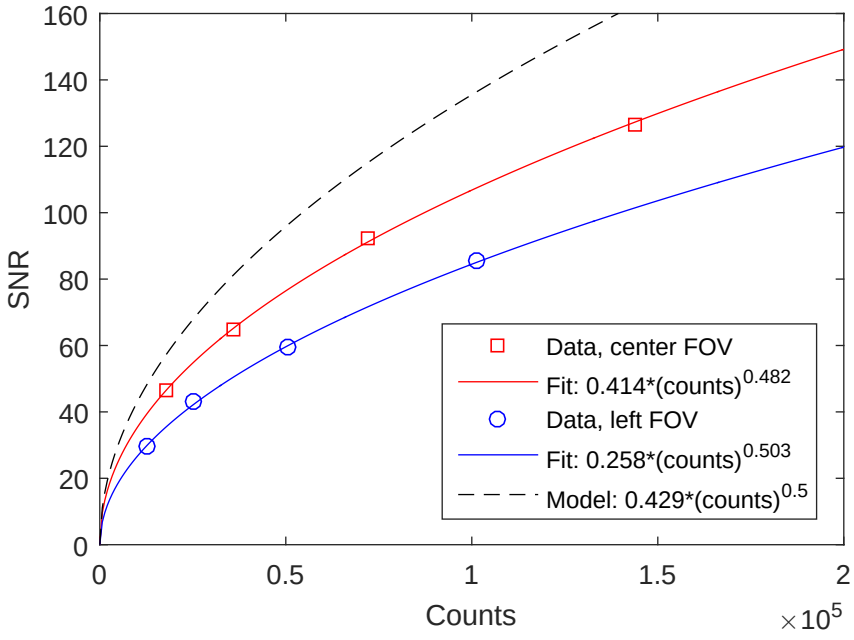

(a)

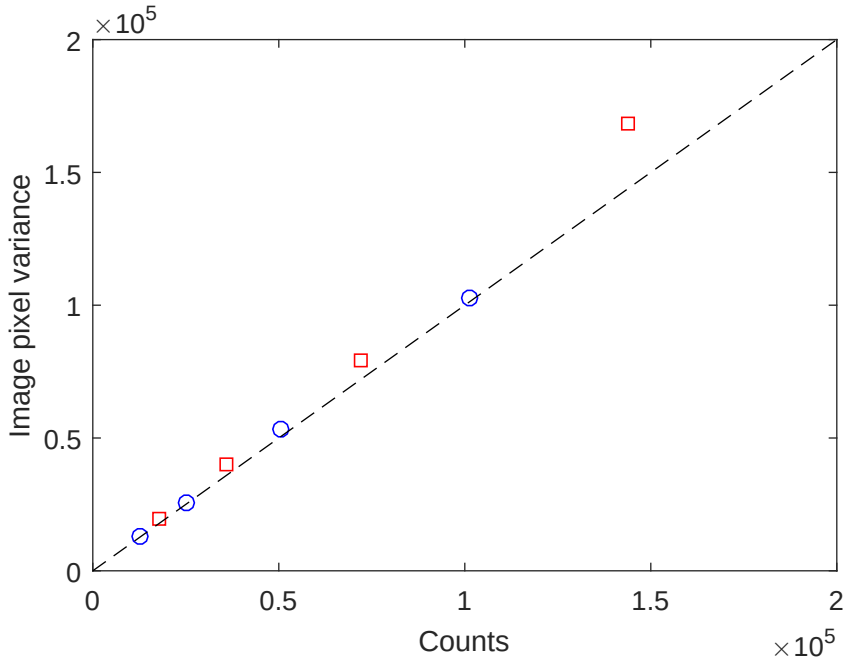

(b)

Figure 8.14: (a) SNR versus counts for first and second data sets, as described in the text. Theory is based on a background estimate made during the first set of measurements and Equation 5.17. (b) Variance of pixels outside of the source region versus number of counts. Dashed line is variance equals counts.

source, moderator, and shielding setup. The moderator's solid angle was entirely covered from the detector's point of view, and 558-keV count rate in this setup was $R_{\text{mod}} = 16.7$ cps. About $R_{\gamma\text{mod}} = 0.65$ cps from gamma rays were blocked by the shield.

The fact that $R_{\text{mod}} > R_{\text{encl}}$ implies that there is room return within the FOV that is not coming directly from the HDPE moderator and shielding. This can be modeled as additional source intensity outside the region of interest, or $\psi < 1$ in Equation 5.17. This parameter was roughly estimated from the previous measurements using $\hat{\psi} = (R_{\text{open}} - R_{\text{mod}} - R_{\gamma\text{mod}})/(R_{\text{open}} - R_{\text{encl}} - R_{\gamma\text{encl}}) = 0.72$, which is the ratio of source counts from the moderator to source counts from the entire FOV. The fractional background rate of Equation 5.17 was then estimated using $\hat{\xi} = (R_{\text{encl}} + R_{\gamma\text{encl}})/(R_{\text{open}} - R_{\text{encl}} - R_{\gamma\text{encl}}) = 0.90$, which is the ratio of counts from background to counts from the total source term. At 0.0253 eV, the theoretical fraction of streaming thermal neutrons through 1 mm BN is $f = 0.033$. Using Equation 5.17 and the aforementioned estimated parameters, SNR during the first measurement was predicted to approximately follow the trend $\text{SNR}(\text{counts}) \approx 0.43\sqrt{\text{counts}}$.

The result of Figure 8.14(a) shows order-of-magnitude agreement between measured and theoretical SNR for the first measurement, and reasonable agreement with the second measurement given the difference in setups. Figure 8.14(b) shows that the variance of the pedestal region of the image in the second setup increases at a faster rate than the sum of all counts, corroborating the hypothesis of additional structure from room return in the background of the image. The setup was moved closer towards the window in an attempt to reduce room return during the second measurement, which resulted in a variance trend that more closely followed the sum of counts, shown in Figure 8.14(b), which suggests that room return within the FOV was indeed reduced. These results indicate that the model of Equation 5.17 is at least a useful tool for roughly estimating time-encoded thermal neutron image SNR, and

that more work should be done to more precisely verify the model to predict count times in the future.

8.5 Discussion and Conclusion

Time-encoded thermal neutron imaging was successfully demonstrated here for the first time. The relative sizes and locations of moderators were consistent with measured values, and perhaps most convincingly, corresponded well with the image from an ^{3}He tube placed behind the mask during the second set of measurements. The results show smooth defocusing of the source in the dimension away from the mask, in contrast to traditional coded aperture approaches. There was also indication that these images can be further improved by neutron-gamma discrimination. It was also shown that a simple theory for SNR is predictive during actual measurement, which suggests it may be used to project imaging performance for other scenarios.

While background was suppressed by means of shielding in this work, more practical solutions should be devised in the future. The borated polyethylene box used to block room return was obviously cumbersome. This could be replaced by a thin boron layer on the outside of the detector housing, for instance. Gamma-rays directly from a spontaneously-fissioning source are also problematic because they generate substantial gamma-ray background. This further motivates the need for neutron-gamma discrimination in CdZnTe.

The SNR reported in Figure 8.14 includes all intensity in the broad distribution of the source. In contrast, the average SNR of the two hottest pixels at 10^5 counts in both measurements is about 10. Since the signal was roughly $10\times$ larger when including neighboring pixels, this indicates roughly 80% of the signal was outside the intended location, i.e., the opening to the HDPE moderator. In terms of solid angle, the scattering material surrounding the opening was about 10 image pixels in size, roughly consistent with the signal's apparent spread.

The primary challenges to thermal neutron imaging with CdZnTe seem to be detection efficiency and background. While efficiency can in principle be improved by around 50% when including all combinations of interactions based on results from Section 4.2, this only increases SNR by about 20% or less, due to added background. The primary means for improving detection efficiency, is therefore adding detectors to the array. Background, on the other hand, must be addressed by using thermal neutron absorbers and neutron-gamma discrimination.

It's useful to make a few approximations to examine the usefulness of an 18-detector array of CdZnTe for thermal neutron imaging in practice. The previous measurement was non-ideal in that the actual thermal neutron source was extended, requiring integration of several image pixels to obtain a reliable estimate of the total signal. However, if the source was truly a point source, all of the signal intensity would be contained within a single image pixel. This, of course, assumes no blurring from 558 keV gamma rays or detector extent. This is a safe assumption on the near field, which is a useful scenario for some applications.

Assuming the same background ratio estimated in Section 8.4, in theory the number of counts necessary to achieve SNR = 10 for a point source in the near field without room return is roughly 400. In the setup of the first experiment, the count rate within the 558 keV window was 5 cps, meaning that about 80 s of measurement time would be required to see a hot spot. As an aside, dead time during the measurement was around 67%, which could feasibly be improved.

Measurement time increases with the solid angle of the source, squared, assuming uniform intensity across the source. Hence, a more realistically-sized moderator under the previous conditions and spanning 16 pixels would require about 5.7 h to resolve. However, this measurement time is also heavily dependent on the type of source, emission rate, shielding material, and proximity. These factors, including background, all govern measurement times and must be considered for any particular

case. However, it should be noted that these results indicate that imaging times are not always prohibitively long, and that there is some potential for practical use of thermal neutron imaging with CdZnTe. The author suggests further studies on SNR to investigate the use of CdZnTe more realistic imaging scenarios.

CHAPTER IX

Summary and Future Work

9.1 Summary

Time-encoded thermal neutron imaging using large-volume pixelated CdZnTe was successfully demonstrated here for the first time. A 19×19 MURA-based pattern of 1-mm-thick BN tiles was used to achieve roughly 4° angular resolution within a 50° FOV. Two 3×3 planes of CdZnTe detectors were used, each 2 cm $\times$ 2 cm $\times$ 1.5 cm. A model for image pixel SNR was also validated by measurement, enabling future investigations on SNR for more specific applications.

One notable challenge for thermal neutron imaging with CdZnTe is suppression of gamma-ray background and room return. While the latter can be addressed using thermal-neutron-absorbing shielding around the detector housing, gamma-ray background is difficult to shield and is always present where there are neutrons. However, various spatial features of gamma-ray events were used here to separate Cd-cascade from background gamma rays. An initial study showed that interactions near the detector surface facing the source provided superior image SNR to other interactions in the bulk. This work paves the way for more sophisticated algorithms such as statistical classification as a means for neutron-gamma discrimination beyond energy windowing.

Although conventional Cd-based neutron detectors are not ideal with regards to

detection efficiency due to the multiplicity and energy distribution of the cascade, signals from coincident interactions in pixelated CdZnTe can be read out separately. Therefore, coincident gamma rays can be individually counted rather than strictly their sum contribution. For a 3×3 array of pixelated CdZnTe, we found that coincident events accounted for about one third of events at 558 keV. Including these events, the measured detection efficiency agreed with calculations without losses from coincidence, and was comparable, per solid angle, to a nominal, 1-in-diameter BF_3 tube.

Prior to the investigation of thermal neutron imaging, the time-encoding system developed for this work was demonstrated using gamma rays and a 1.4-mm-pitch, 79×79 MURA-based W mask. The result was high-resolution gamma-ray images with good uniformity; 0.28° angular resolution within a 22° FOV was demonstrated experimentally. Some artifacts were observed for large extended sources, which are still under investigation. However, these initial results demonstrate the advantage of time coding for pixelated CdZnTe arrays. It confirms the assertion that these systems are quite uniform in terms of their performance as a function of time, and are free from the spatial constraints of coded aperture.

Overall, this work has two main outcomes. First, that thermal neutron imaging with pixelated CdZnTe is possible, and its usefulness for specific applications warrants further investigation. The other is that time-encoded imaging is helpful for imaging with pixelated CdZnTe in general, which tends to be limited by detector spatial extent, resolution, and uniformity. This conclusion does not only apply to pixelated CdZnTe, but to any imaging system that has these spatial limitations and is used to image stationary objects.

9.2 Suggestions for Future Work

The work here is a preliminary demonstration of thermal neutron imaging for pixelated CdZnTe. There are numerous ways to improve upon these experimental results, such as constructing a better-defined thermal neutron source and employing the neutron-gamma discrimination techniques described here. Further work should be done on refining these techniques; some basic spatial features of events are suggested for classification in Section 4.1.3. Furthermore, only two very basic configurations were attempted, and a precise measurement of spatial resolution has yet to be performed.

As an alternative to using the Cd capture reaction for detection, the author suggests investigating the use of another converter material near the surface of CdZnTe, particularly one that results in the emission of an energetic charged particle of MeV-range energy. Not only would this be much easier to discriminate from order 100-keV gamma rays commonly experienced from background, but position resolution from the reaction would be far superior due to the charge particle's short range.

More work should also be done to improve the practicality of thermal neutron imaging with CdZnTe. First of all, significant improvements in gamma-ray background discrimination must be achieved to image extended sources in under an hour using an 18-detector array. In addition, large borated polyethylene shields were used to eliminate room return outside the FOV in this work. A thermal-neutron-absorbing material on the housing of the detector would be a more practical alternative. A more compact mask positioning system should also be designed, to enhance the portability of the system.

Suppressing gamma-ray background remains the biggest challenge to thermal neutron imaging with pixelated CdZnTe, and neutron-gamma discrimination is one possible, albeit challenging, solution. A statistical analysis on neutron-gamma discrimination using the spatial and energy information from pixelated CdZnTe could be done to

estimate the suppressed background rate for specific scenarios, such as finding SNM reflected by low-Z shielding. Once the suppressed background rates are established, one may estimate the expected SNR within some given measurement time using the models found in this work. This type of study should be done as a first step to gauge the worth of thermal neutron imaging with pixelated CdZnTe for any application.

Finally, time-encoded imaging for gamma rays with pixelated CdZnTe has great potential. The results presented here on gamma-ray imaging are not a complete analysis of image quality from time encoding, and were only meant as an initial demonstration of the concept. For instance, spatial resolution can in principle be pushed beyond the geometric spacing of mask elements by using super resolution, where the position resolution of the mask itself is the limiting factor. In addition, the advantages of coded imaging in the combined time and spatial domains has not been explored. Finally, there is much flexibility in the mechanical design of a time-encoding system. Although perfect imaging (flat sidelobe) response in 2-D may be difficult to achieve with a spinning mask, the trade off for a more compact device may prove to be favorable for certain situations.

APPENDICES

APPENDIX A

Experimental Setup For Thermal Neutron Imaging

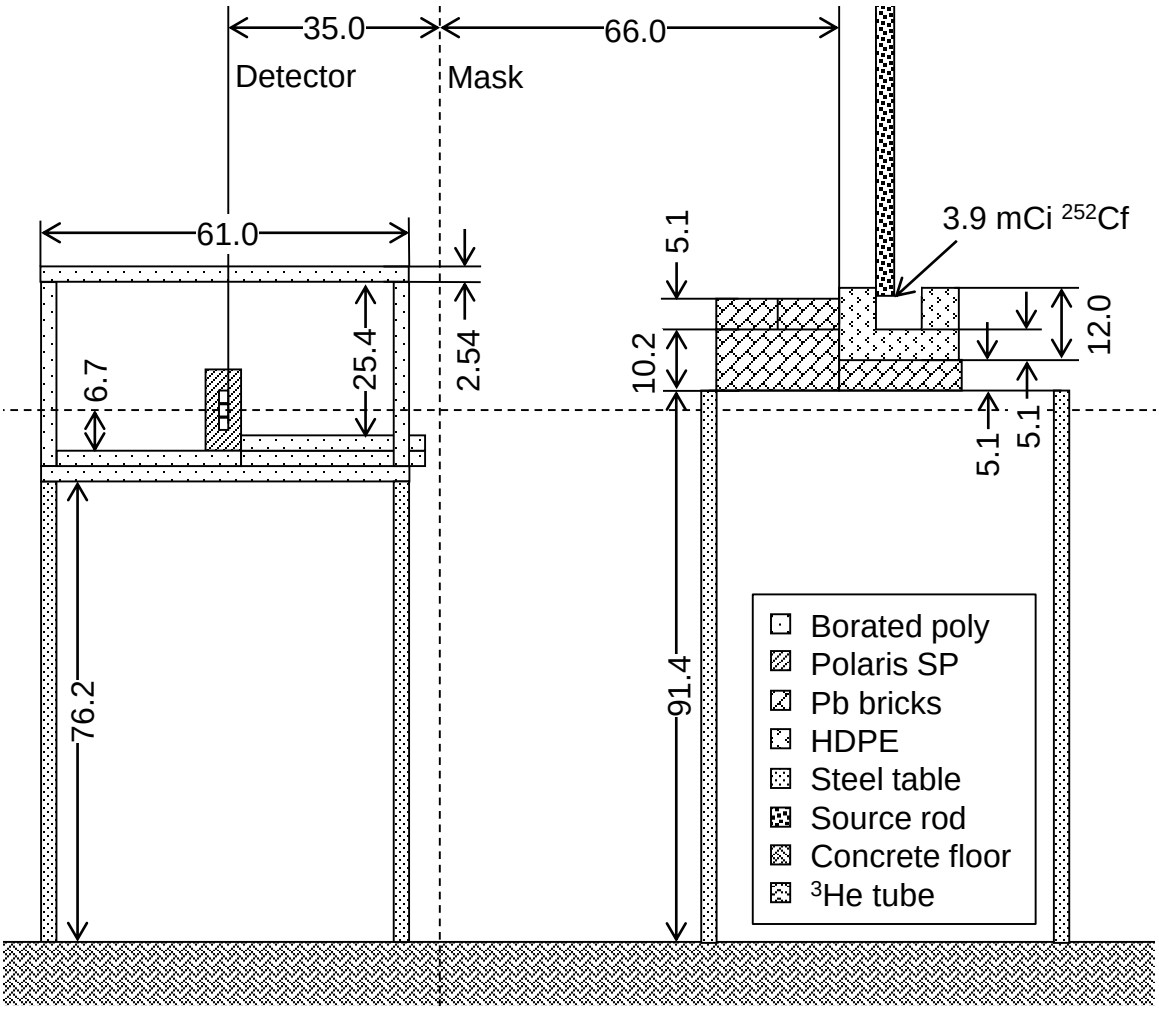

Figure A.1: Side view, single moderator. All lengths in cm.

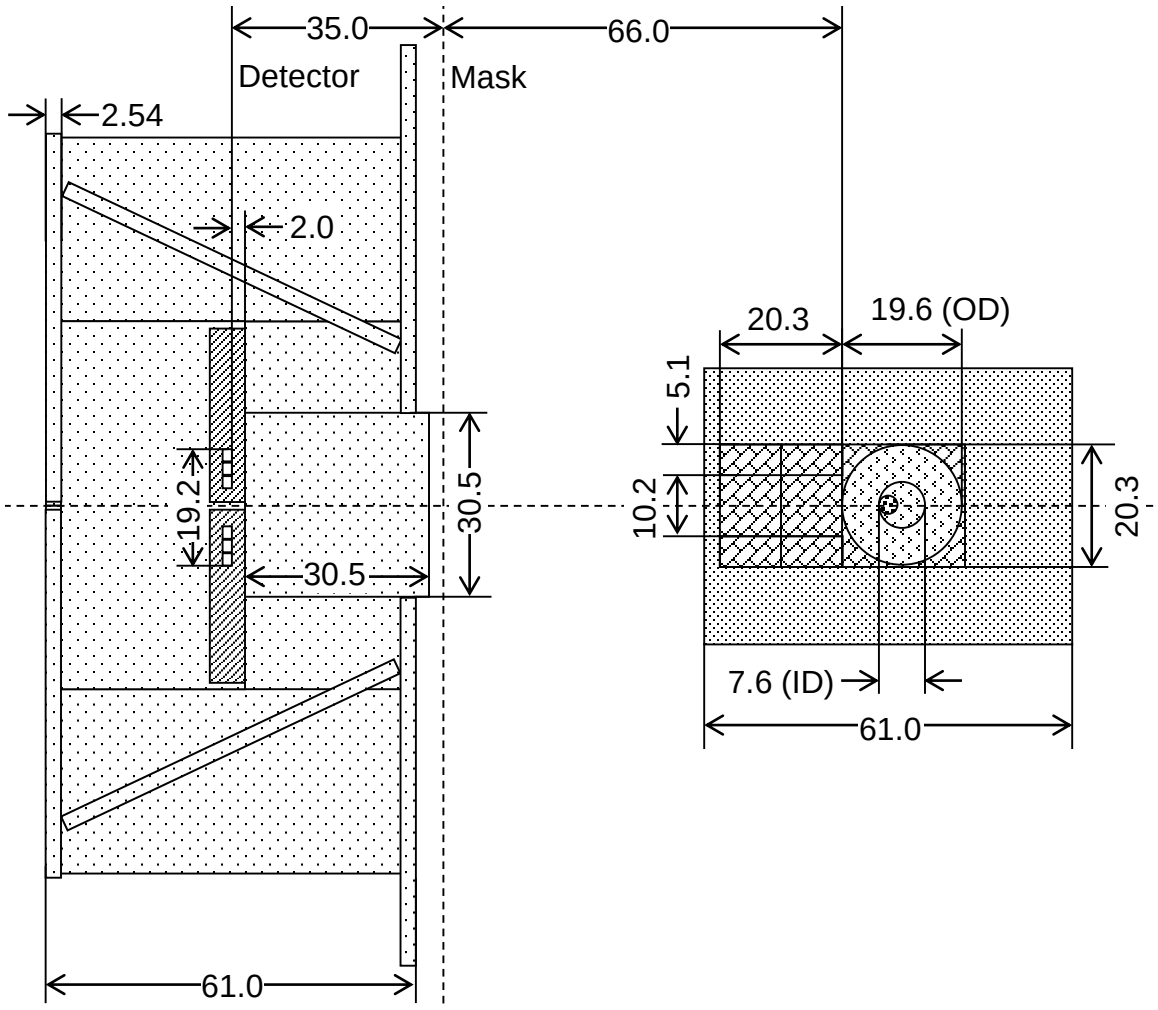

Figure A.2: Top view, single moderator. All lengths in cm.

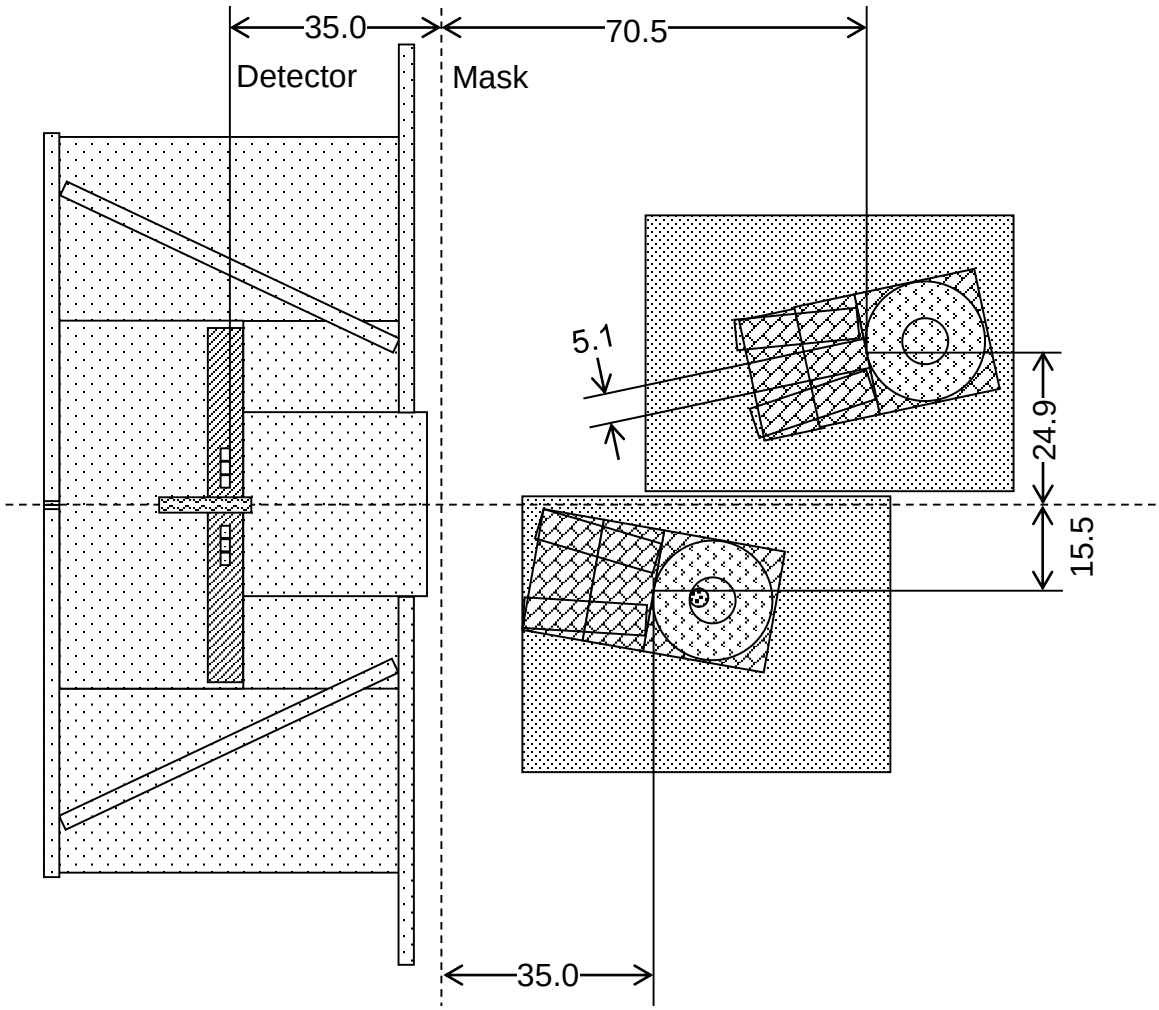

Figure A.3: Top view, two moderators. Moderator nearer to detector was raised an additional 8.3 cm out of page using two Al boxes (not pictured). All lengths in cm.

APPENDIX B

Arduino Program for Mask Movement

```
# Moves mask using x/y stepper motors in back-and-forth raster pattern using incremental x-steps or continuous x-movement
# Author(s): Steven Brown, Jason Jaworski, Kevin Moran
# Copyright Free
# 2016

#include <AccelStepper.h>

// Settings
bool bContinuous = false;

// Length of row in inches
float nLengthInch = 1.6*18/2.54; // = 0.14*78/2.54 (for gamma mask)

// Number of rows
int nNum     = 19; // = 79 (for gamma mask)

// Total live time in ms
long nTime   = 3600000;

// Initial offset in x direction in inches
float xOffsetInch = .25;

// Initial offset in y direction in inches
float yOffsetInch = 3.74;

const int DEBOUNCE_DELAY = 5;
```

```
const int X_LIMIT_LOW = 4;
const int X_LIMIT_HIGH = 5;
const int Y_LIMIT_LOW = 2;
const int Y_LIMIT_HIGH = 3;

class SwitchState
{
  public:
  SwitchState(int nPin, int nState)
  {
    m_nPinID = nPin;
    m_nSetState = nState;
    m_nLastState = nState;
    m_nLastDBTime = 0;
  }

  int CheckSwitch()
  {
    int nReading = digitalRead(m_nPinID);

    if (nReading != m_nLastState)
    {
      m_nLastDBTime = millis();
      m_nLastState = nReading;
    }

    if ((millis() - m_nLastDBTime) > DEBOUNCE_DELAY)
    {
      m_nSetState = m_nLastState;
    }

    return m_nSetState;
  }

  int ResetSwitch()
  {
    long checkTime = millis();
    int reading;
    while(millis() - checkTime < DEBOUNCE_DELAY)
    {
      reading = digitalRead(m_nPinID);
      if (reading != m_nLastState)
      {
        m_nLastState = reading;
        checkTime = millis();
```

```
      }
    }
    m_nSetState = m_nLastState;
    return m_nSetState;
  }

  private:
  int m_nPinID;
  int m_nSetState;
  int m_nLastState;
  long m_nLastDBTime;
};

AccelStepper StepperX(1, 9, 11);
AccelStepper StepperY(1, 12, 13);

SwitchState xLow(X_LIMIT_LOW, LOW);
SwitchState xHigh(X_LIMIT_HIGH, LOW);
SwitchState yLow(Y_LIMIT_LOW, LOW);
SwitchState yHigh(Y_LIMIT_HIGH, LOW);

// Do initializations
float fConversion = 12.6765/10000./2.54; // steps to in
float nLineLength = nLengthInch/fConversion;
float fInterval = nLineLength/float(nNum-1);
float xOffset = xOffsetInch/fConversion;
float yOffset = yOffsetInch/fConversion;

int nMaxSpeed = nNum * nLineLength / (nTime/1000);
int nMaxAccel = 4000;
float fRunway = nMaxSpeed * nMaxSpeed / nMaxAccel + 250;

void setup() {

  pinMode(X_LIMIT_LOW, INPUT_PULLUP);
  pinMode(X_LIMIT_HIGH, INPUT_PULLUP);
  pinMode(Y_LIMIT_LOW, INPUT_PULLUP);
  pinMode(Y_LIMIT_HIGH, INPUT_PULLUP);

  StepperX.setPinsInverted(true);

  // Perform checks
  if (!bContinuous) nMaxSpeed = 1500;
  // Make sure speed is not too fast
  if (nMaxSpeed > 2000)
```

```
  {
    Serial.println("Error: max speed too fast");
    exit(0);
  }
  // Make sure we have enough runway to get up to speed
  if (bContinuous && (xOffset < fRunway || yOffset < fRunway)
    ↪ )
  {
    Serial.println("Error: not enough room to accelerate to
      ↪ speed");
    exit(0);
  }

  StepperX.setMaxSpeed(nMaxSpeed);
  StepperY.setMaxSpeed(nMaxSpeed);

  StepperX.setAcceleration(nMaxAccel);
  StepperY.setAcceleration(nMaxAccel);

  Serial.begin(256000);
  while (!Serial) {
    ; // Wait for serial port to connect. Needed for native
      ↪ USB port only
  }

  delay(3000);
  goHome();
}

void loop() {
  // Main code here

  long x, y;
  if (bContinuous)
  {
    // Reset switches before motion
    xLow.ResetSwitch();
    xHigh.ResetSwitch();
    yLow.ResetSwitch();
    yHigh.ResetSwitch();

    x = xOffset - fRunway;
    y = yOffset;
    GoToPosition(x, y);
```

```
    for (int j=0; j<nNum; j++)
    {
      if (j % 2)
      {
        x = xOffset - fRunway;
      }
      else
      {
        x = xOffset + nLineLength + fRunway;
      }
      if (!GoToPosition(x, y, xOffset, y, xOffset+nLineLength
        ↪ , y)) break;
      y += fInterval;
      if (!GoToPosition(x,y)) break;
    }
  }
  else
  {

    // Reset switch checks after dwell
    xLow.ResetSwitch();
    xHigh.ResetSwitch();
    yLow.ResetSwitch();
    yHigh.ResetSwitch();

    for (int j=0; j<nNum; j++)
    {
      for (int i=0; i<nNum; i++)
      {
        // Reset switch checks after dwell
        xLow.ResetSwitch();
        xHigh.ResetSwitch();
        yLow.ResetSwitch();
        yHigh.ResetSwitch();

        // Calculate position
        if (j % 2) // Go this way for odd rows (-x)
        {
          x = ((nNum-i-1)*fInterval + xOffset);
        }
        else // Go this way for even rows (+x)
        {
          x = (i*fInterval + xOffset);
        }
        y =   j*fInterval + yOffset;
```

```
            // Go to position
            if (!GoToPosition(x, y)) exit(0);

            // Dwell
            delay(nTime / (nNum*nNum));
          }
        }
      }

      goHome();
      exit(0);
}

void goHome()
{

      xLow.ResetSwitch();
      xHigh.ResetSwitch();
      yLow.ResetSwitch();
      yHigh.ResetSwitch();

      float fPrevSpeedX = StepperX.maxSpeed();
      float fPrevSpeedY = StepperY.maxSpeed();

      StepperX.setMaxSpeed(500);
      StepperY.setMaxSpeed(500);

      bool xStillMoving = true;
      bool yStillMoving = true;

      while(xStillMoving || yStillMoving)
      {
        StepperX.move(-100);
        StepperY.move(-100);

        if (xStillMoving && xLow.CheckSwitch() == LOW)
        {
          StepperX.run();
        }
        else
        {
          xStillMoving = false;
        }
```

```
    if (yStillMoving && yLow.CheckSwitch() == LOW)
    {
      StepperY.run();
    }
    else
    {
      yStillMoving = false;
    }

  }

  StepperX.setMaxSpeed(100);
  StepperY.setMaxSpeed(100);

  StepperX.runToNewPosition(StepperX.currentPosition()+200);
  StepperY.runToNewPosition(StepperY.currentPosition()+200);

  StepperX.setCurrentPosition(0);
  StepperY.setCurrentPosition(0);

  StepperX.setMaxSpeed(fPrevSpeedX);
  StepperY.setMaxSpeed(fPrevSpeedY);
}

bool GoToPosition(int xPos, int yPos)
{
  return GoToPosition(xPos, yPos, -1, -1, -1, -1);
}

bool GoToPosition(int xPos, int yPos, int nSigX1, int nSigY1,
   ↪  int nSigX2, int nSigY2)
{
  bool bPassedPos1 = false;
  bool bPassedPos2 = false;

  StepperX.moveTo(xPos);
  StepperY.moveTo(yPos);

  int nCurPosX, nCurPosY;

  Serial.println("Start (" + String(StepperX.currentPosition
     ↪ ()) + "," + String(StepperY.currentPosition()) + ")")
     ↪ ;
  while(StepperX.distanceToGo() != 0 ||
        StepperY.distanceToGo() != 0)
```

```
  {
    nCurPosX = StepperX.currentPosition();
    nCurPosY = StepperY.currentPosition();
    if (!bPassedPos1 && nCurPosX == nSigX1 && nCurPosY ==
      ↪ nSigY1)
    {
      Serial.println("Passing (" + String(nCurPosX) + "," +
        ↪ String(nCurPosY) + ")");
      bPassedPos1 = true;
    }
    if (!bPassedPos2 && nCurPosX == nSigX2 && nCurPosY ==
      ↪ nSigY2)
    {
      Serial.println("Passing (" + String(nCurPosX) + "," +
        ↪ String(nCurPosY) + ")");
      bPassedPos2 = true;
    }

    //if (StepperX.speed() == -StepperX.maxSpeed()) exit(0);
    //Serial.println("Speed: " + String(StepperX.speed()) + "
      ↪  MaxSpeed:" + String(StepperX.maxSpeed()));
    StepperX.run();
    StepperY.run();
    if (xLow.CheckSwitch() == HIGH ||
        xHigh.CheckSwitch() == HIGH ||
        yLow.CheckSwitch() == HIGH ||
        yHigh.CheckSwitch() == HIGH)
    {
      Serial.println("Error (" + String(StepperX.
        ↪ currentPosition()) + "," + String(StepperY.
        ↪ currentPosition()) + ")");
      return false;
    }
  }
  Serial.println("Stop (" + String(StepperX.currentPosition()
    ↪ ) + "," + String(StepperY.currentPosition()) + ")");
  return true;
}
```

APPENDIX C

Matlab Functions for Image Reconstruction

```
function [IMG,PATTERN] = corrRecon(dataSP,detxPos,detyPos,a,
    ↪ b,elSize,G,ns)
%CORRRECON Obtain image via correlation from time-encoded
    ↪ Polaris SP data
%   CORRRECON(dataSP,detxPos,detyPos,a,b,G,ns) Reconstructs
%   an image from data array dataSP using position
%   information detxPos, detyPos, a, b, and elSize
%   via corrlation with decoding matrix G and
%   number of subsamples ns.
%
%   % Example:
%   %   Polaris SP has two detector arrays with 33x33 pixels
    ↪ each and 19x19 time bins
%   %   5-D array dataSP has size [2,33,33,19,19]
%   %   Matrices detxPos and detyPos each have dimension
    ↪ [2,33] and describe x/y distance of each pixel from
    ↪ origin in cm within each detector array
%   %   a = 35.0; % mask-to-object distance in cm
%   %   b = 70.0; % mask-to-detector distance in cm
%   %   elSize = 1.6; % mask element size in cm
%   %   Matrix G has dimension [19,19]
%   %   ns = 10; % number of sub samples
%   %   Matrices img and pattern have dimension [190,190]

%   Author(s): Steven Brown, 2016
%   Copyright Free

m = 1+b/a; % magnification
zpad1 = zeros(ns); zpad1(round(ns^2/2))=1; % zero-padded 1
PATTERN = zeros(size(dataSP,4)*ns,size(dataSP,5)*ns);
```

```
% place detector element counts into 2-D pattern
for i = 1:size(dataSP,1) % array number

    for j = 1:size(dataSP,2) % row of pixel

        % y-distance of detector pixel from center
        yElShift = 1/m * detyPos(i,j)/elSize;
        for k = 1:size(dataSP,3) % column of pixel

            % x-distance of detector pixel from center
            xElShift = 1/m * detxPos(i,k)/elSize;

            % place counts from pixel (i,j,k) into pattern
            pixelSignal = squeeze(dataSP(i,j,k,:,:));
            zeroPaddedSignal = kron(pixelSignal,zpad1);
            PATTERN = PATTERN + circshift(zeroPaddedSignal, [
                ↪ round(yElShift*ns),round(xElShift*ns)]);
        end
    end
end

% Periodic correlation of pattern with decoding matrix
GKRON = kron(G,ones(ns));
IMG = xcorr2sm([GKRON,GKRON;GKRON,GKRON],PATTERN,'valid');

function c = xcorr2sm(a,b, option)
%XCORR2 Two-dimensional cross-correlation.
%   XCORR2sm(A,B) computes the crosscorrelation of matrices A
   ↪  and B.
%   XCORR2sm(A) is the autocorrelation function. Modified
   ↪ from XCORR2
%
%   % Example:
%   %   Find the cross-correlation of two matrices a and b:
%   %   a = [2 1 5; 3 1 3; 5 2 2];     b = [1 4 3; 2 5 6];
%
%   a = [2 1 5; 3 1 3; 5 2 2];
%   b = [1 4 3; 2 5 6];
%   xcorr2(a,b)
%
%   See also CONV2, XCORR and FILTER2, XCORR.

%   Author(s): Y.F. Zhu, 4-25-14
%   Copyright Free
```

```
%   $Revision: 1.0.0.0 $  $Date: 2014/04/25 14:21:09 $

if nargin == 1
        b = a;
    option = 'full';
elseif nargin == 2
    option = 'full';
end

c = conv2(a, rot90(conj(b),2), option);
```

BIBLIOGRAPHY

BIBLIOGRAPHY

[1] MJ Berger, JH Hubbell, SM Seltzer, and J Chang. Xcom: photon cross sections database, 1998. Available at http://www.nist.gov/pml/data/xcom/.

[2] S Del Sordo, L Abbene, E Caroli, and AM Mancini. Progress in the development of CdTe and CdZnTe semiconductor radiation detectors for astrophysical and medical applications. *Sensors*, 2009.

[3] Yuefung Zhu, Feng Zhang, Andy Boucher, Joshua Mann, and Zhong He. Performance comparison of steering-grid and simple-pixel CdZnTe detectors. In *2013 IEEE Nuclear Science Symposium and Medical Imaging Conference (2013 NSS/MIC)*, pages 1–5. IEEE, oct 2013.

[4] JJ Duderstadt and LJ Hamilton. *Nuclear reactor analysis*. John Wiley & Sons, 1976.

[5] M.B. Chadwick, M. Herman, P. Obložinský, M.E. Dunn, Y. Danon, A.C. Kahler, D.L. Smith, B. Pritychenko, G. Arbanas, R. Arcilla, R. Brewer, D.A. Brown, R. Capote, A.D. Carlson, Y.S. Cho, H. Derrien, K. Guber, G.M. Hale, S. Hoblit, S. Holloway, T.D. Johnson, T. Kawano, B.C. Kiedrowski, H. Kim, S. Kunieda, N.M. Larson, L. Leal, J.P. Lestone, R.C. Little, E.A. McCutchan, R.E. MacFarlane, M. MacInnes, C.M. Mattoon, R.D. McKnight, S.F. Mughabghab, G.P.A. Nobre, G. Palmiotti, A. Palumbo, M.T. Pigni, V.G. Pronyaev, R.O. Sayer, A.A. Sonzogni, N.C. Summers, P. Talou, I.J. Thompson, A. Trkov, R.L. Vogt, S.C. van der Marck, A. Wallner, M.C. White, D. Wiarda, and P.G. Young. ENDF/B-VII.1 Nuclear Data for Science and Technology: Cross Sections, Covariances, Fission Product Yields and Decay Data. *Nuclear Data Sheets*, 112(12):2887–2996, 2011.

[6] P.A. Egelstaff. The slow-neutron cross-section of graphite. *Journal of Nuclear Energy (1954)*, 5(2):203–209, 1957.

[7] A Santamarina, D Bernard, P Blaise, and M Coste. The JEFF-3.1. 1 nuclear data library. *JEFF report*, 2009.

[8] J Blachot. Nuclear Data Sheets for A= 114. *Nuclear Data Sheets*, 2012.

[9] Alejandro Sonzogni. Interactive Chart of Nuclides. Available at https://www.nndc.bnl.gov/chart/.

[10] Thermal Neutron Capture y's (CapGam), 2013. Available at http://www.nndc.bnl.gov/capgam/.

[11] Roberto Accorsi. *Design of Near-Field Coded Aperture Cameras for High-Resolution Medical and Industrial Gamma-Ray Imaging*. PhD thesis, Massachusetts Institute of Technology, 2001.

[12] Carter Hull, Jim Tallent, Dennis Tollefson, Martin Williamson, and Justin Curtis. Research Opportunities at the CNS (Y-12 and PANTEX) Nuclear Detection and Sensor Testing Centers (NDSTC), 2015.

[13] CG Wahl, JM Jaworski, and Z He. UMImaging: a software package for image reconstruction from 3D-position-sensitive gamma-ray detectors. *IEEE Transactions on Nuclear Science*, 2012.

[14] D.S. McGregor and H. Hermon. Room-temperature compound semiconductor radiation detectors. *Nuclear Instruments and Methods in Physics Research Section A: Accelerators, Spectrometers, Detectors and Associated Equipment*, 395(1):101–124, 1997.

[15] T Kibedi, TW Burrows, and MB Trzhaskovskaya. Evaluation of theoretical conversion coefficients using BrIcc. *Nuclear Instruments and Methods in Physics Research, Section A: Accelerators, Spectrometers, Detectors and Associated Equipment*, 2008.

[16] Christopher Wahl, Willy R Kaye, Weiyi Wang, Feng Zhang, Jason M Jaworski, Alexis Y King, Andy Y Boucher, and Zhong He. The Polaris-H imaging spectrometer. *Nuclear Instruments and Methods in Physics Research, Section A: Accelerators, Spectrometers, Detectors and Associated Equipment*, 627:120–127, 2011.

[17] M. McCleskey, W. Kaye, D. S. Mackin, S. Beddar, Z. He, and J. C. Polf. Evaluation of a multistage CdZnTe Compton camera for prompt γ imaging for proton therapy. *Nuclear Instruments and Methods in Physics Research, Section A: Accelerators, Spectrometers, Detectors and Associated Equipment*, 785:163–169, 2015.

[18] D. S. McGregor, J. T. Lindsay, and R. W. Olsen. Thermal neutron detection with cadmium1-x zincx telluride semiconductor detectors. *Nuclear Instruments and Methods in Physics Research, Section A: Accelerators, Spectrometers, Detectors and Associated Equipment*, 381(2-3):498–501, 1996.

[19] M. W. Streicher, D. Goodman, Y. Zhu, and Z. He. Low energy threshold measurements using digital 3-d cdznte spectrometers for fast neutron detection. 2016 Nuclear Science Symposium and Medical Imaging Conference, 2016.

[20] Peter E Vanier, Leon Forman, and Elizabeth C Selcow. A Thermal Neutron Source Imager Using Coded Apertures. *Nuclear Materials Management, Proc. 36th Annual Meeting INMM*, 24:842–847, 1995.

[21] Peter E Vanier and Leon Forman. Advances in Imaging With Thermal Neutrons. *Nuclear Materials Management, Proc. 37th Annual Meeting INMM*, (96), 1996.

[22] Peter E Vanier, Leon Forman, Stephen J Hunter, Emma J Harris, and Graham C Smith. Thermal Neutron Backscatter Imaging. *Nuclear Science Symposium Conference Record, 2004 IEEE*, (2):4–8, 2004.

[23] Victor Bom, A. A H Mostafa, and Carel W E Van Eijk. Land mine detection with neutron back scattering imaging using a neutron generator. *IEEE Transactions on Nuclear Science*, 53(1):356–360, 2006.

[24] K.-P. Ziock, G. Caffrey, A. Lebrun, L. Forman, P. Vanier, and J. Wharton. Radiation Imaging of Dry-Storage Casks for Spent Nuclear Fuel. *2005 IEEE Nuclear Science Symposium and Medical Imaging Conference*, pages 1–5, 2005.

[25] A. J. Peurrung, P. L. Reeder, E. A. Lepel, and D. C. Stromswold. Location of neutron sources using moderator-free directional thermal neutron detectors. *IEEE Transactions on Nuclear Science*, 44(3 PART 1):543–550, 1997.

[26] P. E. Vanier and L. Forman. Forming Images with Thermal Neutrons. *SPIE International Symposium on Optical Science and Technology, Conference 4784A, Hard X-rays, Gamma Rays, and Particles*, 4784:183–193, 2002.

[27] Peter E. Vanier, Istvan Dioszegi, Cynthia Salwen, Vinita Ghosh, and Leon Forman. Stand-off detection of special nuclear materials using neutron imaging methods. *2008 IEEE Nuclear Science Symposium Conference Record*, pages 681–685, 2008.

[28] M Strobl, I Manke, N Kardjilov, A Hilger, M Dawson, and J Banhart. Advances in neutron radiography and tomography. *Journal of Physics D: Applied Physics*, 42(24):243001, 2009.

[29] Pascal Mercère, Mourad Idir, Johan Floriot, Xavier Levecq, Alexei Erko, Thomas Krist, and Alan Michette. *Modern Developments in X-Ray and Neutron Optics*, volume 137. 2008.

[30] L Mertz and NO Young. Fresnel transformation of images (Fresnel coding and decoding of images). *Optical Instruments and Techinques*, 1962.

[31] RH Dicke. Scatter-hole cameras for x-rays and gamma rays. *The Astrophysical Journal*, 1968.

[32] JG Ables. Fourier transform photography: a new method for X-ray astronomy. *Proceedings of the Astronomical Society of Australia*, 1968.

[33] Jean in 't Zand and Heiko Groeneveld. A selection of coded aperture instruments designed for astronomical observations, 2005.

[34] T. M. Cannon and E. E. Fenimore. Coded aperture imaging: many holes make light work. 19(3):283–289, 1980.

[35] E. Caroli, J. B. Stephen, G. Di Cocco, L. Natalucci, and A. Spizzichino. Coded aperture imaging in X- and gamma-ray astronomy. *Space Science Reviews*, 45(3-4):349–403, 1987.

[36] Michał J. Cieślak, Kelum A.A. Gamage, and Robert Glover. Coded-aperture imaging systems: Past, present and future development - A review. *Radiation Measurements*, 92:59–71, 2016.

[37] E E Fenimore. Coded aperture imaging with uniformly redundant arrays. *Applied optics*, 17(22):3562–3570, 1978.

[38] A. J. Peurrung, D.C. Stromswold, R. R. Hansen, P. L. Reeder, and D. S. Barnett. Long-Range Neutron Detection. Technical report, Pacific Northwest National Laboratory, Richland, WA, 1999.

[39] Peter E Vanier. Improvements in coded aperture thermal neutron imaging. *Optical Science and Technology, SPIE's 48th Annual Meeting. International Society for Optics and Photonics*, 5199:124–131, 2003.

[40] Peter E. Vanier, Leon Forman, and Daren R. Norman. Thermal neutron imaging in an active interrogation environment. *AIP Conference Proceedings*, 1099:583–586, 2009.

[41] B. Yu, N. A. Schaknowski, G. C. Smith, G. De Geronimo, E. O. Vernon, L. G. Clonts, C. L. Britton, and S. S. Frank. Thermal neutron detectors with discrete anode pad readout. *IEEE Nuclear Science Symposium Conference Record*, pages 1878–1881, 2008.

[42] I. Dioszegi, B. Yu, G. Smith, N. Schaknowski, J. Fried, P. E. Vanier, C. Salwen, and L. Forman. A new pad-based neutron detector for stereo coded-aperture thermal neutron imaging. *IEEE Nuclear Science Symposium Conference Record*, 9215:1–10, 2014.

[43] N.O. Boyce, B.R. Kowash, and D.K. Wehe. Thermal neutron imaging with a Rotationally Modulated Collimator (RMC). In *2009 IEEE Nuclear Science Symposium Conference Record (NSS/MIC)*, pages 1129–1133. IEEE, oct 2009.

[44] B. R. Kowash and D. K. Wehe. A unified near- and far-field imaging model for rotating modulation collimators. *Nuclear Instruments and Methods in Physics Research, Section A: Accelerators, Spectrometers, Detectors and Associated Equipment*, 637(1):178–184, 2011.

[45] GF Knoll. *Radiation detection and measurement*. John Wiley & Sons, 4 edition, 2010.

[46] V. F. Sears. Neutron scattering lengths and cross sections. *Neutron News*, 3(October):26–37, 1992.

[47] T.E Schlesinger, J.E Toney, H Yoon, E.Y Lee, B.A Brunett, L Franks, and R.B James. Cadmium zinc telluride and its use as a nuclear radiation detector material. *Materials Science and Engineering: R: Reports*, 32(4):103–189, 2001.

[48] G. Rusev, M. Jandel, M. Krtička, C. W. Arnold, T. A. Bredeweg, A. Couture, W. A. Moody, S. M. Mosby, and J. L. Ullmann. Cascade gamma rays following capture of thermal neutrons on 113Cd. *Physical Review C - Nuclear Physics*, 88(5):6–9, 2013.

[49] Paul M. Siffert, Alain G. Cornet, Raymond T. Regal, Robert G. Triboulet, and Yves M. Marfain. Nuclear detectors sensitive to alpha, beta, and gamma rays and to thermal neutrons and to methods of treatment of crystals of such detectors, 1975.

[50] M. Fasasi, M. Jung, P. Siffert, and C. Teissier. Thermal Neutron Dosimetry with Cadmium Telluride Detectors. *Radiation Protection Dosimetry*, 23(1-4):429–431, 1988.

[51] A.J Peurrung. Recent developments in neutron detection. *Nuclear Instruments and Methods in Physics Research Section A: Accelerators, Spectrometers, Detectors and Associated Equipment*, 443(2):400–415, 2000.

[52] A. Martín-Martín, M. P. Iñiguez, P. N. Luke, R. Barquero, A Lorente, J Morchón, E. Gallego, G. Quincoces, and J. M. Martí-Climent. Evaluation of CdZnTe as Neutron Detector Around Medical Accelerators. *Radiation Protection Dosimetry*, 133(4):1–7, 2009.

[53] Carolyn E. Seifert, Debra S. Barnett, and Mitchell J. Myjak. Prospects for thermal neutron detection and imaging with the GammaTracker handheld radioisotope identifier. *Proceedings of SPIE*, 7079:707907–707907–9, 2008.

[54] Randall Scott May. *Gamma Ray Image Formation By Stochastic Time Modulation*. PhD thesis, University of Michigan, 1974.

[55] A Busboom, H Elders-Boll, and H.D. Schotten. Uniformly redundant arrays a. busboom, h. eldersboll, and h. d. schotten. *Experimental Astronomy*, 8:97–123, 1998.

[56] R S May, Z Akcasu, and G F Knoll. Gamma-ray imaging with stochastic apertures. *Applied optics*, 13(11):2589–601, 1974.

[57] M. Oda. High-resolution x-ray collimator with broad field of view for astronomical use. *Applied Optics*, 4(1):143–143, 1964.

[58] L Mertz. A dilute image transform with application to an x-ray star camera. *Modern Optics*, 1967.

[59] H. W. Schnopper, R. I. Thompson, and S. Watt. Predicted performance of a rotating modulation collimator for locating celestial X-ray sources. *Space Science Reviews*, 8(4):534–542, 1968.

[60] H. Bradt, G. Garmire, G. Oda, M.; Spada, B. V. Sreekantan, P. Gorenstein, and H. Gursky. The Modulation Collimator in X-ray Astronomy. *Space Science Revie*, 8(4):471–506, 1968.

[61] L. Mertz. Applicability of the rotation collimator to nuclear medicine. *Optics Communications*, 12(2):216–219, 1974.

[62] Benjamin Raymond Kowash. *A Rotating Modulation Imager for the Orphan Source Search Problem*. PhD thesis, University of Michigan, 2008.

[63] Amy C. Sharma, Timothy G. Turkington, Georgia D. Tourassi, and Carey E. Floyd. Near-field high-energy spectroscopic gamma imaging using a rotation modulation collimator. *Nuclear Instruments and Methods in Physics Research, Section B: Beam Interactions with Materials and Atoms*, 266(22):4938–4947, 2008.

[64] L N Mertz, G H Nakano, and J R Kilner. Rotational aperture synthesis for X-rays. *Journal of the Optical Society of America A (Optics and Image Science)*, 3(1):2167–2170, 1986.

[65] E Tanaka and TA Iinuma. Image processing for coded aperture imaging and an attempt at rotating slit imaging. *Journal of Nuclear Medicine and Biology*, 1976.

[66] ElRoy Lester Miller. *Radially symmetrical coded apertures*. PhD thesis, 1978.

[67] Leonard D. Baumert. *Cyclic Difference Sets*, volume 182 of *Lecture Notes in Mathematics*. Springer Berlin Heidelberg, Berlin, Heidelberg, 1971.

[68] Peter Gottlieb. A Television Scanning Scheme for a Detector-Noise-Limited System. *IEEE Transactions on Information Theory*, 14(3):428–433, 1968.

[69] A Z Akcasu, R S May, G F Knoll, W L Rogers, K F Koral, and L W Jones. Coded Aperture Gamma-Ray Imaging with Stochastic Apertures. *Optical Engineering*, 13(2):117–125, 1974.

[70] KF Koral, WL Rogers, and GF Knoll. Digital tomographic imaging with time-modulated pseudorandom coded aperture and Anger camera. *Journal of nuclear medicine:*, 1975.

[71] W L Rogers, K F Koral, R Mayans, P F Leonard, J H Thrall, T J Brady, and J W Keyes. Coded-aperture imaging of the heart. *Journal of nuclear medicine*, 21(4):371–8, apr 1980.

[72] W W Resinger, E A Rose, J W Keyes, K F Koral, W L Rogers, T J Brady, R C Kline, J C Sisson, and J H Thrall. Tomographic thyroid scintigraphy: comparison with standard pinhole imaging: concise communication. *Journal of nuclear medicine : official publication, Society of Nuclear Medicine*, 22(7):638–42, jul 1981.

[73] GF Knoll and JJ Williams. Application of a ring pseudorandom aperture for transverse section tomography. *IEEE Transactions on Nuclear Science*, 1977.

[74] JJ Williams. *Design and investigation of a circular ring emission tomograph*. PhD thesis, University of Michigan, 1979.

[75] JJ Williams, WP Snapp, and GF Knoll. Introducing SPRINT: a single photon ring system for emission tomography. *IEEE Transactions on*, 1979.

[76] G.F. Knoll, W.L. Rogers, K.F. Koral, J.A. Stamos, and N.H. Clinthorne. Application of coded apertures in tomographic head scanning. *Nuclear Instruments and Methods in Physics Research*, 221(1):226–232, 1984.

[77] Jay Williams. Personal communication, October 2016.

[78] Dov Rosenfeld and Albert Macovski. Time Modulated Apertures for Tomography in Nuclear Medicine. *IEEE Transactions on Nuclear Science*, 24(1):570–576, 1977.

[79] W. L. Rogers, R. S. Adler, and K. F. Koral. A Rationale For Optimal Coded Aperture Design. pages 242–249. International Society for Optics and Photonics, aug 1980.

[80] Roberto Accorsi, Francesca Gasparini, and Richard C Lanza. Optimal coded aperture patterns for improved SNR in nuclear medicine imaging. *Nuclear Instruments and Methods in Physics Research Section A: Accelerators, Spectrometers, Detectors and Associated Equipment*, 474(3):273–284, 2001.

[81] Peter Marleau, James Brennan, Erik Brubaker, and John Steele. Results from the coded aperture neutron imaging system. *IEEE Nuclear Science Symposium Conference Record*, pages 1640–1646, 2010.

[82] Peter Marleau, James Brennan, Erik Brubaker, Mark Gerling, Aaron Nowack, Patricia Schuster, and John Steele. Time encoded fast neutron/gamma imager for large standoff SNM detection. *IEEE Nuclear Science Symposium Conference Record*, pages 591–595, 2012.

[83] AP Dempster, NM Laird, and DB Rubin. Maximum likelihood from incomplete data via the EM algorithm. *Journal of the royal statistical society*, 1977.

[84] James Brennan, Erik Brubaker, Aaron Nowack, John Steele, Melinda Sweany, and Daniel Throckmorton. Bubble masks for time-encoded imaging of fast neutrons. *IEEE Nuclear Science Symposium Conference Record*, 2013.

[85] J. Brennan, E. Brubaker, M. Gerling, P. Marleau, K. McMillan, A. Nowack, N. Renard Le Galloudec, and M. Sweany. Demonstration of two-dimensional time-encoded imaging of fast neutrons. *Nuclear Instruments and Methods in Physics Research, Section A: Accelerators, Spectrometers, Detectors and Associated Equipment*, 802:75–81, 2015.

[86] J. G. M. FitzGerald, L. W. Burggraf, B. R. Kowash, and E. L. Hull. A Modulating Liquid Collimator for Coded Aperture Adaptive Imaging of Gamma-Rays. *IEEE Transactions on Nuclear Science*, 60(3):2300–2307, jun 2013.

[87] Jonathan E. Grindlay and JaeSub Hong. Optimizing wide-field coded aperture imaging: radial mask holes and scanning. page 402. International Society for Optics and Photonics, jan 2004.

[88] S.J. Kaye, W.R. Kaye, and Zhong He. Experimental demonstration of coded aperture imaging using thick 3D-position-sensitive CdZnTe detectors. In *2009 IEEE Nuclear Science Symposium Conference Record (NSS/MIC)*, pages 1902–1906. IEEE, oct 2009.

[89] S J Kaye, W R Kaye, J M Jaworski, and Zhong He. Experimental limitations of coded aperture imaging using thick 3D-position-sensitive CdZnTe detectors. In *IEEE Nuclear Science Symposuim & Medical Imaging Conference*, pages 3856–3859. IEEE, oct 2010.

[90] J.F. Butler, C.L. Lingren, and F.P. Doty. Cd1-x Znx Te gamma ray detectors. *IEEE Transactions on Nuclear Science*, 39(4):605–609, 1992.

[91] Z He, W Li, GF Knoll, DK Wehe, and J Berry. 3-D position sensitive CdZnTe gamma-ray spectrometers. *Nuclear Instruments and*, 1999.

[92] Z. He, W. Li, G.F. Knoll, D.K. Wehe, and Y.F. Du. Effects of charge sharing in 3-D position sensitive CdZnTe gamma-ray spectrometers. *Nuclear Instruments and Methods in Physics Research Section A: Accelerators, Spectrometers, Detectors and Associated Equipment*, 439(2):619–624, 2000.

[93] Jae Cheon Kim, Stephen E. Anderson, Willy Kaye, Feng Zhang, Yuefeng Zhu, Sonal Joshi Kaye, and Zhong He. Charge sharing in common-grid pixelated CdZnTe detectors. *Nuclear Instruments and Methods in Physics Research Section A: Accelerators, Spectrometers, Detectors and Associated Equipment*, 654(1):233–243, 2011.

[94] William R Kaye. *Energy and Position Reconstruction in Pixelated CdZnTe Detectors*. PhD thesis, University of Michigan, 2012.

[95] A.E. Bolotnikov, G.S. Camarda, G.A. Carini, Y. Cui, L. Li, and R.B. James. Cumulative effects of Te precipitates in CdZnTe radiation detectors. *Nuclear Instruments and Methods in Physics Research Section A: Accelerators, Spectrometers, Detectors and Associated Equipment*, 571(3):687–698, 2007.

[96] H. H. Barrett, J. D. Eskin, and H. B. Barber. Charge Transport in Arrays of Semiconductor Gamma-Ray Detectors. *Physical Review Letters*, 75(1):156–159, jul 1995.

[97] PN Luke. Unipolar charge sensing with coplanar electrodes-application to semiconductor detectors. *IEEE Transactions on Nuclear Science*, 1995.

[98] D.S McGregor, R.A Rojeski, Z He, D.K Wehe, M Driver, and M Blakely. Geometrically weighted semiconductor Frisch grid radiation spectrometers. *Nuclear Instruments and Methods in Physics Research Section A: Accelerators, Spectrometers, Detectors and Associated Equipment*, 422(1):164–168, 1999.

[99] W. Shockley. Currents to Conductors Induced by a Moving Point Charge. *Journal of Applied Physics*, 9(10):635, 1938.

[100] S Ramo. Currents induced by electron motion. *Proc. Ire*, 1939.

[101] Zhong He. Review of the ShockleyRamo theorem and its application in semiconductor gamma-ray detectors. *Nuclear Instruments and Methods in Physics Research Section A: Accelerators, Spectrometers, Detectors and Associated Equipment*, 463(1):250–267, 2001.

[102] Carolyn E Lehner. *4-pi Compton imaging using a single 3-D position sensitive CdZnTe detector*. PhD thesis, University of Michigan, 2004.

[103] Feng Zhang. *Events Reconstruction in 3-D Position Sensitive CdZnTe Gamma Ray Spectrometers*. PhD thesis, University of Michigan, 2005.

[104] Yuefeng Zhu, Stephen E. Anderson, and Zhong He. Sub-Pixel Position Sensing for Pixelated, 3-D Position Sensitive, Wide Band-Gap, Semiconductor, Gamma-Ray Detectors. *IEEE Transactions on Nuclear Science*, 58(3):1400–1409, jun 2011.

[105] Michael Streicher, Yuefeng Zhu, Feng Zhang, Yvan A. Boucher, Christopher G. Wahl, Hao Yang, and Zhong He. A portable 2 2 digital 3D CZT imaging spectrometer system. In *2014 IEEE Nuclear Science Symposium and Medical Imaging Conference (NSS/MIC)*, pages 1–3. IEEE, nov 2014.

[106] W Kaye, Y A Boucher, Feng Zhang, and Zhong He. Calibration and operation of the polaris 18-detector CdZnTe array. In *IEEE Nuclear Science Symposuim & Medical Imaging Conference*, pages 3821–3824. IEEE, oct 2010.

[107] Willy R. Kaye, Nathan D. Bennett, Christopher G. Wahl, Zhong He, and Weiyi Wang. Gamma-ray source location by attenuation measurements. In *2007 IEEE Nuclear Science Symposium Conference Record*, pages 1294–1298. IEEE, 2007.

[108] L.J. Meng and Z. He. Exploring the limiting timing resolution for large volume CZT detectors with waveform analysis. *Nuclear Instruments and Methods in Physics Research Section A: Accelerators, Spectrometers, Detectors and Associated Equipment*, 550(1):435–445, 2005.

[109] D Xu. *Gamma-ray imaging and polarization measurement using 3-D position-sensitive CdZnTe detectors*. PhD thesis, University of Michigan, 2006.

[110] Dan Xu, Zhong He, Carolyn E. Lehner, and Feng Zhang. 4-pi Compton imaging with single 3D position-sensitive CdZnTe detector. page 144. International Society for Optics and Photonics, oct 2004.

[111] CG Wahl. *Imaging, Detection, and Identification Algorithms for Position-Sensitive Gamma-Ray Detectors*. PhD thesis, University of Michigan, 2011.

[112] W Wang. *Techniques and Applications of Compton Imaging for Position-Sensitive Gamma-Ray Detectors*. PhD thesis, University of Michigan, 2011.

[113] DJ Lingenfelter. *Source Detection and Image Reconstruction with PositionSensitive GammaRay Detectors*. PhD thesis, University of Michigan, 2012.

[114] JM Jaworski. *Compton Imaging Algorithms for Position-Sensitive Gamma-Ray Detectors in the Presence of Motion*. PhD thesis, University of Michigan, 2013.

[115] YA Boucher, F Zhang, and WR Kaye. Study of Long-Term CdZnTe Stability Using the Polaris System. *IEEE Transactions on*, 2013.

[116] CG Wahl, W Kaye, W Wang, and F Zhang. Polaris-H measurements and performance. *2014 IEEE Nuclear*, 2014.

[117] S Joshi. *Coded Aperture Imaging Applied to Pixelated CdZnTe Detectors*. PhD thesis, 2014.

[118] Sonal J. Kaye, Willy R. Kaye, and Zhong He. 4π coded aperture imaging using 3d position-sensitive CdZnTe detectors. In *2008 IEEE Nuclear Science Symposium Conference Record*, pages 711–713. IEEE, oct 2008.

[119] Sonal Joshi Kaye, Jason Michael Jaworski, Willy Robert Kaye, and Zhong He. Source motion compensated coded aperture imaging using thick 3D-position-sensitive CdZnTe detectors. In *2011 IEEE Nuclear Science Symposium Conference Record*, pages 4693–4696. IEEE, oct 2011.

[120] Zane W. Bell, D. A. Carpenter, S. S. Cristy, V. E. Lamberti, Arnold Burger, Brian F. Woodfield, Thomas Niedermayr, I. Dragos Hau, Simon E. Labov, Stephan Friedrich, W. Geoffrey West, Kenneth R. Pohl, and Lodewijk van den Berg. Neutron detection with cryogenics and semiconductors. *physica status solidi (c)*, 2(5):1592–1605, March 2005.

[121] Glen F. Knoll. *Radiation Detection and Measurements*. John Wiley & Sons, Inc., New York, 4 edition, 2010.

[122] Kwang June Park, June-sik Ju, Hee-young Kang, and Hee-sung Shin. Variation of Neutron Moderating Power on HDPE by Gamma Radiation. *Journal of Radiation Protection*, 34(1):9–13, 2009.

[123] J.R. Granada, J. Dawidowski, R.E. Mayer, and V.H. Gillette. Thermal neutron cross section and transport properties of polyethylene. *Nuclear Instruments and Methods in Physics Research Section A: Accelerators, Spectrometers, Detectors and Associated Equipment*, 261(3):573–578, 1987.

[124] FB Brown, RF Barrett, TE Booth, and JS Bull. MCNP version 5. *Trans. Am. Nucl.*, 2002.

[125] KS Krane and D Halliday. *Introductory nuclear physics*. 1988.

[126] S. Agostinelli, J. Allison, K. Amako, J. Apostolakis, H. Araujo, P. Arce, M. Asai, D. Axen, S. Banerjee, G. Barrand, F. Behner, L. Bellagamba, J. Boudreau, L. Broglia, A. Brunengo, H. Burkhardt, S. Chauvie, J. Chuma, R. Chytracek, G. Cooperman, G. Cosmo, P. Degtyarenko, A. Dell'Acqua, G. Depaola, D. Dietrich, R. Enami, A. Feliciello, C. Ferguson, H. Fesefeldt, G. Folger, F. Foppiano, A. Forti, S. Garelli, S. Giani, R. Giannitrapani, D. Gibin, J.J. Gómez Cadenas, I. González, G. Gracia Abril, G. Greeniaus, W. Greiner, V. Grichine, A. Grossheim, S. Guatelli, P. Gumplinger, R. Hamatsu, K. Hashimoto, H. Hasui, A. Heikkinen, A. Howard, V. Ivanchenko, A. Johnson, F.W. Jones, J. Kallenbach, N. Kanaya, M. Kawabata, Y. Kawabata, M. Kawaguti, S. Kelner, P. Kent, A. Kimura, T. Kodama, R. Kokoulin, M. Kossov, H. Kurashige, E. Lamanna, T. Lampén, V. Lara, V. Lefebure, F. Lei, M. Liendl, W. Lockman, F. Longo, S. Magni, M. Maire, E. Medernach, K. Minamimoto, P. Mora de Freitas, Y. Morita, K. Murakami, M. Nagamatu, R. Nartallo, P. Nieminen, T. Nishimura, K. Ohtsubo, M. Okamura, S. O'Neale, Y. Oohata, K. Paech, J. Perl, A. Pfeiffer, M.G. Pia, F. Ranjard, A. Rybin, S. Sadilov, E. Di Salvo, G. Santin, T. Sasaki, N. Savvas, Y. Sawada, S. Scherer, S. Sei, V. Sirotenko, D. Smith, N. Starkov, H. Stoecker, J. Sulkimo, M. Takahata, S. Tanaka, E. Tcherniaev, E. Safai Tehrani, M. Tropeano, P. Truscott, H. Uno, L. Urban, P. Urban, M. Verderi, A. Walkden, W. Wander, H. Weber, J.P. Wellisch, T. Wenaus, D.C. Williams, D. Wright, T. Yamada, H. Yoshida, and D. Zschiesche. Geant4a simulation toolkit. *Nuclear Instruments and Methods in Physics Research Section A: Accelerators, Spectrometers, Detectors and Associated Equipment*, 506(3):250–303, 2003.

[127] Steven T Brown, Andy Y Boucher, Joshua Mann, Yuefung Zhu, and Zhong He. Thermal neutron source location using a 3-D position-sensitive CdZnTe detector array. In *2013 IEEE Nuclear Science Symposium and Medical Imaging Conference (2013 NSS/MIC)*, pages 1–5. IEEE, oct 2013.

[128] Danyal Turkoglu, Joshua Burke, Radoslaw Lewandowski, and Lei R. Cao. Characterization of a new external neutron beam facility at the Ohio State University. *Journal of Radioanalytical and Nuclear Chemistry*, 291(2):321–327, feb 2012.

[129] Gerhard. Erdtmann. *Neutron activation tables*. Verlag Chemie, 1976.

[130] T. S. Sanderson, C. D. Scott, M. Flaska, J. K. Polack, and S. A. Pozzi. Machine learning for digital pulse shape discrimination. In *2012 IEEE Nuclear Science Symposium and Medical Imaging Conference Record (NSS/MIC)*, pages 199–202. IEEE, oct 2012.

[131] Gas-Filled Radiation Detectors Helium-3 Proportional Counters, 2016. Available at http://www.crystals.saint-gobain.com/.

[132] R Sanapala. *Characterization of FR-4 printed circuit board laminates before and after exposure to lead-free soldering conditions*. PhD thesis, University of Maryland, 2008.

[133] Gary W. Phillips and Keith W. Marlow. Automatic analysis of gamma-ray spectra from germanium detectors. *Nuclear Instruments and Methods*, 137(3):525–536, 1976.

[134] DE Cullen, JH Hubbell, and L Kissel. EPDL97: The evaluated photon data library, 97 version. *UCRL-50400*, 1997.

[135] CH Westcott, WH Walker, and TK Alexander. Effective cross sections and cadmium ratios for the neutron spectra of thermal reactors. Technical report, 1959.

[136] Kris Coolsaet. Cyclic difference sets, 1996. Available at http://www.inference.phy.cam.ac.uk/cds/part3.htm.

[137] Domenick Calabro and Jack K. Wolf. On the synthesis of two-dimensional arrays with desirable correlation properties. *Information and Control*, 11(5):537–560, 1967.

[138] Stephen R. Gottesman and E. E. Fenimore. New family of binary arrays for coded aperture imaging. *Applied Optics*, 28(20):4344, oct 1989.

[139] W L Rogers and R S Adller. Time-coded aperture design for nuclear medicine imaging: a study of signal-to-noise ratio. *Applied optics*, 21(2):324–333, 1982.

[140] Alfred O. Hero, Jeffrey a. Fessler, and Mohammad Usman. Exploring estimator bias-variance tradeoffs using the uniform CR bound. *IEEE Transactions on Signal Processing*, 44(8):2026–2041, 1996.

[141] L. J. Meng and N. H. Clinthorne. A modified uniform Cramer-Rao bound for multiple pinhole aperture design. *IEEE Transactions on Medical Imaging*, 23(7):896–902, 2004.

[142] J Mattingly. Polyethylene-reflected plutonium metal sphere: Subcritical neutron and gamma measurements. *SAND2009-5804 Revision*, 2009.

[143] A Sitek. Reconstruction of emission tomography data using origin ensembles. *IEEE transactions on medical imaging*, 2011.

[144] Eckert and Ziegler Reference and Calibration Sources, 2007. Available at http://www.ezag.com/.

[145] Sung Cheol Park, Min Kyu Park, and Moon Gi Kang. Super-resolution image reconstruction: a technical overview. *IEEE Signal Processing Magazine*, 20(3):21–36, May 2003.